Aptasensor development for detection of virus in water

Kirkegaard, Julie

Publication date:
2016

Document Version
Publisher's PDF, also known as Version of record

Aptasensor development for detection of virus in water

Julie Kirkegaard
PhD Thesis September 2016

DTU Nanotech
Department of Micro- and Nanotechnology

Aptasensor development for detection of virus in water

Julie Kirkegaard
MSc Biomedical Engineering

PhD Thesis

Supervisors:
Noemi Rozlosnik, Associate Professor, DTU Nanotech
Lars E. Larsen, Professor, DTU VET
Winnie E. Svendsen, Associate Professor, DTU Nanotech

DTU

PolyMeDiag

DTU Nanotech
Department of Micro- and Nanotechnology
DTU Vet
National Veterinary Institute

Preface

This thesis was done in accordance with the PhD school of the Technical University of Denmark, DTU, to fulfil the requirements for obtaining the PhD degree. The PhD was conducted as part of the AquaVir project funded by the European Union under the 7th Framework Programme (Grant Agreement No: 604069, Call identifier: FP7-NMP-2013-SMALL-7).

The PhD project was initiated on the 1^{st} of October 2013 and ended on the 30^{th} of September 2016. The PhD project was done with supervision of main supervisor Associate Professor Noemi Rozlosnik, DTU Nanotech, and co-supervisioned by Professor Lars Erik Larsen, DTU Vet, and Associate Professor Winnie E. Svendsen, DTU Nanotech.
The research related to the chip development was done in the PolyMeDiag group at DTU Nanotech. The research related to the virus culture, purification and molecular biological testing was mainly performed at DTU Vet, Virology Section and partially at DTU Nanotech.

The research, text and graphics presented in this PhD Thesis are my work. It is clearly stated where the scientific work is a collaboration with others or where research from other scientists have been cited or used as an inspiration.

The reader of this thesis is expected to have a basic knowledge in biosensors, electrochemical impedance spectroscopy and virology.

DTU Nanotech,
Kongens Lyngby, September 2016

Abstract

Contamination of water by waterborne viruses causes serious health issues worldwide. The current virus detection methods are expensive and time-consuming and require access to well-equipped laboratories. This thesis describes the development of an impedimetric all-polymer aptasensor for detection of three types of waterborne viruses: norovirus, rotavirus and hepatitis A virus. The development of the aptasensor involved sample preparation for aptamer selection of rotavirus and hepatitis A virus, an iterative design process of the aptasensor, investigation of the surface immobilisation of aptamers and finally an impedimetric electrical characterisation of the sensor.

The sample preparation of the rotavirus was based on purification and biotinylation of the virus to meet the requirements of the aptamer selection process. The selection process, performed by an external collaborator, was based on streptavidin coated magnetic bead separation, hence the needed biotinylation. It was found that the BPH linker gave the highest yield when the biotinylated rotavirus were immobilised onto the beads.

The design of the viral aptasensor was determined by an iterative design process. The final chip design was based on a SD card design with an injection moulded PC substrate and lid. The electrodes were screen-printed PEDOT:PSS.

The surface immobilisation of aptamers through UV cross-linking onto different polymer substrates was tested. As the success of this step is crucial for the aptasensor specificity and performances, the surface immobilisation was throughly investigated. The aptamer UV cross-linking onto PEDOT:PSS was promising. Furthermore, some passive absorption of the aptamers onto the PEDOT:PSS was found.

The impedimetric electrical characterisation of the aptasensor chip was done with different media salinity and different pH values. The impedimetric measurements of the different media salinity showed the expected behaviour with the greatest change present in the region representing the solution resistance. The pH measurements did not show any significant change of the impedance, hence the chip was stable in the measured pH range, which corresponds to the expected pH range of water samples.. The stability of the aptasensor chip was tested over a 2 week period in continuous flow. It was found that the electrodes were not damaged or degraded during the time period, as a constant impedance signal was measured.

A solid foundation for the further development of the aptasensor for viral detection has been established and from this a new cheap and simple viral detection method can emerge.

Resumé

Forurening af vand ved vandbårne virus forårsager alvorlige sundhedsmæssige problemer på verdensplan. De nuværende virus detektions metoder er dyre og tidskrævende og kræver adgang til veludstyrede laboratorier. Denne afhandling beskriver udviklingen af en impedans baseret polymer aptasensor til påvisning af tre typer af vandbårne virus: norovirus, rotavirus og hepatitis A virus. Udviklingen af aptasensoren involverede prøveforberedelse til aptamer selektion af rotavirus og hepatitis A virus, en iterativ design proces af aptasensoren, undersøgelse af overfladen immobilisering af aptamerer og endelig en impedans baseret elektrisk karakterisering af sensoren.

Prøveforberedelsen af rotavirus var baseret på oprensning og biotinylering af virusset for at opfylde kravene til aptamer selektionsprocessen. Selektionsprocessen, udført af en ekstern samarbejdspartner, var baseret på separation af streptavidin overfladebehandlede magnetiske partikler, deraf nødvendigheden af biotinyleringen. Det blev konkluderet, at BPH linkeren gav det højeste udbytte, når de biotinylerede rotavirus blev immobiliseret på partiklerne.

Designet af den virale aptasensor blev bestemt ved en iterativ designproces. Det endelige chip design var baseret på et SD kort design med et sprøjtestøbt PC substrat og låg. Elektroderne var serigrafitrykt PEDOT:PSS.

Overflade immobilisering af aptamerer gennem UV krydsbinding på forskellige polymersubstrater blev testet. Eftersom succesen af dette trin er afgørende for aptasensorens specificitet og ydeevne, blev overflade immobilisering grundigt undersøgt. UV krydsbindingen af aptamerer på PEDOT:PSS var lovende. Desuden blev der fundet passive absorption af aptamerer på PEDOT:PSS.

Den impedans baserede elektriske karakterisering af aptasensor chippen blev udført med medier af forskellig saltindhold og forskellige pH-værdier. De impedans baserede målinger af forskellige saltindhold viste det forventede signal med den største ændring i regionen der repræsenterer den elektriske modstand af opløsningen. pH-målingerne viste ingen signifikant ændring af impedansen, dermed var chippen stabil i det målte pH-område, som svarer til det forventede pH-område på vandprøver. Stabiliteten af aptasensor chippen blev testet over en 2 ugers periode under kontinuerlig væskestrøm. Det blev konstateret at elektroderne ikke blev beskadiget eller nedbrudt i tidsperioden, da et konstant impedans signal blev målt.

Et solidt fundament for videre udviklingen af aptasensoren til viral detektion er blevet etableret, og ud fra dette kan en ny billig og enkel viral påvisningsmetode opstå.

Acknowledgements

I would like to acknowledge all of the people involved in my PhD project. My supervisors Noemi Rozlosnik, Lars E. Larsen and Winnie E Svendsen for their excellent supervision and great input to my scientific work. My colleagues from the PolyMeDiag group, Solène Cherré and Mark H Olsen with whom I have engaged in interesting discussions and had the pleasure to share office and laboratory with for the last three years. I would also like to acknowledge all of my other colleagues at DTU Nanotech for a nice working environment and great lunch discussions. Furthermore, a special thanks to Tanya Bakmand for providing a good environment in her home for our thesis writing. I would also like to acknowledge the technicians, Ole, Lotte and Lene, at DTU Nanotech who were always ready to help.
I would also like to acknowledge the people at DTU Vet, especially the group of Lars E. Larsen, for their engagement in my PhD project and for the support and help from researchers and technicians. A special thanks to the technicians Hue and Katrine for their kind support and help with PCR and virus culture. Furthermore, I would like to thank Katharina Lahl, DTU Vet, for providing simian rotavirus and MA104 cells for rotavirus culture.
I would also like to acknowledge all of the partners involved in the EU AquaVir project. Especially, Philips BioCell for their close collaboration during the project. Furthermore, I would like to give special thanks to the University of Rome Tor Vergata, especially Prof. Maurizio Divizia, for their hospitality and close collaboration in norovirus and hepatitis A virus related work. I would also like to thank Ramona Valentina Mateiu, DTU CEN, Center For Electron Nanoscopy, for making TEM images of my rotavirus samples.
Finally, I would like to acknowledge my family for their support during the last three years. Especially Casper who have always been ready to cheer me up during hard times and for his help and input to chemistry related discussions.

Contents

List of Figures

List of Tables

Abbreviations

Abbreviation	Description
A	Adenine
Abs	Absorption
AC	Alternating current
ATCC	American Type Culture Collection
bHAV	Biotinylated hepatitis A virus
BNHS	(+)-Biotin N-hydroxysuccinimide ester
BPH	Hydrazide-PEG4-Biotin
bRV	Biotinylated rotavirus
BSA	Bovine serum albumin
DLP	Double-layered particles
DNA	Deoxyribonucleic acid
dsRNA	Double stranded RNA
C	Cytosine (when used in relation to DNA)
C	Capacitor (when used in relation to electrical components and circuits)
cDNA	Complementary DNA
COC	Cyclic olefin copolymer
CPE	Cytopathic effect
CPE	Constant phase element (when used in relation to electrical components)
CsCl	Cesium chloride
Ct	Cycle threshold
DMSO	Dimethyl sulfoxide
EDC	1-Ethyl-3-(3-dimethylaminopropyl)carbodiimide
EIS	Electrochemical impedance spectroscopy
ELASA	Enzyme linked aptasorbent assay
ELISA	Enzyme linked immunosorbent assay
Em	Emission
FBS	Fetal bovine serum
G	Guanine
h	Hour(s)
HAV	Hepatitis A virus
HRP	Horseradish peroxidase
HSB-T	High salt buffer with Triton X

Hz	Hertz
I	Current
K_d	Dissociation constant
kDa	Kilo Daltons
NoV	Norovirus
OD	Optical density
ORF	Open reading frame
PBS	Phosphate buffered saline
PBS-T	Phosphate buffered saline with Tween 20
PC	Polycarbonate
PCR	Polymerase chain reaction
PEDOT:PSS	Poly(3,4-ethylenedioxythiophene) polystyrene sulfonate
PEDOT:TsO	PEDOT doped with tosylate
PEG	Polyethylene glycol
PET	Polyethylene terephthalate
PCB	Printed circuit board
PMMA	Poly(methyl methacrylate)
PDMS	Polydimethylsiloxane
R	Resistor
rcDNA	Reverse complementary DNA
RNA	Ribonucleic acid
RPM	Revolutions per minute
RT-PCR	Reverse transcription polymerase chain reaction
RV	Rotavirus
SD card	Secure Digital card
SDS	Sodium dodecyl sulfate
SDS-PAGE	Sodium dodecyl sulfate polyacrylamide gel electrophoresis
SELEX	Systematic evolution of ligands by exponential enrichment
SLP	Single-layered particles
SSC	Saline-sodium citrate
ssDNA	Single stranded DNA
ssRNA	Single stranded RNA
T	Thymine
TCID	Tissue Culture Infective Dose
TEM	Transmission Electron microscopy
TMB	3,3',5,5'-Tetramethylbenzidine
TNC buffer	Tris-HCl, NaCl, $CaCl_2$ buffer
TLP	Triple-layered particles
U	Potential
USB	Universal Serial Bus
VLP	Virus-like particle(s)

VP	Viral protein
Z	Complex impedance
Z_{IMG}	Imaginary part of the complex impedance
Z_{RE}	Real part of the complex impedance
2D	Two dimensional
3D	Three dimensional
Symbols:	
ω	Angular frequency
$\times$g	Times gravity
$\varnothing$	Diameter

— 1 —

Thesis introduction and overview

Clean water resources are essential for public health and to ensure a well functioning society. Contamination of water resources by pathogens from e.g. sewage overflow caused by heavy rain or inefficient raw or wastewater treatment cause a serious public health risk. Different waterborne pathogenic microorganisms can be found in the water: viruses, bacteria, protozoa or parasites. Each type demands different sample preparation and detection methods. In this thesis the focus will be on waterborne viruses and development of a new virus detection method of three virus types: norovirus (NoV), rotavirus (RV) and hepatitis A virus (HAV).

Most cases of viral gastroenteritis caused by waterborne viruses in the adult population are caused by NoV [1, 2]. RV is the major cause of gastroenteritis in small children [2, 3]. Especially, children in developing countries suffer from gastroenteritis caused by RV due to bad sanitation and hygiene [2]. Apart from gastroenteritis, hepatitis is one of the major diseases caused by waterborne viruses, where HAV causes 50 % of all cases of hepatitis worldwide [2, 4]. Infected people shed viruses in extremely high numbers, up to 10^{10} and 10^{13} viral particles per gram of stool for patients suffering from HAV infection and gastroenteritis, respectively [1–3, 5].

In the case of viral outbreaks, the concentration of viruses in the wastewater greatly increases and effective water treatment for virus inactivation or removal cannot ensure complete virus removal [2]. This creates a serious health risk since small amount of infectious virus (virions) can cause illness. It is thus important to retain contaminated water from the distribution system before it reaches the consumer i.e. as drinking water or from wastewater irrigated food. Ideally, all raw water treatment plants should continuously monitor the water before distribution to avoid pathogenic outbreaks, but unfortunately that is not the case due to the complexity of virus detection.

Due to their small size, approximately 25-100 nm in diameter, the three viruses,

NoV, RV and HAV, cannot be observed by conventional light microscopy or easily filtered to concentrate the sample. This obstacle challenges the current detection methods. Currently, the most used detection technique is polymerase chain reaction (PCR) where specific genomic section of the virus genome is amplified and detected [2, 6]. All of the conventional detection techniques have common disadvantages: they are time consuming, labor intensive and expensive. Furthermore, they all require a full scale laboratory setting to perform the analysis. New detection techniques, e.g. based on biosensors, that overcomes these disadvantages are thus required. In this thesis the conventional viral detection techniques and the basic knowledge of the three viruses, NoV, RV and HAV, are described in chapter 2.1.

The aim of this PhD project was the development of an aptasensor for the detection of waterborne viruses that can overcome the challenges of the conventional detection methods. The iterative steps involved in the development of the aptasensor is illustrated in figure 1.1. The term *aptasensor* is used when aptamers are used as the biorecognition element in a biosensor. The iterative steps listed in the figure: assay requirements, target selection, aptamer selection, aptasensor selection and aptasensor development, will all be touched upon in this thesis.
The developed aptasensor is an all-polymer sensor with a polymer substrate and conducting polymer electrodes for electrochemical detection. The biorecognition elements of the sensor are aptamers which are single stranded oligonucleotides that can be selected to specifically bind a target molecule, much like the principle of antibodies. The aptamer selection is done through a cyclic process called systematic evolution of ligands by exponential enrichment (SELEX). In this thesis the basic concepts of aptamers, aptamer selection and biosensors are described in detail in chapter 2.2 and 2.3. Furthermore, the present development and use of aptasensors for viral detection will be described in chapter 2.3.
Aptamers specific for NoV have already been developed by Beier *et al.* and Escudero-Abarca *et al.* [7, 8]. This PhD project aims to prepare samples for the development of aptamers that specifically targets the surface proteins of RV and HAV. The SELEX process for the aptamer selection is performed by an external collaborator at Fraunhofer Institute for Cell Therapy and Immunology (IZI), Germany. The selection of the right viral genotypes and serotypes for the aptamer selection is important since each viral subtype has different prevalence and virulence. The work related to selection of the right viral genotype and serotype and the sample preparation for aptamer selection of the RV and HAV are described in chapter 3.
The iterative design and fabrication process for the viral sensor chip is described in chapter 4. Parts of the design and fabrication was done in collaboration with Flusens ApS. The initial chip development was based on previous work done by Kiilerich-Pedersen *et al.*, 2011 and 2013, and Daprà *et al.*, 2013 [9–11].

The surface immobilisation of the biorecognition elements onto the electrodes in the biosensor is of pivotal importance to ensure a successfully working biosensor. Thus, surface immobilisation of the aptamers on the electrode material is explored. The electrode material, poly(3,4-ethylenedioxythiophene) polystyrene sulfonate (PEDOT:PSS), is rather chemically inert, which limits the available methods for aptamer immobilisation. The explored immobilisation method is based on UV crosslinking of the aptamers with the polymer substrate through a specific oligonucleotide tag on the aptamer. The concept behind the UV crosslinking with the specific oligonucleotide tag was initially described in the work of Dufva *et al.*, 2004 and 2006, and Sun *et al.*, 2012 [12–14]. The experimental work related to the surface immobilisation is described in chapter 5. The work related to the ELISA based surface immobilisation was done in collaboration with PhD Solène Cherré.
The experimental work related to the characterisation of the developed aptasensor and electrochemical measurements is described in chapter 6.

In summary, the overall aim of this PhD thesis is the development of an aptasensor for viral detection of NoV, RV and HAV. The thesis also aims at locating the relevant viral genotype and serotype for aptamer development and preparing the viral samples for aptamer development. Furthermore, the aim is to explore the surface immobilisation of the aptamers onto the electrode material and to electrochemically characterise the developed aptasensor.

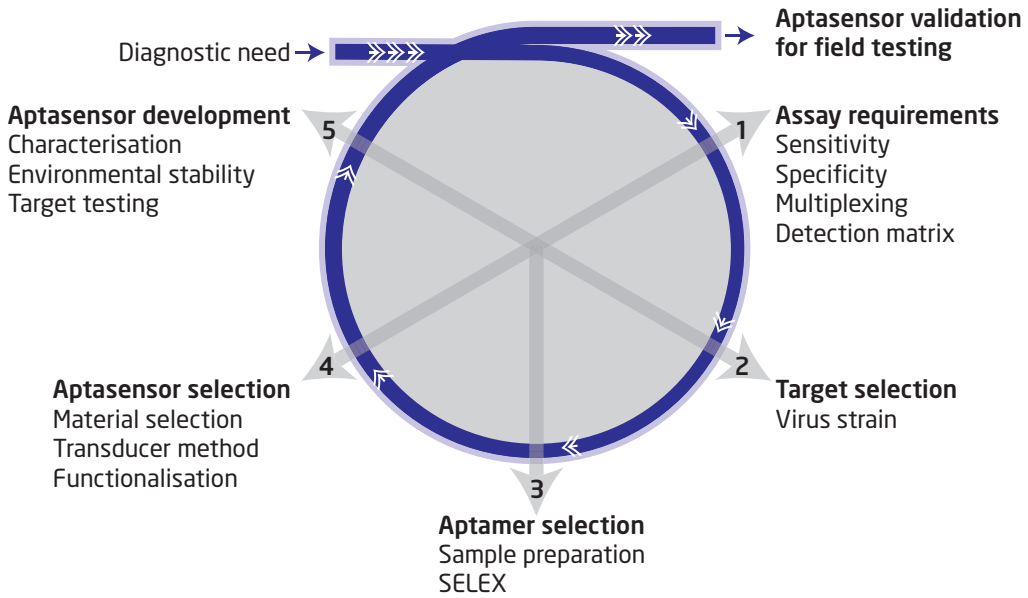

Figure 1.1: *Overview of the iterative steps involved in the aptasensor development for the detection of waterborne virus in environmental samples.*

1.1 Thesis outline

In this section an outline of the thesis is presented. Each chapter is briefly described to give the reader a fast and easy overview of the content and structure of the thesis.

Chapter 2 - Theoretical introduction

This chapter focuses on three main topics: enteric viruses and detection methods, aptamers and biosensors. The theoretical background knowledge needed to understand the practical work of this thesis is presented in the chapter. The chapter also gives the reader an overview of the current status within the field of aptasensors for viral detection.

Chapter 3 - Virus preparation for aptamer selection

The considerations of the relevant viral genotypes and serotypes of RV and HAV for aptamer development are given in this chapter. Furthermore, the viral sample preparation methods for the aptamer development are described.

Chapter 4 - All-polymer aptasensor design and fabrication development

The development of the all-polymer aptasensor chip is described in this chapter. The different iteration steps of the chip design and the chip fabrication are described.

Chapter 5 - Exploring the surface immobilisation of aptamers

This chapter describes the experimental work related to the surface immobilisation of the aptamers. UV crosslinking of the aptamers to the electrodes surface is explored in great detail.

Chapter 6 - Aptasensor characterisation and EIS measurements

The impedimetric characterisation and stability measurements of the aptasensor is described in this chapter.

Chapter 7 - Conclusion and perspective

Concluding remarks of the thesis and future perspectives are given in this chapter.

Appendix A - Step by step protocols and material lists

Appendix B - Aptamer sequences

— 2 —
Theoretical introduction

This PhD thesis touches upon three major topics: enteric viruses, aptamers and biosensors. This chapter gives a short theoretical background introduction to these three topics and gives an overview of the current scientific status within these fields. Enteric viruses are introduced with special emphasis on the three different virus types: norovirus (NoV), rotavirus (RV) and hepatitis A virus (HAV). Furthermore, the detection methods of these enteric viruses in environmental water samples will be described.
This chapter also focuses on aptamers and the selection of these. The usage of aptamers and the advantages and disadvantages compared with antibodies will be discussed.
The last section of the chapter concerns bio- and aptasensors. The section focuses on electrochemical biosensors, aptasensors and aptasensors for viral detection.

2.1 Enteric viruses and virus detection methods

Viruses are very small (20-400 nm) infectious agents [15]. They cannot replicate without a host cell which means that they completely rely on other life forms to replicate [15, 16]. Cells, or viruses, do not have a ribonucleic acid (RNA) genomic proof-reading system which means that RNA viruses are highly prone to genomic mutations and thereby able to generate new viral strains. Once inside the host body, viruses target different cell types for replication depending on the virus type. Viruses contain either deoxyribonucleic acid (DNA) or RNA that code for the proteins needed for virus uptake into host cell and replication and maturation inside the host cell. Furthermore, they are typically host specific i.e. they only infect humans, birds, monkeys, plants or bacteria etc., although some viruses can infect

both humans and animals [16].
Viruses that are shed through the human faeces may cause gastroenteritis or hepatitis through ingestion of water contaminated with viruses of faecal origin [17]. The group of viruses that infect the human host through the faecal-oral route and primarily target and multiply in the cells of the gastrointestinal tract are called enteric viruses [16, 17]. Figure 2.1 shows a schematic overview of the faecal-oral route of infection. NoV, RV and HAV are all part of the group of enteric viruses [16]. All of these viruses are shed in the faeces and both NoV and RV replicate in the epithelial cells of the gastrointestinal tract while HAV replicates in the hepatocytes of the liver. Typically, waterborne viruses are very stable since they do not have a lipid envelope - so called non-enveloped viruses [6].
The major causes of acute non-bacterial gastro-enteritis worldwide in adults and infants are infections caused by NoV and RV, respectively [3, 18]. Outbreaks of NoV are usually observed during the winter months [18]. Infection with HAV can cause acute hepatitis. It is estimated that HAV is responsible for 50 % of acute viral hepatitis cases in the world [2].
Ingestion of virus polluted water can thus lead to severe illness and potentially lead to a lethal outcome. NoV, RV and HAV are shed through the faeces in very high numbers from infected people. Virus levels as high as 10^{10} to 10^{13} viral particles per gram of stool have been reported [1–3, 5]. It is thus important to detect these viruses in the water before they enter the human body and cause new cases of infection [2]. Furthermore, the infectious dose of these virus are as low as 10-100 virus particles [1, 4]. Due to the high prevalence of infections with these three viruses they were chosen as the focus for this PhD thesis.

2.1.1 Enteric viruses: norovirus, rotavirus and hepatitis A virus

As described above, the enteric viruses have similar route of transmission. Figure 2.1 illustrates the faecal-oral route of transmission of enteric viruses. Individuals are infected via the faecal-oral route after ingestion of food or water contaminated with faeces or vomit [1, 4]. Thus, individuals drinking contaminated water or eating food cultivated with contaminated water have a risk of getting infected. Furthermore, infection can be either symptomatic or asymptomatic leading to challenges in preventing the spread of viruses. Secondary cases of infection can also occur after person-to-person contact [4, 18].
This section provides a description of the three enteric viruses.

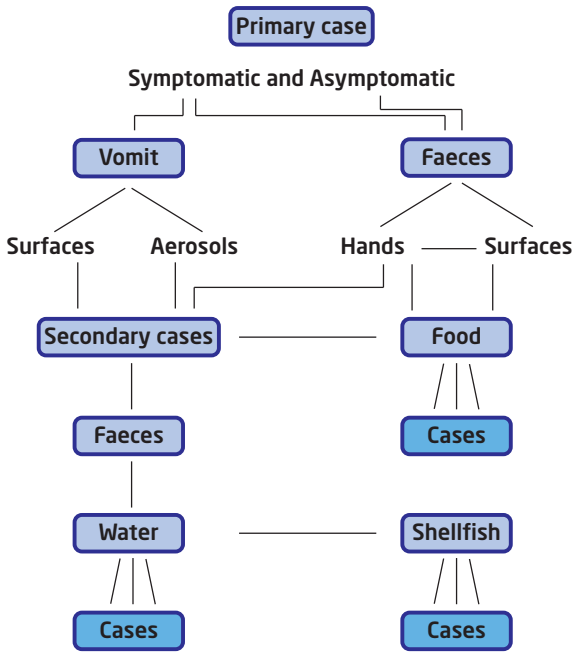

Figure 2.1: *Routes of transmission of enteric viruses [1]. Primary cases of infection with enteric viruses can be either symptomatic or asymptomatic. Primary cases can directly lead to new cases of infection through food contaminated from viruses from a single individual. Secondary cases can also occur through person-to-person contact, by contaminated surfaces or through aerosols. Water contaminated with viruses can also lead to infection. Furthermore, consumption of shellfish that filter virus contaminated water can cause infection.*

NoV

NoV belongs to the *Caliciviridae* family. The virus is a non-enveloped icosahedral positive sense single stranded RNA (ssRNA) virus [19]. The NoV particle has a diameter of 30-38 nm [1]. NoV is divided into five major genogroups: GI through GV where GI, GII, and GIV infect humans [19]. Furthermore, genogroups GI, GII, and GIII are subdivided into 8, 19, and 3 genotypes [19]. It is thus evident that NoV expresses a great genetic diversity. Genogroup GII was associated with 89 % of NoV cases in outbreaks in Europe from 2000-2005 with the predominating genotype GII.4 in 56 % of the cases [19].

The virus capsid consists of the major capsid protein VP1 (90 dimers per virion) and the minor capsid protein VP2 (one or two copies per virion) [20]. Figure 2.2 shows the genomic representation and the capsid structure of the NoV virion. The genomic sequence of the protruding region of VP1 that is present on the virion surface shows the highest genomic variability [19]. It is thus suspected that this region

is the dominating region for formation of antigenic sites and receptor binding sites on the virion [19, 20]. However, the basic understanding of the virus replication is limited since the human NoV cannot be cultured *in vitro* due to the inability of identifying receptor-bearing cell lines [19, 20]. Currently, only a successful cell culture system for murine NoV exists [21]. VP1 can self-assemble into virus-like particles (VLP), without RNA and VP2, and can thus be used as a model virus for NoV research [20].

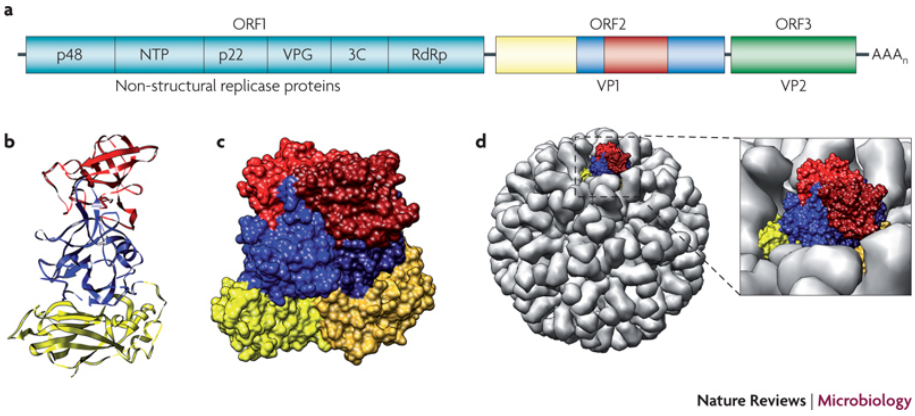

Figure 2.2: *Norovirus capsid structure.* ***a)*** *Structural representation of the NoV genome with the three open reading frames (ORF). ORF1 encodes for the non structural proteins. ORF2 and ORF3 encode for the structural proteins VP1 and VP2, respectively. The colour coding of VP1 represents the genomic sequence for the different protein domains illustrated in* ***b*** *and* ***c****. The shell domain is represented in yellow while the red and blue domain represents protruding domain of VP1. The red subdomain is present on the virion surface thus susceptible to the highest genomic variability.* ***b)*** *Ribbon diagram of the VP1 structure with colour coded domains.* ***c)*** *VP1 dimer.* ***d)*** *Illustration of the the NoV virus like particle formed by 90 VP1 dimers. Figure from [22].*

On a global scale, NoV is the leading cause of nonbacterial gastroenteritis in humans and it usually occurs in outbreaks [19, 20, 23]. NoV outbreaks can occur with attack rates as high as 70 % [1]. It infects people of all ages and rarely causes death [1]. The most common symptoms of infections are diarrhoea, vomiting, fever, and abdominal pain. After an incubation time of approximately 12-72 hours the illness often lasts 1-4 days but viral particles can be found in the patients and shed for up to two weeks [1]. The number of virus particles in the faeces and/or vomit is very large ($>10^9$ particles/g) [1]. Furthermore, the infectious dose of NoV is estimated to be in the order of 10-1000 virus particles and viruses can be infectious years after secretion from the human body [1, 24]. All of these factors combined

illustrates why NoV is the dominating cause of non-bacterial gastroenteritis world wide and why it requires efficient monitoring.

RV

RV belongs to the family of *Reoviridae*. The genome of the virus comprises of 11 double stranded RNA (dsRNA) segments [25]. The RV has an icosahedral structure with a non-enveloped triple-layered protein capsid surrounding the dsRNA. The RV diameter is around 100 nm for the mature virus particle [25]. The capsid of the virion is composed of six structural proteins (VP1-4, VP6-7). VP6 is the intermediate capsid protein which interacts with the core proteins while VP4 and VP7 are the outer capsid proteins [3]. Figure 2.3 illustrates the structure of the virion with the structural and non-structural proteins and the 11 genomic segments of the virus coding for the proteins [3].

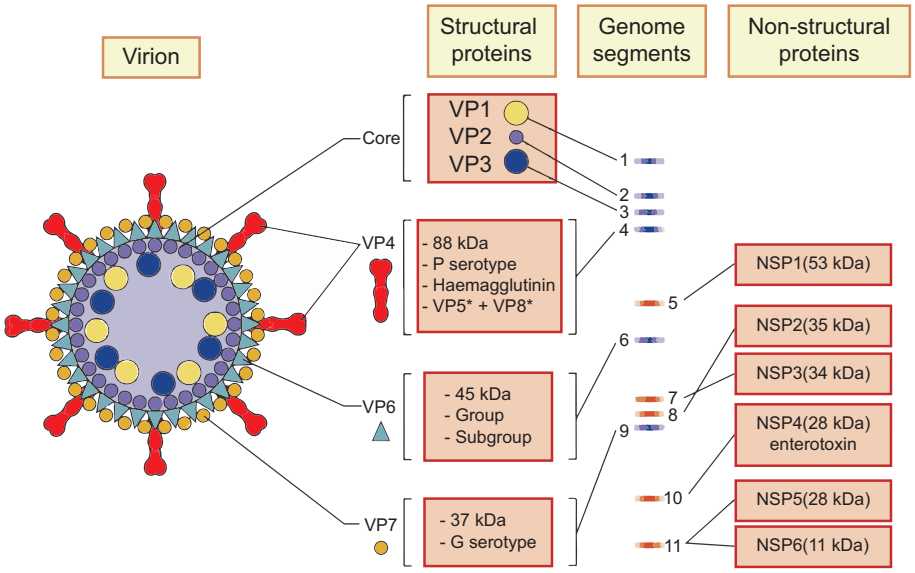

Figure 2.3: *Illustration showing the relationships between the structure of the RV virion and the dsRNA genomic segments. The mature virus particle has a triple-layered capsid structure that surrounds the 11 dsRNA segments. The three layers of the capsid are composed of an outer layer (VP4 and VP7), an intermediate layer (VP6) and an inner core layer (VP1-3) [25]. Figure from [3].*

Seven different serogroups (A-G) of RV have currently been identified. The structural proteins carry epitopes specifying these groups. Groups A, B, and C can cause human infection [3]. Group A is known to cause the most cases of human RV infections [3]. Group A RV is distinguished by two main subgroups, G types, and

P types. G types consist of different VP7 specific serotypes while P types consist of different VP4 specific genotypes [3]. G genotypes and G serotypes correlate to each other and no distinction between the two are made. On the other hand, the correlation between the P genotypes (denoted in square brackets) and serotypes have not been shown completely and the two are thus distinguished [3]. At least 73 different strains of G/P genotype combinations have been shown to infect humans [26]. Four strains are responsible for about 75 % of all human infections: G1P[8] (52 %), G2P[4] (11 %), G4P[8] (8 %), and G3P[8] (3 %) [3].

Group A RV is the dominating cause of acute infantile gastro-enteritis in the world but the virus can also, though rarely, infect adults [3, 25]. RV infection can be lethal especially in developing countries due to poor sanitation and limited medical help. It is estimated that each year 2 million children under the age of 5 years die from diarrhoeal diseases where 40 % is caused by RV [3, 25]. In developing countries 40-50 % of hospitalisations of children is due to a diarrhoeal disease caused by RV [3]. Infections usually occur during cooler months in the winter period [25]. The incubation time is approximately 48 h, or less, with onset of the most common symptoms: fever, diarrhoea and dehydration that lasts for approximately 3 days [25]. Group A RV have been adapted to cell culture and can thus be cultured *in vitro*. A cytopathic effect (CPE) caused by the virus infection in the cells is visible. As a positive consequence of the successful RV culture several live attenuated vaccines produced from cell culture have been licensed [25].

HAV

HAV belongs to the *Picornaviridae* family. The virus is a non-enveloped virus with an icosahedral symmetry of 27-32 nm in diameter [4, 27]. The virus genome is a positive sense ssRNA [27]. The virion structure is composed of four structural proteins VP1-4, where VP1-3 are expressed at the surface of the capsid. Only one HAV serotype exists and within this serotype several strains are found that can be distinguished by genomic sequencing [27]. Genotype I represents most of the human infections and genotype III most of the remaining [27]. Both genotypes I and III are divided into subgroup A and B. HAV IA is the dominating subgenotype since 80 % of isolates from infected individuals were HAV IA [28]

HAV infects people of all ages but infection is more predominant in children and young adults and rarely with a lethal outcome [27]. HAV enters the body via the gastrointestinal tract, replicates in the liver hepatocytes and is excreted in the faeces [27]. The primary symptoms of acute viral hepatitis caused by HAV infection are jaundice, fever, vomiting and diarrhoea [27]. The incubation period is 10-50 days but viruses are shed in faeces before the onset of clinical symptoms and can thereby

lead to secondary cases [27].

HAV can be cultured *in vitro*, but only in primary cells, and the culture is not suited for routine work since the culture and isolation can take up to weeks, successful culture is difficult and CPE is normally not present [4, 27]. The development of the culture system has led to the development of a successful HAV vaccine with inactivated virus. It is possible to inactivate the HAV with formaldehyde without modifying the surface structure of the virion thus preserving the antigenic epitopes of the virion [29, 30].

HAV virions are very stable viral particles since infectivity is preserved when heated up to 80 °C and pH values down to 2 [30]. Furthermore they can remain infectious when dried and stored at 25 °C, humidity 45 %, for at least 1 month and remain infectious for days to several months in wastewater [27]. This illustrates why HAV monitoring is extremely important in relation to public health.

2.1.2 Conventional detection methods for environmental water samples

Once faecal matter, with infectious viruses, are present in the water environment there is a risk of new cases. Even though viruses are diluted in the water they can still cause infection, especially considering the low infectious dose, but the low concentration is impeding detection. A concentration of the water sample before detection is thus necessary. The detection of viruses in environmental water samples is commonly done with molecular detection methods but other techniques exist as well. Faecal indicators have also been used as an indirect way of virus detection. In this section the different techniques will be described.

Concentration and recovery of virus from environmental water samples

Concentration and recovery of enteric viruses from water samples is critical and necessary prior to water analysis due to the low concentration of viruses present in the water. Water sample volumes ranging from 1-1000 L must be reduced to a few mL to enable analysis. Concentration of viruses can be done by utilising the electrokinetic properties of the virus by electropositive or electronegative filters or by size exclusion by ultrafilters [18, 31]. Electronegative filters, e.g. nitrocellulose membranes (Millipore), require acidification and addition of salts to the water sample which is difficult for large water samples [31]. Electropositive filters do not require any pretreatment of the sample but filters are usually more expensive than electronegative filters [31]. The electropositive glass wool filter is an exception to the high cost but

unfortunately glass wool filters show great variance in virus adsorption and hence large difference in virus recovery [31]. Virus concentration can also be performed on the basis of size exclusion by ultrafiltration. Ultrafiltration does not require any pretreatment or adjustment of the water sample but pretreatment of the filter can increase the recovery [31]. Ultrafiltration requires expensive equipment which is not suited for field testing [31]. The virus concentration by the different filters is followed by an elution step, or a backflushing step for ultrafilters, which recovers the viruses from the filters [18, 31]. The elution is performed by an elution buffer which can either be an organic solution containing beef extract and/or glycine or an inorganic solution e.g. sodium polyphosphates or sodium hydroxide [31]. The filter eluate can be further concentrated to reduce the sample volume to an even smaller volume. As an alternative to the filter based concentration methods ultracentrifugation of the virus samples can be performed. Ultracentrifugation is centrifugation with forces $\geq$ 100,000 $\times$g [31]. Due to the small size of the enteric virus ($\varnothing$ 25 nm - 100 nm) the high gravitational forces are necessary in order to exceed the forces needed to pellet the viruses. The ultracentrifugation method is not suitable for large volumes ($>$ 0.5 L) and requires expensive and delicate equipment. The concentration and recovery of virus from environmental samples will not be covered more extensively in this PhD thesis. For a more elaborate description of the concentration and recovery of enteric viruses from water the reader is referred to the review by Ikner *et al.*, 2012 [31].

Virus detection methods of environmental water samples

Virus analysis of environmental samples is a difficult task. The methods for virus detection are numerous and the current techniques are costly, slow and requires trained personnel and specialised laboratory facilities. The most commonly used methods are: molecular detection methods, immunological methods and electron microscopy [18]. Traditional cell culture infectivity assays can also be used to detect the virus but they require a cell culture system where viruses cause a CPE. Furthermore, human faecal indicators have also been proposed as an indirect method for enteric viral detection in the environment but the correlation between the presence of faecal indicators and enteric viruses have been questioned by experts in the field [6]. This section focuses on the three most common detection methods.

Transmission electron microscopy (TEM) is a microscopical method with a sub nanometer resolution. During TEM a beam of accelerated electrons is shot against the sample to make a high resolution image of the sample. Identification of viruses with TEM can be performed rather fast but it requires a high concentration of virus in the sample i.e. a high virus titer (virus/mL) and the sample preparation is time consuming. TEM can be combined with immunological methods, e.g. to aggregate

virus particles, thereby enabling analysis of samples with a lower virus titer. Although lower titer values can be used, the immune TEM (IEM) still requires a virus titer of 10^5 - 10^6 for NoV [18]. The IEM technique was used to discover NoV in 1972 from an outbreak in Norwalk, Ohio, in October 1968 [32]. RV expresses a characteristic surface morphology making this virus type easily distinctive from other virus types when analysing samples with TEM. On the other hand, NoV and HAV do not show characteristic surface morphologies thereby making identification difficult [18]. TEM images of RV, NoV and HAV can be seen in figure 2.4. Furthermore, the

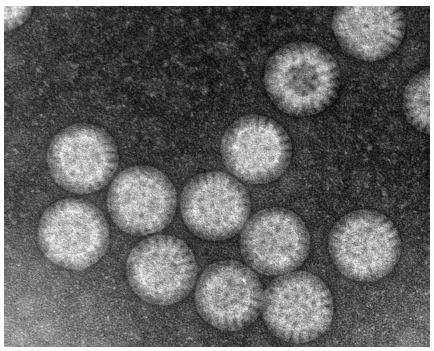

(a) *Rotavirus*

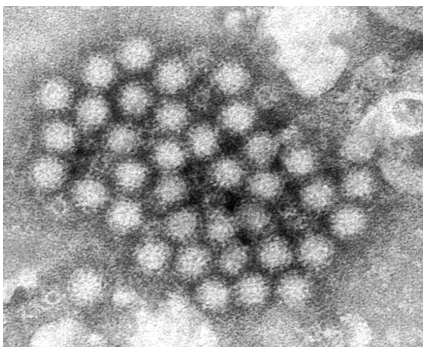

(b) *Norovirus*

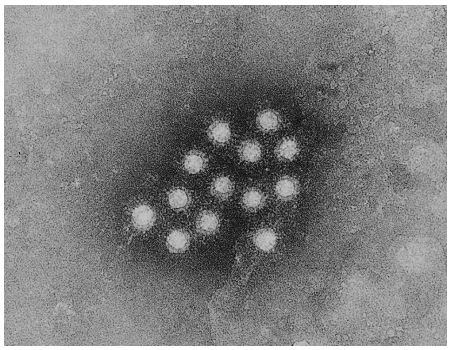

(c) *Hepatitis A virus*

Figure 2.4: *TEM images of rotavirus, norovirus and hepatitis A virus. The characteristic morphological pattern of the RV can be observed on image 2.4a. The The diameter of the RV in this image is around 80 nm. The images 2.4b and 2.4c show no distinct morphology of the NoV and the HAV thus preventing virus distinction by EM. The diameters of HAV and NoV are between 27 and 38 nm. The RV image was made by Ramona Valentina Mateiu, DTU CEN, Center For Electron Nanoscopy, from a TLP RV sample described in chapter 3.2. Images of NoV and HAV were obtained from Centers for Disease Control and Prevention, Public Health Image Library, http://phil.cdc.gov/ .*

TEM equipment is very expensive and must be handled by a trained microscopist [18]. TEM is usually not used for environmental samples, but rather for clinical

samples, due to the disadvantages and requirements of high titer values [18].

The most commonly used immunological method for virus detection is the enzyme linked immunosorbent assay (ELISA). ELISA utilises the antigen-antibody specific interactions and can thus detect viruses with high specificity [18]. Figure 2.5 illustrates the principle of a colorimetric sandwich ELISA. The assay is performed in a microtiter well plate where target (antigen) specific capture antibodies are immobilised in the wells by passive absorption. The antigen-capture antibodies capture the target virus and secondary detection antibodies, conjugated with horseradish peroxidase (HRP), bind to the target. When a 3,3',5,5'-Tetramethylbenzidine (TMB) substrate is added HRP reacts with the TMB substrate and a blue colour develops. When colour development is sufficient the reaction is stopped and the light absorbance (optical density (OD)) through the well is measured. The OD value can be used to estimate the amount of target virus present in the sample. If the target virus is not present the capture antibody does not bind anything and no colour development occurs in the well. The detection method in the ELISA can also be based on fluorescent detection.
The antigen-antibody specific reaction in ELISA limits the use and increases the complexity of the assay since antibodies for each specific virus strain of interest must be included in the assay. Like TEM, the immunological methods is commonly not used for environmental water samples due to the low concentrations of virus in the samples [18].

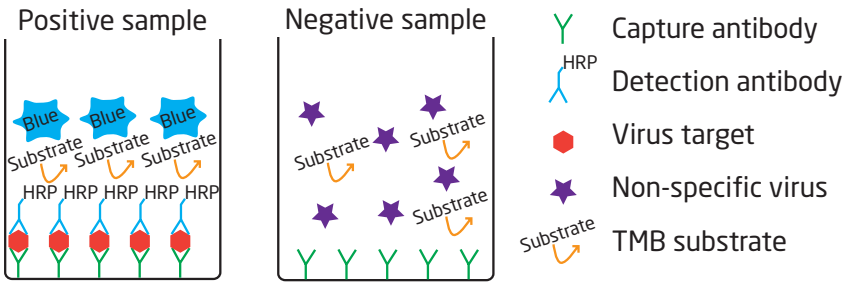

Figure 2.5: *Principle of a sandwich ELISA. The assay illustrated in the figure is a colorimetric assay performed in a microtiter well plate. The assay utilises the enzymatic reaction between the enzyme HRP and the TMB substrate to make a blue colour development when the target virus is present. A capture antibody captures the target virus and a HRP conjugated antibody binds to the target virus. TMB substrate is added to the well and a colour development indicates the amount of target present in the sample by measuring the light absorbance through the well. If there is no target virus or another non-target specific virus is present the capture antibody does not bind anything and no colour development is seen when the TMB substrate is added.*

The most widely used method used for virus detection of environmental water samples is the molecular detection method: real-time reverse transcription polymerase chain reaction (RT-PCR). Real-time RT-PCR is a very sensitive detection technique [6]. During the real-time RT-PCR reaction the genomic material of the virus is exponentially amplified and detected by fluorescent markers. Real-time RT-PCR has a higher sensitivity and reproducibility than conventional PCR where the genomic detection is performed by gel electrophoresis after 30-40 PCR cycles. The PCR analysis is a temperature cyclic process with distinct reaction steps: annealing/hybridisation of primers, enzymatic extension of the DNA with polymerase and finally denaturation of the double DNA strand. The initial step in the RT-PCR analysis is to transcribe the RNA into complementary DNA (cDNA) since the PCR analysis relies on the amplification of DNA. RT-PCR is thus applied to RNA viruses. Figure 2.6 illustrates the principle of the real-time RT-PCR reaction and shows a typical result. After each PCR cycle the amount of genomic material is doubled which means that after 40 cycles 2^{40} cDNA copies are made. The amount of genomic material is measured after each cycle through a fluorescent probe, a TaqMan probe in the figure, and fluorescence is plotted against the cycle number. A threshold value determines whether or not a sample is considered positive. The cycle number at which the fluorescence value increases above the threshold is called the cycle threshold (Ct) value. The Ct value is used as a measure of how much DNA was present in the initial sample, thus a low Ct value means a high DNA concentration in initial sample and vice versa. After PCR analysis the genomic product of the analysis can be sequenced and the genotype of the analysed viral strain can be determined which is an advantage for environmental monitoring.
Although real-time RT-PCR is a powerful tool for virus detection some limitations of the technique do exist. It is important to emphasise that real-time RT-PCR can only be applied to known genetic sequences since the PCR reaction relies on carefully selected primers and probes. This means that the genetic sequence of the virus must be known in order to detect it with RT-PCR. The used primers must be carefully selected to cover a broad range of virus genotypes [18]. The primer selection can thus be challenging especially related to NoV that has a great genetic diversity. Furthermore, PCR only detects genomic material and cannot distinguish between infectious and non-infectious virus particles as long as the genomic sequence of the viral genome is intact. Environmental water samples may contain real-time RT-PCR inhibitory substances e.g. humic acids or beef extract from the pre-concentration [2, 18, 31]. In order to remove or reduce the amount of these inhibitory substances the RNA of the viruses is extracted from the samples before performing the RT-PCR. RNA extraction can be done by e.g. commercial available silica membrane columns but many other methods exist. Even though virus detection with real-time RT-PCR is challenging and standardised common assays does not exist it is still the preferred method for environmental viral analysis.

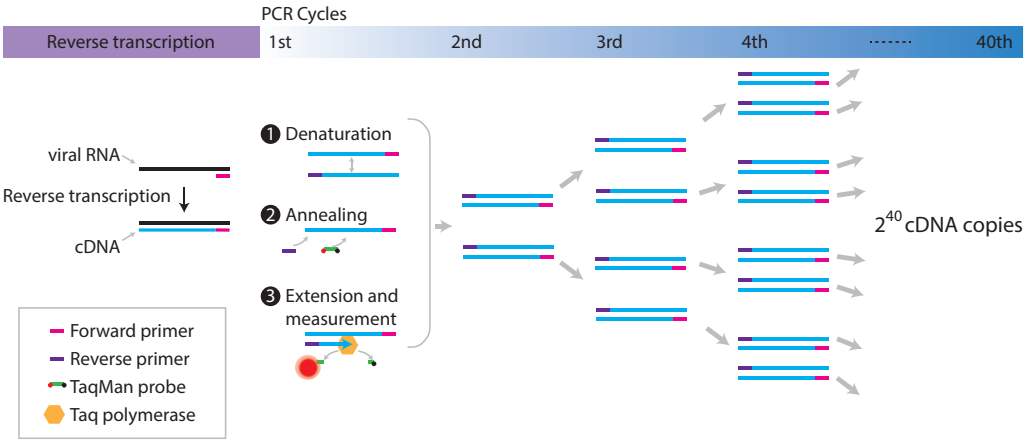

(a) *Principle of real-time RT-PCR*

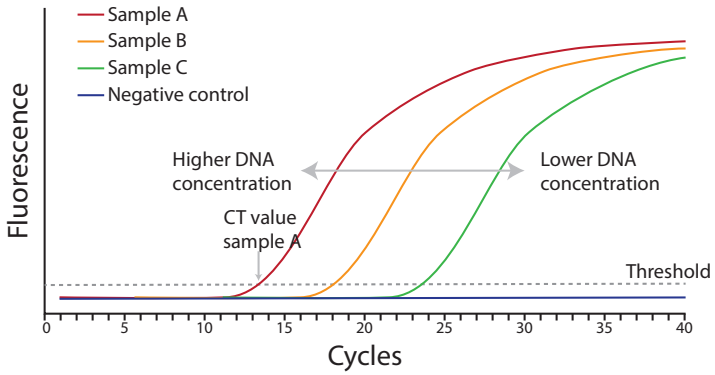

(b) *Schematic illustration of a real-time PCR result*

Figure 2.6: ***(a)*** *Principle of real-time RT-PCR. Viral RNA must be transcripted into cDNA for PCR analysis since polymerase only extends DNA and not RNA. Once transcripted into cDNA the cyclic process of PCR is performed accordingly: 1) denaturation of double stranded DNA (at 95 °C), 2) annealing of primers and TaqMan probe (typically between 45-60 °C) and 3) extension of cDNA with Taq polymerase and fluorescence measurement (typically at 72 °C). The TaqMan probe has a fluorescent label and a quencher. The Taq polymerase cuts the TaqMan probe and thereby separates the fluorescent label and the quencher. Other fluorescent techniques can also be used in real-time PCR like SybrGreen that fluoresces when bound to double stranded DNA. The SybrGreen method is not sequence specific like the TaqMan probe and is thus not preferred.* ***(b)*** *A schematic illustration of a real-time PCR result. The fluorescence is measured at the end of each PCR cycle and plotted against cycle number. A fluorescent threshold value determines when a sample is considered positive. The Ct value of a sample represents the cycle number where the fluorescence is above the threshold value. The Ct value is a measure of relative DNA concentration i.e. the lower the Ct value, the higher the initial DNA concentration.*

2.2 Aptamers

Aptamers are single stranded oligonucleotides folded into a three dimensional (3D) structure that recognise a specific target with high affinity and specificity [33]. The *in vitro* selection of aptamers was first published in 1990 by Tuerk & Gold and Ellington & Szostak, independently [34, 35]. The initial selected aptamers were RNA aptamers but DNA aptamers have since been selected. DNA aptamers are more chemically stable than RNA aptamers but their specificity and affinity do not differ [36]. Both RNA and DNA aptamers have been selected to bind many different targets from cell populations, proteins to small molecules and ions [33, 37, 38]. Furthermore, aptamers have been selected to bind non-immunogenic molecules and toxic targets which is not possible with antibodies [33, 38, 39]. Aptamers can be used as a substitution or replacement of antibodies in biosensing applications or in ELISA but they can also be used in other applications, e.g. as therapeutic agents or in basic medical research [36, 40–42]. The dissociation constant, K_d, for aptamer-protein complexes typically lies in the low nanomolar range, much like antibodies (nM to pM) [38, 41, 43].
Aptamers have many advantages compared to antibodies, in the following these will be described. Aptamers are selected *in vitro*, independent of laboratory animals or cell lines [39]. Once selected and produced no, or little, batch to batch variation is anticipated since aptamers are produced by chemical synthesis and purified [36, 39]. Aptamers are relatively small in size (10-15 kilo Daltons (kDa)), compared to antibodies (around 150 kDa), which means that they can access epitopes otherwise inaccessible to antibodies [37–39]. Their small size is also an advantage in electrochemical biosensing applications where aptamers are immobilised on to the electrode surface and target binding must take place close to the electrode surface to ensure a good signal. Aptamers can enter and function inside the cell which allows for labelling of intracellular molecules to study intracellular mechanisms [38, 39]. Since aptamers are oligonucleotides they are not sensitive to temperature changes as they can be denatured and renatured [36, 37, 39]. Finally, aptamers can be easily modified in order to enhance their stability in fluids like body serum but also to ease immobilisation or detection by e.g. fluorescence [36, 39, 42]. Although, labelling or modifying aptamers with different functional groups cannot always be done without consequences as reduction in aptamer affinity after modifications have been shown [38, 41]. All of these advantages make aptamers highly interesting as binding molecules but it is important to anticipate that very few aptamers have been selected compared to antibodies. Antibodies are still considered the gold standard for many applications with standardised protocols but aptamers are without doubt getting more and more attention due to their obvious advantages over antibodies.

Aptamers are selected from large and complex libraries of random oligonu-

cleotides sequences and the selection is typically done by a process entitled systematic evolution of ligands by exponential enrichment (SELEX) [34]. The SELEX process is described in section 2.2.1.
As this thesis focuses on aptamers and viruses, especially enteric viruses, the current scientific advancement within the field of aptamers selected against viral targets will be described in section 2.2.2.

2.2.1 The selection of aptamers by SELEX

SELEX is a cyclic process of *in vitro* aptamer selection involving three major steps: target-nucleic acid interaction, separation and amplification. The SELEX procedure was discovered and published by Tuerk and Gold in 1990 [34]. In their work, Tuerk and Gold selected a RNA aptamer against a protein target. The SELEX process have since then revolutionised the development of aptamers over the past decades since relatively simple aptamer selection has become possible after the discovery of the SELEX process. It is important to emphasise that SELEX selection is still a labour intensive process that requires much technical experience and it may take several months to years to select an aptamer [38]. Though, it is now possible to reduce the selection time with automated robotic selection systems.
Figure 2.7 shows the principle of DNA aptamer selection by SELEX. Before the SELEX is initiated the target can be immobilised onto a solid support, in this case magnetic beads. Magnetic beads are used for easy separation of the unbound ssDNA. The first step in the SELEX process is incubation of the target with a nucleic acid library of randomised sequences. The starting library usually consists of around 10^{12} - 10^{15} random individual ssDNA sequences [38, 42]. Typically, the randomised region of the ssDNA pool is 30-60 nucleotides and this region is flanked by two constant regions of approximately 20-25 nucleotides [38, 43]. The constant regions act as primers to enable PCR amplification. After the target-ssDNA interaction the unbound ssDNA, or non-binders, are separated and discarded from the target-ssDNA complexes. Separation of non-binders from the target bound ssDNA can be done by different approaches. The separation method used in figure 2.7 is magnetic separation but other techniques such as nitrocellulose membrane filtration, affinity chromatography or capillary electrophoresis are used, among others [38]. The ssDNA is then eluted from the target and amplified by PCR. The PCR amplicons are used as the ssDNA starting pool for the next selection cycle. The affinity is thus increased after each selection cycle. After the amplification step a counter selection, or negative selection, of closely related targets or separation matrices e.g. solid supports like magnetic beads can be done to increase specificity and eliminate non specific binders [38, 44]. The counter selection is performed after several positive selection cycles [44]. When the output of a selection cycle has reached the desired

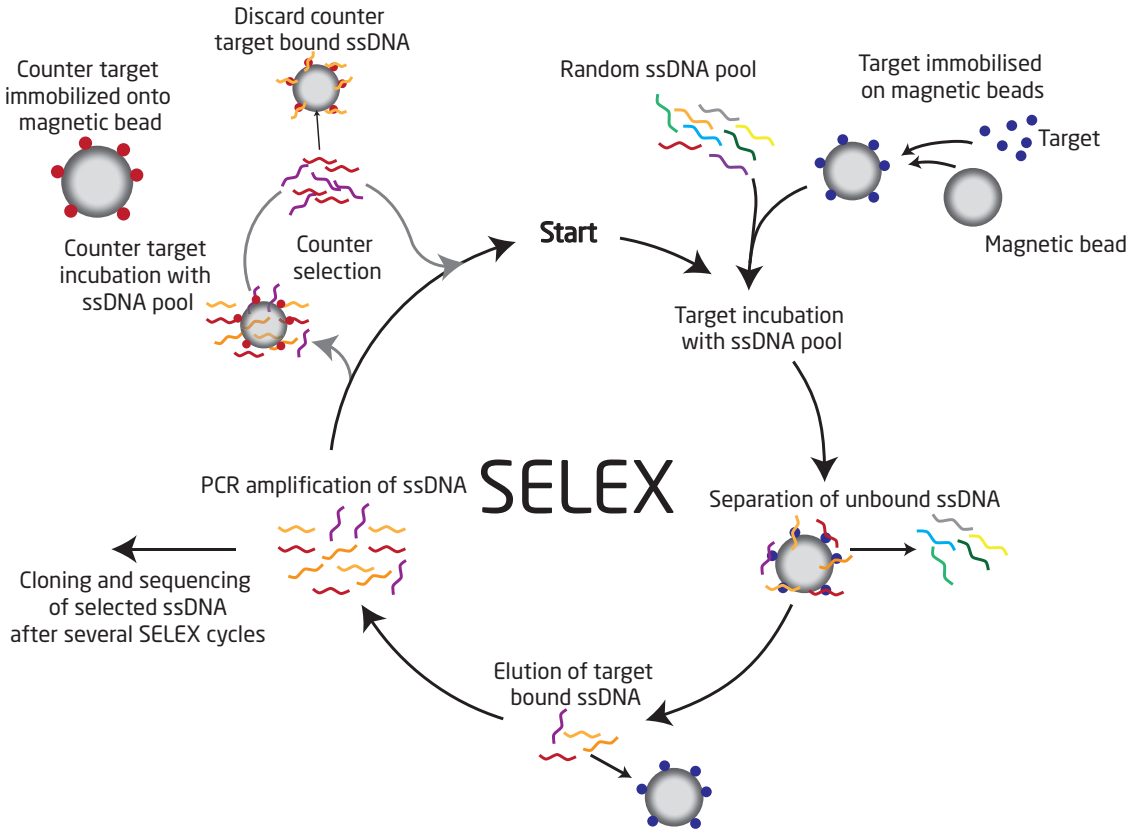

Figure 2.7: *Principle of the cyclic SELEX procedure. The target is bound to magnetic beads for easy separation of the unbound ssDNA. The target is incubated with a random ssDNA library and the unbound ssDNA is separated and discarded from the target bound ssDNA. The target bound ssDNA is eluted from the target and amplified by PCR. A counter selection can be performed to increase specificity by removing ssDNA that binds to a counter target. The counter target can be a target similar to the specific target. The cyclic process is continued until the cycle output is dominated by target specific aptamers. After the cyclic process the ssDNA product is cloned and sequenced for further analysis.*

target affinity the aptamer candidates are cloned and sequenced for further analysis and refining [38]. The number of cycles necessary to get an aptamer candidate with high affinity and specificity usually lies around an average of 12 selection cycles [38]. Several conditions should be considered during the aptamer selection to ensure optimal binding conditions for the aptamer-target complex. It is important that the aptamer binds the target in the working conditions of the anticipated application. As aptamers are nucleic acids the temperature, pH and salt concentration of the medium affects the 3D folding of the aptamer and thus the affinity. The selection conditions and buffers must thus be carefully considered to achieve a high affinity

of the aptamer together with the application [38].

2.2.2 Aptamers selected against viral targets

Aptamer selection for viral targets have mainly been developed for clinical applications like diagnostic or therapeutic tools but aptamers have also been selected for environmental and food borne pathogen analysis. Aptamers as therapeutic tools is an interesting field due to their ability to interfere and inhibit viral penetration and replication in the host cell [33, 44].
The selection process of aptamers against different viruses is commonly done with isolated and purified recombinant structural proteins [7, 45] but selection with the whole virus was also done [8, 46]. The choice of target protein configuration can effect the affinity of the aptamer since the isolated recombinant structural protein of the virus may have distinctively different folding than that of the structural proteins in the complex configuration of the virus capsid [37, 44]. Furthermore, an aptamer selected against a recombinant surface protein may target a site of the protein that does not face outwards from the virus surface which hinders detection of the virion. Whole-virus SELEX is challenging as the sample preparation of the virus, i.e. virus inactivation an purification, is a difficult task that requires dedicated laboratories with high safety levels [47]. When selecting aptamers with whole-virus SELEX it is very hard to determine the targeted surface protein and the specific epitope, or aptatope, of the virus.

This thesis focuses on three enteric viruses: NoV, RV and HAV. Currently no aptamers selected against RV and HAV have been published. Aptamer selection against the whole RV virion may be a challenge, both because of the genetic diversity of the RV but also related to the stability of the infectious TLP RV virions (see section 2.1.1). The outer capsid protein layer of the TLP, VP4 and VP7, can be easily removed by chelating agents (e.g. EDTA) and thereby reducing the virions to the non-infectious double-layered particles (DLP), with VP6 as the outer capsid protein. This reducing step is commonly done in RV diagnostic as the genetic diversity of the DLP is smaller compared to TLP which means that the epitopes of DLP is more constant. Due to this, antibodies targeting the structural proteins of human RV is selected against the VP6 protein.
It is difficult to say why aptamers targeting HAV have not been selected. The isoelectric point of HAV is 2.8 which means that at neutral pH the net charge of the virus is negative [48]. The net charge of DNA is also negative at neutral pH which may make it difficult in the selection process to bind the ssDNA to the target. Generally, aptamer selection of targets with isoelectric points < 6 is not advantageous for aptamer selection [Personal correspondence with Dr. Marcus Menger, Fraun-

hofer Institute for Cell Therapy and Immunology (IZI)]
Currently, two studies on selection of aptamers targeting human NoV have been published [7, 8] and one study on an aptamer targeting murine NoV [49]. Escudero-Abarca *et al.*, 2014, [8], selected aptamers against whole human NoV (GII.2) immobilised onto magnetic beads by antibodies. In their aptamer selection they incorporated counter selection steps with human stool specimens (negative of Human NoV) and the bead-antibody complex. They where able to use the selected aptamers in ELISA and enzyme linked aptasorbent assay (ELASA) to show that the aptamers were able to target several different human NoV strains primarily within genogroup II with a K_d in the range of 1-200 nM [8]. Beier *et al.*, 2014, [7], used a selection approach with the purified recombinant structural proteins, VP1, of the viral strain GII.4 as target. They used counter selection with fecal extract and experimental background materials. Their experimental binding studies are based on surface plasmon resonance where the binding of the recombinant VP1 protein of GII.4 and a non-structural NoV protein are compared. The study does not investigate the binding of the aptamer to whole virus, nor determine the dissociation constant. Giamberardino *et al.*, 2013, [49], used the murine NoV type 1 as a target for aptamer selection. The murine NoV present a great advantage over the human NoV as it can be cultured *in vitro*. In their study they used whole murine NoV as targets and performed counter selection with nitrocellulose filters, feline calicivirus and culture medium. The K_d of the aptamer-target complex was proven to be in the low picomolar range. In their study it was also shown that the aptamer was able to bind human NoV, GII.3. The aptamers selected against NoV is listed in table 2.1.

Table 2.1: *Aptamers selected against NoV*

Virus	Target	Type DNA/RNA	K_d	Reference
Human NoV, GII.2	Whole virus	DNA	100-200 nM	[8]
Human NoV, GII.4	VP1	DNA	Not available	[7]
Murine NoV type 1	Whole virus	DNA	Low pM range	[49]

Comprehensive lists of many of the currently published aptamers selected against viral targets can be found in reviews by Wandtke *et al.*, 2015, Torres-Chavolla *et al.*, 2009, and Kieboom *et al.*, 2015, [33, 44, 47]. It is evident from the reviews that the aptamer selection against viruses are limited to a few different viruses: human immunodeficiency virus [50], hepatitis B [51] and C virus [52], influenza A virus [45, 46, 53], vaccinia virus [54, 55] and SARS coronavirus [56].

2.3 Bio- and aptasensors for viral detection

A biosensor is an analytical device that provides the user with rapid, accurate and valuable information about a specific target in a sample. The biosensor converts an analog biological response into a measurable signal that is processed for interpretation [57]. In 1956 Clark introduced his oxygen electrode which initially set the stage for development of electrochemical biosensors and led to the development and commercialisation of the glucose oxidase biosensor in 1962 and 1974, respectively [57]. Today, biosensor applications have expanded and are now used in many different fields of our society e.g. in medicine, food and water safety, public safety, environmental monitoring etc. [58].
Figure 2.8 illustrates a schematic representation of the principle of a biosensor. A

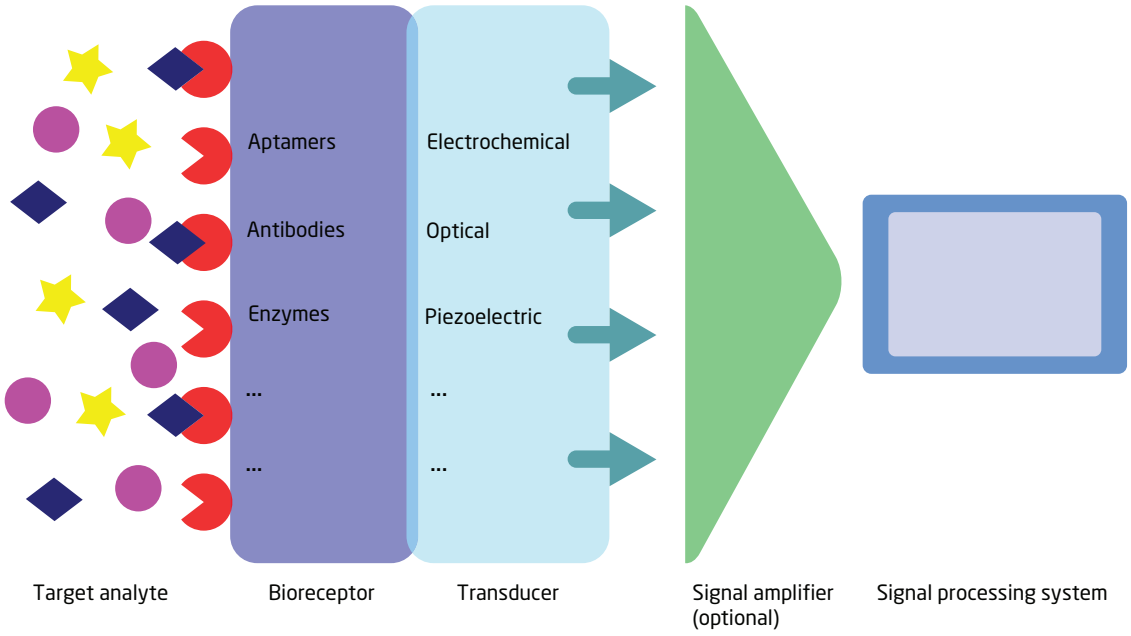

Figure 2.8: *Principle of a biosensor. A biosensor is an analytical device that consists of several components: a bioreceptor, a transducer, an amplifier and a signal processing system for signal analysis. The amplifier may not be present in all biosensors. The biorecognition elements of the detector identifies and binds target molecules. This biorecognition event results in a stimuli that is converted by the transducer into a processable output signal. The output signal is amplified and processed by the signal processing system where the signal is displayed for interpretation. The biorecognition elements of the detector can be different biological components e.g. aptamers, antibodies, enzymes, etc. Likewise, the transducer can be based on different principles e.g. electrochemical detection, optical methods, piezoelectric sensing etc. [58]*

biosensor consists of several different components: a bioreceptor with biorecognition elements to catch the target analyte, a transducer that converts the signal into a processable signal and a signal processing system [57].
In the following sections the general principles of biosensors will be introduced with a focus on electrochemical biosensors, especially impedance based impedimetric aptasensors for viral diagnostics.

2.3.1 Introduction to biosensors

As described above, a biosensor can be described by three major components: a bioreceptor, a transducer that converts biorecognition events into a processable signal and a signal processing system for analysis, as illustrated in figure 2.8. Biosensors may also have a signal amplifier. Biosensors are classified according to the biorecognition element or by the mechanism of the transduced signal [58] [59]. The bioreceptor mechanism can be based on different biorecognition elements, e.g.: aptamers, antibodies, enzymes etc. and the transducer principle can be based on e.g.: electrochemical, piezoelectric, optical etc. [58].
In order for a biosensor to be ideal and successful several conditions must be fulfilled. The biorecognition elements must be highly specific and selective [57]. The biological response of the biorecognition reaction should be precise, accurate and reproducible as well as linear in the desired concentration range [57]. Furthermore, the reaction should be independent of pH changes, temperature changes and sample flow [57]. For fast analysis the biosensor must be able to perform real-time analysis [57]. And last, an ideal biosensor must be cheap, small and easy to use by non-trained personnel with a minimum of sample preparation [57]. It is important to notice that the interaction between the bioreceptor and the transducer and the performance of the two are of paramount importance to have a biosensor with high sensitivity and specificity.

Impedimetric biosensors

A subtype of biosensors are impedimetric biosensors that utilise electrochemical impedance spectroscopy (EIS) to measure the electric changes and perturbations of a biosensor system caused by target binding. The unique ability of impedimetric biosensors to directly convert a biological recognition event into an electrical signal makes them highly interesting as biosensors [57]. The principle of impedimetric biosensing can thus be label-free which means that no further chemical labelling, e.g. fluorescent or enzymatic, is needed in order to detect the biological reaction.
Impedimetric biosensors have several fundamental advantages compared to other types of biosensors. The complexity of the experimental setup of impedimetric

biosensors is low as well as the fabrication cost of the sensors [57]. Furthermore, the sensors are robust, can be miniaturised and have good detection limits [57].
When designing an impedimetric biosensor several important factors must be considered: the choice of biorecognition elements and the surface immobilisation of these, the electrode material and the electrode dimensions [57]. The bioreaction must take place close to the electrode surface in order for the electrodes to detect the reaction [57]. This means that large biorecognition elements or long immobilisation spacer arms must be avoided. Commonly, enzymes, antibodies or nucleic acids are used as biorecognition elements in biosensors but recently aptamers have received increased interest as replacement of antibodies [37, 44, 57]. When aptamers are used as the biorecognition element in a biosensor the sensors is referred to as an aptasensor [44]. The electrode material is commonly gold, carbon or graphite [57], but also conducting polymers are of great interest. To reduce the fabrication cost of the sensor, gold electrodes fabricated in clean-room facilities must be omitted and simpler methods like screen-printing of conducting polymers or carbon can be applied. Furthermore, screen-printing easily facilitates mass production. Depending on the electrode material the right surface immobilisation of the biorecognition elements must be carefully chosen. It is pivotal for the performance of the biosensor that the biorecognition elements are present on the electrode surface in the right amount and in the right configuration.

In general, the properties of the components of an electrical system is described by the electric current, the applied potential and the electric resistance according to Ohm's law. The electrochemical properties of an impedimetric biosensor can thus be measured by either measuring the current generated from an electron transfer, the charge accumulation on the electrodes or the changes of the conductive properties of the medium [57]. Different techniques can be applied to measure these parameters e.g.: EIS, amperometry or potentiometry. EIS is a useful technique for biosensing applications where the changes of the electric properties of the sensor are related to target binding events on the electrode surface [57]. Thus, the experimental work related to the characterisation of the developed aptasensor (described in chapter 6) is based on EIS. Hence, the following theoretical description will focus on the principles of EIS.

2.3.2 Electrochemical Impedance Spectroscopy

This section focuses on the theory of EIS in order to understand the important characteristics of the electrical components of an EIS based biosensor. The biorecognition elements, in this case aptamers, are immobilised on the electrode surface at the electrode-electrolyte interface. The binding event of a target, in this case a virus,

to the aptamers will result in a redistribution of charges at the electrode-electrolyte interface and give rise to a change of the electric parameters of the components of the electrochemical system. The following section will describe the basic theory of the electronic components of a biosensor and an equivalent circuit model in order to get a theoretical understanding of EIS.

Basic theory of EIS

In EIS a small alternating current (AC) excitation potential is applied to the electric system, or cell, and the current response of the system is measured. The impedance of the system can thus be calculated from the applied potential and the current response. By varying the frequency of the excitation potential through a frequency range of interest an impedance spectra of the electric system can be acquired and analysed [57].
The excitation potential, E_t, is a sinusoidal signal expressed by:

$$E_t = E_0 sin(\omega t) \tag{2.1}$$

where E_t is the potential, in volts (V), at time t, E_0 is the amplitude of the signal and ω is the angular frequency [60]. In degrees, ω is given by:

$$\omega = 2\pi f \tag{2.2}$$

where f is the frequency in hertz (Hz).
The current response is also a sinusoidal signal shifted by the phase, ϕ, given by:

$$I_t = I_0 sin(\omega t + \phi) \tag{2.3}$$

where I_t is the current response, in amperes (A), at time t and I_0 is the amplitude of the signal [60].
The total impedance of the system can thus be calculated from the excitation potential and the current response with a relation equivalent to Ohm's law:

$$Z = \frac{E_t}{I_t} = \frac{E_0 sin(\omega t)}{I_0 sin(\omega t + \phi)} = Z_0 \frac{sin(\omega t)}{sin(\omega t + \phi)} = Z_0 e^{j\phi} \tag{2.4}$$

where Z_0 is the magnitude of the impedance and $j^2 = -1$ [60]. By applying Euler's formula to the complex impedance it can be expressed as a function of sine and cosine on a complex plane:

$$Z(\omega) = Z_0 e^{j\phi} = Z_0(cos\phi + jsin\phi) \tag{2.5}$$

The total complex impedance of an electric circuit can thus be divided into a real, Z_{RE}, and an imaginary, Z_{IMG} component:

$$Z_{total}(\omega) = Z_0(cos\phi + jsin\phi) = Z_{RE} + jZ_{IMG} \tag{2.6}$$

and be represented in the non-complex plane by calculating the magnitude, in ohms (Ω), and the phase, in degrees, by:

$$Z_0(\omega) = |Z_{total}(\omega)| = \sqrt{Z_{RE}^2 + Z_{IMG}^2} \tag{2.7}$$

$$\phi(Z_{total}(\omega)) = arctan\left(\frac{Z_{IMG}}{Z_{RE}}\right) 180/\pi \tag{2.8}$$

The total impedance of the electric system can thus be represented by the magnitude and the phase as a function of the log of the frequency by so called Bode plots or on a complex plane by Z_{IMG} as a function of Z_{RE} in a Nyquist plot. The Nyquist plot does not reveal the frequency dependence of the impedance directly on the plot but the high frequency components of the data are always found in the left side of the plot.

An electrical circuit is composed of three basic passive electronic elements: resistors, capacitors and inductors. In this basic theoretical description of EIS the focus will be on resistors and capacitors as these are the relevant elements in a biosensor. More complex circuit elements, like the Warburg impedance or the constant phase element (CPE), can also be present in a biosensor system.
A resistor is an electric element that is able to resist the flow of electric current through the element. The electrical resistance, R, in ohms (Ω), of a resistor is directly proportional to the applied potential over the current flow according to Ohm's law. The resistance of a resistor is not frequency dependent and there is no phase shift of the impedance through the resistor. Thus the impedance, Z_R, of a resistor is equal to the resistance, R.

A capacitor is an electric element that is able to build up charges. The general principle of a capacitor can be illustrated by a plate capacitor where two conducting plates are spaced from each other by a very small distance with an electric insulating layer. By applying a potential across the plates charges build up on one of the plates until a steady state potential is reached. When a AC potential is applied to the capacitor the charges build up on different sides of the capacitor according to the AC frequency. At low frequencies the capacitor blocks the current and at high frequencies the capacitor acts as a conductor. Thus, the impedance of a capacitor is frequency dependent and a phase shift of the impedance of -90 degrees is observed through an ideal capacitor. The complex impedance of a capacitor is given by:

$$Z_C(\omega) = \frac{1}{j\omega C} \tag{2.9}$$

where C is the capacitance of the capacitor in farads (F).

A CPE is a non-ideal capacitor and the impedance of a CPE, Z_{CPE}, is given by [60]:

$$Z_{CPE} = \frac{1}{(j\omega)^{\alpha}C} \tag{2.10}$$

where α is a coefficient between 0 and 1 (typically 0.9 - 1 for a CPE). For an ideal capacitor α equals 1.

The Warburg element is a special case of a CPE where $\alpha = 0.5$. The Warburg element is a complex electrical component that represents the mass transport of diffusive species in the solution [61]. The impedance of a Warburg element, Z_W, is given by [60]:

$$Z_W = \sigma(\omega)^{-1/2}(1 - j) \tag{2.11}$$

where σ is the Warburg coefficient. The Warburg element will not be described in further detail in this thesis. For a thorough theoretical description of the Warburg element the reader is referred to the book *Electrochemical Impedance Spectroscopy and its Applications* by Andrzej Lasia [62].

In an electric circuit the different circuit elements can be combined either in parallel or in series. The total impedance of a parallel RC circuit is given by:

$$\frac{1}{Z_{total}} = \frac{1}{Z_R} + \frac{1}{Z_C} = \frac{1}{R} + j\omega C \tag{2.12}$$

and the total impedance of a serial RC circuit is given by:

$$Z_{total} = Z_R + Z_C = R + \frac{1}{j\omega C} \tag{2.13}$$

Figures 2.9, 2.10 and 2.11 illustrates the electric circuit, the Nyquist plot and the Bode plots for a parallel RC circuit, a serial RC circuit and a RC parallel circuit in series with R, respectively. The total impedance of the circuits is calculated from equations 2.12 and 2.13. And the magnitude and phase of the total impedance for the Bode plots are calculated from equations 2.7 and 2.8.

In the parallel RC circuit the Nyquist plot, figure 2.9b, shows the characteristic semi-circle of such circuit. The diameter of the semi-circle is equal to the resistance of $R_1 = 10\,k\Omega$. In the Bode plots, figure 2.9c, it is evident that the resistor is dominating in the low frequency range as the magnitude of the impedance is equal to the resistance of R_1 and the phase shift of the impedance is equal to 0. At high frequencies the capacitor is dominating and the resistor is bypassed as the magnitude of the impedance is 0 and the phase shift is -90 degrees.

The Nyquist plot of the serial RC circuit, figure 2.10b, does not show a semi-circle but rather a constant value of the real part of the impedance equal to $R_1 = 10\,k\Omega$

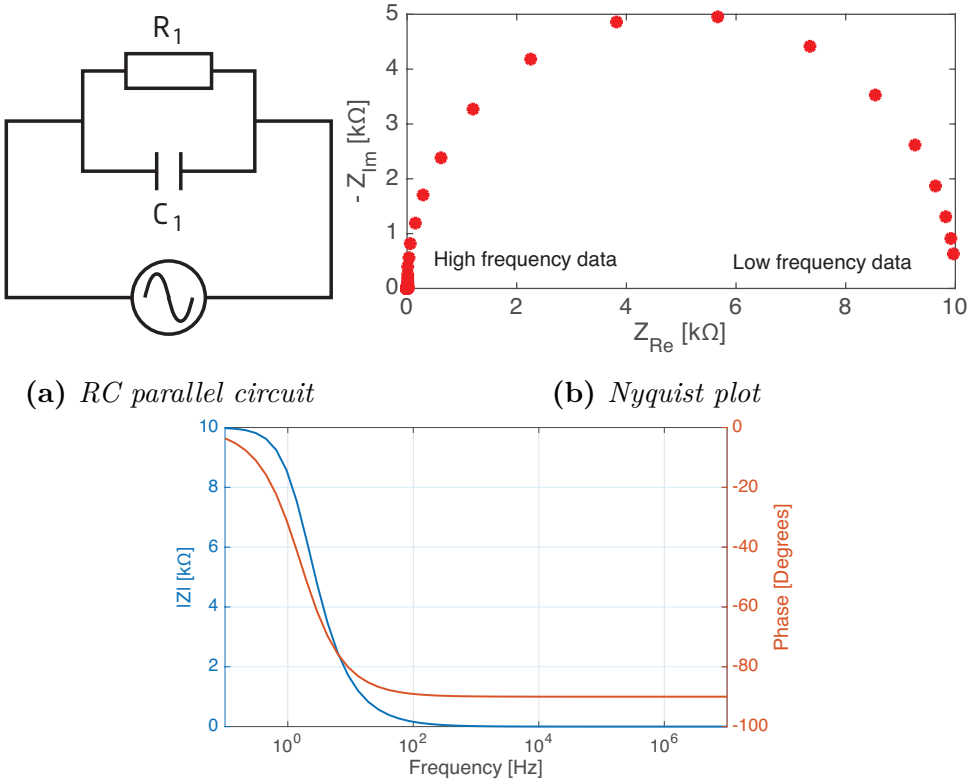

(a) *RC parallel circuit* **(b)** *Nyquist plot*

(c) *Bode plots*

Figure 2.9: *Impedance spectra of a RC parallel circuit. Circuit elements:* $R_1 = 10\,k\Omega$, $C_1 = 10\,\mu F$.

and only the imaginary part of the impedance changes. The Bode plots, figure 2.10c, show that the capacitor is the dominating component at low frequencies as the magnitude of the impedance goes towards infinity and a phase shift of -90 is observed. At high frequencies the resistor is dominating and the magnitude equals R_1 and no phase shift is observed.

By combining the parallel and the serial circuits as illustrated in figure 2.11a the semi circle observed in the Nyquist plot of the parallel RC circuit (figure 2.9b) is preserved but in figure 2.11b it is shifted to the right of the spectra. The shift equals the value of $R_2 = 1\,k\Omega$. The Bode plots, figure 2.11c, reveals that the low frequency range is dominated by the serial connection of the resistors R_1 and R_2 equal to $11\,k\Omega$ and a phase shift close to 0. At high frequencies the circuit is dominated by the resistor R_2. In a frequency range around 10^1 Hz the circuit is dominated by the capacitor seen by the negative phase shift of around -55 degrees. The phase shift

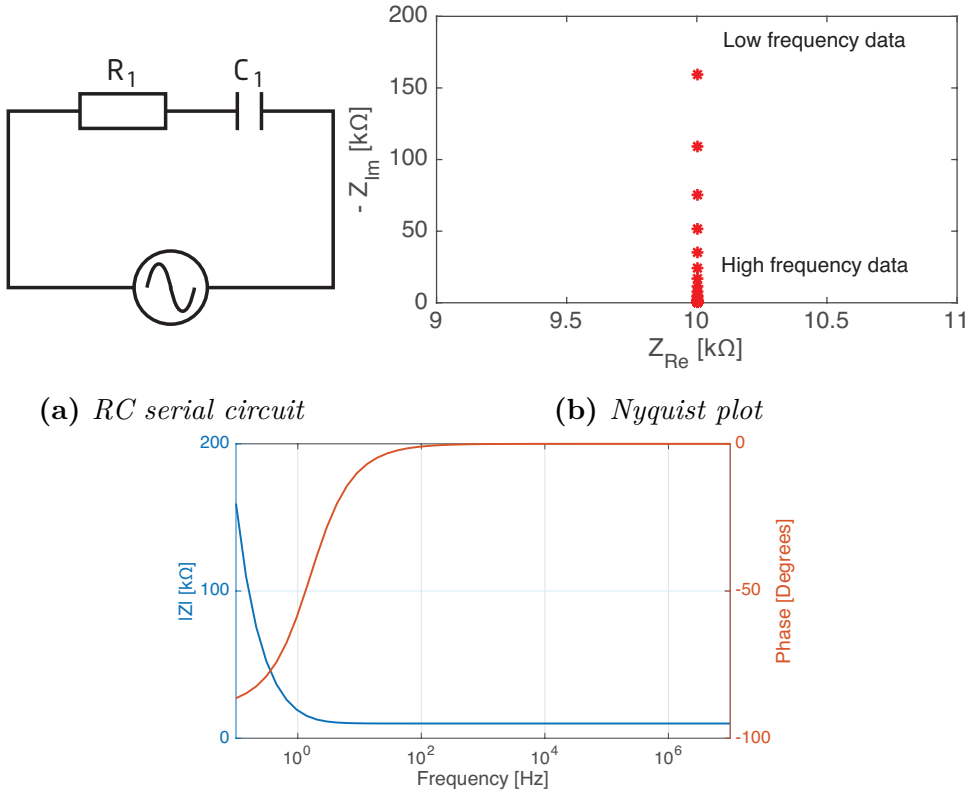

(a) *RC serial circuit* **(b)** *Nyquist plot*

(c) *Bode plots*

Figure 2.10: *Impedance spectra of a RC serial circuit. Circuit elements:* $R_1 = 10\,k\Omega$, $C_1 = 10\,\mu F$.

does not reach -90 degrees due to the serial connection with R_2.
By looking at both the Nyquist and Bode plots for the representation of measured impedance data it is thus possible to simulate a model for an equivalent circuit of e.g. a biosensor. The values of the different circuit elements are fitted to the simulated circuit model and thereby enabling calculation of the changes of the electrical properties of the biosensor when a target binds to the sensor.

Equivalent circuit model for an electrode pair in solution

Figure 2.12 illustrates an equivalent circuit model for an electrode pair in a solution. This circuit model is an ideal simplified circuit model. In the case of the developed all-polymer aptasensor the electrode material is an intrinsic conducting polymer, PEDOT:PSS. This electrode material is not an ideal conductor which means that the electrode has a internal resistance, R_i. At the electrode-electrolyte interface three electrical components are found: the charge transfer resistance, R_{ct}, the double layer

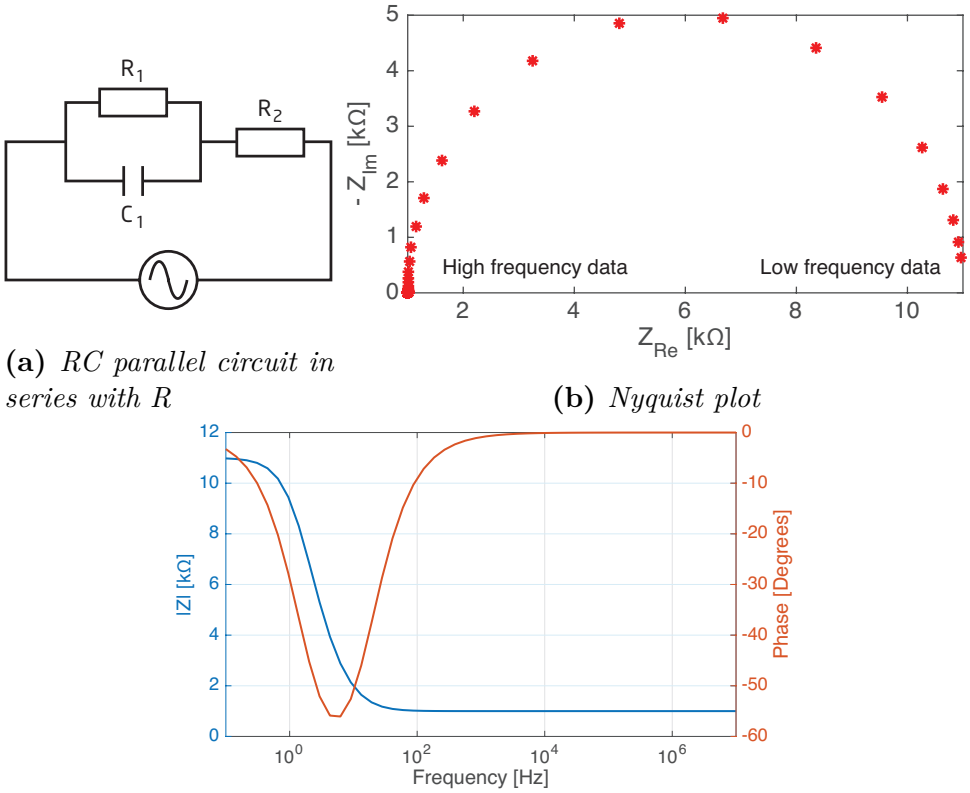

(a) *RC parallel circuit in series with R*

(b) *Nyquist plot*

(c) *Bode plots*

Figure 2.11: *Impedance spectra of a RC parallel circuit in series with R. Circuit elements:* $R_1 = 10\,k\Omega$, $R_2 = 1\,k\Omega$, $C_1 = 10\,\mu F$.

capacitance, C_{dl}, and the Warburg impedance, Z_W. The circuit at the electrode-electrolyte interface is known as a Randles electrical equivalent circuit [61]. The charge transfer resistance, R_{ct}, models how charges are moving across the electrode-electrolyte interface. The double layer capacitance, C_{dl}, represents the built-up of charges on the electrode surface. The double layer capacitance never behaves as an ideal capacitor and can be substituted by a CPE with the coefficient α between 0.9 and 1. As stated earlier, the Warburg element is a complex electrical component that represents the mass transport of diffusive species in the solution [61]. The Warburg impedance represents the steady-state diffusion of ionic species without advection of the solution. In the case of the developed all-polymer aptasensor the sensor is aimed to work in continuous flow which means that the Warburg impedance is of lesser importance due to the advection of the ions in the medium. The solution resistance, R_s, represents the resistance of the bulk solution. The geometrical capacitance, C_{geo}, models the capacitance of the electrode pair. Both the solution resistance and the geometrical capacitance are components with effect at high frequencies. The low

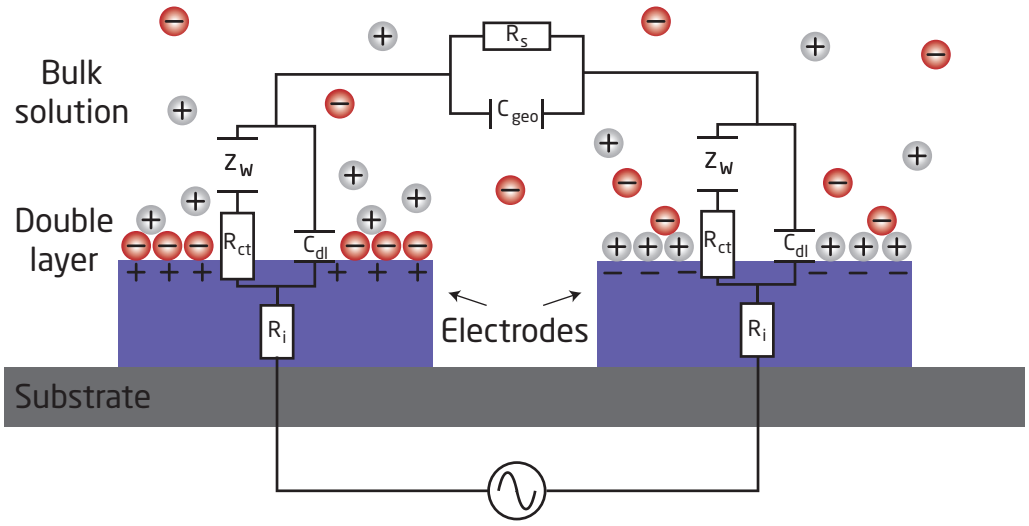

Figure 2.12: *Equivalent circuit model for an electrode pair in a solution. R_i: Internal resistance of PEDOT:PSS, R_{ct}: Charge transfer resistance, C_{dl}: Double-layer capacitance, Z_W: Warburg impedance, C_{geo}: Geometrical capacitance, R_s: Solution resistance*

frequency components of the circuit are the charge transfer resistance, the double layer capacitance, the Warburg impedance and the internal resistance. When a reaction takes place on the electrode surface at the electrode-electrolyte interface, e.g. aptamer immobilisation or target binding, it is these low frequency components that are affected. Thus, a target binding event on the electrode surface must be expected to change either the charge transfer resistance and/or the double layer capacitance.

2.3.3 Intrinsic conductive polymers for electrode material

Intrinsic conductive polymers have gained an increased interest for usage as electrode materials in biosensors due to the ease of processing and low material costs which enables low cost disposable devices. Furthermore, they possess other advantages like good optical properties [63]. The properties of conductive polymers can be chemically tailored to fit a specific application e.g. by different dopants or by different chemical side chains. Conductive polymers have also been found usefull in different fields e.g. flexible solar cells [64], organic light emitting diodes [65] and analysis of cells [9, 66] as conductive polymers have proven to have good biocompatibility with cells.
Common for all intrinsic conductive polymers is the backbone structure of a conjugated system of π-bonds arising from double or triple bonds between atoms e.g.

carbon. The conjugated system of π-bonds allows electron movement along the polymer chain. Conductive polymers are semiconductors and like other semiconducting materials a dopant is used to dope the polymer to increase the conductivity. In the developed all-polymer aptasensor the electrode material is the intrinsic conductive polymer poly(3,4-ethylenedioxythiophene) polystyrene sulfonate (PEDOT:PSS). By doping the PEDOT with PSS to obtain PEDOT:PSS a conductivity of up to 10^3 S/cm can be obtained [67]. It is important to emphasise that conductive polymers can not substitute metals as metals are superior in conductivity, around 10^5 S/cm, but conductive polymers are an interesting class of materials for some applications. Figure 2.13 shows the chemical structure of PEDOT:PSS. The dashed line in the PEDOT structure illustrates the polymer backbone with the conjugated system of π-bonds. Due to the high molecular weight of PSS the molecule is entrapped in the PEDOT matrix which hinders diffusion of PSS out of the matrix thus increasing material stability [67, 68].
PEDOT:PSS is an interesting material choice as the material is commercially available and the conductivity of the material is relatively high. Furthermore, PEDOT:PSS is commercially available as an aqueous dispersion which means that it is possible to directly print PEDOT:PSS patterns on chip substrates [67].

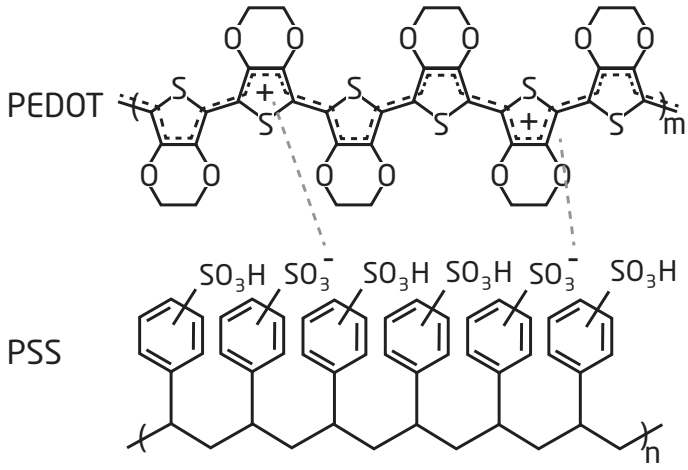

Figure 2.13: *Chemical structure of PEDOT:PSS*

2.3.4 Advancements of electrochemical and impedimetric aptasensors

In 1996, Davis *et al.* published the first work with aptamers as biorecognition elements in a biosensor, in this case an optical aptasensor [69]. In their work they compare the performance of flow cytometry with a fluorescently labelled antibody

and a fluorescently labelled aptamer. The work demonstrates the feasibility of using aptamers instead of, or combined with, antibodies in biosensing applications. Aptamers as biorecognition elements in electrochemical aptasensors was introduced in 2004 by Ikebukuro *et al.*, and further elaborated in 2005 [70] [71]. Radi *et al.* published the first paper on an impedimetric aptasensor for electrochemical detection in 2005 [72]. In their work they used a thrombin binding aptamer to detect thrombin with impedance spectroscopy by detecting a change in the charge transfer resistance [72]. It has also been proven that the conformational change of the aptamer upon target binding can be used in electrochemical sensing to increase the signal. This was shown by Swensen *et al.*, 2009, they used a cocaine binding aptamers tagged with redoxable molecule methylene blue to detect cocaine in serum [73]. Upon target binding the aptamer folds into the folding conformation thereby bringing the methylene blue in close proximity of the electrodes thus increasing electron transfer. For electrochemical aptasensor applications the aptamer immobilisation on the electrodes is of great importance in order to obtain a successful aptasensor. Since many aptamers are selected in solution it is necessary to investigate that immobilisation of the aptamers on a solid support does not interfere and affect the aptamer target interaction e.g. hindering the conformational change upon target binding [43]. Furthermore, other important factors must also be considered like the the molecular orientation of the aptamer and the surface coverage [43].

Since 2004 there has been a rapid increase in the number of published papers on aptasensors and electrochemical aptasensors and recently impedimetric aptasensors as well. This is illustrated by the graphs in figure 2.14 that show the increase in publications with the topic *Aptasensor*, *Aptasensor + electrochemical* and *Aptasensor + impedimetric*. The rapid increase in the number of publications verifies the importance and the interest for aptamers and aptasensors within the scientific community.

Electrochemical aptasensors for viral detection

Currently, only a limited number of published studies on electrochemical aptasensors for viral detection exists. Recently, Kieboom *et al.*, 2015, published an extensive review of aptasensors for viral diagnostics [47]. From the review it is evident that many of the currently published viral aptasensors are based on optical transducer methods.

One of the interesting electrochemical aptasensors for viral detection was published by Giamberardino *et al.*, in 2013 [49]. In their study they selected a murine NoV binding aptamer with the SELEX process and used this aptamer in their aptasensor application. By applying square wave voltammetry to their electrochemical

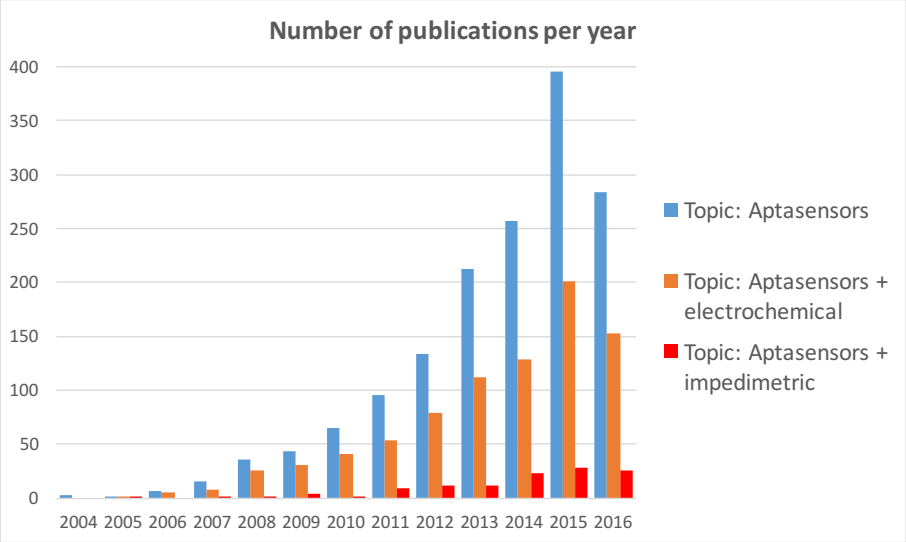

Figure 2.14: *Number of papers published per year with the topics Aptasensor, Aptasensor + electrochemical and Aptasensor + impedimetric. Data from Web of Science, Analysis results tool, August 2016.*

aptasensor they were able to detect murine NoV with a very low limit of detection of approximately 180 viral particles.
Kiilerich-Pedersen *et al.*, 2013, published an all-polymer electrochemical aptasensor with interdigitated micro-electrodes for the detection of influenza A virus in saliva [10]. The aptasensor was able to detect as low as 10^3 plaque forming units/mL in a spiked saliva sample.
Labib *et al.*, 2012, published a impedimetric aptasensor for the detection of intact vaccinia virions [55]. With their sensor they reached a limit of detection of 60 virions/μL by using EIS as the detection method. Furthermore, they developed the aptamer used in the sensor that was able to distinguish between intact and non-intact virus.

The aim of this PhD thesis is the development of an aptasensor for viral detection in environmental water samples. The following chapters of this thesis will describe this development.

— 3 —

Virus preparation for aptamer selection

This chapter concerns the experimental work related to the preparation of RV and HAV samples for aptamer selection. In order to get a good starting point for the aptamer selection a purified virus sample is needed. Thus, the work related to the purification of RV from cell culture will be described in details in this chapter. The HAV culture and purification was done by our collaborators at the Environmental Virological Laboratory, Tor Vergata University, Italy.
The SELEX process for the RV and HAV aptamer selection is based on magnetic separation of the target bound aptamer candidates from the non-binders. The principle of the SELEX process was described elsewhere, in chapter 2.2.1. In order to enable magnetic separation in the SELEX process the viral particles must be immobilised onto magnetic beads. Virus immobilisation on streptavidin functionalised magnetic beads (purchased from a commercial supplier) is possible via a biotin linker, which can be obtained by biotinylation of the viral particles. The work described in this chapter will focus on the biotinylation of the RV and the HAV and the verification of the biotinylation by real-time RT-PCR.
The SELEX aptamer selection will be performed by our collaborators at Fraunhofer Institute for Cell Therapy and Immunology (IZI), Germany.

3.1 Viral genotypes of RV and HAV for aptamer selection

Aptamer target binding is based on structural recognition of the target, in this case a virus, by the folded ssDNA. Thus, the surface proteins of the virus determine the

ability of the aptamer to bind to the virus. RV and HAV are both non enveloped viruses with a icosahedral capsid morphology. Furthermore RV has a more complex capsid structure than HAV since the RV capsid consists of three protein layers. In order for a RV to be infectious all of the three protein layers must be intact. Chapter 2.1.1 describes the basic virology of the two viruses.
American Type Culture Collection (ATCC) is one of the world leading distributors of standard reference biological material for the scientific community. It was thus initially chosen to use ATCC as a supplier of RV and HAV for the aptamer selection as they can provide a broad range of different viral strains. As described in chapter 2.1.1, two group A RV strains are responsible for most human rotavirus infections: G1P[8], 52 % of all infections, and G2P[4], 11 % of all infections [3]. Due to the high level of the infectious nature of these strains it was chosen to use these rotavirus strains for aptamer development. Thus, both RV strains were purchased from ATCC:

- RV strain Wa, sero-/genotype G1P[8], ATCC product number: VR-2018
- RV strain DS-1, sero-/genotype, G2P[4], ATCC product number: VR-2550

Both of these human RV strains, Wa and DS-1, have been adapted to cell culture [74].
The HAV genotype I is responsible for most of the human infections [27]. Within this genotype two subgenotypes exists, IA and IB, where IA is the dominating subtype found in 80 % of isolates from infected individuals [28]. Thus, subgenotypes IA and IB were purchased from ATCC:

- HAV strain HM 175 (uncloned), genotype 1B, ATCC product number: VR-2093
- HAV strain HAS-15, genotype 1A, ATCC product number: VR-2281

Both of these HAV strains, HM 175 and HAS-15, have been involved in the development of HAV vaccines [28]. Unfortunately it is not straight forward to culture HAV in cell culture and due to time constrains it was decided that our collaborators at the Environmental Virological Laboratory, Tor Vergata University, Italy, should culture and purify a HAV virus sample for the aptamer selection. They were able to supply a sample with the subgenotype IB.

3.2 Rotavirus A culture and purification

The work related to the culture and purification of RV in cell culture was divided into six main steps, as illustrated in figure 3.1. The six steps were: 1) RV culture in MA104 cells, 2) RV semi-purification on a sucrose cushion, 3) isopycnic gradient

separation of TLP (infectious) and DLP (non-infectious) virus particles on a self-forming cesium chloride (CsCl) gradient (see figure 2.3 for an illustration of the structure of RV particles), 4) unloading of CsCl gradient into fractions, 5) Sodium dodecyl sulfate polyacrylamide gel electrophoresis (SDS-PAGE) analysis of fractions and 6) dialysis of interesting fractions to remove CsCl. Each of these steps will be described in the following sections.

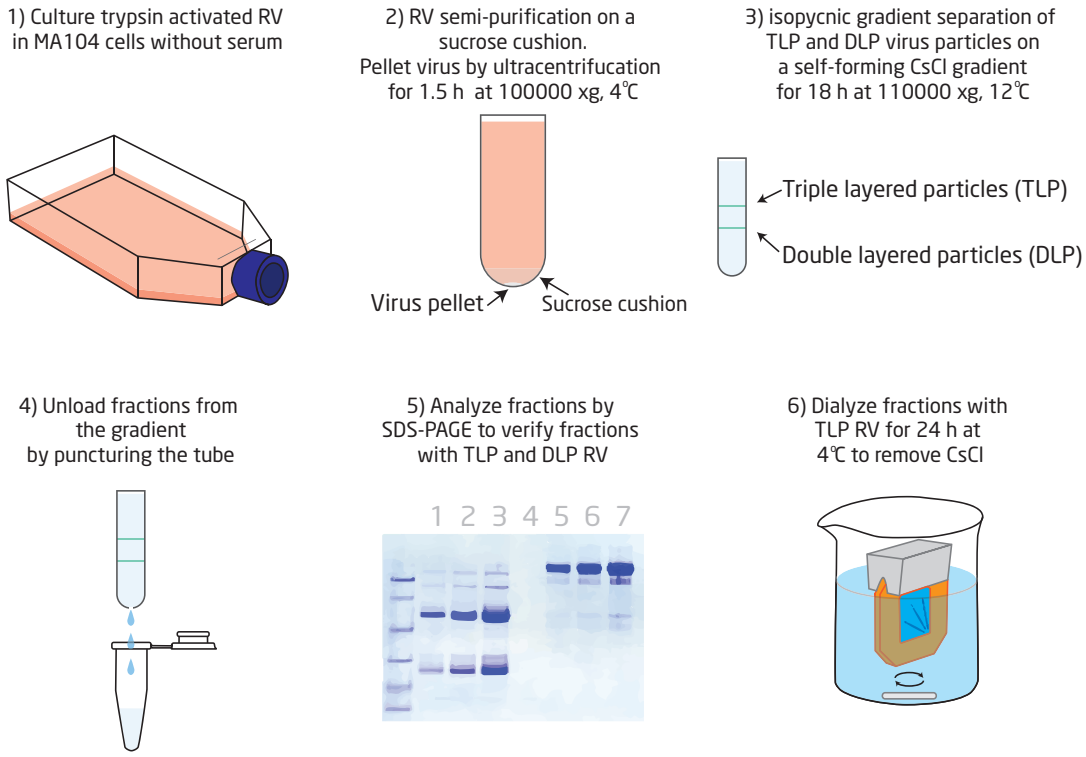

Figure 3.1: *Step by step method for rotavirus culture and purification.*

3.2.1 Rotavirus A propagation in MA104 cells

RV was propagated in MA104 cells. The MA104 cell line is a rhesus monkey kidney cell line. Before the cells were inoculated with virus the cell culture must be maintained and passaged a few times to obtain a stable culture. The RV must be activated with trypsin before they can be propagated in cells. The trypsin cleaves the surface protein VP4 into the protein VP5* and the cell attachment protein VP8*, which allows for virus entry into cells [75]. During virus propagation it was very important to use serum free medium since serum inhibits trypsin and thus inhibits the rotavirus activation [74]. The trypsin or any other reagent used for RV propagation or further handling must not contain EDTA since EDTA strips the outer layer of

the TLP RV particles which means that they are no longer infectious [74].

The protocol for RV propagation was based on protocols from the National Veterinary Institute, DTU VET, and from Arnold *et al.*, 2012 [74]. The step by step protocol and material list for rotavirus A propagation can be found in appendix A.1. MA104 cells were grown in a cell culture flask in Medium 199. When cells had reached approximately 90 % confluence it was possible to inoculate the cell culture with trypsin activated RV.
Infection of RV was done at a multiplicity of infection (MOI) between 0.1 and 1. The MOI is the number of cells / mL divided by the plaque forming unit (PFU) / mL:

$$MOI = \frac{PFU\ needed}{No.cells}$$

The PFU is a measure of the number (or virus titer) of virus particles in a volume that is able to cause an infection (a plaque) in a cell monolayer fixed in agarose. Thus, it is not a measure of number of viral particles present in a sample volume. The viral titer values for the RV virus stocks supplied from ATCC were not given as PFU but as $TCID_{50}$/mL at a time period. The virus titer value $TCID_{50}$ is an expression for the median tissue culture infective dose that causes a cytopathic effect (CPE) in 50 % of the cell cultures over a time period. The $TCID_{50}$ assay is thus an end-point assay. The titer values supplied by ATCC were 2.8 x 10^{-6} $TCID_{50}$/mL in 6 days and 2.8 x10^{-6} $TCID_{50}$/mL in 8 days for the strain Wa (G1P[8]) and DS-1 (G2P[4]), respectively. Like PFU, the $TCID_{50}$ assay was used to estimate the MOI for virus propagation by an assumption of a theoretical correlation between the two titer values where it was assumed that all conditions between the two assays were the same. The theoretical correlation was: PFU/ml = 0.7 $TCID_{50}$/mL [76].
The CPE caused by the activated RV on the MA104 cells was observed every day post infection. The CPE was initially seen as a cell rounding, then detachment of the cells from the flask and finally cell lysis. It was important to keep a control cell culture under the same conditions and media but without virus to verify that the observed CPE was indeed caused by virus infection and not caused by bad handling of the cells or lack of nutrients due to the serum free medium. Figures 3.2, 3.3 and 3.4 show microscopic images of the control cell culture, propagation of RV strain Wa in cell culture and propagation of RV strain DS-1 in cell culture, respectively. Infection was started at time t = 0 h and the cell cultures were observed every day post infection. The morphology of the control cell culture, figure 3.2, did not change significantly over a time period of 120 hours (5 days) which verified that any CPE observed in the cell cultures infected with RV was caused by the viral infection. In the cell culture infected with RV strain Wa, figure 3.3, a CPE was observed after 24 h where cell rounding and detachment in discrete areas were observed. 48 hours post infection almost all of the cells had detached from the cell flask and at 72 hours post

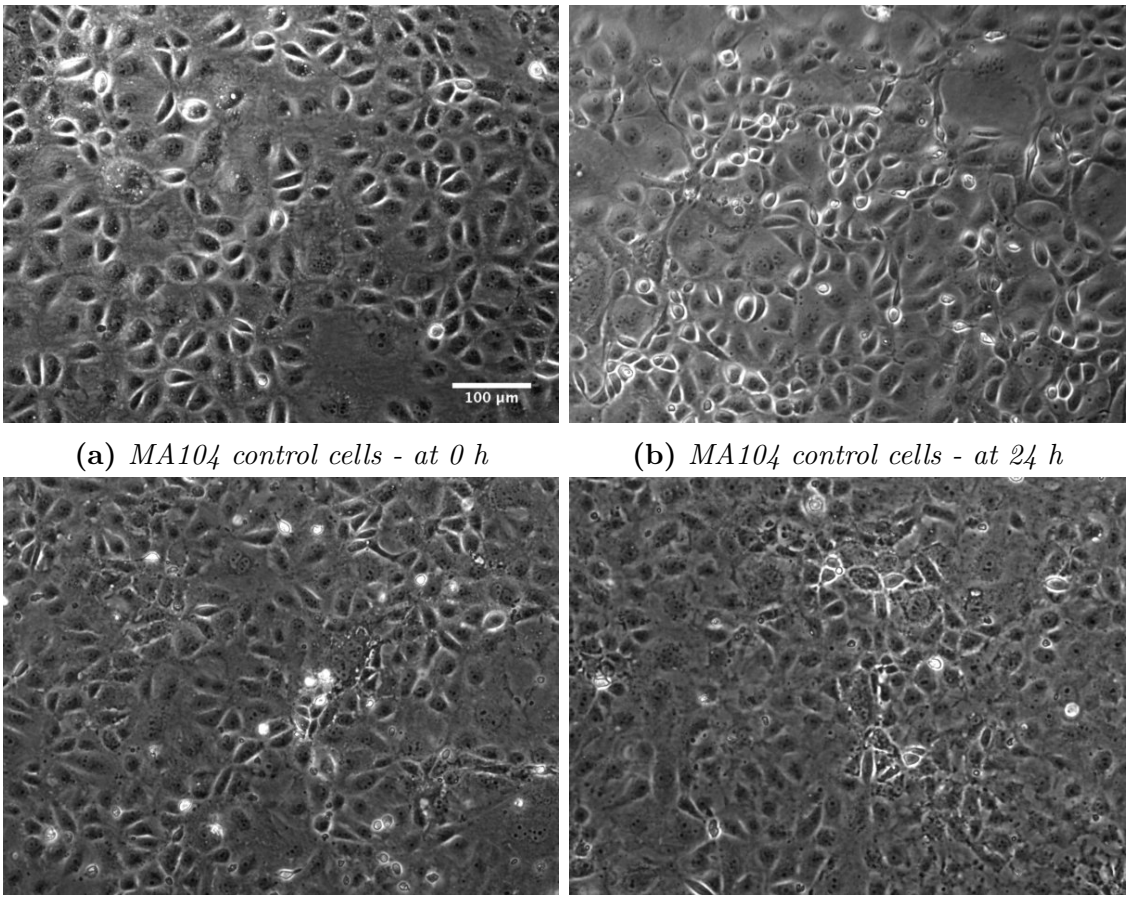

(a) *MA104 control cells - at 0 h*

(b) *MA104 control cells - at 24 h*

(c) *MA104 control cells - at 96 h*

(d) *MA104 control cells - at 120 h*

Figure 3.2: *Microscopic images of control cells for RV culture in MA104 cells at different times: 0 h, 48 h, 96 h and 120 h post infection of the non-control cells (Cells in figure 3.3 and 3.4). Scale bar (100 µm) is the same for all images.*

infection all cells had detached and many of the cells were lysed. At this point in time the RV propagation was stopped by 3 repetitive cycles of freezing and thawing.

The propagation of the RV strain DS-1 in the MA104 cells was not as fast as the RV strain Wa. This was seen in figure 3.4 where the observed CPE did not evolve as fast as RV strain Wa in figure 3.3. 24-48 hours post infection of the DS-1 strain discrete areas of cell detachment and cell rounding were observed. 96 hours post infection approximately half of the cell monolayer had detached and at 120 hours post infection almost all cells had detached and lysed. The RV propagation was stopped by 3 repetitive cycles of freezing and thawing when all cells had detached and lysed.

The observed difference in the evolved CPE of the two strains corresponded with the

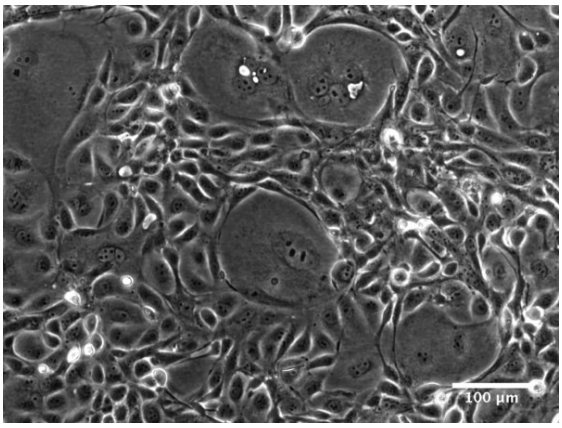

(a) *RV inoculated MA104 cells - at 24 h*

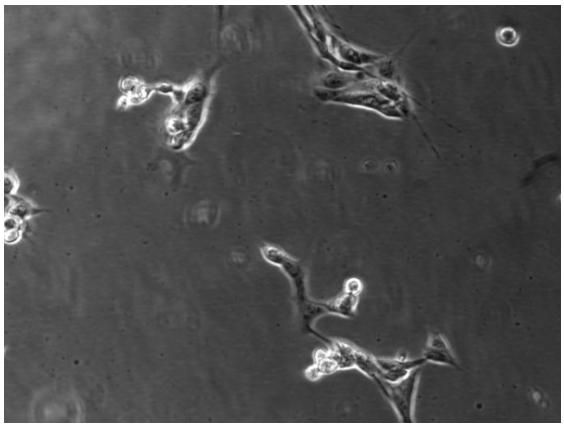

(b) *RV inoculated MA104 cells - at 48 h*

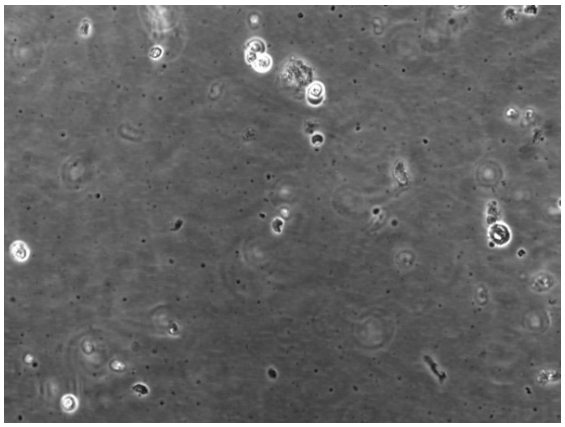

(c) *RV inoculated MA104 cells - at 72 h*

Figure 3.3: *Microscopic images of propagation of RV strain Wa (G1P8) in MA104 cells. MA104 cells were inoculated with RV at 90 % confluence at time 0 h (Corresponding to cell coverage in Figure 3.2a). 24 h after inoculation with RV a CPE was observed as cells began to detach in discrete areas from the culture flask (Figure 3.3a). At 48 hours almost all cells had detached (Figure 3.3b). At 72 h post infection all of the cells had detached from the cell flask and many of the cells had been lysed which means that the RV was ready for further processing e.g. purification (Figure 3.3c). Scale bar (100 µm) is the same for all images.*

reported titer values from ATCC where the same titer value of 2.8 x 10^6 $TCID_{50}$/mL was reached but at different time periods of 6 days and 8 days for RV strain Wa and DS-1, respectively.

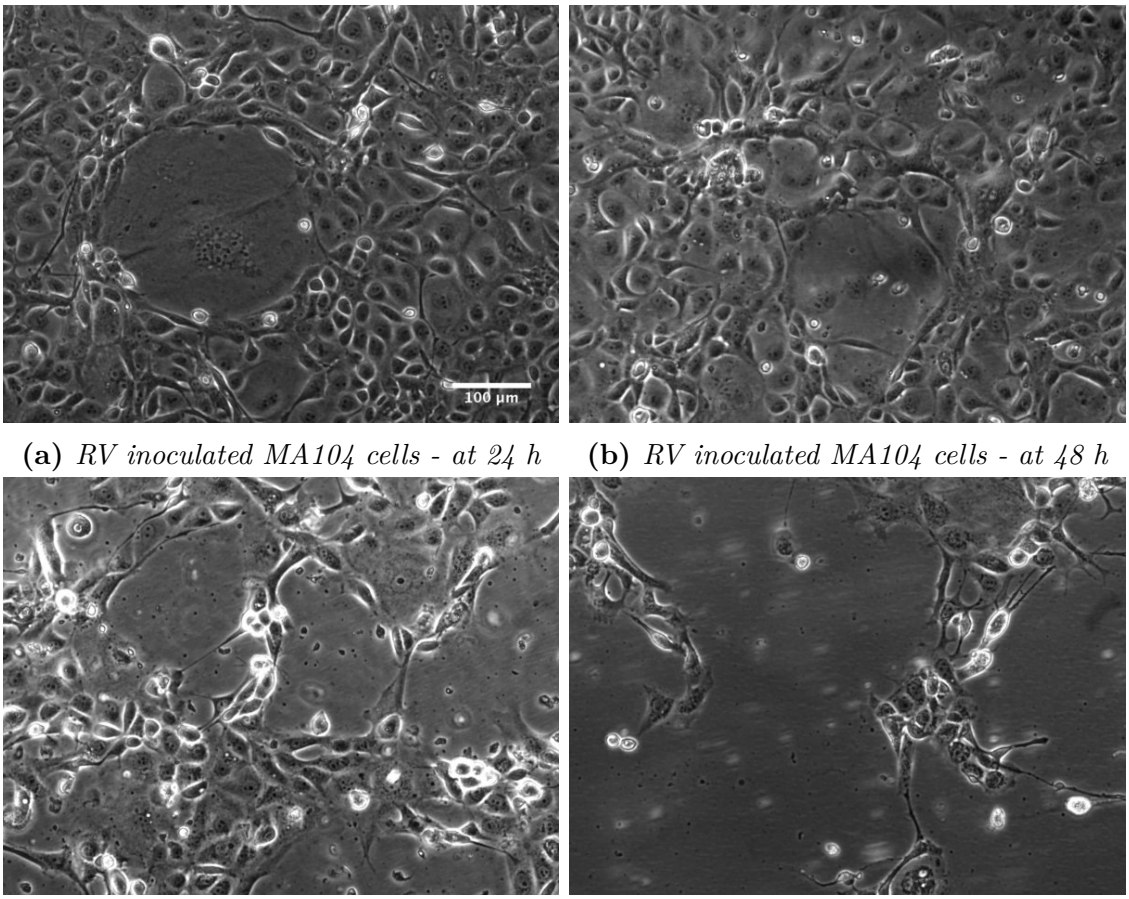

(a) *RV inoculated MA104 cells - at 24 h* **(b)** *RV inoculated MA104 cells - at 48 h*

(c) *RV inoculated MA104 cells - at 96 h* **(d)** *RV inoculated MA104 cells - at 120 h*

Figure 3.4: *Microscopic images of propagation of RV strain DS-1 (G2P4) in MA104 cells. MA104 cells were inoculated with RV at 90 % confluence at time 0 h (Corresponding to cell coverage in Figure 3.2a). After 24 h of RV inoculation a small CPE was observed (Figure 3.4a). Only a small increase in CPE was observed at 48 and 96 hours post infection (Figure 3.4b and 3.4c). After 120 hours most of the cells had detached from the cell flask and been lysed (Figure 3.4d). Scale bar (100 µm) is the same for all images.*

3.2.2 Rotavirus purification

The RV purification was divided into two steps: semi-purification on a sucrose cushion and an isopycnic gradient separation of TLP and DLP virus particles on a self-forming CsCl gradient. Both methods were performed by ultracentrifugation. Ultracentrifugation is a method involving high forces $\geq$ 100,000 $\times$g [31]. The high gravitational forces are needed due to the small size of the RV ($\varnothing$ 75-100 nm [25]). Protocols for both steps for RV purification were based on work done by Arnold *et*

al., 2012 [74]. The step by step protocols and material lists for RV semi-purification and CsCl gradient purification can be found in appendix A.2 and appendix A.3, respectively.

The first purification step, the semi-purification on a sucrose cushion, was intended to concentrate the RV sample and reduce the sample volume. The sample volume was reduced by a factor of approximately 45, as the sample volume allowed in the ultracentrifuge was 6 x 38 mL which was resuspended in a few millilitres after centrifugation. In the bottom of each centrifuge tube, underlying the RV sample, a cushion of a high concentration sucrose solution (35 %) was gently placed. The high concentration of sucrose slowed down the RV particles when they pelleted in the bottom of the tube. The pellet containing the RV was resuspended in a buffer containing calcium. The calcium in the buffer ensured the stability of the outer capsid (VP4 and VP7) of the RV which means that RV should always be maintained in buffers containing calcium [74]. The buffer used in this protocol was denoted TNC buffer: 20 mM Tris-HCl, 100 mM NaCl, 1 mM $CaCl_2$ at pH 8.0 [74]. In the RV purification protocols by Arnold *et al.*, [74], Freon was used as an initial step to separate the viral particles from the cell debris as many of the viral particles remained associated with the cell debris after cell lyses. Freon can be used to release these viruses from the debris [25]. Freon is highly toxic for humans and the environment and work with Freon underlies restriction by international treaties. Due to these restrictions it was not possible to use Freon for the RV purification of this thesis. This may compromise the concentration of the recovered RV but it was assumed that the outcome of the purification (i.e. the concentration) was sufficient for the aptamer selection.

The aptamer selection, which was the endpoint of the RV purification, was intended to target the outer structural proteins of the RV virions as these proteins will be present on the mature infectious virions (TLP). As described earlier, the aptamer selection is thus targeting the outer structural proteins VP4 and VP7 of the RV. In a RV cell culture both mature TLP and immature DLP are present. The mature TLP RV particles must thus be separated from the immature DLP RV particles. This was done by isopycnic gradient separation on a self-forming CsCl gradient where a density gradient from the bottom to the top of a centrifuge tube was self formed during ultracentrifugation. The relatively heavy Cs^+ ions in the solution were forced in the direction of the gravitational forces, towards the bottom of the centrifuge tube, at the same time the Cs^+ ions diffused towards the top of the centrifuge tube thus creating a density gradient from the bottom to the top of the tube. Virus particles in the CsCl gradient separated according to their density since they migrated to the position in the density gradient that matches their density, the so called isopycnic point [31]. The density of the TLP and DLP RV particles

were 1.36 g/cm^3 and 1.38 g/cm^3, respectively [74]. Figure 3.5 shows images of the self formed CsCl gradient with two distinct bands containing the TLP and DLP viral particles after ultracentrifugation of the two human RV strains. An inverted (normal visual) light source was used to illuminate the viral particles. The images showed that the two bands lie closer to each other in the DS-1 strain compared to the Wa strain. This could be caused by a small difference in the density of the TLP of the two strains caused by the difference in amino acid sequence of the structural proteins. At the top of each centrifuge tube a third band containing RV viral particles (not possible to see in the image of the Wa strain) was present. This band may contain aggregates of viral particles. As aggregates are more loosely packed it was assumed that the density of the aggregates was lower than the single particles which forced the aggregates to the top of the tube during centrifugation. Aggregates can be removed by using a homogenizer after the semi-purification. Unfortunately, this equipment was not available in the laboratory facilities used for the RV purification. The purified RV were unloaded from the centrifuge tube in sample fractions. This

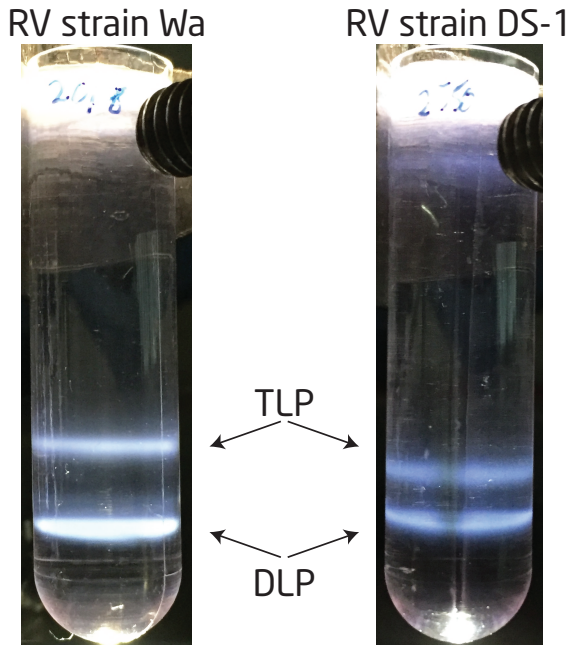

Figure 3.5: *RV purified on a CsCl gradient. The two bands seen in the tube was the separated TLP and DLP RV particles. The RV particles was separated due to their difference in density.*

was done by puncturing a hole in the bottom of the centrifuge tube to allow the sample to slowly drip into eppendorf tubes. The fractions containing the TLP and DLP were carefully labelled. In order to verify the content of the collected fractions the fractions were analysed by SDS-PAGE. The SDS-PAGE gel was stained

by silver stain, which allowed visualisation of the protein bands. Coomassie blue staining was initially tested for the band visualisation, but this staining method was not sensitive enough. Figure 3.6 shows the SDS-PAGE gels for the two RV strains. Table 3.1 lists the structural proteins of the RV, proteins in bold were the interesting structural proteins of the TLP and DLP particles. In the figure 3.6 the positions

Table 3.1: *Mass and location of structural proteins of RV [77]*

Protein	Mass (kDa)	Location (no. of copies)
VP1	125	SLP (12)
VP2	95	SLP (120)
VP3	88	SPL (12)
VP4 (VP5* + VP8*)	85 (58 + 27)	TLP (120)
VP6	45	DLP (780)
VP7	34	TLP (780)

of the structural proteins were calculated from the marker positions and the marker mass. A logarithmic correlation between the displacement and the marker position was assumed (See figure A.3 for elaboration of the logarithmic correlation). The identified positions of the structural proteins were labelled in the figure. During the unloading of the gradient it was intended to have the DLP and the TLP RV in fraction 3 and fraction 5 of both RV strains, respectively. The SDS-PAGE gel of RV strain Wa (figure 3.6a) revealed that RV was present in all fractions as bands of VP6 were present in all fractions. Unfortunately, there was a small mixing in the gradient during the unloading of the fractions which can explain the presence of RV in all fractions. The fraction with the highest content of VP7 was fraction 5 as expected, indicating the presence of TLP in this fraction. It was not possible to identify VP4, VP5* or VP8* in the gel. Fraction 8 contained the band that was present at the top of the centrifuge tube. In this fraction a high concentration of RV was present, seen by the high VP6 intensity, and all of the interesting structural proteins could be identified.
The SDS-PAGE gel of the RV strain DS-1 (figure 3.6b) showed a high content of VP6 in fraction 3 but fraction 5 contained a low concentration of VP6 and VP7 was not visible in this fraction. From the unloading of the gradient it was known that fraction 5 contained TLP RV but the gel revealed that the concentration of VP7 was very low, below the detection limit of the silver stain. As seen with the RV strain Wa fraction 8 contained a high concentration of RV. The marker position of the marker diluted 1:50 (right side marker) did not match with the 1:10 diluted marker. This was caused by an error during the running of the gel. Since the interesting

proteins could be identified in the gel it was assumed that the misalignment could be disregarded.
Both of the SDS-PAGE gels were performed before the CsCl was removed by dialysis. It was not clear if the CsCl interfered with the gel but both gels required long development times (approximately 3 min) and the protein bands seemed smeared out to some extend. Figure A.2 shows a SDS-PAGE gel performed on a simian RV strain after dialysis to remove the CsCl. This gel required less development time than the gels in figure 3.6 and the protein bands appeared more confined and clear. After the SDS-PAGE gel analysis the CsCl was removed from the interesting fractions (3 and 5) by dialysis.

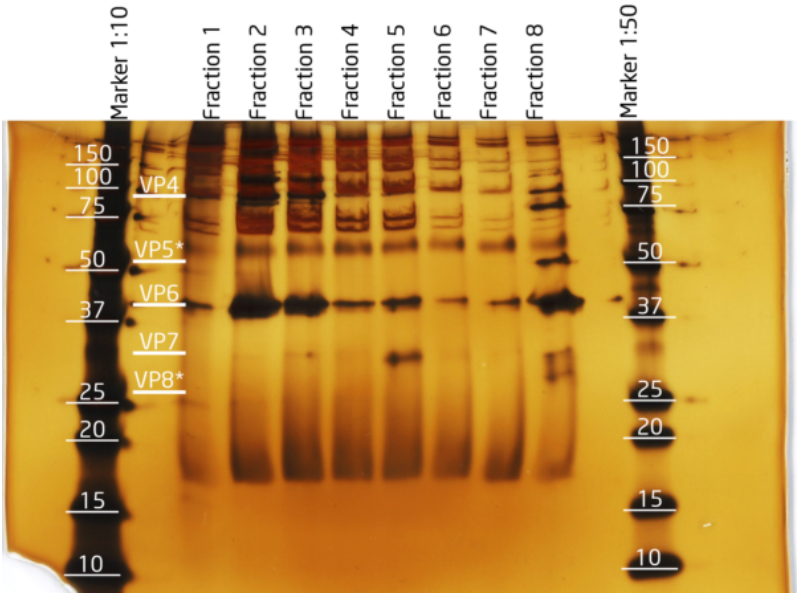

(a) *SDS-PAGE of RV, strain Wa, purified on CsCl gradient*

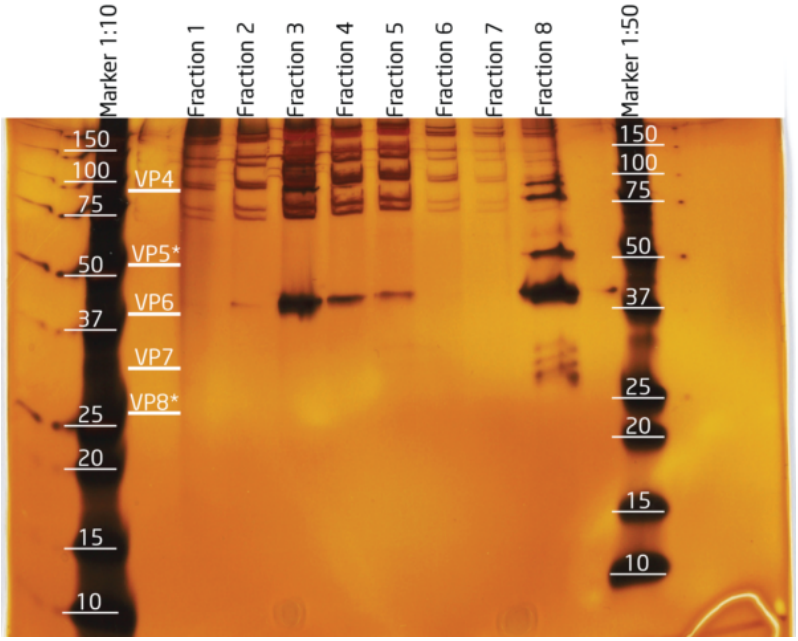

(b) *SDS-PAGE of RV, strain DS-1, purified on CsCl gradient*

Figure 3.6: *SDS-PAGE of RV, strain Wa and DS-1, purified on CsCl gradient. The protein bands were stained with silver stain. VP4 (85 kDa), VP8* (27 kDa), VP7 (34 kDa) and VP5* (58 kDa) were proteins specific to TLP virus particles. VP6 (45 kDa) was present in both DLP and TLP RV (see table 3.1). Marker and protein positions are given in kDa. The protein positions were identified by calculating the logarithmic relation between the marker position and the marker mass (in kDa) (See figure A.3 for further elaboration).*

3.3 TEM images of the TLP and DLP RV

TEM images of the TLP and DLP virus particles for each RV strain were made by Ramona Valentina Mateiu, DTU CEN, Center For Electron Nanoscopy, in order to visually confirm the content of fraction 3 and 5 from the CsCl gradient. The samples were negative stained with 2 % uranyl acetate and the imaging was performed in bright field TEM in an FEI Tecnai G2T20 microscope.

Figure 3.7 shows the TEM images obtained of the TLP and DLP RV, strain Wa and DS-1, respectively. ImageJ (National Institutes of Health, USA) was used to measure the average diameters of the viral particles.
The average diameters of the RV strain Wa of TLP and DLP were measured to be 81.3 nm and 68.7 nm respectively. The figures 3.7a and 3.7b show a clear morphological difference between the TLP and the DLP particles of strain Wa. The TLP particles have a much smoother and more defined circular structure than the DLP. Furthermore, it was seen that the sample was very clean since no impurities were observed in the TEM images.
In the figures 3.7c and 3.7d the diameters of TLP and DLP, RV strain DS-1, were measured to be 70.0 nm and 63.4 nm, respectively. The TEM images also showed that the concentration of the particles was low since only a few viral particles were present in the images. Thus, the number of particles used to determine the average diameters was limited especially for the DLP where only two clear particles were observed.

The TEM images confirms that the content of the two fractions, 5 and 3, was indeed the TLP and the DLP RV particles for both strains. The diameter of the RV particles were smaller than the diameter reported in the literature (⌀ 75-100 nm [25]). The TEM images showed that the diameters of the particles are strain dependent, which could explain why there was a difference compared to the literature.

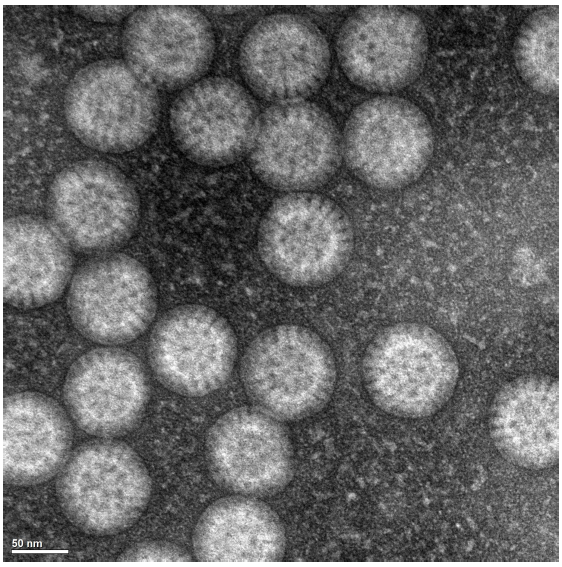

(a) *TLP RV, strain Wa, average diameter: 81.3 nm*

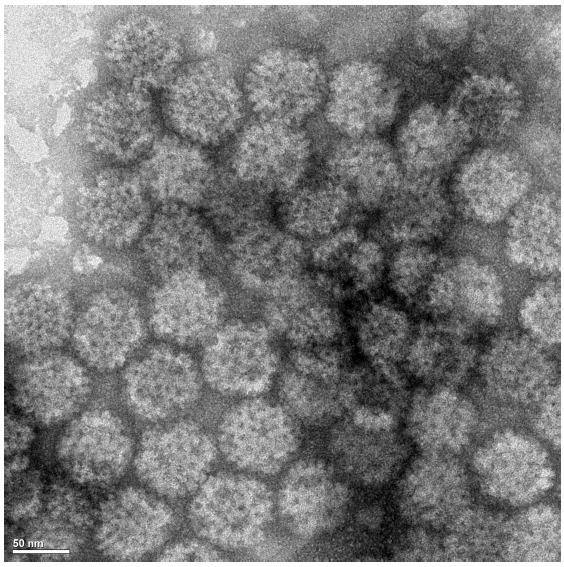

(b) *DLP RV, strain Wa, average diameter: 68.7 nm*

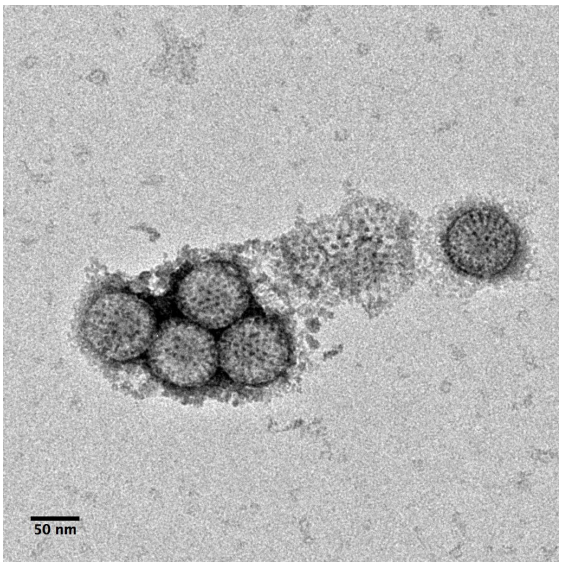

(c) *TLP RV, strain DS-1, average diameter: 70.0 nm*

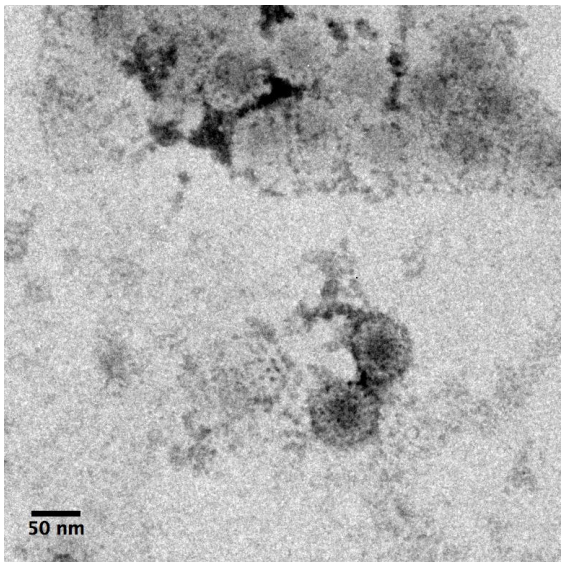

(d) *DLP RV, strain DS-1, average diameter: 63.4 nm*

Figure 3.7: *TEM images of TLP and DLP RV, strain Wa and DS-1. Scale bar in the lower left corner is 50 nm. Images were made by Ramona Valentina Mateiu, DTU CEN, Center For Electron Nanoscopy.*

3.4 $TCID_{50}$ assay of fraction 5 from CsCl gradient

50 % endpoint - $TCID_{50}$ assays were performed in order to calculate the titer values of fraction 5 of both RV strains. The assays were performed in 96 microtiter well plates by culturing cells and inoculating with 50 μL activated virus for 1 hour and then adding 200 μL serum free medium with 0.5 μg/mL trypsin, according to protocol in appendix A.1. The CPE was observed every day post infection to determine the 50 % end point dilution and at which point in time this was reached. A 10 fold dilution series of fraction 5 of each virus strain was examined in the assay. The calculation of the titer value for the assay was based on the Reed and Muench method [78]. The titer values were calculated according to the following formula [78]:

$$\text{Difference of logarithms} = \frac{(\text{mortality at dilution next above 50\%}) - 50\%}{(\text{mortality next above 50\%}) - (\text{mortality next below 50\%})} \tag{3.1}$$

where the 50 % endpoint dilution is $10^{\text{Difference of logarithms}}$, and the virus titer is $10^{\text{Difference of logarithms}}$/(volume virus sample used).

Table 3.2 and table 3.3 shows the results of the $TCID_{50}$ assay of RV strain Wa and DS-1, respectively. Using equation 3.1 the titer values of fraction 5 were found to be:

- RV strain Wa: 4.64 x 10^{-6}/50μL (9.28 x 10^{-5}/mL), after 6 days
- RV strain DS-1: 3.16 x 10^{-4}/50μL (6.32 x 10^{-3}/mL), after 8 days

The titer values of the purchased virus sample from ATCC were 2.8 x 10^{-6}/mL after 6 and 2.8 x 10^{-6}/mL after 8 days of RV strain Wa and DS-1, respectively. As the titer value of the $TCID_{50}$ assay determines the dilution factor of the virus sample where 50 % of the cell cultures contain dead cells, a virus titer value of e.g. 10^{-3}/mL means a lower virus concentration compared to a titer value of e.g. 10^{-8}/mL. Thus, concentrations of fraction 5 of both strains were lower than the initial sample from ATCC. This means that a lot of virus material was lost during the purification of the samples or the viral particles loose their infectious nature during purification. Furthermore, the RV strain DS-1 showed a very low $\log_{10}$ virus dilution which means that already at a $\log_{10}$ virus dilution of -4 there is no visible CPE.

Table 3.2: *$TCID_{50}$ assay of fraction 5, RV strain Wa, after 6 days*

	Wells		Cumulative total			
Log10 virus dilution	Dead	Alive	Dead	Alive	Total	Percent mortality
-3	4	0	11	0	11	100
-4	4	0	7	0	7	100
-5	3	1	3	1	4	75
-6	0	4	0	5	5	0
-7	0	4	0	9	9	0
-8	0	4	0	13	13	0
-9	0	4	0	17	17	0
-10	0	4	0	21	21	0

Table 3.3: *$TCID_{50}$ assay of fraction 5, RV strain DS-1, after 8 days*

	Wells		Cumulative total			
Log10 virus dilution	Dead	Alive	Dead	Alive	Total	Percent mortality
-3	4	0	4	0	4	100
-4	0	4	0	4	4	0
-5	0	4	0	8	8	0
-6	0	4	0	12	12	0
-7	0	4	0	16	16	0
-8	0	4	0	20	20	0
-9	0	4	0	24	24	0
-10	0	4	0	28	28	0

3.5 Biotinylation of virus particles and coupling to magnetic beads

The aptamer selection performed by our collaborator, Fraunhofer Institute for Cell Therapy and Immunology (IZI), is based on magnetic bead manipulation. During the aptamer development the ssDNA library is incubated with a target, in this case a virus. For the aptamer selection the target is coupled to magnetic beads through a biotin linker. The motivation of using magnetic beads separation is that it facilitates the process of separating any unbound ssDNA from the target bound ssDNA in the SELEX procedure. The following section will thus describe the experimental work

related to biotinylation of the viral particles.
Initially, the viral particles were biotinylated and then linked to the streptavidin coated magnetic beads as illustrated in figure 3.8. The diameter of the magnetic bead was 2.8 μm which means that there was a possibility to immobilise several viral particles on one bead. The principle of biotinylation was to covalently bind biotin to the surface proteins of the viral particles. Two biotinylation mechanisms were tested: one with Biotin-PEG4-Hydrazide (BPH) linker and one with (+)-Biotin N-hydroxysuccinimide ester (BNHS) linker.

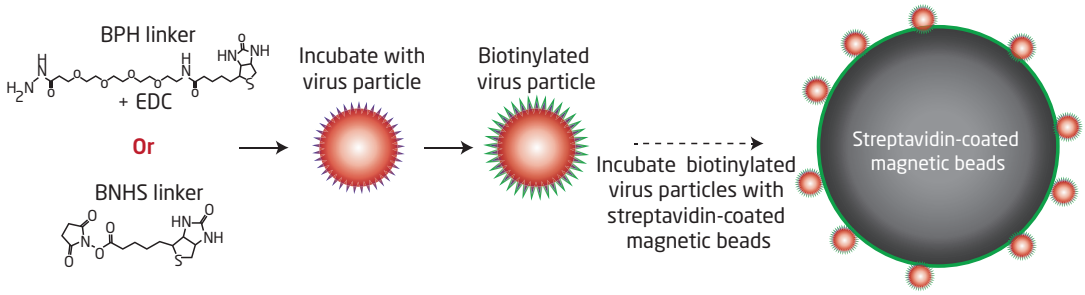

Figure 3.8: *Principle of biotinylation of virus particles with a BPH linker or BNHS linker and coupling of biotinylated virus particles to streptavidin coated magnetic beads.*

The BPH linker molecule has a pegylated spacer arm to increase the hydrophilic nature of the molecule (see figure 3.8 for molecular structure). The hydrazide biotin linker (BPH linker) binds to aldehydes. However, with the use of 1-Ethyl-3-(3-dimethylaminopropyl)carbodiimide (EDC) the hydrazide group can react with other carboxyl groups, in this case with carboxylic acids [79]. Thus, the amino acids in the protein backbone must contain carboxylic acids as side groups in order to bind to the hydrazide terminal end of the linker molecule. The only two natural amino acids that contain carboxylic acids as side groups are aspartic acid and glutamic acid. It is also a possibility to bind the linker molecule to the terminal carboxylic acid of the protein backbone.
The BNHS linker reacts with primary amines in the protein [80]. The amino acid lysine and the N-terminus of the protein backbone can thus be biotinylated with BNHS. Since the BNHS reacts with primary amines it is important to avoid buffers with amines or any protein content. The BNHS linker has a shorter spacer arm than the BPH linker (see figure 3.8 for molecular structure).
The two biotinyaltion mechanisms were examined and analysed with real-time RT-PCR to compare the performance of the two linkers. Furthermore, the infectivity of the biotinylated virus was examined by a cell assay.
Step by step protocols and material lists for biotinylation and magnetic bead cou-

pling of RV with the BPH linker and the BNHS linker can be found in appendix A.4 and appendix A.5. The protocols were based on protocols from Fraunhofer Institute for Cell Therapy and Immunology (IZI) and from the National Veterinary Institute, DTU VET.

3.6 Real-time RT-PCR analysis of biotinylated RV and RV samples

Real-time RT-PCR analysis of the biotinylated RV (bRV) samples and samples of the RV culture and purification was performed in order to quantify the yield of the biotinylation and the subsequent coupling of the virus to the magnetic beads. The principle of real-time RT-PCR was described in chapter 2.1.2.
The real time RT-PCR assay used for this PCR analysis was a one step reaction, hence reverse transcriptase and the real time PCR were performed in the same tube. Each sample was analysed in duplicates to get a repetition (average) Ct value for a precise result. If one of the two samples showed up negative and the other sample positive the Ct value was discarded for that particular sample and the result was considered negative. The RNA of the virus samples was extracted beforehand with a viral RNA extraction kit. The material list, primer/probe sequences and the protocol are found in appendix A.6.
The bRV samples and samples of the purification of both RV strains were analysed together with a dilution series of the RV strain Wa cell culture. PCR results of samples listed in table 3.4, table 3.5 and table 3.6 were done in the same PCR run together with negative controls containing nuclease free water. The negative controls showed up negative. From the Ct values of the PCR analysis of the dilution series of the cell culture (table 3.4) a relation between the Ct value and the dilution factor was found. The relation is illustrated in figure 3.9 where the relation was found from an exponential fit to be:

$$\text{Sample dilution} = 847666 \cdot e^{-0.754 \cdot \text{Ct value}} \tag{3.2}$$

This relation was used to calculate a (theoretical) dilution factor of the remaining analysed samples.

Table 3.5 and table 3.6 shows the results of the real-time RT-PCR of the bRV and the purified samples of RV strain Wa and DS-1, respectively. In each table an explanation of the sample is given together with the repetition Ct value and the calculated dilution factor (calculated from equation 3.2). The correlation between the Ct values and the calculated dilution factors is displayed graphically in figure

Table 3.4: *Real time RT-PCR analysis of virus culture dilutions, RV strain Wa*

Sample dilution	Repetition Ct value	Calculated dilution factor
10^{-1}	21,19	$0.97 \cdot 10^{-1}$
10^{-2}	24	$1.17 \cdot 10^{-2}$
10^{-3}	27,07	$1.16 \cdot 10^{-3}$
10^{-4}	30,92	$6.36 \cdot 10^{-5}$
10^{-5}	33,32	$1.04 \cdot 10^{-5}$
10^{-6}	–	–
10^{-7}	39,27	$1.17 \cdot 10^{-7}$
10^{-8}	–	–
10^{-9}	–	–

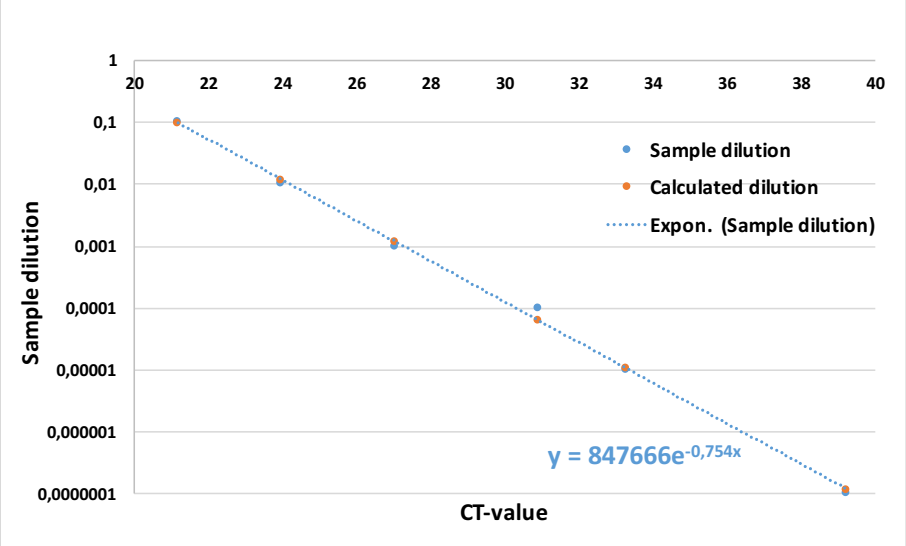

Figure 3.9: *Real time RT-PCR analysis of virus culture dilutions, RV strain Wa. An exponential relation between the Ct values and the dilution factor was assumed and a correlation between the two was found.*

3.10. The data displayed in blue corresponds to the RV strain Wa samples and the orange data points corresponds to the RV strain DS-1. From the figure it was evident that the sample concentration, i.e. the viral sample content, of the RV strain Wa was relatively higher than the concentration of the RV strain DS-1. The titer value of the $TCID_{50}$ assay was added to the figure. The Ct value of the titer value was calculated from equation 3.2. Since 140 μL was used for the RNA extraction of

the PCR analysed samples the volume of the titer value was corrected accordingly (1.3 x 10^{-5}/140μL after 6 days for RV strain Wa and 8.85 x 10^{-4}/140μL after 8 days for RV strain DS-1)

Table 3.5: *Samples and result of real time RT-PCR analysis of bRV and RV culture samples, strain Wa. Samples Wa 3 - 9 were diluted 10 times for the PCR analysis.*

Sample no.	Sample label	Sample explanation	Repetition Ct value	Calculated dilution factor
Wa 1	cell culture	Virus culture (with cell debris removed)	18.1	$1 \cdot 10^{0}$
Wa 2	1. Centri	Supernatant of first ultracentrifugation step	22.04	$5.14 \cdot 10^{-2}$
Wa 3	fract. 5	Fraction 5 (diluted 1:10 - compared to the original fraction 5 sample)	20.9	$1.21 \cdot 10^{-1}$
Wa 4	bRV BPH	Biotinylated virus with BPH (diluted 1:10)	23.18	$2.18 \cdot 10^{-2}$
Wa 5	bRV BNHS	Biotinylated virus with BNHS (diluted 1:10)	22.62	$3.32 \cdot 10^{-2}$
Wa 6	beads BPH	Biotinylated virus with BPH, bound to beads (diluted 1:10)	28.07	$5.45 \cdot 10^{-4}$
Wa 7	beads BNHS	Biotinylated virus with BNHS, bound to beads (diluted 1:10)	29.13	$2.45 \cdot 10^{-4}$
Wa 8	beads BPH S	Supernatant of biotinylated virus with BPH, bound to beads (diluted 1:10)	23.09	$2.33 \cdot 10^{-2}$
Wa 9	beads BNHS S	Supernatant of biotinylated virus with BNHS, bound to beads (diluted 1:10)	22.12	$4.84 \cdot 10^{-2}$

Real-time RT-PCR analysis of RV strain Wa

The correlation found in equation 3.2 was found from a dilution series of RV strain Wa. As expected the cell culture sample, RV strain Wa, showed a calculated dilution factor of 1, i.e. a non diluted sample. Fraction 5, RV strain Wa, showed a 10

Table 3.6: *Samples and result of real time RT-PCR analysis of bRV and RV culture samples, strain DS-1. Samples DS-1 3 - 9 were diluted 10 times for the PCR analysis.*

Sample no.	Sample label	Sample explanation	Repetition Ct value	Calculated dilution factor
DS-1 1	cell culture	Virus culture (with cell debris removed)	25.84	$2.93 \cdot 10^{-3}$
DS-1 2	1. Centri	Supernatant of first ultracentrifugation step	27.00	$1.22 \cdot 10^{-3}$
DS-1 3	fract. 5	Fraction 5 (diluted 1:10 - compared to the original fraction 5 sample)	23.31	$1.97 \cdot 10^{-2}$
DS-1 4	bRV BPH	Biotinylated virus with BPH (diluted 1:10)	26.18	$2.27 \cdot 10^{-3}$
DS-1 5	bRV BNHS	Biotinylated virus with BNHS (diluted 1:10)	24.87	$6.09 \cdot 10^{-3}$
DS-1 6	beads BPH	Biotinylated virus with BPH, bound to beads (diluted 1:10)	29.9	$1.37 \cdot 10^{-4}$
DS-1 7	beads BNHS	Biotinylated virus with BNHS, bound to beads (diluted 1:10)	29.43	$1.95 \cdot 10^{-4}$
DS-1 8	beads BPH S	Supernatant of biotinylated virus with BPH, bound to beads (diluted 1:10)	26.60	$1.65 \cdot 10^{-3}$
DS-1 9	beads BNHS S	Supernatant of biotinylated virus with BNHS, bound to beads (diluted 1:10)	25.03	$5.39 \cdot 10^{-3}$

times dilution compared to the cell culture. It is important to notice that fraction 5 was diluted 10 times for the PCR analysis as 140 μL sample was required for the RNA extraction and too much sample material would have been used if the sample had not been diluted. Thus, the concentration of fraction 5 corresponded to the concentration of the cell culture when corrected for the dilution. The PCR analysis of the supernatant of first ultracentrifugation step (sample: 1. Centri) strain Wa, revealed that the semi-purification was able to concentrate the virus with an efficiency of 95 % since the RV concentration of the supernatant was 20 times diluted compared to the cell culture.

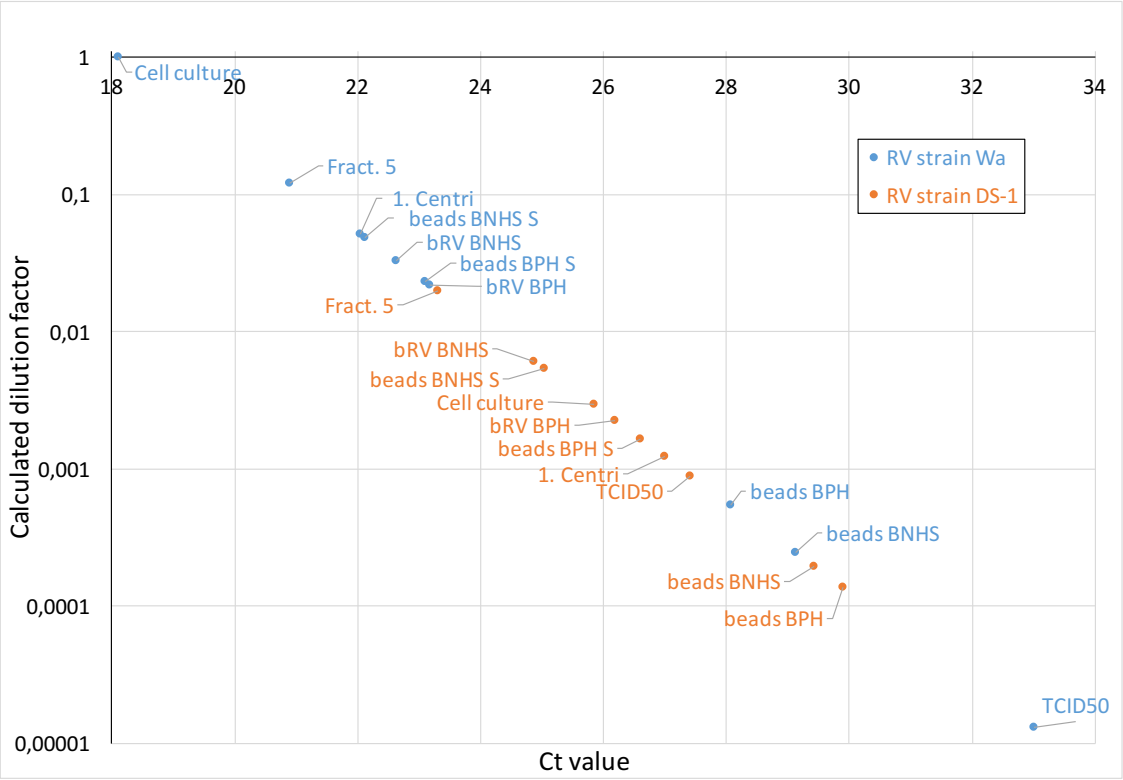

Figure 3.10: *Real time RT-PCR analysis of bRV and purification samples, RV strain Wa and DS-1. The calculated dilution factor was found from equation 3.2. The Ct values of the $TCID_{50}$ assays were calculated from equation 3.2 using the virus titer value as the dilution factor in the equation: $9.28 \cdot 10^{-5}/mL \cdot 0.14$ mL and $6.32 \cdot 10^{-3}/mL \cdot 0.14$ mL for RV strain Wa and DS-1, respectively. 0.14 mL was used as this was the volume used for the RNA extraction. Further explanation of the data labels can be found in table 3.5 and 3.6.*

Samples from the biotinylation of the two biotin linkers BPH and BNHS were analysed, six samples in total were analysed: the bRV sample, bRV sample bound to beads and the supernatant of the bRV sample bound to beads for each linker. All of these samples were diluted 10 times for the PCR analysis, hence the dilution factors must be 10 times higher to compensate for this. In general the concentration of the bead supernatant samples were higher than the concentration of the bRV samples coupled to beads. The relative concentration of the bead BPH supernatant sample and the bead BPH sample was approximately 40 times higher for strain Wa. The relative concentration of the bead BNHS supernatant sample and the bead BNHS sample was approximately 200 times for strain Wa. From this it was concluded that the BPH linker had a higher yield as more virus bound to the beads using the BPH linker. It was still evident that only a fraction of the virus indeed did bind to the

beads as the concentration of the bead BPH samples was 40 times lower than the bRV BPH sample. The relative concentrations are summarised in table 3.8.

Table 3.7: *Relative concentrations of RV strain Wa samples*

Samples	Relative concentration
Fraction 5 / bRV BPH	56
Fraction 5 / bRV BNHS	47
bRV BPH / BPH bead	40
bRV BNHS / BNHS bead	135
bead BPH S / BPH bead	43
bead BNHS S / BNHS bead	197

Real-time RT-PCR analysis of RV strain DS-1

The calculated dilution factors of RV strain DS-1 were relative to the RV strain Wa since the relation (equation 3.2) was made from a dilution series of RV strain Wa. As the amount of genomic material (i.e. 11 dsRNA per RV virus) and the real-time RT-PCR assay with primers and probe were the same for the two strains it was assumed that the relation (equation 3.2) could be used for RV DS-1. In general, the concentrations of the DS-1 strain samples were lower than the samples of the Wa strain as illustrated in figure 3.10. The first centrifugation step, the semi-purification on a sucrose cushion, was not as efficient for the DS-1 strain as 42 % of the RV was present in the supernatant of the first centrifugation step (1. Centri/Cell culture * 100). On the other hand fraction 5 of the CsCl purification had a 67 times higher RV concentration than the cell culture, taken into account that the fraction 5 was 10 times diluted for the PCR analysis. Comparison of fraction 5 of the RV strain DS-1 with the RV strain Wa revealed that the DS-1 strain had a 6 times lower RV concentration than the Wa strain.
The relative concentrations of the bRV samples and fraction 5 are listed in table 3.8. The relative concentration of the supernatant of the bead BPH sample was 12 times higher than the BPH bead sample. For the BNHS linker the relative concentration of the two sample was 28. This indicated that the relative amount of immobilised RV DS-1 on the beads was relatively higher than for the RV Wa strain where the relative concentrations were 43 and 197 for the BPH and BNHS linkers, respectively. The relative concentrations of the RV DS-1 bRV bPH and BNHS compared to the BPH bead and BNHS bead samples were 17 and 31, respectively. Again, this showed that the relative amount of immobilised bRV DS-1 onto the beads was higher than

the RV strain Wa. Thus, it seemed like the biotinylation of the DS-1 strain was more efficient than the RV Wa strain. It is still important to note that the concentration of RV Wa was higher than the concentration of the RV DS-1 strain, which may have an impact on the results.

Table 3.8: *Relative concentrations of RV strain DS-1 samples*

Samples	Relative concentration
Fraction 5 / bRV BPH	87
Fraction 5 / bRV BNHS	32
bRV BPH / BPH bead	17
bRV BNHS / BNHS bead	31
bead BPH S / BPH bead	12
bead BNHS S / BNHS bead	28

The difference between the two biotin linkers was most predominant in the RV strain Wa where the BPH linker performed best. Since the most interesting RV strain was strain Wa, based on the high level of infectious nature of this strain, and the highest yield of the RV strain Wa coupled to the beads was obtained using the BPH linker it was chosen to use this linker for the biotinylation for the aptamer selection.

3.6.1 Control of passive absorption of RV onto beads

The passive absorption of the two RV strains, Wa and DS-1, was tested in order to compare the passive absorption to the biotin-strepatvidin binding of the bRV to the beads. Fraction 5 for both RV strains were diluted 1:50 and incubated with the magnetic beads as described in appendix protocol A.4 but without the biotinylation step. The rationale behind diluting the fraction 5 samples 1:50 was based on a relative concentration of 56 of samples, RV strain Wa, fraction 5 compared to the bRV BPH sample (see table 3.8). After incubation of the RV with the beads the supernatant of the bead suspension was collected and the beads were washed 3 times before RNA extraction. Table 3.9 shows the results of the real-time RT-PCR analysis. The calculated dilution factor was calculated from equation 3.2. The real-time RT-PCR analysis was performed according to the protocol A.6 in the appendix. The negative PCR control was negative and the positive PCR control had a Ct value of 26.21. The relative concentrations of the analysed samples are listed in table 3.10.

The relative concentration of samples *Frac. 5, RV Wa, 1:50 / beads neg. Wa* was 0.97, which means that almost all of the virus was present in the bead sample.

Table 3.9: *Samples and result of real time RT-PCR analysis of control of passive absorption of RV onto beads*

Sample label	Sample explanation	Repetition Ct value	Calculated dilution factor
Frac. 5, RV Wa, 1:50	Original fraction 5 sample, RV strain Wa diluted 1:50	23.37	$1.89 \cdot 10^{-2}$
Beads neg. Wa	Sample *Frac. 5, RV Wa*, incubated with beads	23.33	$1.94 \cdot 10^{-2}$
Neg. bead S Wa	Supernatant of sample *Beads neg. Wa*	24.23	$9.86 \cdot 10^{-3}$
Frac. 5, RV DS-1, 1:50	Original fraction 5 sample, RV strain DS-1 diluted 1:50	25.65	$3.38 \cdot 10^{-3}$
Beads neg. DS-1	Sample *Frac. 5, RV DS-1*, incubated with beads	28.04	$5.58 \cdot 10^{-4}$
Neg. bead S DS-1	Supernatant of sample *Beads neg. DS-1*	26.21	$2.22 \cdot 10^{-3}$

Table 3.10: *Relative concentrations of PCR analysis of control of passive absorption of RV onto beads. Samples: Frac. 5, RV Wa and DS-1, were the original fraction 5 samples analysed in table 3.5 and 3.6, corrected for the 10 times dilution for the PCR analysis.*

Samples	Relative concentration
Frac. 5, RV Wa / frac. 5, RV Wa, 1:50	64
Frac. 5, RV Wa, 1:50 / beads neg. Wa	0.97
Neg. bead S Wa/ beads neg. Wa	0.51
Frac. 5, RV DS-1 / frac. 5, RV DS-1, 1:50	58
Frac. 5, RV DS-1, 1:50 / beads neg. DS-1	6.1
Neg. bead S DS-1/ beads neg. DS-1	4.0

The relative concentration of the supernatant sample compared to the bead sample was 0.51, which indicates that the concentration of the bead sample was twice as high as the supernatant sample. The analysed samples og the DS-1 strain showed a relative concentration of 6 for the diluted fraction 5 compared to the bead sample

and a relative concentration of 4 for the supernatant of the bead sample compared to the bead sample.
The results indicated that the passive absorption of the non-biotinylated virus samples onto the magnetic beads was quite large compared to the bRV samples immobilised onto the beads. It was unclear how strong this binding was since the RNA of the virus samples were extracted just after the incubation. It was thus a possibility that the viral particles can disassociate with the bead over a period of time since it must be assumed that the biotin-streptavdin binding is stronger than the passive absorption.

3.7 Examining the infectivity of bRV

Information about the infectivity of the bRV samples is important, especially in relation to the aptamer development as infectious material must be handled with extra precautions and requires classified laboratory settings. The infectivity of the bRV, RV strain Wa and DS-1, with either the BNHS and BPH linker was tested along with a control of purified RV without biotinylation (results of the purified RV sample was described in the $TCID_{50}$ assay, section 3.4). The infectivity assays were performed in the same way as the $TCID_{50}$ assay in 96 microtiter well plates with cultured MA104 cells by inoculating 50 μL activated virus per well for 1 hour and then adding 200 μL serum free medium with 0.5 μg/mL trypsin, according to protocol in appendix A.1. A dilution series, compared to the concentration of fraction 5, ranging from 10^{-3} to 10^{-10} of the bRV BPH and bRV BNHS of each RV strain was tested. The infectivity study was done on bRV samples without coupling the bRV to magnetic beads, i.e. no magnetic beads were added to the cell culture. The CPE was observed on a daily basis post infection. Before infection at day 0 the cell culture had reached a confluence of approximately 90 %.
Tables 3.11 and 3.12 shows the results of the bRV strain Wa with the BPH and the BNHS linker, respectively. The results for the bRV strain DS-1 for the BPH and BNHS linker is listed in tables 3.13 and 3.14, respectively. All of the results of the four tables are the same: none of the infected wells of the titer plates for all of the analysed samples showed any CEP caused by a viral infection. Thus, it was concluded that the bRV was not infectious. The lack of infectivity of the virus could be caused by a too low concentration of the activated virus samples. This explanation is not likely since the highest concentration of bRV samples used was $10^{-3}/50\mu$L, which was higher than the titer values of the $TCID_{50}$ assay(4.64 x $10^{-6}/50\mu$L, after 6 days for RV strain Wa and 3.16 x $10^{-4}/50\mu$L, after 8 days for RV strain DS-1). Another plausible explanation of the lack of infectivity could be that the biotin linker binds to the structural viral protein VP4 and thereby blocks the ability of the virus to enter into the host cell, which means that the virus looses

its infectivity.

Table 3.11: *Infectivity assay of bRV BPH, strain Wa, 8 days post infection*

	Wells		Cumulative total			
Log10 virus dilution	Dead	Alive	Dead	Alive	Total	Percent mortality
-3	0	4	0	4	0	0
-4	0	4	0	8	0	0
-5	0	4	0	12	0	0
-6	0	4	0	16	0	0
-7	0	4	0	20	0	0
-8	0	4	0	24	0	0
-9	0	4	0	28	0	0
-10	0	4	0	32	0	0

Table 3.12: *Infectivity assay of bRV BNHS, strain Wa, 8 days post infection*

	Wells		Cumulative total			
Log10 virus dilution	Dead	Alive	Dead	Alive	Total	Percent mortality
-3	0	4	0	4	0	0
-4	0	4	0	8	0	0
-5	0	4	0	12	0	0
-6	0	4	0	16	0	0
-7	0	4	0	20	0	0
-8	0	4	0	24	0	0
-9	0	4	0	28	0	0
-10	0	4	0	32	0	0

Table 3.13: *Infectivity assay of bRV BPH, strain DS-1, 8 days post infection*

	Wells		Cumulative total			
Log10 virus dilution	Dead	Alive	Dead	Alive	Total	Percent mortality
-3	0	4	0	4	0	0
-4	0	4	0	8	0	0
-5	0	4	0	12	0	0
-6	0	4	0	16	0	0
-7	0	4	0	20	0	0
-8	0	4	0	24	0	0
-9	0	4	0	28	0	0
-10	0	4	0	32	0	0

Table 3.14: *Infectivity assay of bRV BNHS, strain DS-1, 8 days post infection*

	Wells		Cumulative total			
Log10 virus dilution	Dead	Alive	Dead	Alive	Total	Percent mortality
-3	0	4	0	4	0	0
-4	0	4	0	8	0	0
-5	0	4	0	12	0	0
-6	0	4	0	16	0	0
-7	0	4	0	20	0	0
-8	0	4	0	24	0	0
-9	0	4	0	28	0	0
-10	0	4	0	32	0	0

3.8 Biotinylation of HAV samples

The HAV sample prepared for the aptamer selection was cultured and purified by ultracentrifugation and resuspended in phosphate-buffered saline (PBS) at the Environmental Virological Laboratory, Tor Vergata University, Rome, Italy. Inactivation of the HAV was performed before the biotinylation. Inactivation was done to reduce the risk related to work with HAV and to ease shipment of samples to our collaborators at the Fraunhofer Institute for Cell Therapy and Immunology (IZI). According to Wang *et al.*, 2015, [30], inactivation of HAV with formaldehyde did not show any structural modifications of the virus. They based their conclusion

on high resolution X-ray crystallography. Inactivation of HAV was performed with formaldehyde diluted 1:2000 and left for 8 days at 4 °C as described by Wang *et al.* [30]. Material list and protocol for HAV inactivation can be found in appendix A.7. After inactivation, biotinylation of the HAV was performed with the BPH linker based on the same principle as the biotinylation of the RV. Protocol and material list can be found in appendix A.8.

3.8.1 Real-time RT-PCR analysis of biotinylated inactivated HAV samples

The biotinylated HAV (bHAV) samples were analysed with real-time RT-PCR. The PCR assay used for this purpose was a two step reaction, i.e. the reaction was divided into the reverse transcription followed by the real-time PCR in two separate tubes. We did not have a fluorescent probe for the real-time PCR and Sybr Green was used instead. Sybr Green binds to all dsDNA and is not sequence specific like a probe. This means that this assay was more sensitive to false positive results caused by primer-dimer formation or wrong primer annealing. The protocol, primer sequences and material list for the real-time RT-PCR analysis of the HAV can be found in appendix A.9.
Due to the small amount of HAV sample provided (approximately 4 mL) it was not beneficial to make a dilution series of the HAV sample like it was done with the RV strain Wa. In total, 5 HAV samples were analysed in duplicates with real-time RT-PCR, results are listed in table 3.15. Negative samples containing nuclease free water were analysed together with the HAV samples and they showed up negative. From the results listed in table 3.15 it was clear that the concentration of the original HAV sample was low as a Ct value of 28.13 corresponds to a low concentration. A Ct value of 33 or higher was considered negative. As a general rule, a three step reduction of Ct value corresponds to a 1-log reduction in concentration. The Ct value of the inactivated HAV sample was 31.15 which corresponds to a 10 times lower virus concentration than the original HAV sample. This reduction in concentration can either be caused by the formaldehyde that may disrupt the DNA during the inactivation or a physical reduction of the amount of virus during the dialysis. The inactivated bHAV sample showed a Ct value of 36.61, which was above the threshold of 33 and was considered negative. This was confirmed in the melting point analysis where the melting point for the duplicate samples were 83.0 °C and 81.0 °C. The melting point of the to samples must be the same and equal to the original HAV sample (82.7 °C) since the amplified genomic material was the same. The samples of the inactivated bHAV coupled to beads and the supernatant of inactivated bHAV coupled to beads did not show up positive in the PCR analysis. Thus, the concentrations of the samples were below the detection point of the PCR analysis. The low

concentration of the inactivated bHAV coupled to beads may be a hindrance in the aptamer selection as a certain amount of target must be present on the magnetic beads in order for the selection to be specific to the HAV.

Table 3.15: *Real-time RT-PCR analysis of biotinylated inactivated HAV samples with melting point data. Sample A and sample B correspond to the duplicate samples used for the analysis.*

Sample	Repetition Ct value	Melting point - °C [Sample A / Sample B]
Original HAV sample	28.13	82.7 / 82.7
Inactivated HAV	31.15	82.7 / 82.7
Inactivated bHAV	36.61	83.0 / 81.0
Inactivated bHAV coupled to beads	–	–
Supernatant of inactivated bHAV coupled to beads	–	–

3.9 Conclusion

The main purpose of the experimental work described in this chapter was to prepare viral samples for the aptamer selection. For the RV, the preparation involved virus propagation in cell culture, purification, biotinylation and analysis of the yield with real-time RT-PCR. The HAV sample was cultured and purified by our collaborators at the Environmental Virological Laboratory, Tor Vergata University, Rome, Italy and the experimental work related to the sample preparation involved inactivation, biotinylation and analysis of the yield with real-time RT-PCR.
The yield of the bRV and the bHAV samples was low compared to the original cell culture samples. For the bRV coupled to the magnetic beads with the BPH biotin linker the concentration was 40 (RV strain Wa) and 17 (RV strain DS-1) times lower compared to the bRV samples. The bRV samples with the BPH linker showed a 56 and 87 times lower concentration for the RV strains Wa and DS-1 compared to fraction 5 of the CsCl purification, respectively. This indicated that the coupling of the bRV to the magnetic beads was inefficient or it could be caused by low efficiency of the biotinylation. Furthermore, the control of the passive absorption of the non-biotinylated beads to the beads showed a high level of passive absorption. It was unclear how stable this passive absorption was compared to the biotin-streptavidin

binding of the bRV and the beads as this would require further testing.
For the HAV sample it was not possible to calculate a relative concentration of the original HAV sample compared to the inactivated bHAV coupled to beads since the latter was negative in the PCR analysis. Furthermore, the sample of the inactivated bHAV showed a Ct value above 33 and was considered negative.
The low concentration of the bRV and the bHAV samples may be problematic during the aptamer selection, especially for the aptamer selection against the HAV. The samples were shipped to our collaborators at the Fraunhofer Institute for Cell Therapy and Immunology (IZI), Berlin, Germany. In the time of this writing, the aptamer selection is still proceeding by the Fraunhofer Institute for Cell Therapy and Immunology (IZI).

— 4 —

All-polymer aptasensor design and fabrication development

Sensor development requires considerations of many different parameters that are usually intercorrelated. Some of the important considerations related to design inputs are choice of materials, fabrication methods, electrode design, possibility of multiplexing, electrical interface, transducer method etc. The different design inputs and their correlations are listed in figure 4.1. The transducer method for the viral aptasensor was initially decided to be electrochemical impedance spectroscopy (EIS). The principle of EIS was described in chapter 2.3.2. EIS was chosen as the transducer method since impedimetric biosensors are able to directly convert a biological recognition event into an electrical signal, thus enabling real-time label-free measurements. Furthermore, it was initially decided to make an all-polymer aptasensor, i.e. both sensor substrate and electrodes should be made of polymer materials. The choice of using polymer materials was based on a desire for cheap and easy fabrication and unit price of each sensor chip. By using polymer materials instead of noble metals and silicon based devices, expensive materials and fabrication methods that require clean room facilities could be avoided. Clean room chip fabrication enables advantages like low size limitations in the sub micrometer range due to the clean environment. For the viral aptasensor development the smallest structures of the electrodes were estimated to be around 100 μm, therefore the clean room fabrication was not necessary and was a disadvantage due to the high costs and complicated processes. Furthermore, polymer materials can be casted and moulded in almost all shapes not limited to two dimensional (2D) structures, which is usually the case for silicon fabrication methods.
This chapter will describe different important design inputs, requirements and specifications related to the design and development of the viral aptasensor. The chapter

will focus on the iterative development for the aptasensor design, choice of materials and fabrication methods.

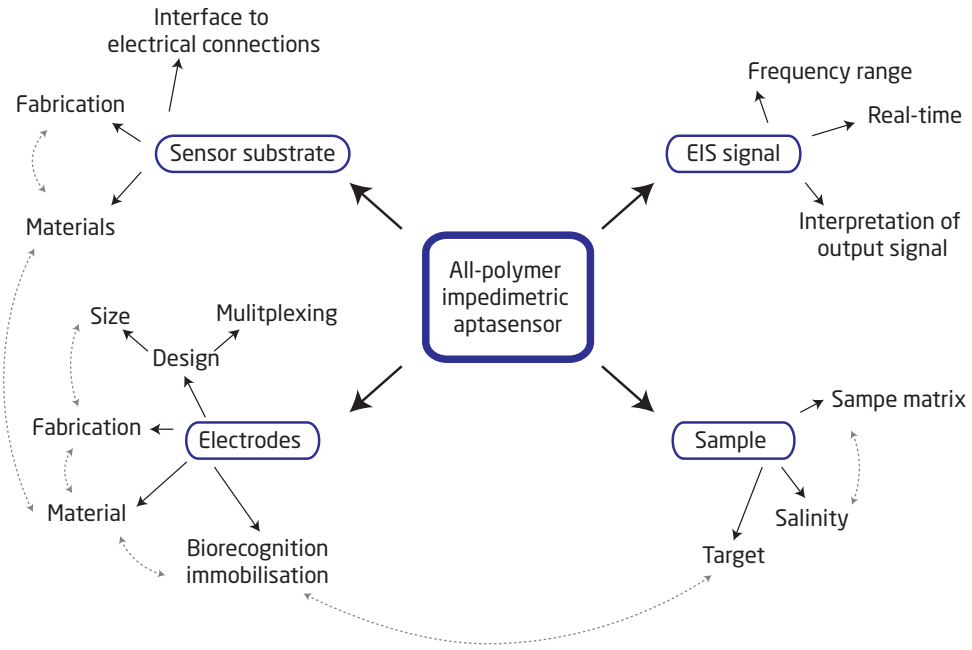

Figure 4.1: *Considerations for design inputs for the viral aptasensor development. Many of the different design inputs are intercorrelated (grey dashed arrows).*

4.1 Initial design requirements for the viral aptasensor

These following initial design and fabrication requirements were defined in order to frame the further design and fabrication phases of the aptasensor development.

Multiplexing platform

The overall long term goal of the viral aptasensor is to do real-time detection of the three different enteric viruses: NoV, RV and HAV, in a water sample, simultaneously. It was thus necessary to design the sensor as a multiplex sensing platform that allowed for the detection of several targets in one sample. Hence, the sensor design required at least three electrode pairs for viral detection and a control/reference electrode pair for differential impedance measurements in order to subtract the control baseline signal. Subtraction of the baseline signal from the signal of the

sensing electrodes made it possible to remove any unwanted external signal effects and interferences that did not originate from the actual viral detection.

PEDOT:PSS as electrode material

In order to avoid noble metals in the sensor an alternative conducting material for the sensing electrodes had to be found. PEDOT:PSS was chosen as the electrode material since this intrinsic conducting polymer is one of the best conducting polymers and our group at DTU Nanotech had experience in using PEDOT based materials for biosensing applications. Furthermore, as a printing material PEDOT:PSS is available as a commercial aqueous dispersion paste for screen-printing. PEDOT:PSS was described in chapter 2.3.3.
In the initial design phases we were exploring different methods for electrode fabrication. Previously, our group at DTU Nanotech had experimented with agarose stamping as a fabrication method for PEDOT doped with tosylate (PEDOT:TsO) biosensor electrodes [11]. It was found that the agarose stamping had several disadvantages in the form of difficulty in electrode size reproduction, which resulted in great size variation. Furthermore, the agarose stamping method was a slow fabrication method, which was not suitable for large scale production. In the early prototyping of the viral aptasensor, CO_2 laser ablation was used as a fabrication method to define electrodes by removing the unwanted areas of a PEDOT:TsO dry film on a polymer substrate. This turned out to be difficult as the CO_2 laser beam burned the PEDOT and the polymer substrate to an extend where an electrically insulating film was deposited on top of the electrodes. This insulating film originated from condensed vapours from the laser ablated polymers. Furthermore, the diameter of the laser beam was around 140 μm, which meant that fabrication of reproducible electrode structures of 100 μm in size was not possible. Finally, the fabrication method was changed to screen-printing since this method suited many of the requirements related to the electrode size and material choice. As mentioned earlier, PEDOT:PSS is available as a commercial aqueous dispersion paste for screen-printing which makes electrode fabrication by screen-printing a highly interesting method. Furthermore, screen-printing is a fabrication method that is suitable for large scale production with a size limit of printable structures of around 100 μm. Using screen printing, the changes in the electrode design can easily and inexpensively be performed, since a new design only requires preparation of a new screen.

Polymer substrate material

The aptasensor chip substrate material was decided to be a polymer material. Many different polymer materials are suitable as a chip substrate and they all have ad-

vantages and disadvantages. The requirements for the polymer substrate material was thus related to the chosen fabrication method but also the adherence of the PEDOT:PSS paste had an impact on the material choice. In the early design iterations, CO_2 laser ablation was used as the fabrication method for fast prototyping. Poly(methyl methacrylate) (PMMA) was used as substrate material since this material was suitable for this fabrication method. In the later design iterations the fabrication method was changed to injection moulding where different substrate materials, Cyclic Olefin Copolymer (COC) and Polycarbonate (PC) were tested for substrate material. Injection moulding is a suitable method for cheap large scale production but the tools used for the mould are expensive, which explains why laser ablation was applied in the initial design phases before design-lock of the chip substrate. The injection moulding was made by our external collaborator Michael Lundbech A/S, Denmark.

4.2 Iterative design and fabrication development of the viral aptasensor chip

The iterative design process of the viral aptasensor can be divided into two main designs based on the electrical interface:

1. The Universal Serial Bus (USB) chip
2. The Secure Digital (SD) card chip

All of the chip designs were designed using the Autodesk AutoCAD software. The following sections will describe the different design iterations and the evolvement of the design from the USB chip to the final SD card chip design. A detailed description of the chip fabrication will only be described for the SD card chip, version 2, in section 4.3 and 4.5.

4.2.1 The USB chip

The USB chip design was the initial design for the viral aptasensor with two electrode pairs. The two electrode pair configuration did not meet the design requirements for multiplexing as described in section 4.1 of this chapter. The main purpose of this chip design was to investigate the different fabrication methods for the polymer substrate and the electrodes and to do initial EIS testing of the electrodes. The USB chip design iterations were divided into three phases:

1. USB chip, version 1: laser cut PMMA, laser ablated PEDOT:TsO, no lid for liquid interface

2. USB chip, version 2: injection moulded COC chip, screen-printed PEDOT:PSS, lid with wells

3. USB chip, version 3: laser cut PMMA, screen-printed PEDOT:PSS, polydimethylsiloxane (PDMS) liquid channels

USB chip, version 1: laser cut PMMA, laser ablated PEDOT:TsO, no lid for liquid interface

The USB chip, version 1, was made by laser ablation with a CO_2 laser. Both electrodes and chip substrate were defined by laser ablation. The substrate material was PMMA since this material was suited for laser ablation. Figure 4.2 shows the technical drawing, images of the chip, microscope image of chip surface and the sensor principle for USB chip, version 1. The chip was made to fit into a 1.5

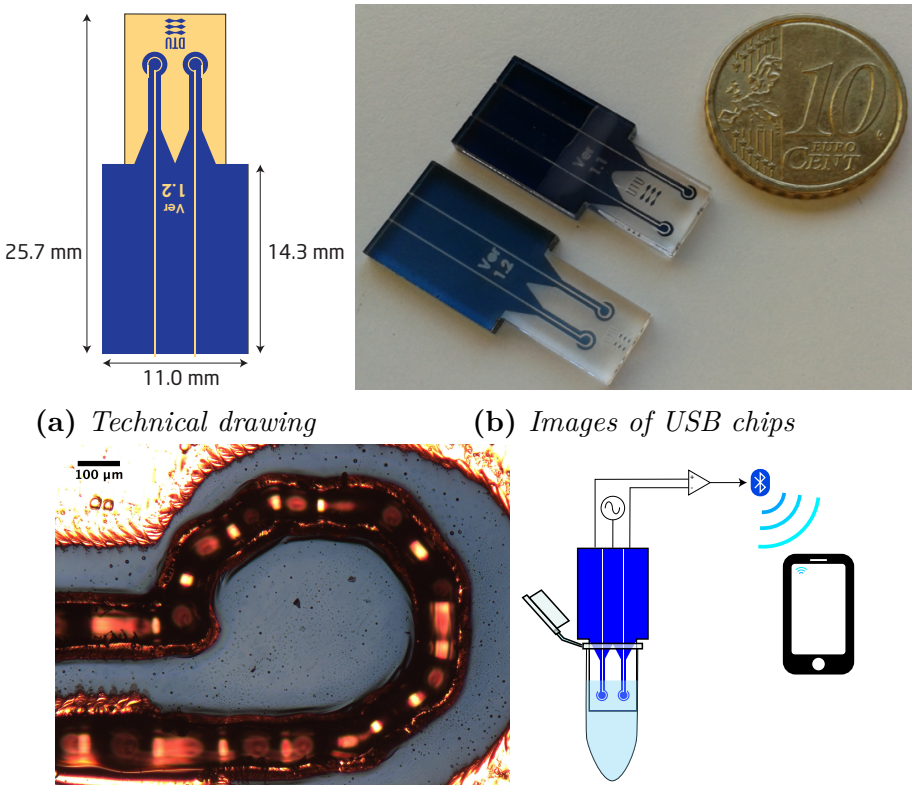

(a) *Technical drawing*

(b) *Images of USB chips*

(c) *Microscope image of chip surface*

(d) *Sensor principle of the USB sensor system*

Figure 4.2: *USB chip, version 1: laser cut PMMA, laser ablated PEDOT:TsO, no lid for liquid interface.*

mL Eppendorf tube and dipped directly into the sample solution with a wireless

connection to a mobile device as illustrated figure 4.2d.
The electrode material was PEDOT:TsO. The electrodes were made by spin coating a thin layer of PEDOT:TsO onto a 10 x 10 cm, 2 mm thick, PMMA sheet and then removing the PEDOT:TsO in the unwanted areas by laser ablation. PEDOT:TsO was used since our group had previous experience in spin coating this material. Figure 4.2a shows the technical drawing of the chip, the blue areas are PEDOT:TsO and the beige areas are removed by laser ablation. Figure 4.2b shows an image of two of the USB chip, version 1. As described earlier the diameter of the laser beam of the CO_2 laser was around 140 μm, which proved to be a challenge in the fabrication process. Two different settings were used for defining the electrode with the laser: vector and raster setting. The vector setting was used to cut the lines between the electrodes and the raster setting was used to remove the surrounding material. Figure 4.2c shows a microscope image of the electrode surface. The image illustrates several problems with this fabrication method: limited spacial resolution of the laser, large diameter of the laser compared to electrode structures and sputtering of evaporated material on top of the electrode surface. Especially, the sputtering of evaporated material turned out to be a large hindrance as the electrode became electrically isolated, which meant that electric connection to the electrodes was impossible. Based on the observations and the problems with the CO_2 laser ablation the fabrication of the electrodes was changed for the USB chip, version 2, to screen-printing and a chip substrate was made by injection moulding to avoid the CO_2 laser.

USB chip, version 2: injection moulded COC chip, screen-printed PEDOT:PSS, lid with wells

The substrate of the USB chip, version 2, was fabricated in COC by injection moulding and the electrodes were screen-printed PEDOT:PSS. Figure 4.3 shows the technical drawing of the electrodes, the two injection moulded parts: chip substrate and lid and an image of the disassembled chip with PEDOT:PSS electrodes. The PEDOT:PSS electrodes are very hard to see in the image as the PEDOT:PSS has a light blue transparent colour.

The active part of the electrode pair was the part of the PEDOT:PSS directly in contact with the sample. The active part of each electrode pair was designed as two concentric circles with an outer diameter of 700 μm and 500 μm with a thickness og 100 μm spaced 100 μm apart. Like the USB chip, version 1, the electrode design was made as a three electrode configuration in such a way that the centre electrode was shared between the two electrode pairs. This was changed in future designs as it was a disadvantage that the electric signal from the electrode pairs was intercorrelated. The lid was designed with a simple sample/liquid interface, which had two small wells for addition of sample with a pipette. In this way it was possible to control

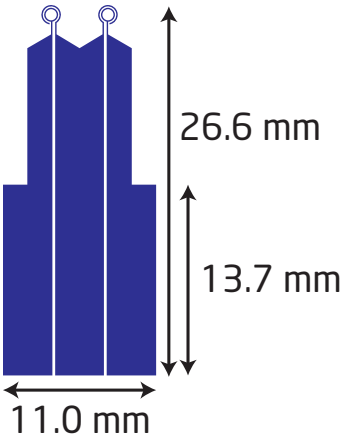

(a) *Technical drawing*

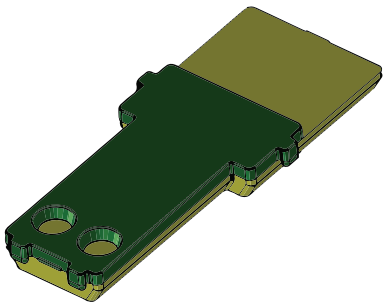

(b) *The two injection moulded chip parts: chip substrate (light green) and lid (dark green)*

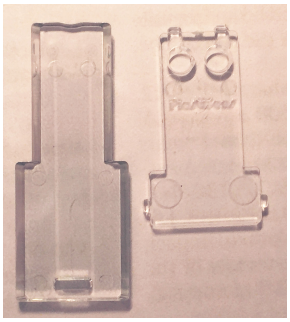

(c) *Image of the disassembled chip with PEDOT:PSS electrodes*

Figure 4.3: *USB chip, version 2: injection moulded COC chip, screen-printed PEDOT:PSS, lid with wells*

the electrode area directly in contact with the sample and the sample volume. The small area of the chip substrate limited the possibility of channels for continuous liquid flow. This led to the USB chip, version 3, where this issue was solved. During the development of the PEDOT:PSS screen-printing process, it was observed that a spacing of 100 μm between the electrodes often led to a short circuit between the electrodes, hence a low yield of usable chips was obtained. The development of the screen-printing process for the electrode print is described in details in section 4.3. The development was made partly at DTU Nanotech and partly in cooperation with Vesterbro Serigrafi A/S, Denmark, at their facilities.

USB chip, version 3: laser cut PMMA, screen-printed PEDOT:PSS, PDMS liquid channels

The USB chip, version 3, solved some of the previous problems concerning the shared centre electrode and the liquid interface. Figure 4.4 shows the technical drawing of the chip, the chip substrate with printed electrodes and an image of four assembled chips with liquid tubings connected in series.

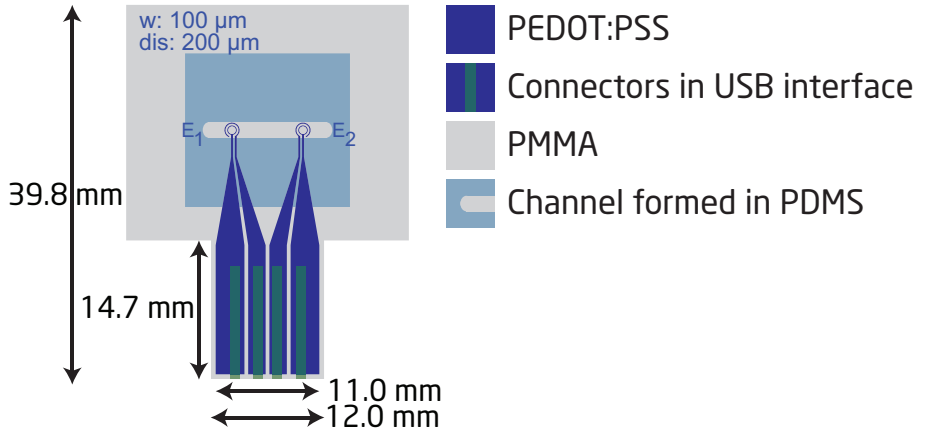

(a) *Technical drawing*

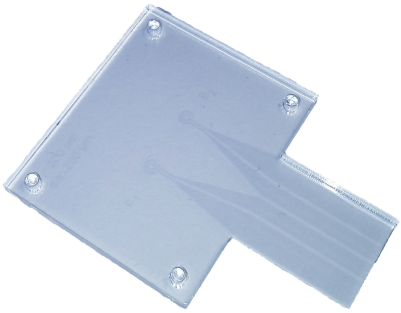

(b) *Chip substrate with printed electrodes*

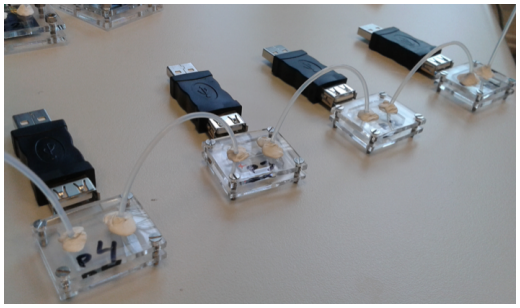

(c) *Four assembled chips with liquid tubings connected in series*

Figure 4.4: *USB chip, version 3: laser cut PMMA, screen-printed PEDOT:PSS, PDMS liquid channels*

The chip substrate was fabricated in PMMA by CO_2 laser ablation. Laser ablation was used for fabricating the substrate as this method allowed for fast prototyping and experimenting with the design of the substrate. The PEDOT:PSS electrodes were printed onto the substrate by screen-printing. The design of the active part of the electrodes was the same as for the USB chip, version 2, but the spacing between the electrodes was increased to 200 μm to avoid short circuit of the electrode paris. The area of the chip substrate was increased in this design iteration in order to

allow enough space for a liquid channel. The liquid channel was casted in PDMS and clamped between the substrate and a laser cut PMMA lid. It was thus possible to experiment with EIS measurements with continuous sample flow. The assembly of the chips with the PMMA substrate, the PDMS channel and the PMMA lid was a cumbersome process. For the next design iterations this was intended solved.
As pointed out earlier the USB chip did not suit the requirements for the multiplexing platform. As a consequence of this, the designs of the substrate and electrodes were changed to fit an SD card interface for the next design iteration.

4.2.2 The SD card chip

In order to meet the design requirements of a four electrode pair multiplexing configuration the electrical interface and substrate design was changed to a design based on a SD card interface. The SD card electrical interface has nine electrical connector pins which suited our need for eight connectors. Furthermore, the SD connector is designed to insert a chip by a click-and-lock system where the chip is locked inside the connector once it is mounted. This ensures that the chip is fixed inside the connector and reduces the possibility that the chip is accidentally dismounted during measurements. Figure 4.5 illustrates a cross section of an SD card chip mounted inside a SD card connector.

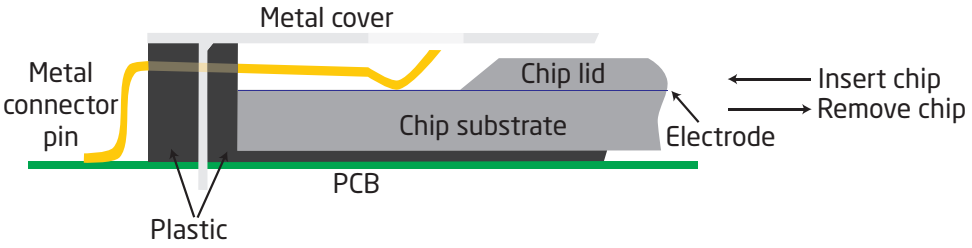

Figure 4.5: *Illustration of a cross section of an SD card chip mounted in a SD card connector.*

The design phases of the SD card chips were divided into three design versions:

1. SD card chip, version 1: laser cut PMMA, screen-printed PEDOT:PSS, double sided adhesive tape channels

2. SD card chip, version 2: laser cut PMMA, screen-printed PEDOT:PSS, double sided adhesive tape channels

3. SD card chip, version 3: injection moulded COC or PC, screen-printed PEDOT:PSS, injection moulded lid with channel and tubing connectors, assembled with screen-printing glue

The technical drawings and images of the three SD card chip versions can be seen in figure 4.6. The figure also shows the relative position of the SD card connector and the original dimensions of a SD card (green and purple line in figure 4.6a, respectively). The three designs will be described below.

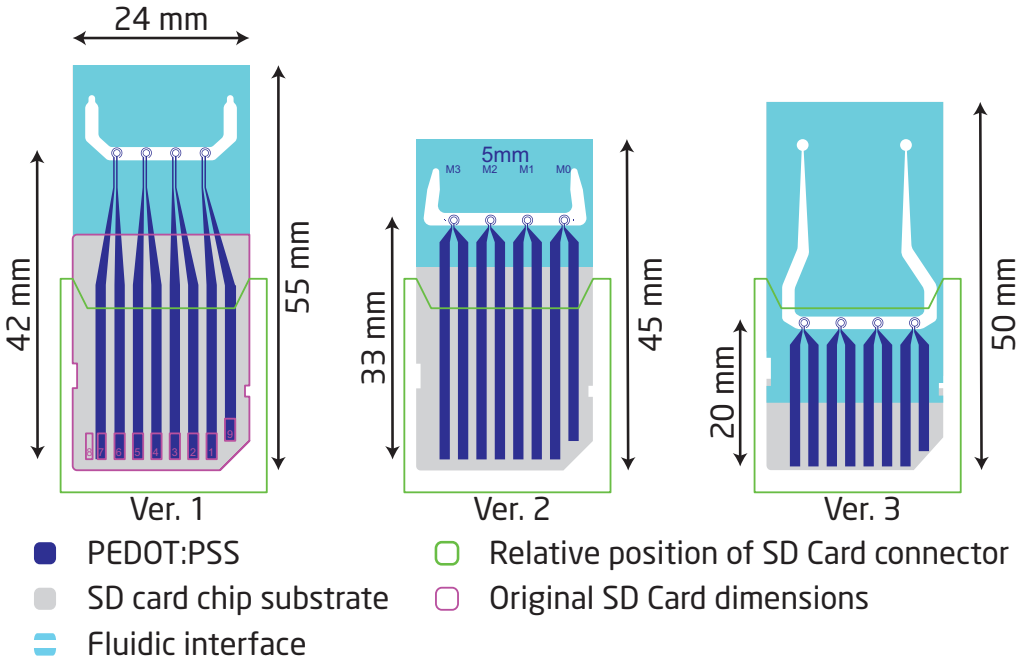

(a) *Technical drawings of SD card chip, version 1-3*

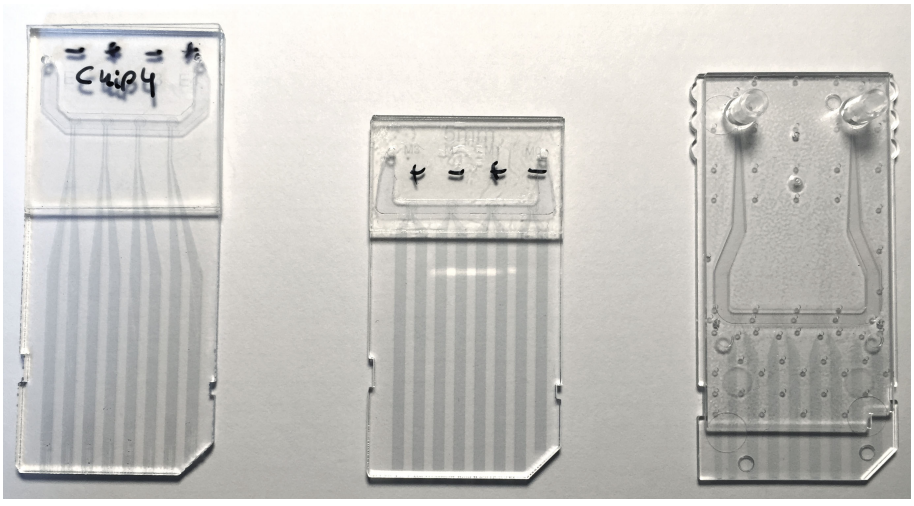

(b) *Images of SD card chip, version 1-3*

Figure 4.6: *Technical drawings and images of the SD card chip, version 1-3. A zoom of an electrode pair of SD card chip version 3 can be found in figure 4.7.*

The active part of the electrodes (PEDOT:PSS in contact with liquid sample) for all of the SD card chips had the same design with two concentric circles with an outer diameter of 750 μm and 500 μm with a thickness og 100 μm spaced 150 μm apart. A spacing of 150 μm was found suitable for obtaining a good electrode print with a high yield of usable chips. A zoom of the technical drawing (figure 4.6a) showing the active part of the electrodes and the liquid channel of the SD card chip, version 3, is illustrated in figure 4.7.

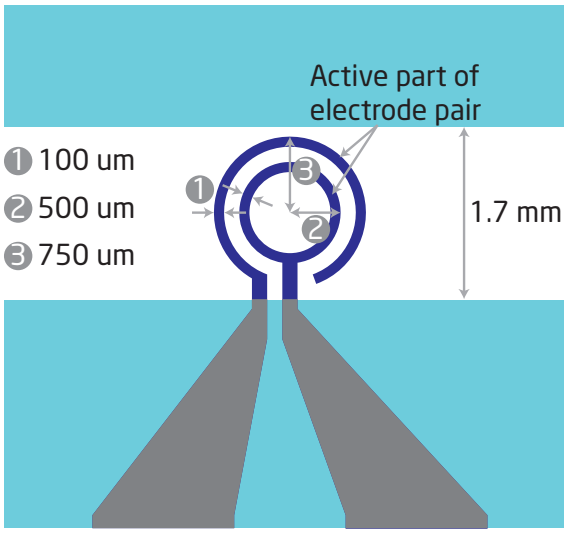

Figure 4.7: *Zoom on an electrode pair, SD card chip, version 3*

SD card chip, version 1: laser cut PMMA, screen-printed PEDOT:PSS, double sided adhesive tape channels

The substrate of the SD card chip, version 1, was made from 1.5 mm PMMA sheets by laser ablation. A channel for sample flow was defined in double sided adhesive tape and sealed with a lid of 1 mm thick PMMA with through holes for the sample introduction into the chip. Both channels and lid were made by laser ablation. Tubings for the sample were connected to the channel through a PDMS gasket on top of the lid which was clamped between two PMMA sheets. This methods of assembling the chip required many different parts and time.
The chip and the electrodes were both relatively long, 42 and 55 mm, respectively. This design was made in order to fit the liquid interface of the chip outside of the SD card connector. It was not possible to fit the liquid interface inside the connector since the total thickness of the chip was 2.5 mm and the maximum thickness of a chip inside the connector could not exceed 2.1 mm. The long electrodes were found to be a disadvantage since the electrodes had a high electrical resistance caused by

the relatively low conductivity of PEDOT:PSS compared to metal conductors.

SD card chip, version 2: laser cut PMMA, screen-printed PEDOT:PSS, double sided adhesive tape channels

The fabrication principle of the SD card chip, version 2, was the same as SD card chip, version 1. The difference between the chips was the length of the electrodes and the liquid interface. The length of the electrodes was reduced to 33 mm and the width of the electrodes were wider until the active part of the electrodes in order to reduce the electrical resistance of the electrodes. The principle of assembly of the chips was the same as SD card chip, version 1. The cumbersome assembly of the chips was solved for the next design iteration.
Section 4.3 and 4.5 of this chapter describes the chip fabrication for the SD card chip, version 2.

SD card chip, version 3: injection moulded COC or PC, screen-printed PEDOT:PSS, injection moulded lid with channel and tubing connectors, assembled with screen-printing glue

The substrate for the SD card chip, version 3, was injection moulded in order to have a thickness of 1.2 mm, corresponding to a slightly thinner thickness compared to the thickness of an original SD card of 1.4 mm (thickness inside the connector over the metal connector pins). The SD card chip, version 1 and 2, were both made from 1.5 mm thick extruded PMMA sheets. Often, a variance of the thickness of the extruded sheets of up to 0.2 mm was observed. This meant that some of the chips were thicker than intended and the SD card connector pins were damaged. The lid of the SD card chip, version 3, was injection moulded and designed with an integrated channel and connectors for the tubing. Once assembled, the thickness of the chip was 2.1 mm, which suited the demands of the SD card connector.
The total thickness of 2.1 mm of the assembled chip allowed a design where the liquid interface was partly placed inside the SD card connector once the chip was mounted. This meant that the length of the electrodes could be reduced to 20 mm, which was an advantage in relation to the electrical resistance of the electrodes. The liquid channel and tubing connectors were designed as part of the lid. This design proved the advantage of injection moulding since this design would have been impossible to make with laser ablation due to the 3D structures. The height of the channel was 100 μm with a width of 1.7 mm around the electrodes. With the tubing connectors integrated as part of the lid, chip assembly was possible to do without any PDMS gasket and clamping. Figure 4.8 shows a 3D illustration of the assembled SD card chip, version 3, with tubings. Different approaches for chip assembly

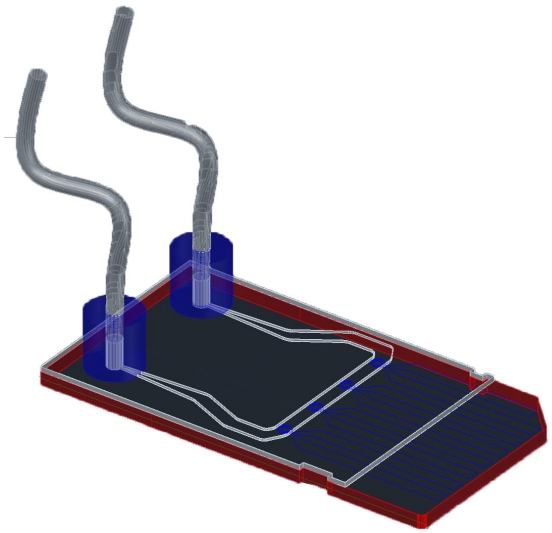

Figure 4.8: *3D illustration of the assembled SD card chip, version 3, with tubings*

were tested. Initially, the chips were assembled by double sided adhesive tape. This approach was discarded since it required careful alignment of the channel and the tape. Furthermore the tape increased the thickness of the chip with approximately 100 μm. The second approach for assembling the chip was done with a UV curable glue. The glue was spotted onto the chip with a micro spotting robotic system (Autodrop Professional Positioning System for spotting is described in section 4.5). This method was very labour intensive and the glue had a tendency to flow into the channels and block the flow. The final assembling approach was based on screen-printed glue. This method was fast to do and the glue sealed the chip nicely with out any blockage of the flow.
We experimented with two different substrate materials: COC and PC. Initially, COC was tested but the PEDOT:PSS did not adhere well to this material, which resulted in easily damaged electrodes. This issue had previously been observed with the PMMA substrate. Different approaches to overcome this problem was tested by applying air plasma, corona treatment or a hydrophilic surface coating. The best surface treatment was the air plasma where both the adherence and the shape of the electrodes were found to be best. The substrate material was changed to PC and a good adherence of the PEDOT:PSS was observed using the air plasma. Thus, the final material choice for the chip substrate and lid was PC.

4.3 Screen-printing

Screen-printing is an old printing technique where the desired design is printed, or transferred, through an ink permeable screen to an underlying substrate. Screen-printing can be performed either by hand or by large advanced screen-printing machines that can control all of the parameters in the printing process. Figure 4.9 illustrates the principle of the screen-printing process of the aptasensor chips.

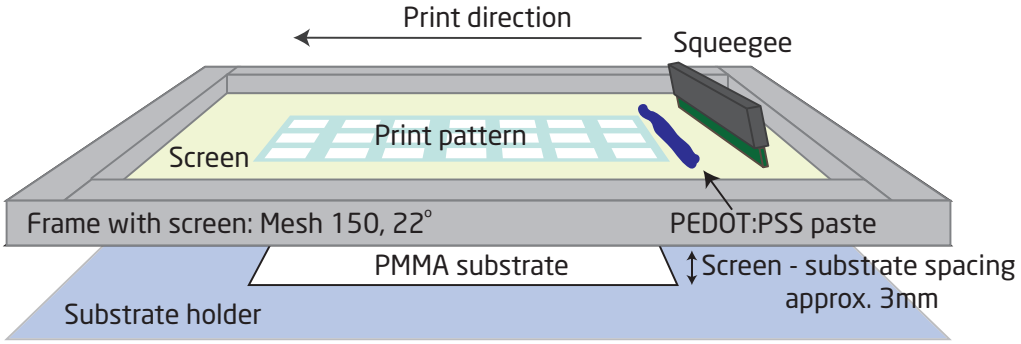

Figure 4.9: *Principle of screen-printing*

Three different PEDOT:PSS screen-printing pastes were tested in order to find the best suited paste for our electrode design and substrate material. The three different pastes were:

1. Clevios ™ S V3
2. Clevios ™ S V3 HV
3. Clevios ™ S V4 STAB

The latter paste was UV, heat and damp stabilised by the commercial supplier (hence: STAB). All of the pastes were purchased from Heraeus Precious Metals GmbH & Co. KG, Germany. Clevios ™ S V3 was used in the initial screen-printing tests but it was soon realised that this paste was not suited for our 100 μm structures as the structures of the print were flowing together. Thus, the Clevios ™ S V3 HV paste was used instead as this paste was suited for fine line structures. During our printing development the commercial supplier ended the production of the Clevios ™ S V3 HV paste and we found that the Clevios ™ S V4 STAB was a suitable replacement.
Protocol and material list for manual screen-printing of PEDOT:PSS electrodes, SD card chip version 2, can be found in the publication *Screen-printed all-polymer aptasensor for impedance based detection of influenza A virus*, in section 4.5 of this chapter.
The following section describes the development of the screen-printing process.

4.3.1 Development of the PEDOT:PSS screen-printing process

The size limitation of the PEDOT:PSS printable structures was initially tested with a test print illustrated in figure 4.10 on COC sheets. The test print was designed to test the USB chip, version 1 and 2, parallel lines and concentric circles with a width and distance ranging from 100 μm to 500 μm. The PEDOT:PSS Clevios ^{TM} S V3 was used for the test. The test print was done at the facilities of Vesterbro Serigrafi A/S, Denmark, using their professional screen-printing machines.

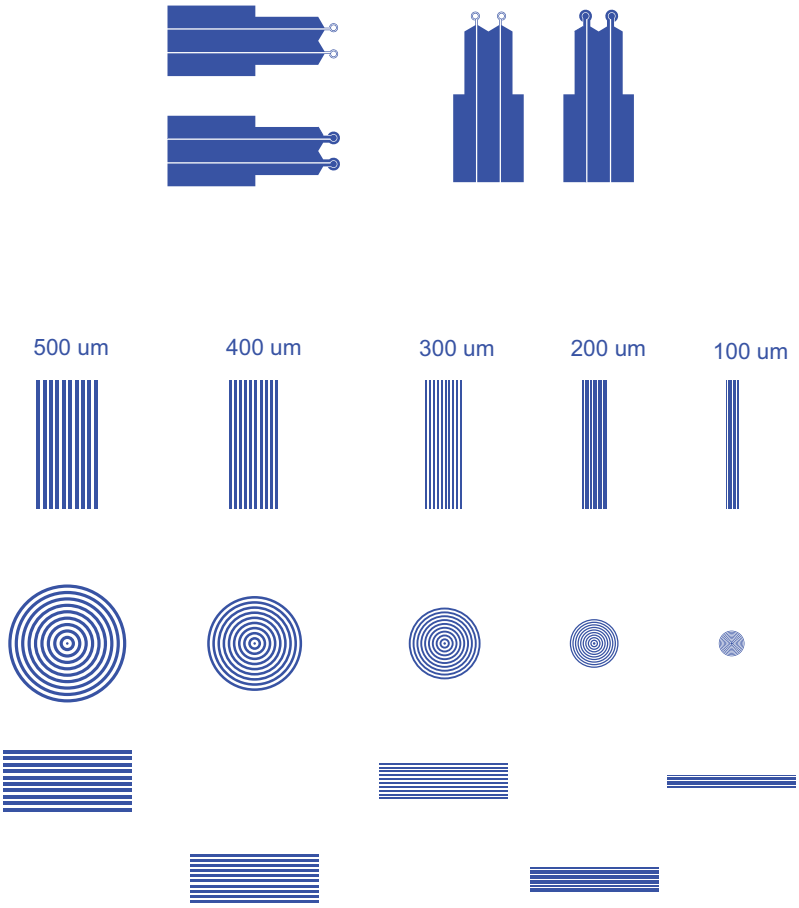

Figure 4.10: *Screen-printing test layout with the USB chip, versions 1 and 2, parallel lines and concentric circles with a width and distance ranging from 100 μm to 500 μm*

Figures 4.11 and 4.12 shows the result of the test print. Figure 4.11 shows the active part of the electrode area of USB chip, version 1 and 2. The left (4.11a and

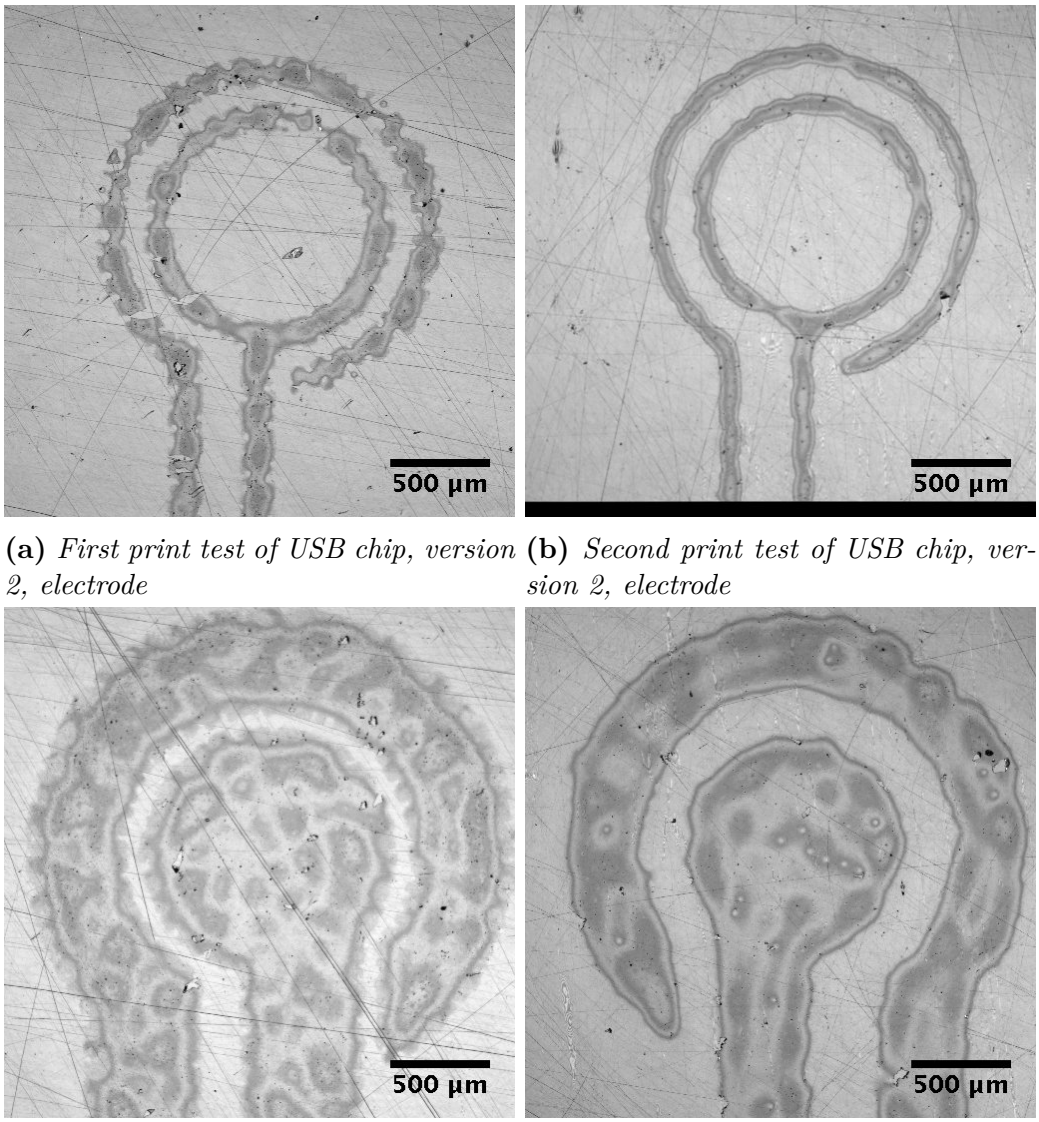

(a) *First print test of USB chip, version 2, electrode*

(b) *Second print test of USB chip, version 2, electrode*

(c) *First print test of USB chip, version 1, electrode*

(d) *Second print test of USB chip, version 1, electrode*

Figure 4.11: *Screen-print test of USB electrodes, version 1 and 2*

4.11c) images shows the first print while the right (4.11b and 4.11d) images illustrates the printed structures of the second print where the screen-printing parameters were altered to obtain a better print. The parameter alterations were performed by the printing expert at Vesterbro Serigrafi A/S. The difference between the first and second prints convinced us that screen printing of 100 μm structures indeed was possible. The width of the electrodes of USB, version 2, was 100 μm according

to the technical drawing. The width of the printed electrode in figure 4.11b was ranging between 65 and 105 μm which was considered good for a first print but it left room for improvement.

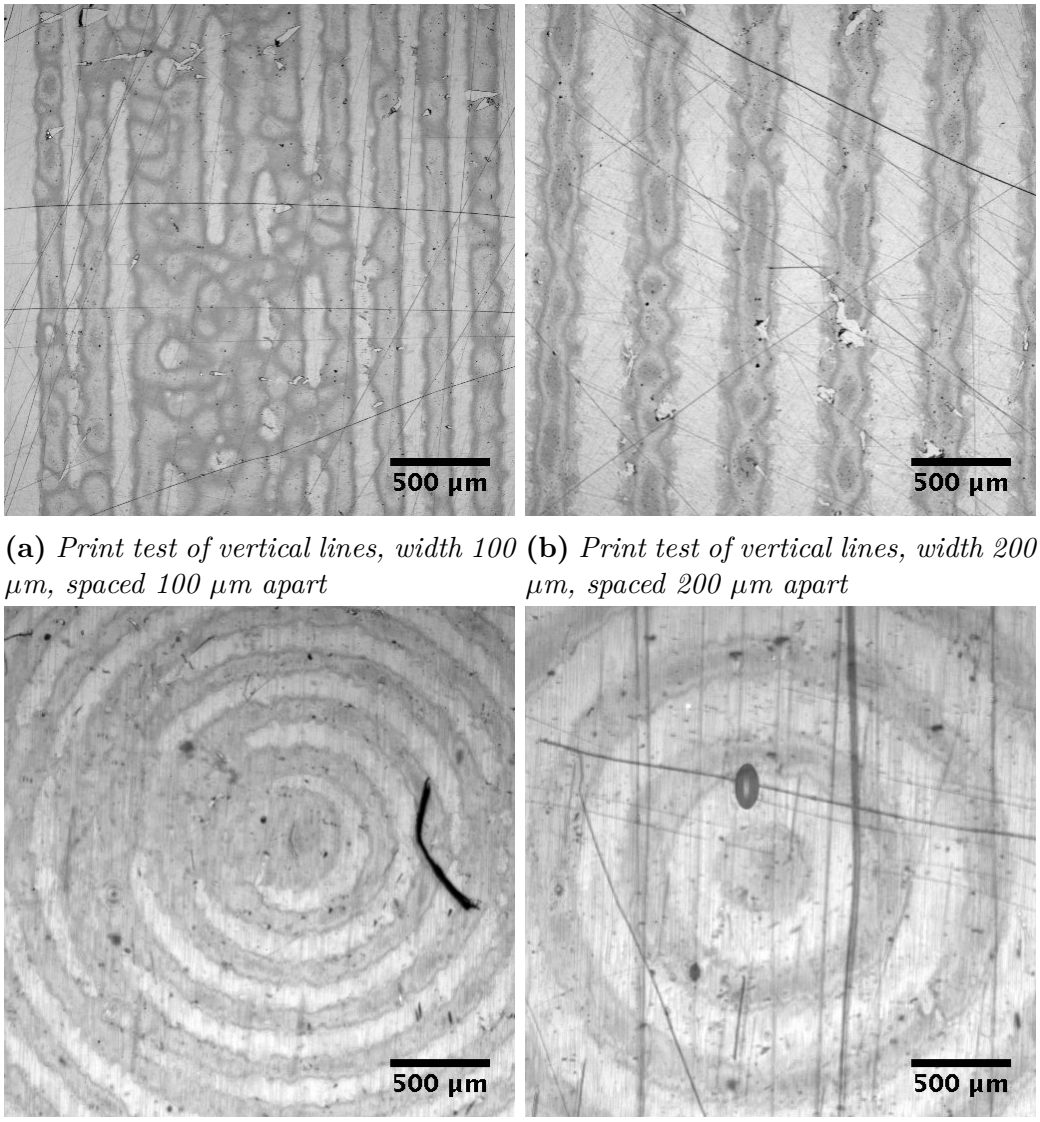

(a) *Print test of vertical lines, width 100 μm, spaced 100 μm apart*

(b) *Print test of vertical lines, width 200 μm, spaced 200 μm apart*

(c) *Print test of concentric circles, width 100 μm, spaced 100 μm apart*

(d) *Print test of concentric circles, width 200 μm, spaced 200 μm apart*

Figure 4.12: *Screen-print test of parallel lines and concentric circles.*

Figure 4.12 shows the 100 μ and 200 μm printed parallel lines and concentric circles. The images of the parallel lines shows that it was possible to print parallel

lines with a distance of 100 and 200 μm but the lines with 100 μm apart had a tendency to collapse with each other. The same tendency was observed for the concentric circles.
The surface properties of the COC film was not altered for these first prints which mean that the the hydrophobicity of the film was quite high. As described in section 4.2 of this chapter, different approaches to alter the hydrophobicity of the substrates and the adherence of the PEDOT:PSS to the substrates were tested in order to obtain a better print. The adherence of the PEDOT:PSS of test prints (figures 4.11 and 4.12) to the substrate was very bad. By looking carefully at the prints small scratches can be observed. The prints had been handled with great care in order to avoid any scratches but it was not possible to avoid damage. After the first test prints the PEDOT:PSS was changes to the PEDOT:PSS Clevios ^{TM} S V3 HV, which was better suited for small fine line structures. Unfortunately, the production of this PEDOT:PSS was terminated by the manufacturer and we changed to the Clevios ^{TM} S V4 STAB PEDOT:PSS. The PEDOT:PSS Clevios ^{TM} S V4 STAB was found successful for printing small structures. Figure 4.13 shows the final print of the active part of the electrodes of the SD card chip, version 3, after optimising the printing procedure and surface treatment. This electrode print was in good agreement with the technical drawing, figure 4.7. The substrate material was PC and an air plasma treatment was applied to the substrate before printing.

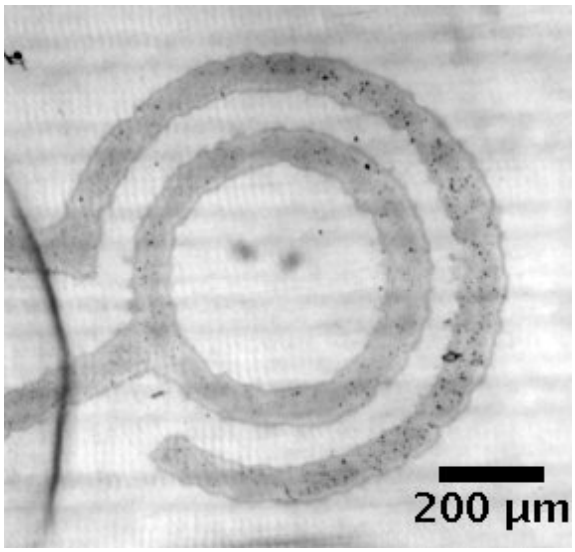

Figure 4.13: *Screen-print of SD card chip, version 3, electrode pair*

4.4 Conclusion

After several design iterations the final chip design that suited the design inputs and requirements of the viral aptasensor was based on a SD card interface with four electrode pairs. The active part of the electrode pairs was designed as two concentric circles with width of 100 μm, spaced 150 μm apart. The chip substrate and the chip lid were fabricated in PC by injection moulding. A channel (100 μm high) and tubing inter connectors were integrated into the lid for easy assembly. The assembly was done with screen-printing glue. The best method for fabricating the PEODT:PSS electrodes was found to be screen-printing where printed structures of 100 μm in size were possible to reproduce. The best suited substrate material was found to be PC with an air plasma treatment of the substrate before printing the electrodes. The air plasma reduced the hydrophobicity of the substrate and increased the adherence of the PEDOT:PSS to the substrate.

4.5 Screen-printed all-polymer aptasensor for impedance based detection of influenza A virus

This book chapter was submitted for second revision, March 2016, to:

Biosensors and Biodetection
Methods and Protocols
Methods in Molecular Biology series, Springer
Editors: Avraham Rasooly and Ben Prickril

The submitted book chapter is a methods chapter intended to describe all details of the experimental methods involved in the described experimental setup. The methods described involve the chip fabrication, aptamer immobilisation and EIS measurements of water samples containing influenza A virus (IAV). Thus, the different fabrication steps of the SD card chip, version 2, are described in detail in the book chapter.

N.b. Chapter not included in online version of this PhD thesis.

— 5 —

Exploring the surface immobilisation of aptamers

Immobilisation of a biorecognition element in a biosensor application is crucial and of pivotal importance in order to get a successful and reliable sensor. The surface coverage, orientation and stability of the biorecognition elements all affect the performance of the sensor [43]. The final design iteration of the all-polymer aptasensor described in chapter 4 uses PEDOT:PSS as electrode material and PC as substrate material. Surface immobilisation of aptamers, or ssDNA, onto solid surfaces is usually done through a chemical modification of the 5' or 3' end of the ssDNA. Physical absorption of the aptamer onto the substrate can also be used but this simple method is not suitable due to low stability of the electrostatic interactions leading to desorption of the ssDNA [43]. For gold substrates, chemisorption of ssDNA with a 3' or 5' end thiol linker is the preferred method for immobilisation as this method creates a self assembled monolayer of covalently bound ssDNA on the gold surface while assuring correct orientation of the ssDNA [81] [82]. Biotin labelling of aptamers can also be used to link aptamers to a modified substrate surface. In this case, the surface of the substrate is modified with a coverage of avidin, streptavidin or neutravidin and subsequently linked with the biotinylated aptamer [43]. The biotin - avidin/streptavidin/neutravidin complex is a large molecular complex which will increase the distance between the target recognition (or bioreaction) and the electrode surface. If this immobilisation approach is used in an electrochemical biosensor the output signal from the sensor will be reduced, leading to a lower sensitivity. Another possibility is to modify the aptamer with a primary amine group at the end of the oligonucleotide sequence. The amine group covalently binds to functional groups on the substrate, e.g. carbonyl groups.
In the literature, immobilisation of ssDNA onto different polymer materials has

been done by different approaches, e.g. Fixe *et al.*, 2004, described a method for immobilising amine modified ssDNA onto aminated PMMA sheets with the use of glutaraldehyde [83]. Dufva *et al.*, 2004, described a method for UV cross-linking of unmodified ssDNA onto an agarose film coated on a solid support of glass for DNA microarrays [12]. The UV cross-linking of ssDNA probes on agarose films was further improved by Dufva *et al.*, 2006, by an addition of a terminal poly(T)10-poly(C)10 tag (TC-tag) on the ssDNA [13]. In their study they showed a significant signal improvement in DNA hybridisation experiments with the addition of the TC-tag on the cross-linked ssDNA compared to unmodified ssDNA and other tags (Poly(T)10, Poly(T)20, Poly(C)10). The chemical mechanism behind the UV cross-linking is unknown, but it is suggested by Dufva *et al.*, 2006, that the TC-tag is directly involved in the crosslinking [13]. Kimura, 2006, investigated the UV cross-linking method and immobilisation of poly(dT) modified ssDNA onto unmodified PMMA, PC and PET substrates [84]. Sun *et al.*, 2011 [14], used the TC-tag described by Dufva *et al.*, 2006, to immobilise ssDNA probes on unmodified COC, PC, PMMA and PDMS substrates. They demonstrated an application of the UV crosslinking in a COC microfluidic biochip for DNA hybridisation experiments [14]. Furthermore, UV cross-linking of ssDNA has been demonstrated on unmodified glass substrates [85] and the UV cross-linking method has been used to immobilise an aptamer on a polyester cloth for thrombin detection [86].

PEDOT:PSS is a chemically inert polymer material with no direct available reactive groups for thiol or amine linking for immobilising aptamers to the polymer surface. The UV cross-linking approach for immobilising ssDNA onto polymer substrates is an interesting approach for aptamer immobilisation on PEDOT:PSS due to the inertness of the material and the simple method of the UV cross-linking. Furthermore, unmodified DNA is considered more cost effective than modified DNA (e.g. amino modified DNA) as it is estimated that unmodified DNA sequences cost up to 300 times less than amino modified DNA [13]. In the following sections of this chapter the UV cross-linking method will be experimentally investigated for immobilising aptamers on PEDOT:PSS based on the method described by Dufva *et al.*, 2006 [13]. Figure 5.1 illustrates a UV immobilised aptamer with the TC-tag and a spacer and the target recognition. The TC-tag binds to the electrode surface and is linked to the aptamer sequence by a spacer. The spacer increases the distance between the tag and the aptamer, thus increasing the possibility that the aptamer will be oriented away from the electrode surface and thus folds correctly upon target binding. When a target comes into close proximity of the aptamer, the target is recognised and bound to the aptamer.

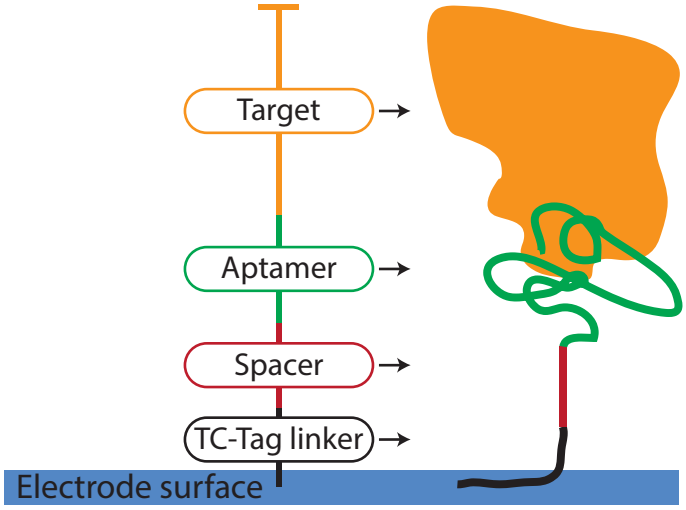

Figure 5.1: *Theoretical principle of a cross-linked UV immobilised aptamer on an electrode surface and target recognition.*

5.1 UV cross-linking of aptamers onto different polymer substrates

The UV cross-linking of ssDNA onto a solid support is a rather simple approach compared to chemical immobilisation, which usually requires many and long incubation steps. The UV cross-linking procedure can be divided into four main steps as illustrated in figure 5.2: 1) A clean and dry surface is prepared, 2) A droplet

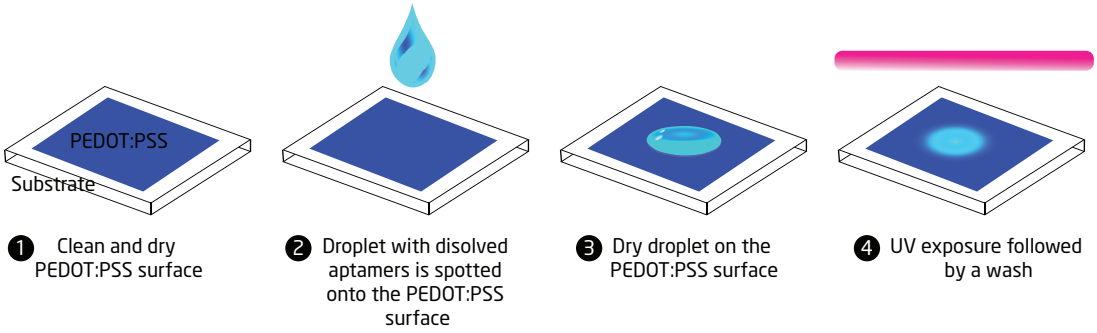

Figure 5.2: *Illustration of the four main steps involved in aptamer immobilisation onto a solid support, in this case PEDOT:PSS, by the UV cross-linking method*

with an aptamer solution (typically 0.1 - 10 μM) is spotted onto the surface, 3) The droplet is dried onto the surface and 4) The surface with the dried aptamer solution is exposed to UV illumination (typically 1-10 min) and subsequently thoroughly

washed to remove any unbound aptamers.
As described above, the aptamer is labelled with a TC-tag and a spacer between the tag and the aptamer. Ideally, only the TC-tag binds to the surface of the substrate but this is unknown since the chemical reaction, or modification, during the UV exposure is unknown. Of the four DNA bases, the molecular structure of T and C can be changed by UV exposure, as they may form dimers upon UV radiation. Hence, it makes sense to have a TC rich label that can become "chemically activated" by UV exposure and thereby bind to the substrate. This also means that if an aptamer sequence is rich in T or C bases, parts of the aptamer may be linked to the surface or create dimers. This can potentially alter the chemistry of the aptamer, which leads to reduced or impossible target recognition. Thus, several important aspects must be examined experimentally in order to determine if the UV immobilisation method is an appropriate method for aptamer immobilisation. The critical aspects to be determined in order to evaluate the applicability of the procedure are the adherence of the aptamer and the subsequent interaction between the reverse complementary DNA (rcDNA) strand or the target. The interaction of the rcDNA with the aptamer is a more simple interaction than the aptamer-target recognition, which depends on a conformational change of the aptamer. Thus, the rcDNA interaction was used to test the adherence and the DNA interaction since, logically, the complex target recognition would not be possible if the simple DNA interaction did not work.
The adherence and the interaction of the aptamer onto different polymer substrates were examined by different approaches. Initially, a fluorescently labeled rcDNA was used to investigate the adherence and interaction of the UV immobilised aptamer spotted onto PEDOT:PSS and PC. The aptamer adherence and interaction were further investigated by a colorimetric enzyme linked aptasorbent assay (ELASA) onto PEDOT:PSS, different microtiter plates and PC. A PCR based assay was attempted used for the investigation of the adherence of aptamers onto PMMA and COC. The subsequent interaction with the primers used in the aptamer selection was tested with both conventional PCR and real-time PCR. It was not possible to make a PCR assay that did not result in false positive due to problems with the assay and the sample preparation in the lab, hence, the PCR assay was discarded. The following sections of this chapter will describe the experimental work related to the investigation of UV cross-linked aptamers by fluorescently labeled rcDNA and ELASA.

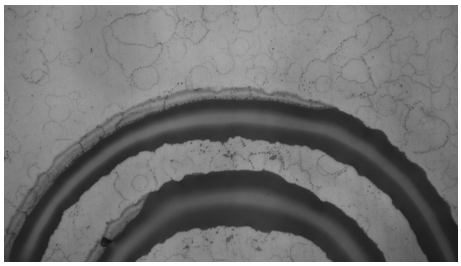

(a) *Spotting on PEDOT:PSS, wet*

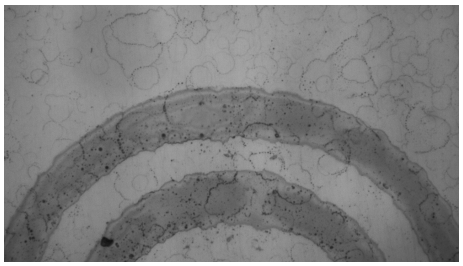

(b) *Spotting on PEDOT:PSS, dry*

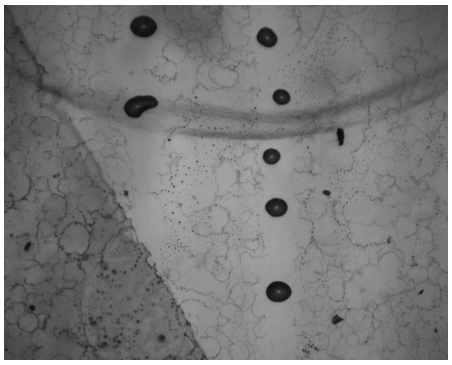

(c) *Spotting on PC and PEDOT:PSS, wet*

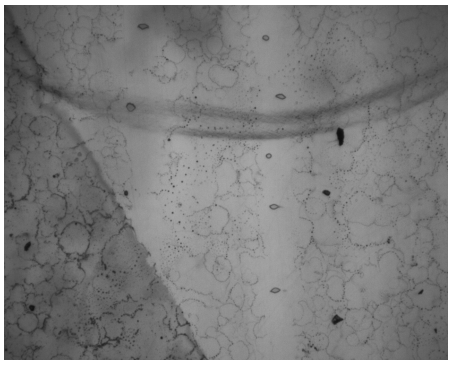

(d) *Spotting on PC and PEDOT:PSS, dry*

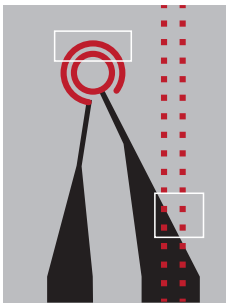

(e) *Illustration of where images was acquired on chip.*

Figure 5.3: *Wet and dry images of the aptamer spotting process with the Autodrop system. A horizontal drop distance 0.15 mm was used to spot the droplets in the images.*

5.2 UV cross-linking of aptamers and detection with a fluorescent label

The immobilisation of aptamers onto PEDOT:PSS and PC by the UV cross-linking method was examined by immobilising aptamers onto the surface and subsequently hybridising a fluorescently labeled rcDNA to the aptamer. The aptamers were spotted onto SD card chips, version 3, with a robotic spotting system: the Autodrop Professional Positioning System. UV exposure was done in a Stratagene UV Stratalinker 2400 UV illuminator. A confocal microscope was used to measure the fluorescence. The purposes of these experiments were to determine if the PEDOT:PSS and the PC substrate bound aptamers differently and to see if the adherence could be improved by tuning different parameters in the immobilisation process. Figure 5.3 shows microscopic images of the wet and dry stages of the spotting process. The PEDOT:PSS is a hydrophilic material while the PC is hydrophobic. The aptamer solution was nicely spread on the PEDOT:PSS electrodes (see figure 5.3a). Due to the small amount of spotted solution (only a few nL/electrode), the solution dried

fast within one minute. The wet and dry stages of a linear droplet array is seen in figures 5.3c and 5.3d. Each spot had a volume of approximately 300 pL. The spots on the PEDOT:PSS dried before it was possible to acquire an image of the wet stage. This indicated that the spots were spread out on the PEDOT:PSS and the larger surface area made the droplets evaporate faster.
The step by step protocol and material list for the UV cross-linking of aptamers spotted with the Autodrop system onto chips and subsequent rcDNA hybridisation can be found in appendix A.10.

5.2.1 Examining the adherence of cross-linked aptamers and rcDNA hybridisation - before and after washing and after hybridisation

The first experiment was performed to test the adherence of a fluorescently labelled aptamer with a target specificity towards ampicillin, herein denoted as Amp3 (see appendix B.5 for the aptamer sequence). The Amp3 aptamer was used for this purpose as our group had previous experience in working with this aptamer. The aptamer was labelled with an ATTO550 dye (Absorption (Abs): 554 nm, emission (Em): 576 nm), the TC-tag and a spacer at the 5' end.
Aptamers were diluted to a final concentration of 5 μM in a spotting buffer solution of 50 % dimethyl sulfoxide (DMSO) and 50 % MilliQ water (ultrapure water). The DMSO was added to the spotting buffer to increase the evaporation time. Spotting layout for the Amp3 aptamer is illustrated in figure 5.4. The red lines in the figure illustrate where the aptamers were spotted. 6 chips were spotted in total. After

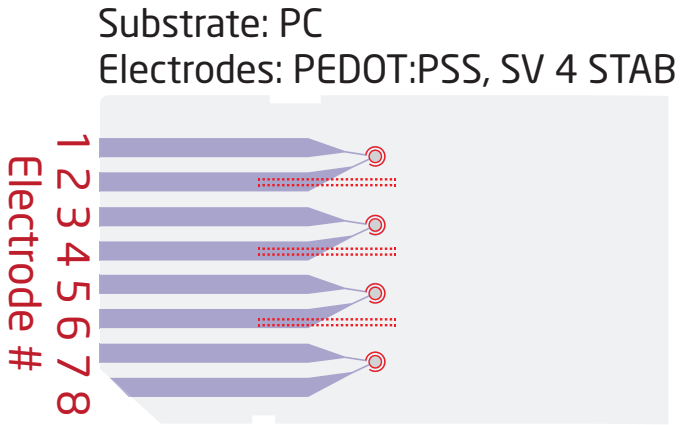

Figure 5.4: *Spotting layout for Amp3 aptamer. Red lines represents where on the chip the aptamers were spotted. The concentric electrode area and a linear droplet array with two parallel lines were spotted.*

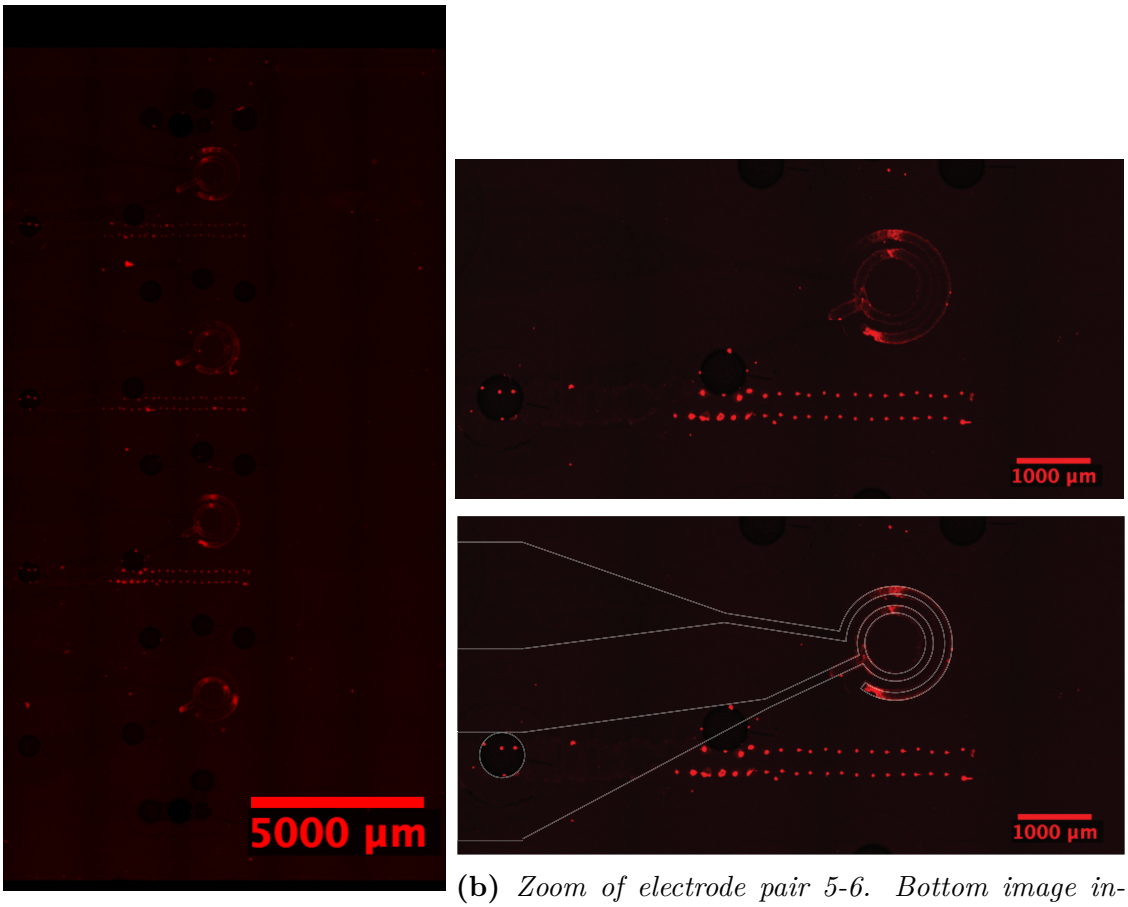

(a) *Full spotting layout*

(b) *Zoom of electrode pair 5-6. Bottom image includes an outline of the PEDOT:PSS electrode.*

Figure 5.5: *Fluorescent microscope images of PEDOT:PSS electrodes and PC substrate with Amp3 spotted aptamer before the first washing step. The fluorescent aptamer is visible on the concentric circles of the electrode pairs but not in the linear spotting array that is only visible on the PC substrate.*

spotting, the aptamers were cross-linked with 5 minutes of UV illumination. One of the chips was imaged after the spotting and the UV illumination but before the wash. The chip was imaged before the washing step to visualise the fluorescence on the PEDOT:PSS as it was suspected that the PEDOT:PSS might have a quenching effect on the fluorescence. Figure 5.5 shows a fluorescent microscope image of the spotted area of the chip before the washing step. Figure 5.5a shows the full area with spotted aptamers. As it is difficult to see the fluorescence and the structures in the image a zoom of electrode pair 5-6 is seen in figure 5.5b. The bottom image includes an outline of the PEDOT:PSS electrode pair. From figure 5.5b we could elucidate that the linear spotting arrays were only clearly visible on the PC

substrate. By looking careful at the original full scale image (image too large for the thesis layout) the linear array could be seen on the PEDOT:PSS as a smeared out cloudy structure. On the concentric circles of the electrodes it was possible to observe the fluorescent aptamers. From this, it was concluded that the fluorescence indeed was possible to see on the PEDOT:PSS but the fluorescence signal was not homogeneous over the whole electrode surface. Thus, It could not be rejected that the PEDOT:PSS had a tendency to quench the fluorescence.

After the UV cross-linking three different washing procedures with different buffers were tested, denoted first washing step. Saline-sodium citrate (SSC) was used in two of the three washing buffers as this buffer is a commonly used buffer for DNA hybridisation. One of the washing buffer contained 0.1 x SSC with 0.1 % Sodium dodecyl sulfate (SDS) since this was the washing buffer used by Sun *et al.*, 2012, [14] in their UV cross-linking experiments. The three different washing procedures were:

- Chip 1+2: Quick rinse with MilliQ water after UV exposure
- Chip 3+4: Wash for 10 min in 2 x SSC buffer after UV exposure
- Chip 5+6: Wash for 10 min in 0.1 x SSC with 0.1 % SDS after UV exposure

The Amp3 rcDNA with a Cy3 dye (Abs: 550 nm, Em: 570 nm) label at the 3' end was hybridised to the Amp3 aptamer and washed with three different washing procedures with different buffers, denoted second washing step:

- Chip 1+2: Quick rinse with 2x SSC and MilliQ water after rcDNA hybridisation
- Chip 3+4: Quick rinse with 2x SSC followed by a 10 min wash with 2 x SSC after rcDNA hybridisation
- Chip 5+6: Quick rinse with 2x SSC followed by a 10 min wash with 0.1 x SSC with 0.1 % SDS after rcDNA hybridisation

Figure 5.6 shows fluorescent microscope images of one electrode pair of chips 1, 3 and 5. Chips 1+2, 3+4 and 5+6 were repetitions and showed the same tendency after the washing steps, thus only one of each repetition is shown in the figure. Left images show the chips after the first washing step and right images show the chips after hybridisation and the second washing step. The florescent dye on the rcDNA strand has the same absorption and emission as the dye on the aptamer. Hence, the same filters were used to acquire the different images. This also means that it was not possible to distinguish the two DNA dyes from each other but it was possible to compare the amount of fluorescence before and after hybridisation.
The first wash of chip 1 was only a brief washing step with a quick rinse with MilliQ water. Figure 5.6a clearly showed the fluorescence of the linear spotting array and

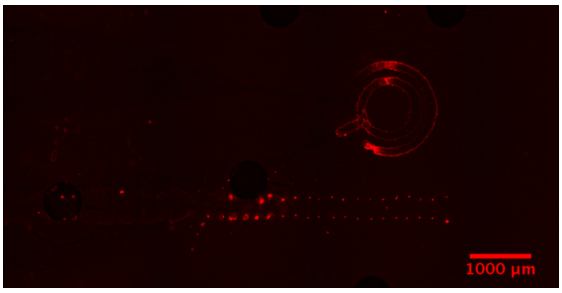

(a) *Chip 1 - after the UV illumination and first washing step*

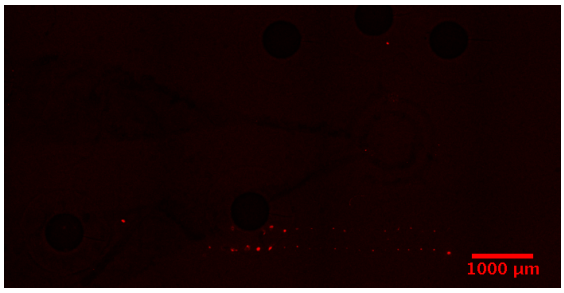

(b) *Chip 1 - after second washing step and after hybridisation*

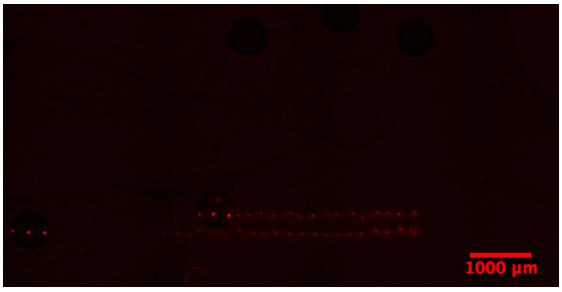

(c) *Chip 3 - after the UV illumination and first washing step*

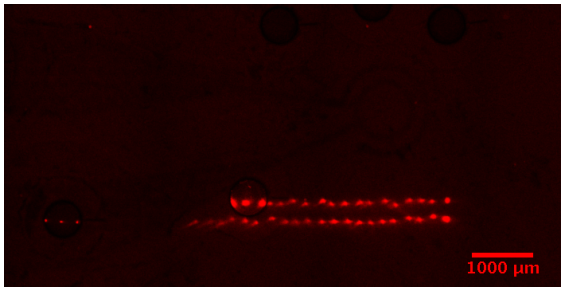

(d) *Chip 3 - after second washing step and after hybridisation*

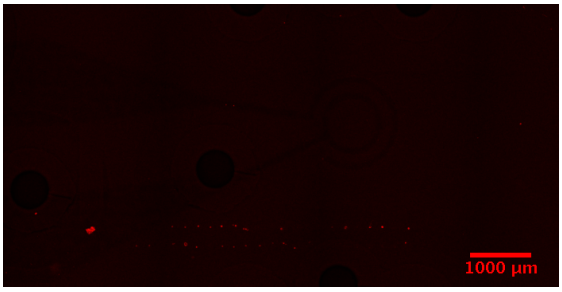

(e) *Chip 5 - after the UV illumination and first washing step*

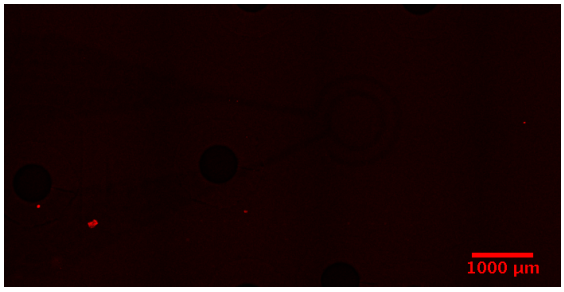

(f) *Chip 5 - after second washing step and after hybridisation*

Figure 5.6: *Fluorescent microscope images of PEDOT:PSS electrodes and PC substrate with Amp3 spotted aptamer after the first washing step (left images) and after hybridisation and second washing step (right images). Only one of the electrode pairs of each chip is shown as this was representative of all of the electrode pairs for each chip.*

the concentric electrode circles which means that a lot of aptamer was present on the chip. After the first wash of chip 3 (figure 5.6c) and chip 5 (figure 5.6e) it was not possible to see any fluorescence on the concentric electrode circles and only a weak fluorescent signal was visual on the linear spotting arrays. It was thus possible to conclude that a brief wash with MilliQ was not sufficient to remove the unbound excess aptamers on the chip.
After the second wash and the rcDNA hybridisation a weak fluorescent signal was visible in chip 1 (figure 5.6b). This indicated that the excess aptamers were washed away during the hybridisation and the second wash. It was thus a possibility that the rcDNA had bound to the excess unbound aptamers and was subsequently washed away, which could explain the lower fluorescent signal. The fluorescent signal from the spotting array on chip 3 (figure 5.6d) was increased after the hybridisation and second wash which indicated that the rcDNA had bound to the aptamer. The fluorescent signal of chip 5 (figure 5.6f) after the hybridisation and second wash was very low. The ionic concentration of the washing buffer was 20 times lower for chip 5 than the washing buffer for chip 3. It was thus a possibility that the ionic strength of the chip 5 washing buffer was too weak to keep a stable hybridisation between the two DNA strands and they had disassociated during the wash. It was concluded that thorough washing steps were needed in order to remove unbound excess aptamers but a low ionic concentration of the wash buffer could compromise the DNA hybridisation. Common for all chips was that no fluorescent signal was present on the PEDOT:PSS after the hybridisation and the second washing step. Three possible reasons could explain this: either the PEDOT:PSS quenched the fluorescent signal, the amount of immobilised aptamer was below the detection limit of the microscope, or it was not possible to immobilise the aptamers onto the PEDOT:PSS by the UV cross-linking method. To investigate these theories further, experiments were made where different parameters, the UV illumination time and the aptamer concentration, of the cross-linking method were altered. This experiment is described in the following section.

5.2.2 Examining the rcDNA hybridisation with different aptamer concentrations and UV exposure times

The purpose of this experiment was to explore how changes of two parameters in the cross-linking method could alter the aptamer immobilisation onto PEDOT:PSS and PC. The two parameters which were changed during the experiments were: the UV illumination time and the aptamer concentration. In the previous hybridisation experiment (section 5.2.1) it was not possible to test for unspecific hybridisation as only one aptamer and the rcDNA were used. In this experiment, unspecific hybridisation was included. Two arrays on the chip were prepared: one with a known

aptamer and one with a random aptamer mix with the TC-tag at the 5' end. The known aptamer used for this experiment was an aptamer with a target specificity towards VP1 of the human NoV, herein denoted HNV-VP1 (see appendix B.1 for the aptamer sequence). The HNV-VP1 aptamer has a long sequence (90 bases) as it includes the primers used in the aptamer selection process. The rcDNA to the HNV-VP1 aptamer was labelled with a Quasar 570 dye (Abs: 548 nm, Em: 566 nm) at the 5' end.
Three different aptamer concentrations were tested: 1 μM, 0.5 μM and 0.05 μM. All of the aptamers were diluted in a spotting buffer containing 2 % DMSO in MilliQ water. Furthermore, two different UV exposure times were tested: 1 minute and 5 minutes. Four chip repetitions of each parameter combination were made. Figure 5.7 illustrates the aptamer spotting layout and the experimental layout. A total of

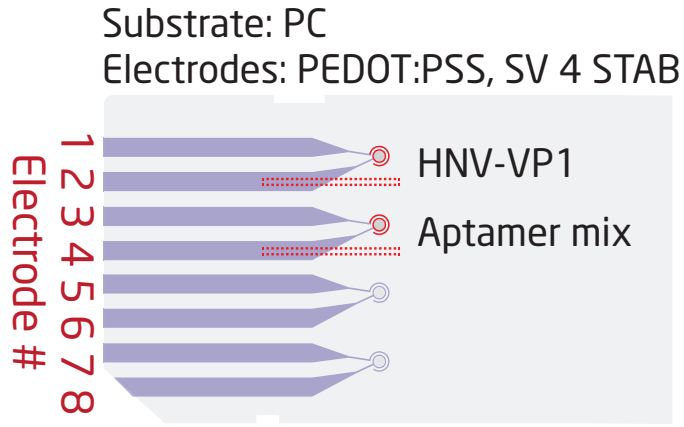

(a) *Spotting layout for HNV-VP1 aptamer and random aptamer mix*

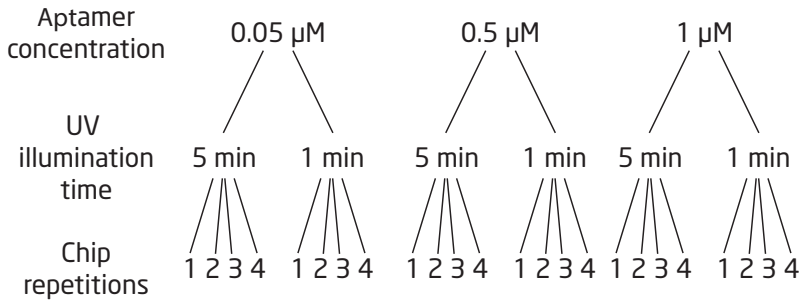

(b) *Experimental layout*

Figure 5.7: *Experimental and spotting layout for examining the adherence and rcDNA hybridisation with different aptamer concentrations and UV exposure times. Red lines in figure 5.7a represent where on the chip the aptamers were spotted. The concentric electrode area and a linear droplet array with two parallel lines were spotted.*

24 chips were examined. The washing buffer was PBS with 2 mM $MgCl_2$ and each washing step (1: after UV exposure and 2: after hybridisation) was carried out for 10 minutes. Bright-field and fluorescent images of the chips were acquired after the hybridisation and second wash by a confocal microscope. The ImageJ software was used to process and analyse the images. To remove the background signal of the fluorescent images, an average grey value background signal (grey value: 28) was calculated for all images and subsequently subtracted the images. The results of 1 μM spotted aptamer concentration for 1 and 5 minutes of UV illumination are illustrated in figure 5.8. It is difficult to see the fluorescent spots in the images since one spot has a diameter of around 10 μm and the images are approximately 9000μm wide. The hybridisation of the rcDNA of the HNV-VP1 aptamer was possible to see in both figure 5.8b and figure 5.8d where it was expected to be. In figure 5.8d unspecific hybridisation of the rcDNA to the aptamer mix solution was present. The results of 0.5 μM and 0.05 μM, 1 and 5 minutes did not show any fluorescence in either the concentric circle electrode area or in the linear spotted arrays (covering both PC and PEDOT:PSS areas). The images of these results can be found in appendix A.10, figure A.4 and figure A.5.

In order to quantify the fluorescence of the images in figure 5.8, an area of 9000 x 200 μm was defined and the grey values along the longest axis of the box were calculated using the Plot Profile function in ImageJ. The profile plots were only made for the spotted linear arrays of the chips imaged in figure 5.8 as the arrays of the rest of the chips were not present in the fluorescent image due to lack of immobilised aptamers. The yellow boxes in figure 5.9 explain where on the fluorescent images the profile plot arrays were acquired. The plots of the array profiles for 1 μM spotted aptamer solution and 1 or 5 minute UV exposure are found in figure 5.10 and figure 5.11, respectively. The first 2-3000 μm of all plots represent the grey value profile of the PEDOT:PSS, while the remaining distance up until 9000 μm represents the grey value profile of the PC substrate. The arrays: E2-1 and E2-2, are values of the HNV-VP1 aptamer and arrays: E4-1 and E4-2, are plots of the aptamer mix arrays. E2 and E4 refer to the electrode numbers in figure 5.7a.

The grey value peaks in the profile plots of 1 μM spotted aptamer solution and 1 minute UV exposure (figures 5.10a and 5.10b) revealed specific binding of the rcDNA to the immobilised HNV-VP1 aptamer on the PC. It was not possible to identify any fluorescent signal in the area of the PEDOT:PSS. Only a weak signal from unspecific hybridisation was seen on the immobilised aptamer mix (figures 5.10c and 5.10d).

The plots of the 1 μM aptamer concentration and 5 minutes UV exposure (figure 5.11) revealed many grey value peaks representing both specific and unspecific hybridisation of the rcDNA in the PC area. No peaks, hence no aptamer immobilisation, were present on the PEDOT:PSS.

It was concluded from the experiment that the aptamer concentration and time of

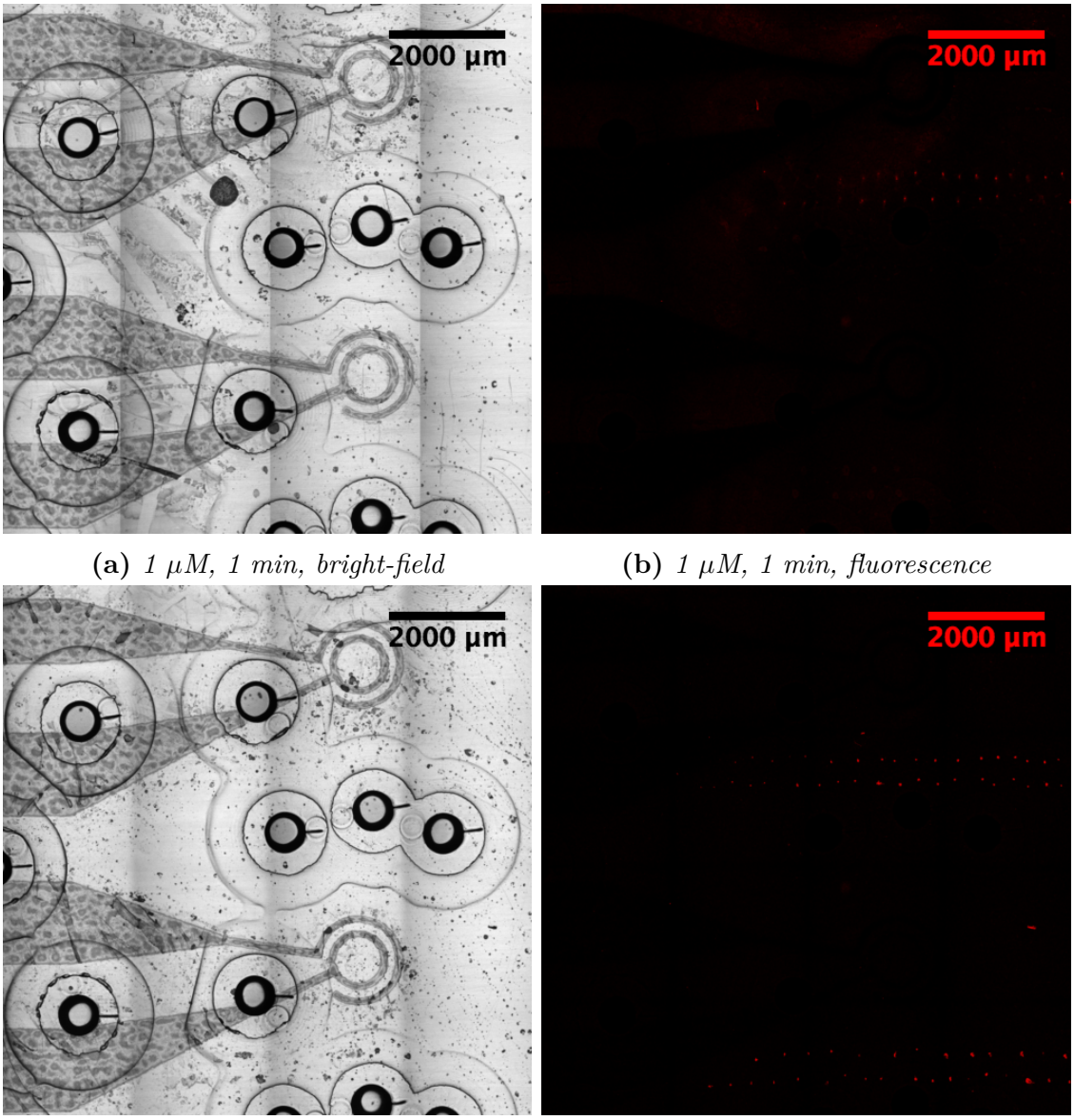

(a) *1 µM, 1 min, bright-field*

(b) *1 µM, 1 min, fluorescence*

(c) *1 µM, 5 min, bright-field*

(d) *1 µM, 5 min, fluorescence*

Figure 5.8: *Bright-field and fluorescent images of spotted aptamers after rcDNA hybridisation, aptamer concentration: 1 µM, 1 or 5 min UV exposure. The fluorescent signal of the linear spotting array of HNV-VP1 aptamer is visible in both fluorescent images. A fluorescent signal of unspecific hybridisation of the rcDNA to the spotted aptamer mix solution was visible in figure 5.8d.*

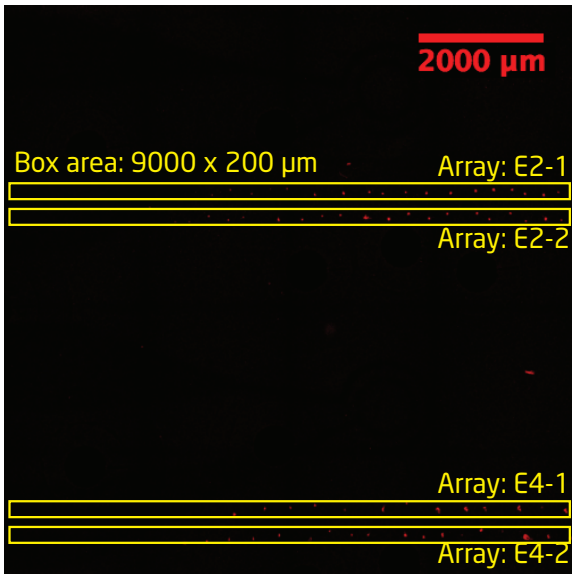

Figure 5.9: *Profile plot array area explanation for the plots in figure 5.10 and 5.11.*

the UV exposure were important parameters in the UV cross-linking method. An aptamer concentration below 1 μM was not suitable for the cross-linking method when fluorescent microscopy was used as the method for detection. It was not possible to see the fluorescent signal from the cross-linking and subsequent hybridisation of the aptamers on the PEDOT:PSS. It was still not clear if this was caused by quenching of the fluorescent signal by the PEDOT:PSS, if the aptamer concentration was too low or if the fluorescent signal was below the detection limit of the confocal microscope. Thus, a different method based on colorimetric amplification and not dependent on fluorescent labelling of the aptamers was thought of. This method will be described and examined in the following section.

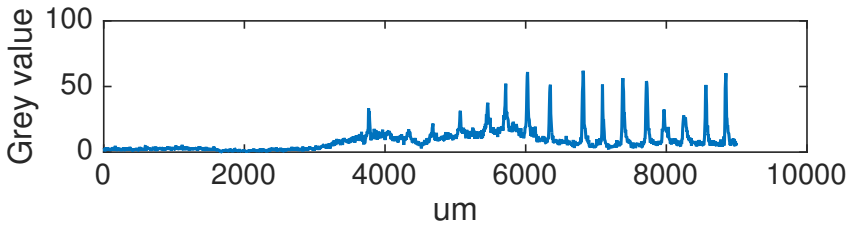

(a) *1 µM, 1 min, Array: E2-1, HNV-VP1 aptamer*

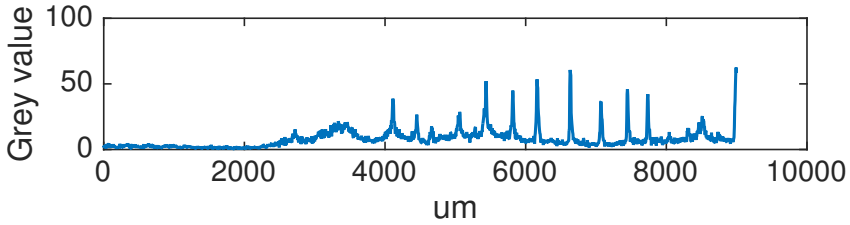

(b) *1 µM, 1 min, Array: E2-2, HNV-VP1 aptamer*

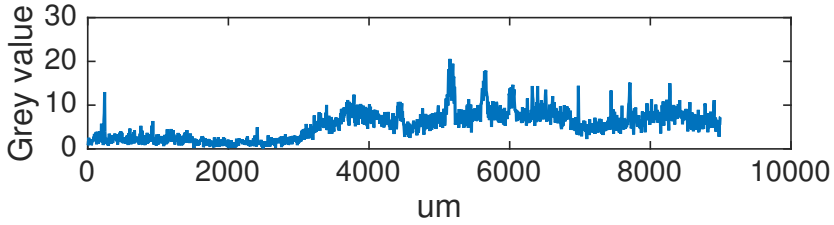

(c) *1 µM, 1 min, Array: E4-1, aptamer mix*

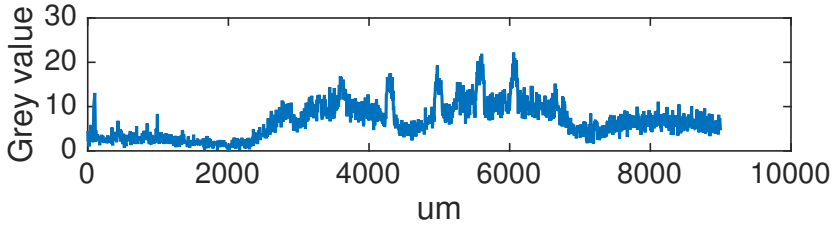

(d) *1 µM, 1 min, Array: E4-2, aptamer mix*

Figure 5.10: *Grey value profile plots, aptamer concentration: 1 µM, 1 min UV exposure. See figure 5.9 for elaboration on where on the chips the arrays were measured. The grey value peaks are peaks of high fluorescent signal in the measured image (figure 5.8b). The first 2-3000 µm of all plots represents the grey value profile of the PEDOT:PSS, while the remaining distance up until 9000 µm represents the grey value profile of the PC substrate.*

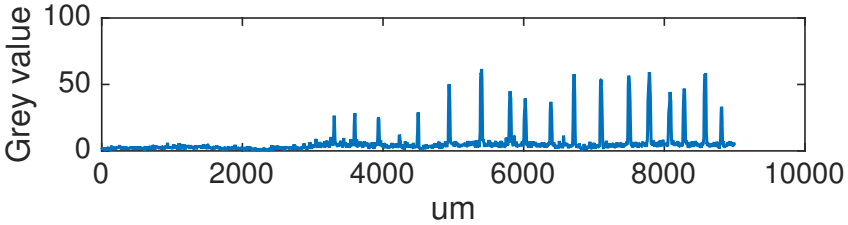

(a) *1 µM, 5 min, Array: E2-1, HNV-VP1 aptamer*

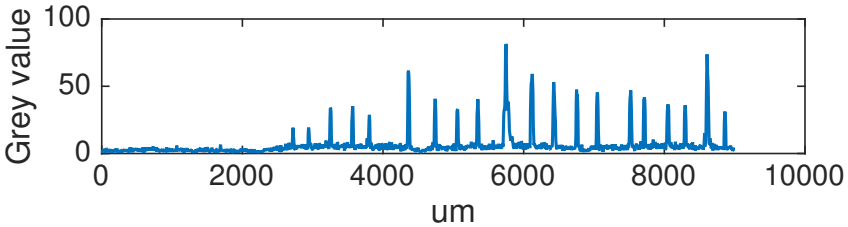

(b) *1 µM, 5 min, Array: E2-2, HNV-VP1 aptamer*

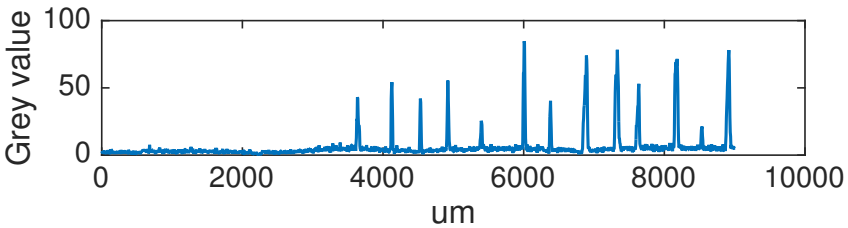

(c) *1 µM, 5 min, Array: E4-1, aptamer mix*

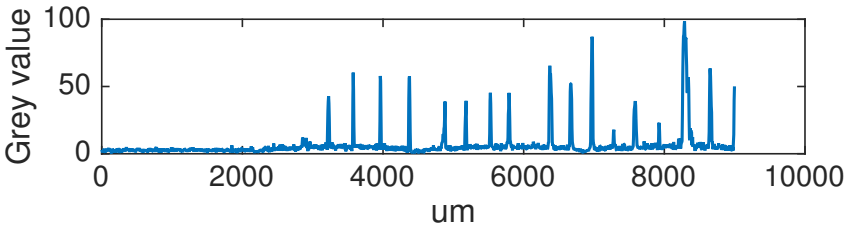

(d) *1 µM, 5 min, Array: E4-2, aptamer mix*

Figure 5.11: *Grey value profile plots, aptamer concentration:1 µM, 5 min UV exposure. See figure 5.9 for elaboration on where on the chips the arrays were measured. The grey value peaks are peaks of high fluorescent signal in the measured image (figure 5.8d). The first 2-3000 µm of all plots represents the grey value profile of the PEDOT:PSS, while the remaining distance up until 9000 µm represents the grey value profile of the PC substrate.*

5.3 ELASA hybridisation assay for examining the UV immobilisation of aptamers on polymer substrates

To experimentally test the immobilisation of aptamers with the UV cross-linking method without the usage of a fluorescent label a colorimetric ELASA was developed. The ELASA is equivalent to an ELISA but aptamers are used instead of antibodies. The principle of ELISA was described in chapter 2.1.2.
The developed ELASA tested the hybridisation of the rcDNA strand to the immobilised aptamer. The UV cross-linking method was used to immobilise aptamers in 96 microtiter well plates, on PC substrates and on PEDOT:PSS in order to test the method on different substrates. Two different aptamers specific to NoV were used in the experiments: VP1T and SMV25, sequences are found in appendix B.2 and B.3. Figure 5.12 illustrates the principle of the developed ELASA. The aptamers were

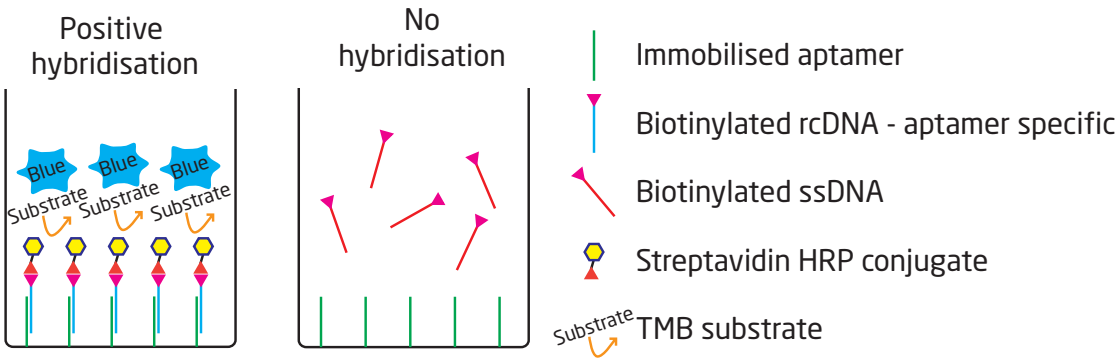

Figure 5.12: *Principle of the developed ELASA.*

immobilised in the wells of the microtiter plate and the rcDNA or a non specific ssDNA were incubated with the aptamer. Both the rcDNA and the ssDNA were biotinylated. The unbound rcDNA and ssDNA were washed away in the subsequent washing step. In the figure the ssDNA is present in the well, but this is only to clarify that it does not hybridise to the aptamer. A streptavidin HRP conjugate was added to the wells. If biotin was present in the wells the streptavidin HRP conjugate would bind to this. The detection was done with a TMB substrate that reacts with the HRP and develops a blue colour. The development was stopped with a stop solution and the blue colour turned yellow. The optical density (OD) of the light absorption of the assay was read with a plate reader at 450 nm. The protocol and material list for the ELASA hybridisation assay can be found in appendix A.11. In a normal ELISA a standard curve is made for each experiment and the OD values of the analyte are compared to the standard curve in order to compare the result to

other equivalent ELISA or determine the analyte concentration. This is not possible with the ELASA as no standard curve exists for this assay since it is not the analyte but the method we are testing. It is thus not possible to directly compare the OD values of the experiments to each other but it is possible to compare the OD values within each experiment and compare the trends between experiments. All of the OD values for the described experiments can be found in appendix A.11.1.
The ELASA experiments were divided into two main parts: 1) experiments in microtiter plates and 2) experiments on PC SD card chips with or without PEDOT:PSS. The two parts will be described below.

5.3.1 ELASA hybridisation experiments in microtiter plates

The first ELASA hybridisation experiments were done in microtiter plates to test the applicability of the assay in standard microtiter plates. Two different microtiter plates were tested, herein denoted Nunclon plates and PolySorp plates:

- Nunclon plate: Nunc MicroWell 96-Well Microplates, nunclon delta surface, Surface Coating: Cell Culture (Thermo Fisher Scientific)
- PolySorp plate: Nunc-Immuno MicroWell 96 well solid plates, PolySorp, flat bottom plate, pinchbar design (Sigma-Aldrich)

The Nunclon plates were hydrophilic and were intended used for cell culture while the PolySorp plates were hydrophobic and intended used for ELISA.

Comparison of wet and dry stage of aptamer solution during the UV exposure

The importance of the drying step of the aptamers onto the substrate before the UV exposure was investigated. To test this, the UV cross-linking method was performed in a wet liquid stage rather than drying the aptamers in the microtiter well. A volume of 50 μL, 1 μM - 10 nM, aptamer solution was added to the wells of Nunclon microtiter plates and UV exposed for 5 minutes. After the UV exposure the ELASA was performed according to protocol A.11. Table 5.1 illustrates the experimental layout of the tested plates. Nunclon plates were used as test substrates in this experiment. The plate layout and data can be found in appendix A.11.1 figure A.7. The results revealed that the UV cross-linking method did not work in liquid. The results also revealed that there seems to be no difference between no-UV and UV exposure of the dry stage aptamers on the Nunclon plates. This could be caused by the hydrophilic surface treatment of the Nunclon plates. No signal was detected from the incubation of rcSMV25 with VP1T or rcVP1T with SMV25, indicating that the hybridisation assay was specific.

Table 5.1: *Experimental layout of comparison between wet and dry stage of aptamer solution during the UV exposure*

Plate no.	Plate type	Wet/Dry	UV exposure
1	Nunclon plate	Dry	UV
2	Nunclon plate	Dry	no UV
3	Nunclon plate	Wet	UV
4	Nunclon plate	Wet	no UV

Comparison of the UV cross-linking on Nunclon and PolySorp plates and Nunclon plates with PEDOT:PSS

The UV cross-linking method was tested on two types of microtiter plates: Nunclon and PolySorp plates, to compare the method on the two plates. To test the UV cross-linking on PEDOT:PSS, PEDOT:PSS was spray-coated inside the wells of the microtiter plates and dried overnight at 60 °C. The PEDOT:PSS was diluted 1:2.5 in MilliQ water and filtered with a syringe filter (5 μm) before spray-coating. It was not possible to get a complete and homogeneous PEDOT:PSS coverage on the PolySorp plates due to the hydrophilic surface of these plates. Hence, only Nunclon plates were tested with PEDOT:PSS coating. The tested concentrations of the VP1T and SMV25 aptamers were: 1 μM, 100 nM and 10 nM. The experimental layout of the plates used in the experiment is given in table 5.2. The OD data

Table 5.2: *Experimental layout of comparison of the UV cross-linking on Nunclon and PolySorp plates and Nunclon plates with PEDOT:PSS*

Plate no.	Plate type	PEDOT:PSS coating	UV exposure
1	Nunclon plate	PEDOT:PSS	UV
2	Nunclon plate	PEDOT:PSS	no UV
3	Nunclon plate	–	UV
4	Nunclon plate	–	no UV
5	PolySorp	–	UV
6	PolySorp	–	no UV

values and plate layout for each plate can be found in appendix A.11.1 figure A.8 and A.9. The results confirmed the previous observations of the Nunclon plates, where no difference between UV an no-UV exposure was observed (plates 3 and 4). It was thus concluded that the Nunclon plates were not suitable for the testing of

the UV cross-linking method. Conversely, the UV cross-linking worked as intended on the PolySorp plates. The OD signals of 1 μM and 100 nM aptamer solution were high in the plate that had been UV exposed (plate 5). The OD values of the VP1T aptamer was slightly higher than the OD values of the SMV25 aptamer. A low insignificant OD signal was seen in the PolySorp plate with no UV exposure (plate 6). The OD values of the UV exposed Nunclon plates coated with PEDOT:PSS (plate 1) revealed positive OD values of the VP1T aptamer at a concentration of 1 μM that indicated that the method worked on PEDOT:PSS surfaces. Although, the OD values of plate 1 were half or lower than the PolySorp plate. The Nunclon plates coated with PEODT:PSS and with no UV exposure (plate 2) revealed a low OD signal at 1 μM for both aptamers. It was thus not possible to conclude if the UV cross-linking method worked on the PEDOT:PSS. There was a possibility that some of the aptamers were immobilised onto the underlying Nunclon plate if the PEDOT:PSS coverage was inhomogeneous. It could be concluded that the method worked on the Polysorp plates. Thus, the PolySorp plates were used for the next experiment.

Comparison of the UV cross-linking on PolySorp plates with or without PEDOT:PSS and with or without TC-tag

The ELASA was performed on PolySorp plates with or without PEDOT:PSS. As mentioned above, it was not possible to get a good coverage of PEDOT:PSS on the plates without a pre-treatment. Thus, oxygen plasma treatment was applied to the plates before spray-coating the plates with PEDOT:PSS. The oxygen plasma increased the hydrophilicity of the plates and ensured a good coverage of the PEDOT:PSS. Furthermore, the importance of the TC-tag in the UV cross-linking method was examined. The experimental layout is listed in table 5.3. The OD data values and plate layout for each plate can be found in appendix A.11.1 figure A.10 and A.11. As expected, the PolySorp plates with UV exposure and TC-tag (plate 5) showed high OD values. Again, the OD values of the VP1T aptamer were higher than the SMV25 aptamer. The PolySorp plate with UV exposure and no TC-tag (plate 7) showed very low OD values for the VP1T aptamer but OD values comparable to the plate 5 for the SMV25 aptamer. It thus seemed like the TC-tag made a greater difference in the UV cross-linking of the VP1T aptamer than the SMV25 aptamer. The PolySorp plates, with and without TC-tag, and no UV exposure (plates 6 and 8) showed no OD values of significance.
The PolySorp plates with PEDOT:PSS coverage and UV exposure, with and without TC-tag (plates 1 and 3) revealed a positive trend. The difference between the plates, and thus the difference between the UV cross-linking with and without the TC-tag, was low. The plates without UV exposure (plates 2 and 4) revealed lower OD values than the UV exposed plates. It was thus concluded that a positive trend

Table 5.3: *Experimental layout for the comparison of the UV cross-linking on PolySorp plates with or without PEDOT:PSS and with or without TC-tag*

Plate no.	Plate type	Pre-treatment	PEDOT:PSS coating	Aptamer tag	UV exposure
1	PolySorp	O_2 Plasma	PEDOT:PSS	TC-tag	UV
2	PolySorp	O_2 Plasma	PEDOT:PSS	TC-tag	No UV
3	PolySorp	O_2 Plasma	PEDOT:PSS	No TC-tag	UV
4	PolySorp	O_2 Plasma	PEDOT:PSS	No TC-tag	No UV
5	PolySorp	–	–	TC-tag	UV
6	PolySorp	–	–	TC-tag	No UV
7	PolySorp	–	–	No TC-tag	UV
8	PolySorp	–	–	No TC-tag	No UV

of the UV cross-linking of aptamers onto PEDOT:PSS was observed. There was a clear difference between the applicability of the UV cross-linking method on the PolySorp plates and on the PEDOT:PSS. From this experiment, and the previous experiment in the Nunclon microtiter plates, we observed a difference of the functionality of the UV cross-linking depending on the underlying substrate of the PEDOT:PSS coating. Since our aptasensor chip substrate was PC, it was obvious to test this material and the PC coated with PEDOT:PSS. These experiments are described in the following section.

5.3.2 ELASA hybridisation experiments on PC SD card chips with or without PEDOT:PSS

The UV cross-linking was tested with the right combination of materials for the final aptasensor design: PEDOT:PSS on PC. Unfortunately, it was not possible to purchase PC microtiter plates. Instead, we used the SD card chip substrates and designed a well layout that resembled a 96 microtiter well plate. The PEDOT:PSS was applied to the SD card chip substrates with a paint applicator in 1 or 2 layers and dried at 60 °C for 15-30 minutes. The PEDOT:PSS was allowed to dry between layers when 2 layers were applied. To do ELASA on the chips, an array of 2 x 5 well per chip was designed to fit on one SD card chip. The wells were made in PMMA with the CO_2 laser and assembled with the chip by double sided adhesive tape. The wells were 10 mm deep and had the same diameter (i.e. 7 mm) as the wells of a 96 microtiter plate. Figure 5.13a shows the chip substrate coated with PEDOT:PSS and an image of the assembled chip. Figure 5.13b shows an assembly of four chips,

(a) **(b)**

Figure 5.13: *Image of the PEDOT:PSS coated PC chip substrate and micro wells. (a) SD card chip substrate with 1 layer of PEDOT:PSS applied by the paint applicator and the chip substrate assembled with the well array. (b) An assembly of four chips with wells for ELASA experiments, herein denoted a chip plate.*

herein denoted a chip plate.

In the ELASA hybridisation assays on PC substrates and PEDOT:PSS coated chips several parameters were investigated:

- The UV exposure time (1 min, 5 min or 10 min) and no UV exposure
- Difference between blank PC substrate and 1 or 2 layers of PEDOT:PSS on the substrate
- TC-tag or no TC-tag on the aptamer

In general the UV immobilisation of the VP1T aptamer showed a higher OD signal than the SMV25 aptamer. It is unknown why this occurs, as the TC-tag and spacer is the same of the two strands. It must thus be concluded that the reason must be sequence specific. It could also be that the hybridisation conditions were better for the VP1T strand than for SMV25, thus leading to a higher hybridisation efficiency and hence a higher signal. The following section will describe the data and results for the VP1T aptamer only.

UV exposure time dependence

The dependence of the UV exposure time (0, 1, 5 or 10 minutes) was experimentally tested on the PC chips. Furthermore, chips with 1 and 2 layers of PEDOT:PSS on the PC substrate were compared in this experiment. Two repetitions were made

and the OD data for each experiment was normalised to the OD value of the PC chips, 5 μM aptamer, 1 μM rcVP1T, 5 min UV exposure after subtraction of the background. This OD value was chosen for the normalisation as it was assumed that the efficiency of the UV cross-linking was relatively constant on the PC substrate and the 5 μM aptamer concentration was present in both repetitions. Figure 5.14 lists the normalised data for the time exposure dependence experiment. The data was coloured accordingly: <0.1 white, >1.0 dark. The full data set (not normalised data) can be found in appendix A.11.1, figures A.12, A.13 and A.14. The UV cross-linking method was successful on the PC chips and the two repetitions corresponded to each other. It was possible to detect the immobilised VP1T aptamer down to a concentration of 100 nM with 5 or 10 min UV exposure. There was a clear signal dependence between the UV exposure time and the VP1T aptamer concentration. The difference between 5 and 10 minutes was low but there was a clear signal reduction for 1 minute UV exposure. A low degree of passive absorption of the aptamer onto the PC was observed when the aptamers were not cross-linked (0 minutes UV). The negative controls with the biotinylated rcSMV25 were negative for the PC chips, showing the specificity of the ELASA.
The UV cross-linking of 1 layer of PEDOT:PSS showed no clear dependence between the different UV exposure times. Although, a positive trend was observed at the high aptamer concentrations. There was a clear difference between the experiments with the rcVP1T and the negative controls with the rcSMV25. The experiments with the 2 PEDOT:PSS layers were not as convincing as the 1 PEDOT:PSS layer experiment. The normalised data values were low compared to both the PC chips and the 1 layer PEDOT:PSS. Between the two repetitions, the data were poorly reproducible. The difference between the 1 or 2 layers PEDOT:PSS indicates that the thickness of the PEDOT:PSS layer has an influence on the availability of the immobilised aptamers for hybridisation with the complementary strand or that the 1 layer PEDOT:PSS was not covering the PC chip substrate homogeneously. The negative controls for the 2 layers PEDOT:PSS were indeed negative.
Based on these experiments it was concluded that 5 minutes of UV cross-linking was sufficient for the aptamer immobilisation. The concentration for the aptamer immobilisation should be as high as possible, preferably 10 μM or higher. The high aptamer concentration is not an advantage in the viral aptasensor fabrication process as higher concentrations increase the amount of material needed.

Dependence of TC-tag, UV exposure and PEDOT:PSS layers

The dependence of the TC-tag in the cross-linking was examined together with the UV exposure (0 or 5 minutes) and 1 or 2 layers of PEDOT:PSS on the PC substrate. The conditions were examined by three experimental repetitions listed in figure 5.15. The OD data for each repetition was normalised to the OD value of the PC chips,

First repetition

rcVP1T: 1 µM

PEDOT:PSS, 2 layers

	5 µM	1 µM	100 nM	10 nm
No UV (0 min)	0,079	0,078	0,068	0,062
UV (1 min)	0,150	0,122	0,107	0,076
UV (5 min)	0,211	0,205	0,102	0,061
UV (10 min)	0,124	0,253	0,182	0,062

PC chips

	5 µM	1 µM	100 nM	10 nm
No UV (0 min)	0,327	0,382	0,039	0,003
UV (1 min)	0,914	0,603	0,078	0,011
UV (5 min)	1,000	0,984	0,748	0,113
UV (10 min)	1,182	1,038	0,789	0,130

Second repetition

rcVP1T: 1 µM

PEDOT:PSS, 1 layers

	10 µM	5 µM	1 µM	100 nm
No UV (0 min)	0,109	0,330	0,198	0,135
UV (1 min)	0,903	0,761	0,263	0,094
UV (5 min)	0,399	0,212	0,166	0,112
UV (10 min)	0,509	0,214	0,290	0,218

PEDOT:PSS, 2layers

	10 µM	5 µM	1 µM	100 nm
No UV (0 min)	0,544	0,070	0,107	0,120
UV (1 min)	0,163	0,021	0,043	0,043
UV (5 min)	0,154	0,171	0,105	0,001
UV (10 min)	0,390	0,205	0,214	0,208

PC chips

	10 µM	5 µM	1 µM	100 nm
No UV (0 min)	0,544	0,366	-0,001	-0,032
UV (1 min)	0,563	0,447	0,181	-0,026
UV (5 min)	0,937	1,000	1,116	0,713
UV (10 min)	1,115	1,011	1,089	0,647

(a)

First repetition -Negative controls

rcSMV25: 1 µM

PEDOT:PSS, 2 layers

	5 µM	1 µM	100 nM	10 nm
No UV (0 min)	0,005	0,001	0,064	-0,010
UV (1 min)	0,030	-0,012	-0,001	0,005
UV (5 min)	-0,026	-0,028	-0,023	-0,025
UV (10 min)	0,011	-0,007	-0,002	-0,022

PC chips

	5 µM	1 µM	100 nM	10 nm
No UV (0 min)	0,086	0,013	-0,001	-0,002
UV (1 min)	0,172	0,526	0,012	-0,005
UV (5 min)	0,132	0,252	0,001	-0,003
UV (10 min)	0,110	0,129	0,063	0,003

Second repetition - Negative controls

rcSMV25: 1 µM

PEDOT:PSS, 1 layers

	10 µM	5 µM	1 µM	100 nm
No UV (0 min)	-0,060	-0,074	-0,076	-0,078
UV (1 min)	-0,074	-0,083	-0,076	-0,088
UV (5 min)	-0,033	-0,087	-0,091	-0,094
UV (10 min)	-0,105	-0,118	-0,114	-0,123

PEDOT:PSS, 2layers

	10 µM	5 µM	1 µM	100 nm
No UV (0 min)	-0,124	-0,089	-0,117	-0,123
UV (1 min)	-0,104	-0,103	-0,118	-0,118
UV (5 min)	-0,127	-0,133	-0,128	-0,140
UV (10 min)	-0,098	-0,143	-0,142	-0,143

PC chips

	10 µM	5 µM	1 µM	100 nm
No UV (0 min)	-0,040	-0,039	-0,039	-0,038
UV (1 min)	-0,048	-0,048	-0,047	-0,047
UV (5 min)	0,038	-0,022	-0,025	-0,024
UV (10 min)	-0,017	-0,018	0,012	-0,020

(b)

Figure 5.14: *Normalised OD data for VP1T aptamer, UV exposure time dependence. The data was normalised from PC chips, 5 µM, 5 min UV exposure. Two repetitions of the 2 layers PEDOT:PSS and PC chips were made. The second repetition included concentrations of 10 µM VP1T aptamer solution. Colour scheme: <0.1 white, >1.0 dark. The full data set can be found in appendix A.11.1, figures A.12, A.13 and A.14. (a) Experiments with the rcVP1T. (b) Negative controls with the rcSMV25.*

First repetition

rcVP1T: 1 µM

PC, TC-tag

	5 µM	1 µM	100 nM	10 nM
UV (5 min)	1,000	0,799	0,536	0,020
No UV	0,201	0,020	-0,001	-0,003

PEDOT:PSS, 1 layer, TC-tag

	5 µM	1 µM	100 nM	10 nM
UV (5 min)	0,249	0,335	0,186	0,090
No UV	0,296	0,179	0,132	0,094

Second repetition

rcVP1T: 1 µM

PC, TC-tag

	5 µM	1 µM	100 nM	10 nM
UV (5 min)	1,000	0,829	0,642	0,181
No UV	0,277	0,299	0,013	-0,001

PC, no TC-tag

	5 µM	1 µM	100 nM	10 nM
UV (5 min)	0,387	0,484	0,296	0,092
No UV	0,080	0,314	0,103	0,051

PEDOT:PSS,2 layer, TC-tag

	5 µM	1 µM	100 nM	10 nM
UV (5 min)	0,154	0,152	0,089	0,048
No UV	0,069	0,057	0,055	0,087

PEDOT:PSS,2 layer, no TC-tag

	5 µM	1 µM	100 nM	10 nM
UV (5 min)	0,115	0,062	0,070	0,053
No UV	0,130	0,076	0,086	0,073

Third repetition

rcVP1T: 1 µM

PC, TC-tag

	10 µM	5 µM	1 µM	100 nM
UV (5 min)	1,203	1,000	0,764	0,641
No UV	0,193	0,276	-0,051	-0,097

PC, no TC-tag

	10 µM	5 µM	1 µM	100 nM
UV (5 min)	0,238	0,336	0,203	0,028
No UV	0,019	0,000	0,004	-0,015

PEDOT:PSS, 1 layer, TC-tag

	10 µM	5 µM	1 µM	100 nM
UV (5 min)	0,761	0,676	0,378	0,214
No UV	0,286	0,252	0,255	0,067

PEDOT:PSS, 1 layer, no TC-tag

	10 µM	5 µM	1 µM	100 nM
UV (5 min)	0,412	0,609	0,287	0,075
No UV	0,836	0,333	0,129	0,066

PEDOT:PSS,2 layers, TC-tag

	10 µM	5 µM	1 µM	100 nM
UV (5 min)	0,436	0,376	0,316	0,177
No UV	0,145	0,155	0,130	0,067

PEDOT:PSS,2 layers, no TC-tag

	10 µM	5 µM	1 µM	100 nM
UV (5 min)	0,323	0,260	0,183	0,102
No UV	0,022	0,007	0,005	0,004

(a)

First repetition - Negative controls

rcSMV25: 1 µM

PC, TC-tag

	5 µM	1 µM	100 nM	10 nM
UV (5 min)	0,041	-0,024	-0,032	-0,031
No UV	0,031	-0,039	-0,023	-0,031

PEDOT:PSS, 1 layer, TC-tag

	5 µM	1 µM	100 nM	10 nM
UV (5 min)	0,455	0,016	-0,005	-0,008
No UV	0,099	-0,004	-0,007	-0,005

Second repetition - Negative controls

rcSMV25: 1 µM

PC, TC-tag

	5 µM	1 µM	100 nM	10 nM
UV (5 min)	0,028	0,013	0,009	0,004
No UV	0,020	-0,004	-0,002	-0,006

PC, no TC-tag

	5 µM	1 µM	100 nM	10 nM
UV (5 min)	0,153	0,002	0,009	-0,003
No UV	0,011	0,006	-0,003	-0,005

PEDOT:PSS,2 layer, TC-tag

	5 µM	1 µM	100 nM	10 nM
UV (5 min)	0,020	-0,008	-0,009	-0,011
No UV	0,026	-0,003	0,020	-0,022

PEDOT:PSS,2 layer, no TC-tag

	5 µM	1 µM	100 nM	10 nM
UV (5 min)	-0,016	-0,009	-0,006	-0,012
No UV	-0,004	-0,011	-0,011	-0,004

Third repetition - Negative controls

rcSMV25: 1 µM

PC, TC-tag

	10 µM	5 µM	1 µM	100 nM
UV (5 min)	-0,031	-0,075	-0,059	-0,095
No UV	-0,039	-0,103	-0,099	-0,100

PC, no TC-tag

	10 µM	5 µM	1 µM	100 nM
UV (5 min)	0,014	-0,016	-0,017	-0,018
No UV	-0,014	-0,017	-0,016	-0,015

PEDOT:PSS, 1 layer, TC-tag

	10 µM	5 µM	1 µM	100 nM
UV (5 min)	-0,053	-0,036	-0,041	-0,052
No UV	-0,058	-0,055	-0,054	-0,057

PEDOT:PSS, 1 layer, no TC-tag

	10 µM	5 µM	1 µM	100 nM
UV (5 min)	-0,018	-0,043	-0,052	-0,056
No UV	-0,034	-0,039	-0,040	-0,037

PEDOT:PSS,2 layers, TC-tag

	10 µM	5 µM	1 µM	100 nM
UV (5 min)	0,040	-0,003	-0,020	-0,040
No UV	-0,012	-0,031	-0,034	-0,038

PEDOT:PSS,2 layers, no TC-tag

	10 µM	5 µM	1 µM	100 nM
UV (5 min)	-0,019	-0,049	-0,051	-0,059
No UV	-0,005	-0,057	-0,058	-0,066

(b)

Figure 5.15: *Normalised OD data for VP1T aptamer, dependence of TC-tag, UV exposure and PEDOT:PSS layers. The data was normalised from PC chips, 5 µM, 5 min UV exposure and TC-tag. Three independent experiments were made with repetitions of the 1 or 2 layers PEDOT:PSS and PC chips. The third repetition included concentrations of 10 µM VP1T aptamer solution. Colour scheme: <0.1 white, >1.0 dark. The full data set can be found in appendix A.11.1, figures A.15, A.16 A.17 and A.18. (a) Experiments with the rcVP1T. (b) Negative controls with the rcSMV25.*

5 μM aptamer, 1 μM rcVP1T, 5 min UV exposure, TC-tag. The data in the figure was coloured accordingly: <0.1 white, >1.0 dark. The full data set (non-normalised data) can be found in appendix A.11.1, figures A.15, A.16 A.17 and A.18.
The data for the PC chips confirmed the previous observations that the UV cross-linking worked on this material with a low degree of passive absorption on the material when no UV exposure was applied. The TC-tag made a clear difference on the PC substrate, hence a low signal was seen when the TC-tag was missing on the aptamer. The signal with TC-tag was approximately 2.7 times higher than without TC-tag. The negative controls were all negative for the PC chips.
The normalised OD data of the chip with 1 PEDOT:PSS layer indicated that exposure to UV light lead to a specific binding of the aptamer on the PEDOT:PSS (approximately 2 times higher signal with UV compared to no UV). However, we did not observe any clear difference of signal between the aptamers with TC-tag and the ones without the TC-tag. The 2 layers PEDOT:PSS showed the same trend as the 1 layer PEDOT:PSS but with reduced signal intensity. This confirms the previous observations between 1 or 2 layers PEDOT:PSS. Hence, this indicates that covering the PC chip substrate with 1 layer PEDOT:PSS is not sufficient to get a homogeneous coverage. Thus, the results of the 2 layer PEDOT:PSS must be assumed to represent the most accurate PEDOT:PSS surface. Furthermore, there was a clear difference between the experiments with the rcVP1T and the negative controls. It must be concluded that the aptamers were indeed immobilised onto the PEDOT:PSS but the exact mechanism is still not clear.
It can be concluded that the aptamer concentration was a very important factor as the OD signal increased for higher aptamer concentrations. The results indicate that immobilisation of aptamers onto PEDOT:PSS was possible and a positive trend of the UV cross-linking of aptamers onto PEDOT:PSS was observed. It must be assumed that some passive absorption is involved in the aptamer immobilisation as the immobilisation works without UV light and the TC-tag.

5.4 Conclusion

This chapter described the experimental work related to the testing of the UV cross-linking method for aptamer immobilisation onto different polymer substrates including PEDOT:PSS. Two detection methods were applied to analyse the usability of the method: fluorescent labelling and colorimetric amplification. The fluorescent labelling did not show any fluorescent signal of the hybridised rcDNA of the UV cross-linked aptamers and it was thus not possible to conclude that the method could be used on PEDOT:PSS. The method seemed to work on PC substrates. It was concluded that the lack of fluorescent signal on the PEDOT:PSS could be a consequence of quenching of the fluorescent signal by the PEODT:PSS, or a high

detection limit of the confocal microscope above the fluorescent signal or finally it was a possibility that the used parameters were not optimal for the method. A colorimetric ELASA was developed to test the UV cross-linking method without fluorescent labelling. The ELASA showed good adherence of the UV cross-linked aptamers on the PolySorb plate and the PC substrate. The aptamer immobilisation onto the PEDOT:PSS showed a positive trend to which it was concluded that the UV cross-linking of aptamers onto PEDOT:PSS works but with lower efficiency than on PC. Furthermore, it was concluded that passive absorption onto the PEDOT:PSS was involved in the aptamer immobilisation.
The work with the aptamer immobilisation with the UV cross-linking method should continue to find the best conditions for the immobilisation of aptamers onto PEDOT:PSS. The method should be compared with known functionalisation methods e.g. amino functionalisation. This will give an indication of whether or not the UV cross-linking method works as efficient as other immobilisation methods. Furthermore, the method should be tested with the target for which the aptamer was selected and not only the rcDNA since the target recognition is a much more complex mechanism.

— 6 —

Aptasensor characterisation and EIS measurements

Electrical characterisation of the stability of the measurement system is important for the success of the sensor development. The longterm purpose of the developed viral aptasensor is to measure the virus content of the water at the water intake of water treatment plants or upstream from the intake. The characteristics of the water at either the intake or upstream from the intake changes during the day or from day to day. This means that the sensor must be stable at different water conditions e.g. changes in salinity, over a time period or at different pH values.
Impedimetric detection by EIS is used as the characterisation and detection method for the viral aptasensor. In some EIS measurements it is an advantage to introduce redox mediators (e.g. the ferric ferrocyanide redox couple) in the sample to e.g. increase or obtain an EIS signal. Redox mediators are commonly used when the reaction is a bulk reaction, i.e. not a reaction on the electrode surface. Furthermore, the detection of redox mediators requires a different detection method e.g. amperometric detection where the redox potential is reached. The target recognition of the viral aptasensor takes place on the electrode surface. Furthermore, it is not possible to introduce redox agents in an environmental sample during a continuous flow. Hence, impedimetric detection, without redox mediators, is the method best suited for the viral aptasensor. The basic theoretical background of impedimetric detection by EIS and an equivalent circuit model for an electrode pair in solution were described in chapter 2.3.2. The equivalent circuit model is redisplayed in figure 6.1. During a target binding event on the electrode surface the electrical characteristics of the surface change. The charge transfer resistance, R_{ct}, increases as the target binds to the aptamers on the electrode surface and thereby hindering the transfer of ions in the buffer solution to the electrode surface. The double layer capacitance

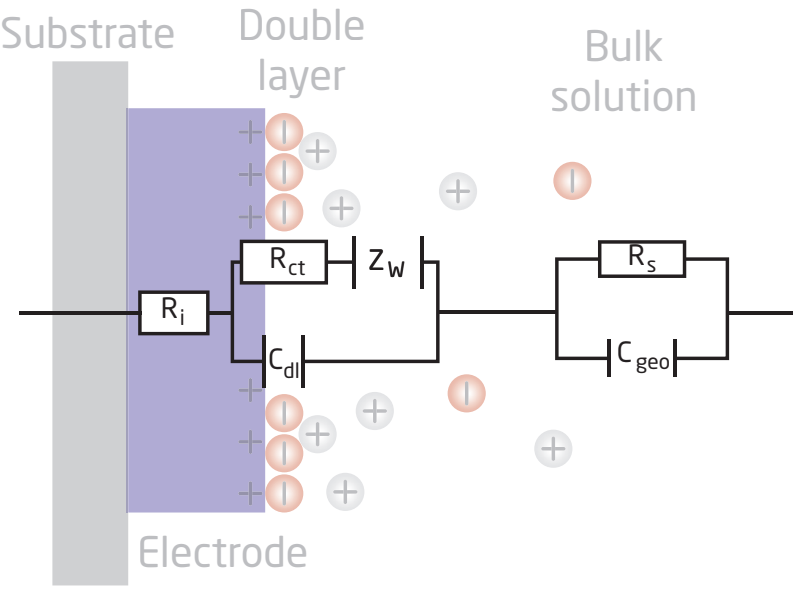

Figure 6.1: *Proposed equivalent circuit model for the viral aptasensor. R_i: Internal resistance of PEDOT:PSS, R_{ct}: Charge transfer resistance, C_{dl}: Double-layer capacitance, Z_W: Warburg impedance, C_{geo}: Geometrical capacitance, R_s: Solution resistance.*

C_{dl} will change as charges will be redistributed. The C_{dl} is commonly represented as a constant phase element (CPE) as it is not an ideal capacitor. Furthermore, the Warburg impedance, Z_W, which represents the diffusion of ionic species in the polymer film and media will also change to a certain degree. It is thus anticipated that the charge transfer, the double layer capacitance and the Warburg impedance are the most important elements in the impedimetric detection. These elements are all part of a larger circuit for the viral aptasensor, which means that it is not possible only to measure the specific elements separately but rather the whole circuit. The whole impedance spectra must thus be acquired and the changes in the impedance must be identified in the spectra. It is not straight forward to describe and model these three elements in a electrode system with conducting polymers. It is anticipated that the impedance changes upon target binding are found in the low frequency regime (< 5 Hz) where the surface elements are dominating. It is possible to measure the impedance change over time at a fixed frequency after identification of the frequency where the effect of the target binding is clearly observable.
The following sections of this chapter will describe a circuit model, the system setup for EIS measurements and the characterisation of the impedance system. The electrical characterisation was done by a commercial potentiostat with a home-build multiplexer to change between electrode pairs. The electrical characterisation was done by measuring the impedance response of the viral aptasensor chip at differ-

ent salinity and pH values and the stability of the aptasensor chip over a period of 2 weeks in continuous flow. This characterisation was done without immobilised aptamers on the electrode surface.

6.1 Modelling of a circuit of the acquired data

To evaluate the equivalent circuit model for the viral aptasensor an impedance sweep from 0.5 Hz to 100 kHz was acquired in a 1:1000 PBS dilution. The measurements were done on a IM6, company Zahner elektrik potentiostat with an amplitude of 100 mV. The recorded data was fitted to a circuit model using the EIS Spectrum Analyser software (Research Institute for Physical-Chemical Problems, Belarusian State University). Figure 6.2 shows the circuit model that showed the best fit, together with the element values, and the Nyquist plot of both the acquired data and the circuit model. The model and the data were plotted with MATLAB, the script can be found in appendix A.13. The Bode plots of both the acquired data and the model is found in figure 6.3.
The impedance of the different model elements were found to be:

$$Z_{C_{geo}} = \frac{1}{j\ \omega\ 1.16nF}$$

$$R_s = 190\ k\Omega$$

$$R_{ct} = 61\ k\Omega$$

$$Z_W = 1.1\ M\Omega\ s^{-1/2}(\omega)^{-1/2}(1-j)$$

$$Z_{CEP} = \frac{1}{(j\ \omega)^{0.93}\ 3.7\mu F}$$

The total impedance of the model circuit was found to be:

$$Z_{total} = \frac{1}{\frac{1}{Z_{C_{geo}}}\frac{1}{R_s}} + \frac{1}{\frac{1}{Z_W}\frac{1}{R_{ct}}} + Z_{CEP} \tag{6.1}$$

The difference between the circuit model and the proposed equivalent circuit is visible in the different configuration of the low frequency elements. In the circuit model the R_{ct} is found in parallel rather than in series with the Z_W. Furthermore the CPE is found in series with the parallel connection of R_{ct} and Z_W. The proposed equivalent circuit was made from the assumption that the electrode material is a metal conductor. The intrinsic conductive polymer does not behave as an ideal conductor and the electrode solution interface is not a clear physical boundary. This could explain the difference between the two circuits.
The Nyquist plot of the data and circuit model (Figure 6.2b) showed good agreement

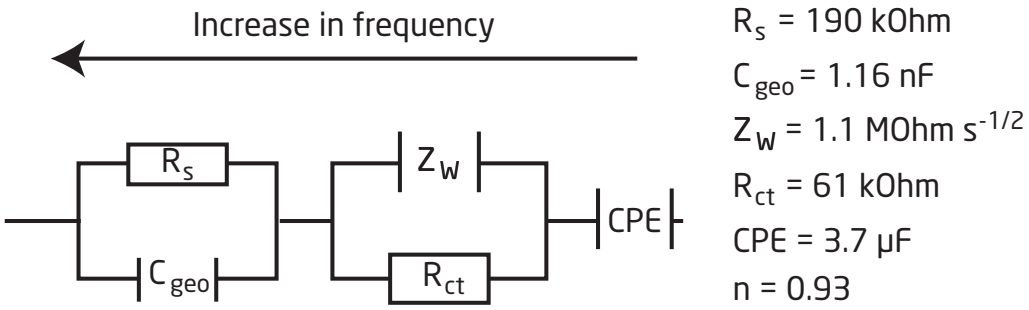

(a) *Circuit model*

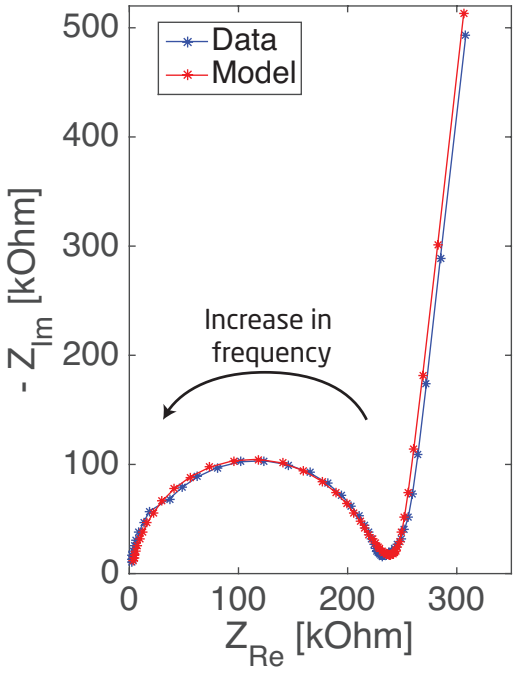

(b) *Nyquist plot*

Figure 6.2: *Circuit model and Nyquist plots of both the model circuit and data acquired of the SD card chip. The measurement was done with a 1:1000 PBS dilution.*

between the model and the data. The data points in the plot represent a specific frequency within the measured frequency range of both the data and modelled circuit. The difference between the frequency points of the data and model was small.

The Bode plots are plotted in figure 6.3. The Bode phase plot of the data and the model was in good agreement. The phase of the low frequency range (< 5 Hz) showed a capacitive behaviour as the phase decreased towards a phase shift of - 60 degrees. In the frequency range between $10^1 - 10^3$ Hz the phase was close to 0 degrees which means that a resistive behaviour was present. This resistive behaviour

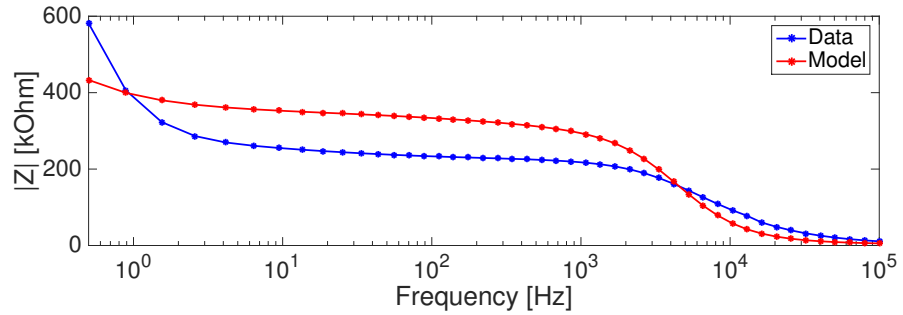

(a) *Bode modulus plot*

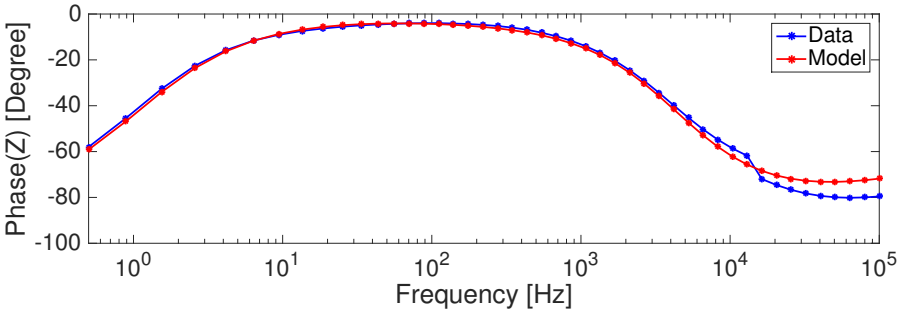

(b) *Bode phase plot*

Figure 6.3: *Bode plots of modelled data and data acquired of the SD card chip. The measurement was done with a 1:1000 PBS dilution.*

originated from the solution resistance of the diluted PBS. At higher frequencies the phase shifted to negative values approximating -90 degrees which represented the geometrical capacitance and eventually the parasitic capacitance of the whole system. The Bode modulus plot did not show as good of a fit as the Bode phase and the Nyquist plot. The shape of the model and data plot were the same but there was a shift in the modulus through out the entire plot but mainly in the frequency range dominated by the solution resistance. This shift could be explained by the difference between the simplified model compared to the real life circuit. It is important to state that the model circuit is a simplified version of the real system. The real life circuit is much more complex which means that it can not be truly modelled by a few circuit elements. The model circuit helps in understanding the behaviour of the system and gives a good approximation to the real circuit.

6.2 System setup for EIS measurements

The system setup for the EIS measurements was composed of three main parts:

- SD card chip
- Homebuilt multiplexer (made by Noemi Rozlosnik)
- Potentiostat: VersaSTAT 3, Princeton Applied Research, USA

Figure 6.4 illustrates a schematic overview of the setup. The potentiostat was connected to the home-build multiplexer and the SD card chip was mounted in the multiplexer. Furthermore, it was possible to connect tubings and a peristaltic pump to the SD card chip to enable sample flow. A computer with the VersaStudio software controlled the potentiostat. The multiplexer was controlled by an Arduino micro board and a home made script (made by Noemi Rozlosnik). The potentiostat applied a voltage of 10 mV and a small AC current to the system and recorded the current response. The current range of the AC signal was set to change automatically on the potentiostat in the range of 0.1-1 μA. The current response and the potential were used by the potentiostat to calculate the impedance of the system. We made two different impedance measurements: fixed frequency measurements over time and impedance spectra from 0.5 Hz to 10 kHz (or higher).

The sensor had four electrode pairs: three electrodes to detect the viral targets

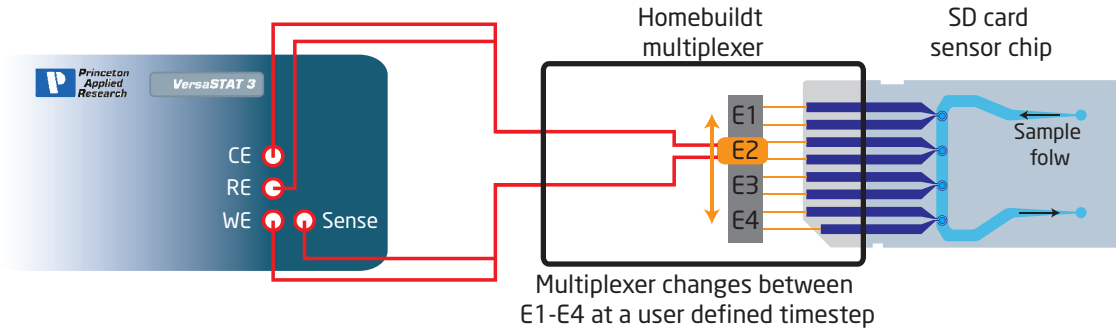

Figure 6.4: *EIS measurement setup. The potentiostat was connected to the home-build multiplexer and the SD card chip was mounted in the multiplexer. The multiplexer changed between electrode pairs E1-4 at a user defined time frame. The applied voltage was 10 mV.*

and an electrode pair for reference measurements. The multiplexer was designed to change between these electrode pairs (E1-4) during the impedance measurements with a user defined time frame.

The data analysis was done using the MATLAB software, MathWorks, with a home written script. The three main steps involved in the data analysis of data acquired at a fixed frequency over time are illustrated in figure 6.5. The script used for the data analysis can be found in appendix A.12. The raw data from the potentiostat consisted of 16 data columns (See appendix A.12 for elaboration of data content). The first step in the data analysis was to calculate the modulus (|Z|) and the phase (phase(Z)) of the impedance and plot the data. Second, the electrode specific data

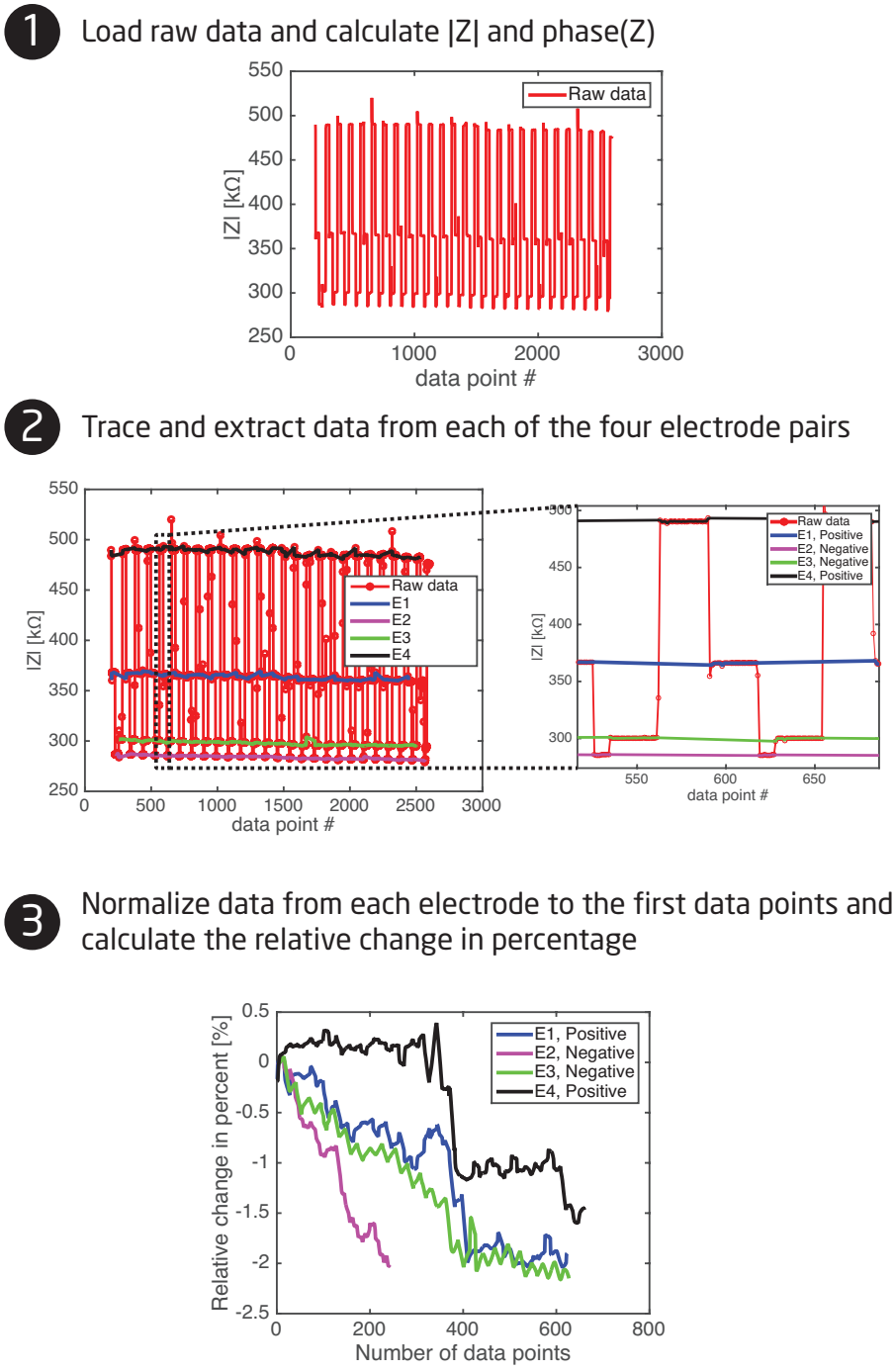

Figure 6.5: *Overview of the three main steps involved in the EIS data analysis with MATLAB*

was extracted from the raw data. Identification of the electrodes in the data was done by setting the multiplexer time frame different in one of the electrodes, which enabled identification of that specific electrode. The multiplexer always changed between electrodes in numerical order. The extracted data was filtered by a running average filter and drift was removed. Third, the data was normalised to the first, e.g. 100, data points and the relative change in percent of the signal was calculated.

6.3 Electrical characterisation of the viral aptasensor system

Testing of the electrical characterisation of the viral aptasensor system was needed to ensure a stable system for the viral measurements. The two parts to be tested were the multiplexer and the SD card chip. The multiplexer was tested with a capacitor and resistor with known capacitance and resistance. The SD card chip was tested with sample solution of different salinity and pH values. Furthermore, the SD card chip was tested in continuous flow over a two week period at a fixed frequency of 1 Hz. The following section describes the characterisation. The chips used for the characterisation were all the SD card chip version 3, which was described in chapter 4.2.2.

6.3.1 Stability of the home-build multiplexer

The stability of the multiplexer was tested with a known resistor and capacitor in parallel. The parallel configuration was tested as this configuration was relevant for the aptasensor where the R_{ct} and C_{dl} are connected in parallel according to the equivalent circuit model. Four different combinations of RC circuits were tested:

- E1: 3.3 μF and 470 kΩ
- E2: 1 nF and 470 kΩ
- E3: 10 nF and 470 kΩ
- E4: 100 nF and 470 kΩ

Figure 6.6 illustrates the output of the data analysis of the stability measurements of the multiplexer measured at 1 Hz over a period of 120 minutes/electrode pair. The relative change in percent for all electrode pairs was between -0.02 and 0.02 %. It can be argued that a sinusoidal with a period $>$ 60 minutes can be observed in the plot but it must be considered insignificant due to the small change in percent. It must be concluded that the multiplexer does not introduce any significant noise components during the measurements or when it changes between electrode pairs.

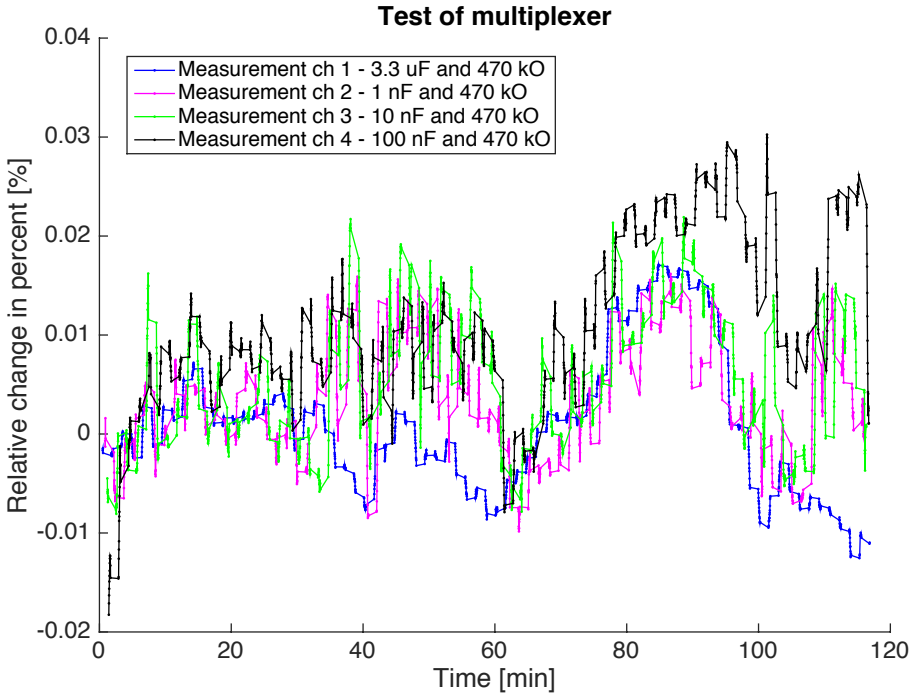

Figure 6.6: *Multiplexer characterisation with RC circuits. A fixed frequency of 1 Hz was used.*

6.3.2 Salinity measurements with the aptasensor

The characterisation of the SD card chip with different salinity of the media was performed with dilutions of PBS. A ten-fold dilution series of PBS in MilliQ water was prepared: 1:1000, 1:100, 1:10, 1:1 and 10:1. The conductivities of the 1:1 PBS and MilliQ water were 15.83 mS/cm and 0.00 mS/cm, respectively. EIS measurements of the PBS dilutions in the chip were measured from low to high concentration and the measurements were done without sample flow. Five impedance spectra from 0.5 Hz to 10 kHz were acquired for each dilution. The average impedance values for each dilution were calculated and plotted. The Nyquist plots and Bode plots are displayed in figure 6.7. The 50 Hz noise component, originating from the electrical power supply, was removed from the plots. The Nyquist plot of the 1:1000 PBS dilution (blue line) was the only dilution that showed parts of the semicircle at high frequencies. As described in chapter 2.3.2, a semicircle in a Nyquist plot represents a capacitor and a resistor in parallel. The high frequency data is represented to the left and low frequency data to the right in a Nyquist plot. The high frequency components in the aptasensor circuit model are the solution resistance, R_s and the geometrical capacitance, C_{geo}. Hence, as the solution resistance decreases, due to

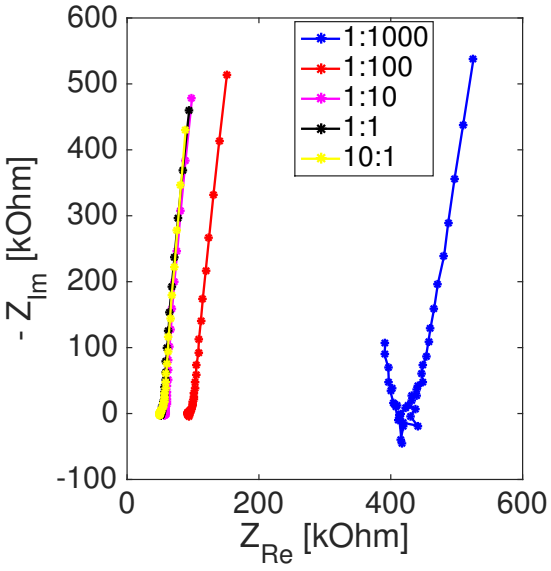

(a) *Nyquist plot*

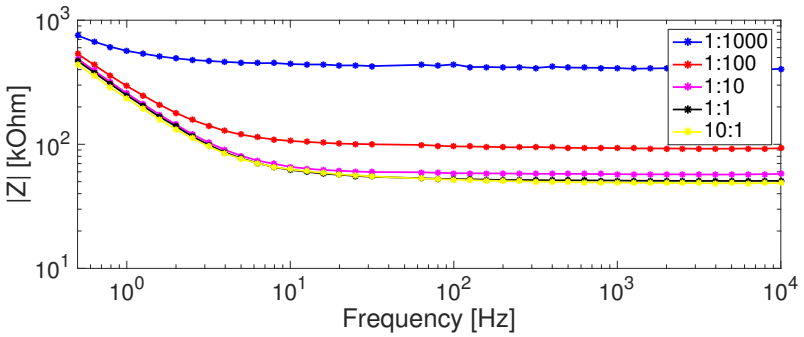

(b) *Bode modulus plot*

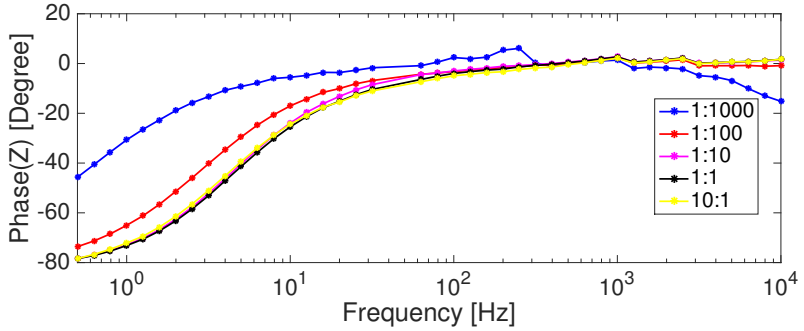

(c) *Bode phase plot*

Figure 6.7: *Nyquist and Bode plots of the salinity measurements of the PBS serial dilution. The data represents measurements of one electrode pair on an SD card chip. A total of five impedance sweeps were acquired for each PBS dilution and the average values were calculated and displayed on the plots. The 50 Hz noise component originating from the power supply was removed.*

an increase in the ionic content of the media, the diameter of the semi-circle decreases and the plot is shifted to the left in the Nyquist plot. The low frequency components of the circuit model, i.e. R_{ct}, Z_W and C_{dl} (or CPE) were identified in the Nyquist plot as the linear part of the plot, from 400 to 525 $k\Omega$ in the real part of the impedance, Z_{Re}. As the capacitive low frequency components do not act as ideal capacitors the linear part is not a vertical line but slightly tilted.
As the PBS dilution increased the Bode modulus plots were shifted towards higher impedance in the frequency range from $10^1 - 10^4$ Hz. This was caused by the higher solution resistance of the diluted PBS. The Bode phase plots all showed resistive behaviour (phase close to 0 degrees) in the same frequency range. In the low frequency range (< 5 Hz) the phase decreased towards a capacitive behaviour. The phase did not reach -90 degrees, which confirmed that the system did not behave as an ideal capacitor at low frequencies. From the Bode phase plots it was evident that the ionic content of the solution had an impact on the behaviour of the low frequency components as the Bode phase plots were shifted to the left at lower PBS concentrations.
From the salinity measurements it was concluded that the system and the chip behaved as expected as a consequence of changes in the salinity of the media.

6.3.3 pH measurements with the aptasensor

The characterisation of pH changes in the measured solution in the chip was measured by a pH series from 4 to 9. The pH series was made by pH adjusting PBS with NaOH or HCl. The measured pH values and conductivities of the pH series are listed in table 6.1. The conductivity of the different pH solutions was approximately the

Table 6.1: *pH values and conductivities of the samples for the pH measurements with the aptasensor chip.*

pH series	Measured pH	Conductivity [mS/cm]
pH 4	3.94	15.99
pH 5	4.80	15.85
pH 6	6.03	15.83
pH 7	7.00	15.80
pH 8	7.80	15.80
pH 9	9.03	15.80

same, which meant that any observable differences in the Nyquist and Bode plots did not originate from changes in conductivity of the solutions. The Nyquist plots

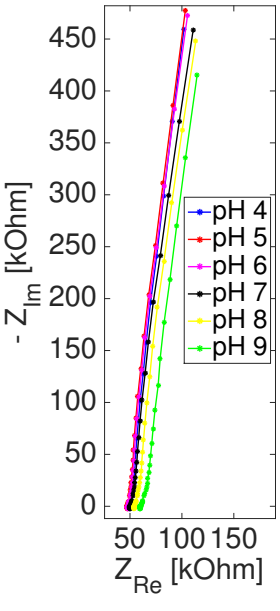

(a) *Nyquist plot*

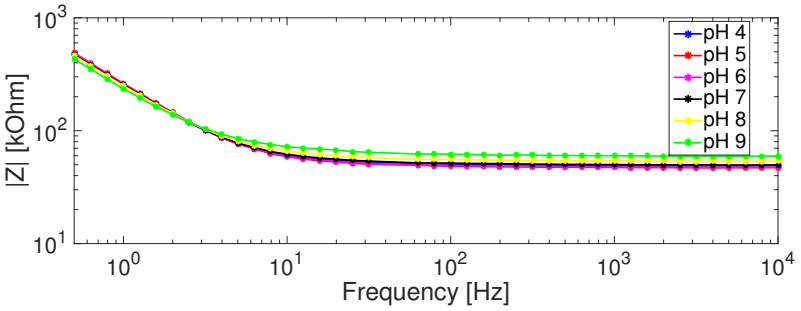

(b) *Bode modulus plot*

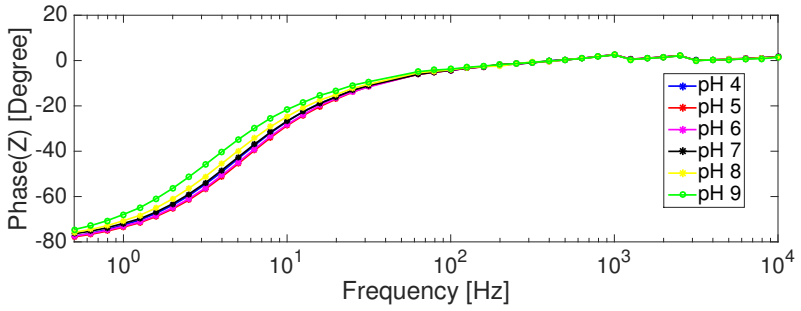

(c) *Bode phase plot*

Figure 6.8: *Nyquist and Bode plots of the pH measurements of the pH series. The data represents measurements of one electrode pair on an SD card chip. A total of five impedance sweeps were acquired for each pH value and the average values were calculated and displayed on the plots. The 50 Hz noise component originating from the power supply was removed.*

and Bode plots of the measured pH series are found in figure 6.8. Both the Nyquist plots and the Bode plots did not show any significant behavioural changes or shift caused by the pH changes. The only small observable change in the plots was related to the pH 9 but this change was considered insignificant.
It was concluded from the pH measurements that the pH change did not alter the EIS signal to a degree where it was significant.

6.3.4 Stability of the SD card chip over a period of two weeks in continuous flow

The stability of the SD card chip was characterised by a long term measurement over time in continuous flow with a 1:20 PBS dilution in MilliQ water. The conductivities of tap water and PBS were measured to be 0.82 mS/cm and 15.83 mS/cm, respectively. This means that tap water is 20 times less conductive than PBS, hence a 1:20 PBS dilution was prepared. In order to have a clean sample with no possibility of biofilm formation on the electrodes the 1:20 PBS dilution was chosen as the measurement media instead of tap water. The measurements were done on four electrode pairs on the same SD card chip with a fixed frequency of 1 Hz. A total of 5000 data points were measured for all four electrode pairs each day. The electrode specific data from each day was extracted as illustrated in figure 6.5 and the average and standard deviation of the 1 Hz impedance for each electrode were calculated using MATLAB. Figure 6.9 shows the plots of the stability analysis of each electrode pair with the standard deviation for each day over a period of two weeks. The average impedance of the four electrode pairs lies within a range of 180 and 290 $k\Omega$. Common for all electrode pairs were a large impedance change from day 0 to day one between 10 to 27 $k\Omega$. Electrode pairs E1-3 showed a constant impedance after day 1, where the impedance of electrode pair E4 showed a small drift towards higher impedance. Furthermore, the standard deviation of all electrode pairs for each day was low which meant that the impedance of the electrode pairs were constant during the daily measurements.
The stability measurement showed that the SD card chip was stable in flow over a two week period. It was thus concluded that the PEDOT:PSS electrodes were not degrading due to the flow. The initial impedance change within the first day must be kept in mind for further measurements and development of the viral aptasensor system. Especially, if the measurements are to be done as short term measurements. The dynamics of the initial impedance change should thus be examined further.

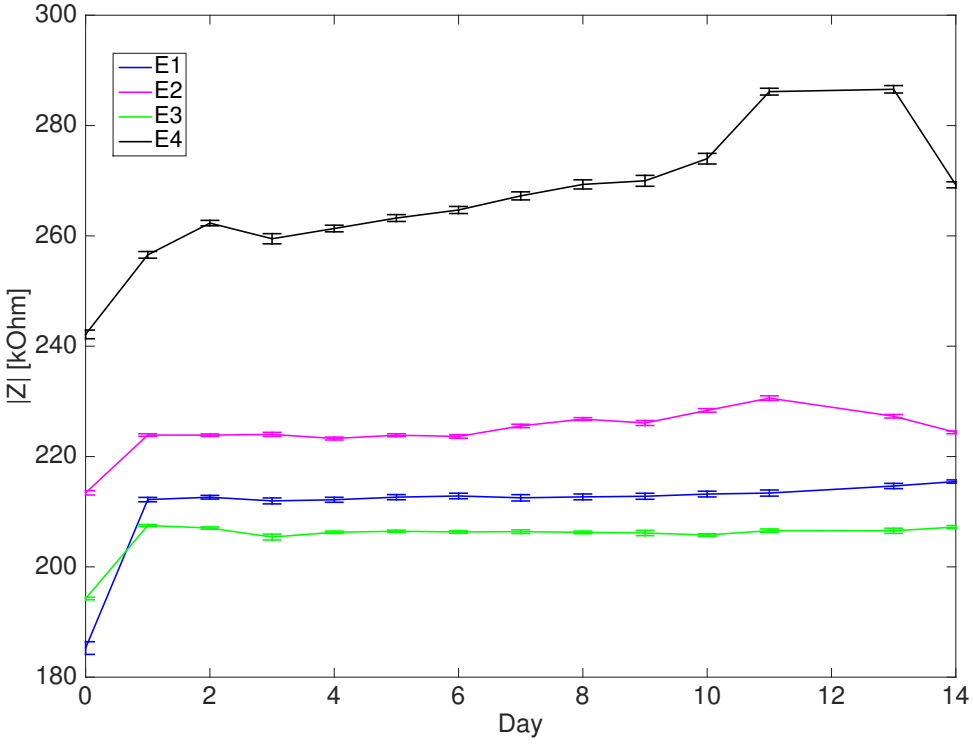

Figure 6.9: *Characterisation of the stability of the SD card chip over a two week period in continuous flow at a fixed frequency of 1 Hz.*

6.4 Conclusion

The long term aim of the viral aptasensor is to do impedimetric detection of virus in environmental water samples. In this chapter, the characterisation and the stability of the multiplexer and the SD card chip were experimentally investigated. Furthermore, a circuit model was proposed based on an EIS measurement of the SD card chip. The model circuit was in good agreement with the acquired data. It was concluded that the model was a good representation of the real circuit but it was acknowledged that differences did occur since the real life circuit is much more complex than a simple model.
The stability of the multiplexer was measured with RC circuits with known resistance and capacitance. The multiplexer showed good stability and it was concluded that no significant noise disturbances were introduced in the EIS signal as a consequence of the multiplexer.
The SD card chip was characterised by measurements with different media salinity and different pH values. The salinity measurements showed the expected tendency

where the greatest changes were observed in the frequency range representing the solution resistance. No significant changes caused by difference in pH was observed in the measurements. The stability of the SD card chip was investigated in a continuous flow over two weeks, where daily EIS measurements were made on four electrode pairs of an SD card chip. The average impedance and standard deviation at a fixed frequency of 1 Hz were calculated for each electrode pair, each day. The chip showed good stability and it was concluded that the electrodes did not degrade during the two weeks of constant flow. The largest change of the impedance was observed from day 0 to day 1.
The next step of the EIS measurements will be to immobilise virus specific aptamers on the electrodes and make EIS measurements of spiked virus samples. Good aptamer surface immobilisation is of pivotal importance for successful viral detection. The surface immobilisation is still under development as described in chapter 5. Eventually, environmental water samples should be measured with the SD card chip. Furthermore, the chip to chip variations should be investigated to assure a good reproducibility of the measurements.

— 7 —

Conclusion and perspective

The overall aim of this PhD thesis was the development of an aptasensor which was intended for the use of detection of waterborne viruses: NoV, RV and HAV, in environmental water samples. The process involved different aspects of the development of the aptasensor. The developed aptasensor was an impedimetric all-polymer sensor.

This PhD thesis aimed at preparing samples of RV and HAV for the selection of aptamers targeting these viruses. Aptamers selected against NoV were already published in the literature. The actual aptamer selection was performed by an external collaborator, where the SELEX was based on magnetic bead separation of the target and non-binders. Two different RV strains, Wa and DS-1, were purified and biotinylated for the aptamer selection. The RV was biotinylated to be immobilised onto streptavidin coated magnetic beads. Two different biotinylation linkers were tested and it was found that the BPH biotin linker showed the highest yield. Control experiments of non-biotinylated RV to the magnetic beads showed a high degree of passive absorption. It was thus concluded that further testing and optimisation were required to ensure a better binding of the bRV, compared to the RV, to the beads.
A HAV sample, purified by an external collaborator, was inactivated and biotinylated with the BPH linker. Unfortunately, the initial concentration of the HAV sample was very low and it was not possible to estimate the yield of the biotinylation. The bRV and bHAV samples were shipped to our external collaborator for the aptamer selection.

The iterative design phase of the viral aptasensor was divided into two main designs based on an USB and SD card interface. The USB chip was designed with

two electrode pairs and different approaches of liquid interfaces. The USB chip did not meet the multiplexing requirements for detection of three different viral targets simultaneously. Thus, the SD card chip was designed with four electrode pairs, three for virus detection and one reference/control electrode. The chip substrate and the lid of the final viral aptasensor, the SD card chip version 3, were made by injection moulding of PC and the electrodes were made by screen-printing PEDOT:PSS directly onto the substrate. A channel, integrated in the lid, ensured a liquid connection and allowed continuous sample flow in the chip.

The aptamer immobilisation onto different polymer substrates was tested in this PhD thesis. It was important to investigate the immobilisation of aptamers onto PEDOT:PSS as this was crucial for a successful aptasensor. The tested immobilisation method was based on UV cross-linking of the aptamers through a TC-tag. This method was chosen due to the chemical inertness of the PEDOT:PSS which hindered immobilisation by e.g. thiol or amine linking. The UV cross-linking was initially tested by a hybridisation assay based on fluorescent labelling. The florescent detection did not show any clear conclusion of the aptamer immobilisation and a colorimetric hybridisation ELASA was tested instead. The ELASA was tested in microtiter plates and on the PC SD card chip substrate, both with and without PEDOT:PSS. The UV cross-linking worked very convincingly on the PolySorp microtiter plate and on the PC card chip substrate. The PC card chip substrate coated with 1 or 2 layers of PEDOT:PSS showed a positive trend. It was concluded that immobilisation of aptamers with UV cross-linking method was possible on PEDOT:PSS but with lower efficiency compared to the PC substrate. Furthermore, passive absorption of the aptamers onto the PEDOT:PSS was observed in experiments without the TC-tag on the aptamers and without UV exposure.
In the future the UV cross-linking method should be further optimised. Furthermore, the UV cross-linking method should be compared to known immobilisation methods such as amino functionalisation in order to investigate the applicability of the method. The UV cross-linking method should also be tested with the specific aptamer targets and not only hybridisation of the rcDNA, as the latter method is a simplified process compared to target recognition. This will also clarify whether or not the UV exposure damages the aptamers to a degree where target binding is reduced or impossible.

The electrical characterisation of the aptasensor and the system setup involved a circuit model and impedimetric characterisation of the multiplexer and the SD card chip, version 3.
A circuit model was made based on an impedance sweep of the SD card chip filled with a solution of diluted PBS. The model and the data showed good agreement and the model was accepted as a representation of the SD card chip.

The EIS characterisation of the multiplexer revealed that the multiplexer did not introduce any significant noise and it was concluded that the multiplexer could be used without noise concerns.
The EIS characterisation of different media salinity and pH values was performed in the SD card chip. The impedimetric measurements of the different salinity of the media behaved as expected with the greatest change present in the region representing the solution resistance. The pH measurements did not show any significant signal changes and it was concluded that the chip was stable in the measured pH range. Furthermore, the stability of the SD card chip was measured over a 2 week period with a continuous flow of diluted PBS. The measurements confirmed that the electrodes were not degraded or damaged by the flow. The largest change in impedance was observed between day 0 and day 1.

Future work should focus on integration of the different steps involved in the viral aptasensor development described in this thesis. The aptamers, once selected, targeting the enteric viruses should be immobilised onto the electrodes. The characterisation and development of the immobilisation method must be complete to ensure a good coverage and orientation of the aptamers on the electrodes. When the immobilisation of the aptamers onto PEDOT:PSS is a controlled process the efficiency of the target binding must be determined. Finally, impedimetric measurements and detection of spiked virus samples and environmental water samples should be done.
When the listed development aspects of the aptasensor work in coherence with each other an efficient aptasensor will be obtained for the detection of virus in water, in the future.

Bibliography

[1] W. D. Cubitt, "Caliciviruses and astroviruses". In: *Medical microbiology : a guide to microbial infections : pathogenesis, immunity, laboratory diagnosis and control*. Ed. by D. Greenwood et al. 17th ed. Churchill Livingstone/Elsevier, 2007. Chap. 56, pp. 565–572.

[2] A. Bosch et al., *New tools for the study and direct surveillance of viral pathogens in water*. Current opinion in biotechnology, 19 (3) **2008**, pp. 295–301.

[3] N. Cunliffe and O. Nakagomi, "Reoviruses". In: *Medical microbiology : a guide to microbial infections : pathogenesis, immunity, laboratory diagnosis and control*. Ed. by D. Greenwood et al. 17th ed. Churchill Livingstone/Elsevier, 2007. Chap. 54, pp. 545–552.

[4] S. M. Burns, "Picornaviruses". In: *Medical microbiology : a guide to microbial infections : pathogenesis, immunity, laboratory diagnosis and control*. Ed. by D. Greenwood et al. 17th ed. Churchill Livingstone/Elsevier, 2007. Chap. 48, pp. 476–488.

[5] M. I. Costafreda, A. Bosch, and R. M. Pintó, *Development, evaluation, and standardization of a real-time TaqMan reverse transcription-PCR assay for quantification of hepatitis A virus in clinical and shellfish samples*. Applied and Environmental Microbiology, 72 (6) **2006**, pp. 3846–3855.

[6] R. Girones et al., *Molecular detection of pathogens in water–the pros and cons of molecular techniques.* Water research, 44 (15) **2010**, pp. 4325–39.

[7] R. Beier et al., *Selection of a DNA aptamer against norovirus capsid protein VP1*. FEMS Microbiology Letters, 351 (2) **2014**, pp. 162–169.

[8] B. I. Escudero-Abarca et al., *Selection, Characterization and Application of Nucleic Acid Aptamers for the Capture and Detection of Human Norovirus Strains.* PloS one, 9 (9) **2014**, e106805.

[9] K. Kiilerich-Pedersen et al., *Polymer based biosensor for rapid electrochemical detection of virus infection of human cells*. Biosensors and Bioelectronics, 28 (1) **2011**, pp. 386–392.

[10] K. Kiilerich-Pedersen et al., *High sensitivity point-of-care device for direct virus diagnostics.* Biosensors & bioelectronics, 49 **2013**, pp. 374–9.

[11] J. Daprà et al., *Comparative study on aptamers as recognition elements for antibiotics in a label-free all-polymer biosensor*. Biosensors and Bioelectronics, 43 (1) **2013**, pp. 315–320.

[12] M. Dufva et al., *Characterization of an inexpensive, nontoxic, and highly sensitive microarray substrate*. BioTechniques, 37 (2) **2004**, pp. 286–296.

[13] M. Dufva et al., *Detection of mutations using microarrays of poly(C)10-poly(T)10 modified DNA probes immobilized on agarose films.* Analytical biochemistry, 352 (2) **2006**, pp. 188–97.

[14] Y. Sun et al., *Direct immobilization of DNA probes on non-modified plastics by UV irradiation and integration in microfluidic devices for rapid bioassay.* Analytical and Bioanalytical Chemistry, 402 (2) **2012**, pp. 741–748.

[15] P. Quinn et al., *Veterinary Microbiology and Microbial Disease, Section V, Introductory Virology*. October. Wiley-Blackwell, 2011, pp. 504–563.

[16] HealthCanada, *Guidelines for Canadian Drinking Water Quality: Guideline Technical Document - Enteric Viruses*. Tech. rep. Water, Air, Climate Change Bureau, Healthy Environments, and Consumer Safety Branch, Health Canada, Ottawa, Ontario, 2011, Catalogue No H129–6/2011E. `http://healthycanadians.gc.ca/publications/healthy-living-vie-saine/water-enteric-virus-enterique-eau/index-eng.php`.

[17] a. P. Wyn-Jones and J. Sellwood, *Enteric viruses in the aquatic environment.* Journal of applied microbiology, 91 (6) **2001**, pp. 945–62.

[18] M. R. Karim and M. W. LeChevallier, *Detection of noroviruses in water: Current status and future directions*. Journal of Water Supply: Research and Technology - AQUA, 53 (6) **2004**, pp. 359–380.

[19] K. Y. Green, "Caliciviridae : The Noroviruses". In: *Fields Virology, 5th Edition*. Ed. by D. M. Knipe and P. M. Howley. Vol. I. Lippincott Williams & Wilkins, 2007. Chap. 28, pp. 949–979.

[20] M. J. Hardy, G. Kuczera, and P. J. Coombes, *Norovirus protein structure and function*. FEMS Microbiology Letters, 253 (1) **2005**, pp. 1–8.

[21] C. E. Wobus et al., *Replication of Norovirus in cell culture reveals a tropism for dendritic cells and macrophages.* PLoS biology, 2 (12) **2004**, e432.

[22] E. F. Donaldson et al., *Viral shape-shifting: norovirus evasion of the human immune system.* Nature reviews. Microbiology, 8 (3) **2010**, pp. 231–241.

[23] C. H. Rambo and S. Pillai, "Pathogen Testing in Fresh Produce and Irrigation Water". In: *Rapid detection, characterization, and enumeration of foodborne pathogens.* Ed. by J. Hoorfar. ASM Press, 2011. Chap. 22, pp. 321–332.

[24] P. F. M. Teunis et al., *Norwalk Virus : How Infectious is It ?* Journal of Medical Virology, 80 (April) **2008**, pp. 1468–1476.

[25] M. K. Estes and A. Z. Kapikian, "Rotaviruses". In: *Fields Virology, 5th Edition.* Ed. by D. M. Knipe and P. M. Howley. Vol. II. Lippincott Williams & Wilkins, 2007. Chap. 53, pp. 1917–1974.

[26] J. Matthijnssens and M. Van Ranst, *Genotype constellation and evolution of group A rotaviruses infecting humans.* Current Opinion in Virology, 2 (4) **2012**, pp. 426–433.

[27] F. B. Hollinger and S. U. Emerson, "Hepatitis A Virus". In: *Fields Virology, 5th Edition.* Ed. by D. M. Knipe and P. M. Howley. Vol. I. Lippincott Williams & Wilkins, 2007. Chap. 27, pp. 911–947.

[28] T. Y. Bondarenko, V. A. Ternovoi, and S. V. Netesov, *Hepatitis A Virus: Structure - Functional Features of Genome, Molecular Diagnostics, and Cultivation.* Molecular Genetics, Microbiology and Virology, 28 (3) **2013**, pp. 99–109.

[29] X. Wang et al., *A sensor-adaptor mechanism for enterovirus uncoating from structures of EV71.* Nature structural & molecular biology, 19 (4) **2012**, pp. 424–9.

[30] X. Wang et al., *Hepatitis A virus and the origins of picornaviruses.* Nature, 517 (7532) **2015**, pp. 85–8.

[31] L. A. Ikner, C. P. Gerba, and K. R. Bright, *Concentration and recovery of viruses from water: a comprehensive review.* Food and environmental virology, 4 (2) **2012**, pp. 41–67.

[32] A. Z. Kapikian et al., *Visualization by immune electron microscopy of a 27-nm particle associated with acute infectious nonbacterial gastroenteritis.* Journal of virology, 10 (5) **1972**, pp. 1075–1081.

[33] T. Wandtke, J. Wozniak, and P. Kopinski, *Aptamers in Diagnostics and Treatment of Viral Infections.* Viruses, 7 (2) **2015**, pp. 751–780.

[34] C. Tuerk and L. Gold, *Systematic evolution of ligands by exponential enrichment: RNA ligands to bacteriophage T4 DNA polymerase.* Science (New York, N.Y.), 249 (4968) **1990**, pp. 505–510.

[35] a. D. Ellington and J. W. Szostak, *In vitro selection of RNA molecules that bind specific ligands.* Nature, 346 (6287) **1990**, pp. 818–22.

[36] S. Y. Toh et al., *Aptamers as a replacement for antibodies in enzyme-linked immunosorbent assay.* Biosensors and Bioelectronics, 64 **2015**, pp. 392–403.

[37] W. Zhou et al., *Aptamer-based biosensors for biomedical diagnostics.* The Analyst, 139 (11) **2014**, p. 2627.

[38] T. Wang, X. Cong, and M. Nilsen-hamilton, "In Vitro Selection of Aptamers". In: *Making and Using Antibodies.* Ed. by G. C. Howard and M. R. Kaser. 2nd ed. Taylor & Francis/CRC Press, 2014. Chap. 8, pp. 173–206.

[39] R. Stoltenburg, C. Reinemann, and B. Strehlitz, *SELEX-A (r)evolutionary method to generate high-affinity nucleic acid ligands.* Biomolecular Engineering, 24 (4) **2007**, pp. 381–403.

[40] A. D. Keefe, S. Pai, and A. Ellington, *Aptamers as therapeutics.* Nature Reviews Drug Discovery, 9 (7) **2010**, pp. 537–550.

[41] W. James, "Aptamers". In: *Encyclopedia of Analytical Chemistry.* 2000, pp. 4848–4871.

[42] E. N. Brody and L. Gold, *Aptamers as therapeutic and diagnostic agents.* Molecular Biotechnology, 74 (1) **2000**, pp. 5–13.

[43] T. Hianik and J. Wang, *Electrochemical aptasensors - recent achievements and perspectives.* Electroanalysis, 21 (11) **2009**, pp. 1223–1235.

[44] E. Torres-Chavolla and E. C. Alocilja, *Aptasensors for detection of microbial and viral pathogens.* Biosensors and Bioelectronics, 24 (11) **2009**, pp. 3175–3182.

[45] S. H. Jeon et al., *A DNA aptamer prevents influenza infection by blocking the receptor binding region of the viral hemagglutinin.* The Journal of biological chemistry, 279 (46) **2004**, pp. 48410–9.

[46] S. C. B. Gopinath et al., *An RNA aptamer that distinguishes between closely related human influenza viruses and inhibits haemagglutinin-mediated membrane fusion.* Journal of General Virology, 87 (3) **2006**, pp. 479–487.

[47] C. H. van den Kieboom et al., *Aptasensors for viral diagnostics.* 2015. `http://dx.doi.org/10.1016/j.trac.2015.05.012`.

[48] B. Michen and T. Graule, *Isoelectric points of viruses.* Journal of Applied Microbiology, 109 **2010**, pp. 388–397.

[49] A. Giamberardino et al., *Ultrasensitive norovirus detection using DNA aptasensor technology.* PloS one, 8 (11) **2013**, e79087.

[50] R. Yamamoto et al., *A novel RNA motif that binds efficiently and specifically to the Tat protein of HIV and inhibits the trans-activation by Tat of transcription in vitro and in vivo*. Genes to Cells, 5 (5) **2000**, pp. 371–388.

[51] J. Liu et al., *Development of HBsAg-binding aptamers that bind HepG2.2.15 cells via HBV surface antigen*. Virologica Sinica, 25 (1) **2010**, pp. 27–35.

[52] F. Chen et al., *CS-SELEX generates high-affinity ssDNA aptamers as molecular probes for hepatitis C virus envelope glycoprotein E2*. PLoS ONE, 4 (12) **2009**.

[53] I. Shiratori et al., *Selection of DNA aptamers that bind to influenza A viruses with high affinity and broad subtype specificity*. Biochemical and Biophysical Research Communications, 443 (1) **2014**, pp. 37–41.

[54] A. Nitsche et al., *One-step selection of Vaccinia virus-binding DNA aptamers by MonoLEX*. BMC biotechnology, 7 **2007**, p. 48.

[55] M. Labib et al., *Aptamer-based viability impedimetric sensor for viruses.* Analytical chemistry, 84 (4) **2012**, pp. 1813–6.

[56] S. J. Cho et al., *Novel system for detecting SARS coronavirus nucleocapsid protein using an ssDNA aptamer*. Journal of Bioscience and Bioengineering, 112 (6) **2011**, pp. 535–540.

[57] D. Grieshaber et al., *Electrochemical Biosensors - Sensor Principles and Architectures*. Sensors, 8 (3) **2008**, pp. 1400–1458.

[58] V. Perumal and U. Hashim, *Advances in biosensors: Principle, architecture and applications*. Journal of Applied Biomedicine, 12 (1) **2014**, pp. 1–15.

[59] L. D. Mello and L. T. Kubota, *Review of the use of biosensors as analytical tools in the food and drink industries*. Food Chemistry, 77 (2) **2002**, pp. 237–256.

[60] GamryInstruments, *Basics of Electrochemical Impedance Spectroscopy, Applicaiton Note*. `http://www.gamry.com/application-notes/EIS/basics-of-electrochemical-impedance-spectroscopy/` (visited on 09/01/2016).

[61] B.-Y. Chang and S.-M. Park, *Electrochemical impedance spectroscopy.* Annual review of analytical chemistry (Palo Alto, Calif.), 3 **2010**, pp. 207–29.

[62] A. Lasia, *Electrochemical Impedance Spectroscopy and its Applications*. Vol. 29. 3_4. Springer, 2014.

[63] R. Ravichandran et al., *Applications of conducting polymers and their issues in biomedical engineering.* Journal of the Royal Society, Interface / the Royal Society, 7 Suppl 5 (July) **2010**, S559–S579.

[64] F. Krebs, S. Gevorgyan, and J. Alstrup, *A roll-to-roll process to flexible polymer solar cells: model studies, manufacture and operational stability studies.* Journal of Materials Chemistry **2009**, pp. 5442–5451.

[65] U. Mitschke and P. Bäuerle, *The electroluminescence of organic materials.* Journal of Materials Chemistry, 10 (7) **2000**, pp. 1471–1507.

[66] M. Asplund, T. Nyberg, and O. Inganäs, *Electroactive polymers for neural interfaces.* Polymer Chemistry, 1 (9) **2010**, p. 1374.

[67] S. Kirchmeyer and K. Reuter, *Scientific importance, properties and growing applications of poly(3,4-ethylenedioxythiophene).* Journal of Materials Chemistry, 15 (21) **2005**, p. 2077.

[68] N. Rozlosnik, *New directions in medical biosensors employing poly(3,4-ethylenedioxy thiophene) derivative-based electrodes.* Analytical and Bioanalytical Chemistry, 395 (3) **2009**, pp. 637–645.

[69] K. A. Davis et al., *Use of a high affinity DNA ligand in flow cytometry.* Nucleic Acids Research, 24 (4) **1996**, pp. 702–706.

[70] K. Ikebukuro, C. Kiyohara, and K. Sode, *Electrochemical Detection of Protein Using a Double Aptamer Sandwich.* Analytical Letters, 37 (14) **2004**, pp. 2901–2909.

[71] K. Ikebukuro, C. Kiyohara, and K. Sode, *Novel electrochemical sensor system for protein using the aptamers in sandwich manner.* Biosensors and Bioelectronics, 20 (10 SPEC. ISS.) **2005**, pp. 2168–2172.

[72] A.-E. Radi et al., *Reusable Impedimetric Aptasensor complex formed between the aptamer and thrombin using.* Analytical Chemistry, 77 (19) **2005**, pp. 6320–6323.

[73] J. S. Swensen et al., *Continuous, real-time monitoring of cocaine in undiluted blood serum via a microfluidic, electrochemical aptamer-based sensor.* Journal of the American Chemical Society, 131 (12) **2009**, pp. 4262–4266.

[74] M. Arnold, J. T. Patton, and S. M. Mcdonald, *Culturing, Storage, and Quantification of Rotaviruses.* Current Protocols in Microbiology **2012**, pp. 15C.3.1–15C.3.24.

[75] C. F. Arias et al., *Trypsin activation pathway of rotavirus infectivity.* Journal of virology, 70 (9) **1996**, pp. 5832–5839.

[76] H. R. Pourianfar, A. Javadi, and L. Grollo, *A colorimetric-based accurate method for the determination of enterovirus 71 titer.* Indian Journal of Virology, 23 (3) **2012**, pp. 303–310.

[77] J. B. Pesavento et al., *Rotavirus proteins: structure and assembly.* Current topics in microbiology and immunology, 309 **2006**, pp. 189–219.

[78] Muthannan Andavar Ramakrishnan, *Determination of 50% endpoint titer using a simple formula*. World Journal of Virology, 5 (2) **2016**, pp. 85–86.

[79] ThermoFisher and Scientific, *Carbodiimide Crosslinker Chemistry*. 2016. `https://www.thermofisher.com/dk/en/home/life-science/protein-biology/protein-biology-learning-center/protein-biology-resource-library/pierce-protein-methods/carbodiimide-crosslinker-chemistry.html` (visited on 09/09/2016).

[80] ThermoFisher and Scientific, *Amine-Reactive Crosslinker Chemistry*. 2016. `https://www.thermofisher.com/uk/en/home/life-science/protein-biology/protein-biology-learning-center/protein-biology-resource-library/pierce-protein-methods/amine-reactive-crosslinker-chemistry.html` (visited on 09/09/2016).

[81] T. M. Herne and M. J. Tarlov, *Characterization of DNA probes immobilized on gold surfaces*. J Am Chem Soc, 119 (38) **1997**, pp. 8916–8920.

[82] S. D. Keighley et al., *Optimization of DNA immobilization on gold electrodes for label-free detection by electrochemical impedance spectroscopy*. Biosensors and Bioelectronics, 23 (8) **2008**, pp. 1291–1297.

[83] F. Fixe et al., *Functionalization of poly(methyl methacrylate) (PMMA) as a substrate for DNA microarrays*. Nucleic acids research, 32 (1) **2004**, e9.

[84] N. Kimura, *One-step immobilization of poly(dT)-modified DNA onto non-modified plastic substrates by UV irradiation for microarrays*. Biochemical and Biophysical Research Communications, 347 (2) **2006**, pp. 477–484.

[85] H. Gudnason et al., *An inexpensive and simple method for thermally stable immobilization of DNA on an unmodified glass surface: UV linking of poly(T)10-poly(C)10-tagged DNA probes*. BioTechniques, 45 (3) **2008**, pp. 261–71.

[86] S. Smiley, M. Derosa, and B. Blais, *Immobilization of DNA aptamers on polyester cloth for antigen detection by dot blot immunoenzymatic assay (aptablot)*. Journal of Nucleic Acids, 2013 **2013**, pp. 3–8.

[87] X. L. Pang et al., *Increased Detection of Rotavirus Using a Real Time Reverse Transcription-Polymerase Chain Reaction (RT-PCR) Assay in Stool Specimens from Children with Diarrhea*. Journal of Medical Virology, 72 (October 2003) **2004**, pp. 496–501.

[88] K. M. Song et al., *Aptasensor for ampicillin using gold nanoparticle based dual fluorescence-colorimetric methods*. Analytical and Bioanalytical Chemistry, 402 (6) **2012**, pp. 2153–2161.

— A —

Step by step protocols and material lists

All reagents are from Sigma-Aldrich, Denmark, unless otherwise stated.

A.1 Protocol for MA104 cell culture and rotavirus A propagation in MA104 cells

Material list

- MA104 cell line, kindly provided by Katharina Lahl, DTU Vet, National Veterinary Institute, Denmark
- Human rotavirus A strains from ATCC
  - Strain Wa, Serotype G1, genotype P8: Rotavirus A (ATCC VR-2018)
  - Strain DS-1, Serotype G2, genotype P4: Human rotavirus (ATCC VR-2550)
- T75 and T175 cell culture flasks with filter cap
- M199 medium (Thermo Fisher Scientific, cat. no. 11150-059)
- Penicillin-Streptomycin-Glutamine (Thermo Fisher Scientific, cat. no. 10378-016)
- Fetal bovine serum (FBS) (Biowest SAS, France)
- Trypsin-EDTA solution, 1x, sterile, sterile-filtered
- Dulbecco's Phosphate Buffered Saline, Modified, without calcium chloride and magnesium chloride (PBS)
- Trypsin from Porcine Pancreas, Type IX, lyophilized powder

- Incubator set to 37 °C, 5 % CO_2
- Centrifuge that fits 15 and 50 mL falcon tubes

All media and reagents for cell culture and virus propagation must be sterile and should be heated to 37 °C before usage.

Full cell culture medium: M199 medium supplemented with 5 mL/500mL Penicillin-Streptomycin-Glutamine and 5 % fetal bovine serum

Protocol for MA104 cell culture

1. Thaw a 1 mL MA104 cell line vial and mix cells with 10 mL full cell culture medium. Spin down cells and discard supernatant and resuspend cells in 10 mL full cell culture medium.
2. Seed cells in a T75 cell culture flask with a total of 40 mL full cell culture medium and place flask in the incubator at 37 °C, 5 % CO_2.
3. After 2-3 days, or when cells have reached 90 % confluence, the cells are split into 3 T75 flasks. Wash cells with 10-20 mL 0.025 % (w/v) trypsin-EDTA solution (diluted in PBS) to remove any FBS. Cells are released from the culture flask by briefly flushing cells with 10-20 mL 0.025 % (w/v) trypsin-EDTA solution (diluted in PBS), in order to have only a thin film of trypsin-EDTA covering the cells, and placed in the incubator for 3-5 min. When all cells have detached 10 mL full cell culture medium is added to the flask and divided into 3 new T75 flasks. Flasks are filled with full cell culture medium to a total of 40 mL in each flask.
4. Cell culture is continued as described in point 3. Cells from a 1 T75 flask can be split into 3-5 T75 flasks or passaged to 1 T175 flask when the cell culture is running.
5. Cells are frozen in 10 % DMSO in 1 mL stocks in cryo tubes. Keep cells at -140 °C.

Protocol for rotavirus propagation in MA104 cells

1. Culture MA104 cells in T175 flasks with full cell culture medium. When cells have reached 90 % confluence after approximately two days they are ready for inoculation. One T175 flask, cultured with same medium and conditions, without virus should be kept in parallel of the T175 flasks with virus propagation as a cell control.

2. A multiplicity of infection (MOI) of 0.1 - 1 is used to propagate the virus in the cell culture. In order to calculate the MOI one need to know the number of cells in the flask and the plaque forming unit (PFU) of the virus:

$$No.cells \cdot MOI = PFU\ needed$$

3. Aliquot the amount of virus needed into a 2 mL tube and add serum free medium (Medium 199 with 5 mL/500mL Penicillin-Streptomycin-Glutamine) to a final volume of 1 mL. Add 2.5 μL trypsin from Porcine Pancreas (2 mg/mL stock diluted in M199) to get a final concentration of 5 μg/mL. Incubate at 37°C for 15-20 min.

4. Wash cell culture with serum free medium to remove any serum.

5. Add 4 mL of serum free medium to the activated virus to a total volume of 5 mL. Add the activated virus to the flask and incubate at 37°C for 45-60 min.

6. Add 20 mL serum free medium with 0.5 μg/mL trypsin from Porcine Pancreas and allow the virus to propagate in the cells at 37°C 5 % CO_2.

7. The cytopathic effect (CPE) should be observed every day until complete cell death - usually 2-5 days post infection.

8. Freeze-thaw the flask 3 times. Freeze at -80 °C and thaw at room temperature. Collect the lysate in a clean tube.

9. Remove cell debris from the lysate by low speed centrifugation (3500 ×g) for 10 min. Collect the clarified cell supernatant in a clean tube.

10. Store the clarified cell supernatant containing the virus stock at -80 °C.

A.2 Protocol for semi-purification of RV on a sucrose cushion

Materials list

- Approximately 240 mL of clarified rotavirus cell lysate without large cell debris is thawed from -80 °C to room temperature in a hot water bath.
- Ultra-clear centrifuge tubes 25 x 89 mm (Beckman Coulter, Item No: 344058)
- SW 28 Ti Rotor (Beckman Coulter, Item No: 342204)
- Optima XE 90k Ultracentrifuge (Beckman Coulter)

- Scale with 3 digits precision
- TNC buffer (20 mM Tris-HCl, 100 mM NaCl, 1 mM $CaCl_2$ at pH 8.0, store at 4 C°)
- 35 % sucrose in TNC buffer
- Long needle, e.g. 0.90 x 70 mm, 20 G x 2 3/4
- 25 gauge needle and 10 mL syringe

Protocol

1. Fill 35 mL of rotavirus cell lysate in three Ultra-clear centrifuge tubes.
2. Gently underlay 2 mL of 35 % sucrose in TNC buffer with a long needle in each centrifuge tube and fill tube up 3 mm from top.
3. Balance the centrifuge tubes by weight down to an accuracy of the second decimal.
4. Centrifuge tubes at 100000 ×g at 4 °C for 2.0 h.
5. Discard supernatant and resuspend each pellet in 0.5 mL TNC buffer.
6. Pool the pellets and fill up with TNC buffer to a total volume of 4 mL.
7. Pass the virus suspension several times in a 25 gauge needle and syringe to ensure a homogenous suspension of virus particles.
8. Store the virus suspension at 4 °C.

A.3 Protocol for cesium chloride gradient purification of RV

Materials list

- Semi-purified RV prepared according to protocol A.2
- Cesium chloride, ReagentPlus®, 99.9 %
- SW 65 rotor (Beckman Coulter)
- Refractometer
- LB-70M Ultracentifuge (Beckman Coulter)
- Ultra-clear centrifuge tubes, 13 x 51 mm (Beckman Coulter, Item No: 344057)
- Light source, e.g. a light-emitting diode

- Slide-A-Lyzer Dialysis Cassettes, 10K MWCO, 0.5-3 mL Capacity(Thermo Fisher Scientific)
- SDS-PAGE reagents (from Bio-Rad, USA):
  - Mini-PROTEAN Tetra Vertical Electrophoresis Cell and voltage supply
  - Any kD Mini-PROTEAN TGX Precast Protein Gels, 15-well, 15 μl, cat no.4569036
  - 2x Laemmli Sample Buffer, cat no. 1610737
  - 10x Tris/Glycine/SDS, cat no. 1610732
  - Precision Plus Protein All Blue Prestained Protein Standards, cat no. 161-0373, control: 350001702
- Pierce Silver Stain Kit (Thermo Fisher Scientific)
- Rack heater, e.g. Eppendorf Thermomixer R
- Flatbed scanner

Protocol

1. Dissolve 2 g CsCl in the 4 mL semi-purified RV sample to obtain a density of 1.37 g/cm^3. A refractive index of 1.3684 equals a density of 1.37 g/cm^3 at 25 °C, see table A.1 (Check with a refractometer).

2. Fill one Ultra-clear centrifuge tube with the virus suspension and balance the rotor with centrifuge tubes with TNC buffer with CsCl, density 1.37 g/cm^3.

3. Balance the centrifuge tubes by weight down to an accuracy of the second decimal.

4. Centrifuge tubes at 110000 ×g (35500 RPM) at 12 °C for 18 h.

5. Remove the rotor from the centrifuge without shaking or in other way disturbing the gradient.

6. Place the centrifuge tube with the virus suspension over an inverted light source and inspect the gradient. Two bands should be visible as seen in figure A.1. The upper band is the TLP RV and the lower band the DLP RV.

7. Gently unload the gradient from the bottom of the tube by puncturing a small hole in the bottom. Unload fractions of approximately 500 μL or the volume needed to get fractions with TLP and DLP.

8. Analyse the fractions on a SDS-PAGE gel to verify the protein content of the TLP and the DLP fractions. See table 3.1 for mass and location of the RV structural proteins. See figure A.2 for an example of the silver stained gel with the structural proteins identified.

a) Mix 5 μL 2 x Laemmli Sample Buffer with 5 μL virus sample and denature sample on a rack heater for 5 min at 90-100 °C. Spin down sample.

b) Prepare 1 x Tris/Glycine/SDS buffer. Remove protective film and comb from the Any kD Mini-PROTEAN TGX Precast Protein Gel and mount this into the electrophoresis cell. Add the buffer to the buffer chamber.

c) Load 10 μL 10 x diluted Precision Plus Protein All Blue Prestained Protein Standards (marker) to the first well and add 10 μL 50 x diluted marker to the last well. Load 10 μL denatured sample to the wells.

d) Run gel at 200 V for approximately 30 min until the dye reaches the reference line.

e) Disassemble the gel cassette and stain the gel with Pierce Silver Stain Kit according to manufactures manual.

f) Scan the gel in a flatbed scanner and calculate the relation (assume an exponential relation) between the position of the marker and the mass (in kDa) of the marker as done in figure A.3 . Use the relation to identify the structural proteins of the RV.

9. Dialyse the interesting fractions containing the TLP (and DLP) RV particles in TNC buffer against CsCl for 24 h with 3 buffer changes, after approximately 2 h, 8h and 14 h.

Table A.1: *Refractive index (RI) and density (ρ) of CsCl at 25 °C. The density and refractive index is linear dependent by: $RI = 0.0946\rho + 1.2388$*

Density [g/cm^3]	Refractive index
1.35	1.3665
1.36	1.3675
1.37	1.3684
1.38	1.3694
1.39	1.3702

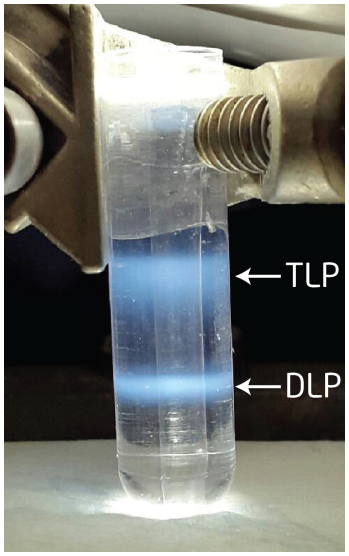

Figure A.1: *Simian RV purified on a CsCl gradient. The two bands seen in the tube is the separated TLP and DLP RV particles. The RV particles have been separated due to their difference in density.*

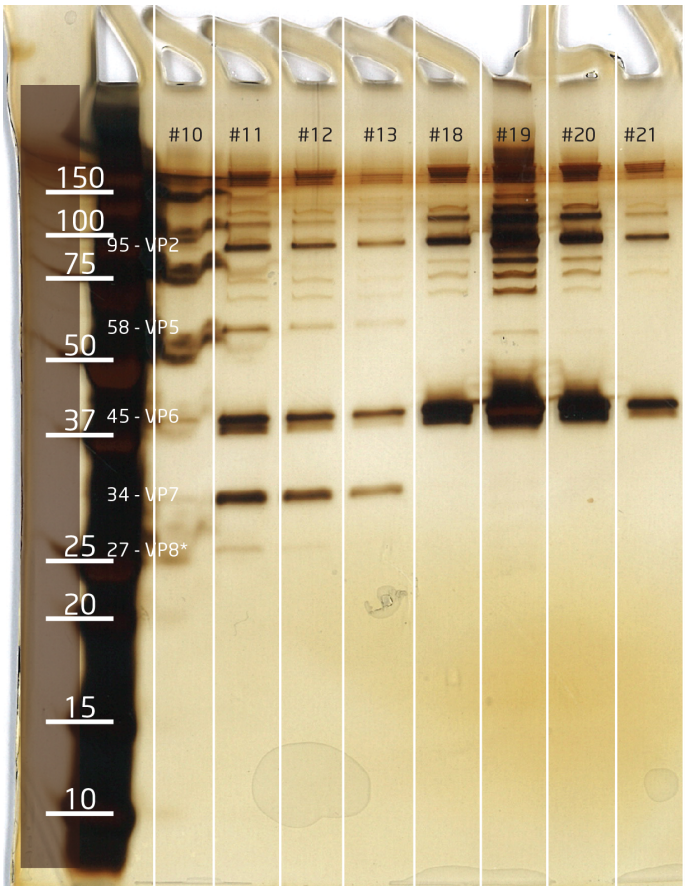

Figure A.2: *SDS-PAGE of simian rotavirus purified on CsCl gradient (from figureA.1). The protein bands are stained with silver stain. Samples* $\#10-13$ *and* $\#18-21$ *are fractions from the CsCl gradient with TLP and DLP, respectively. The samples were dialysed before performing the SDS-PAGE. VP8* (27 kDa), VP7 (34 kDa) and VP5* (58 kDa) are proteins specific to TLP virus particles (see table 3.1) and these protein bands are only visible in samples* $\#10-13$ *as expected. Marker is in kDa. The protein positions are calculated from the position of the marker.*

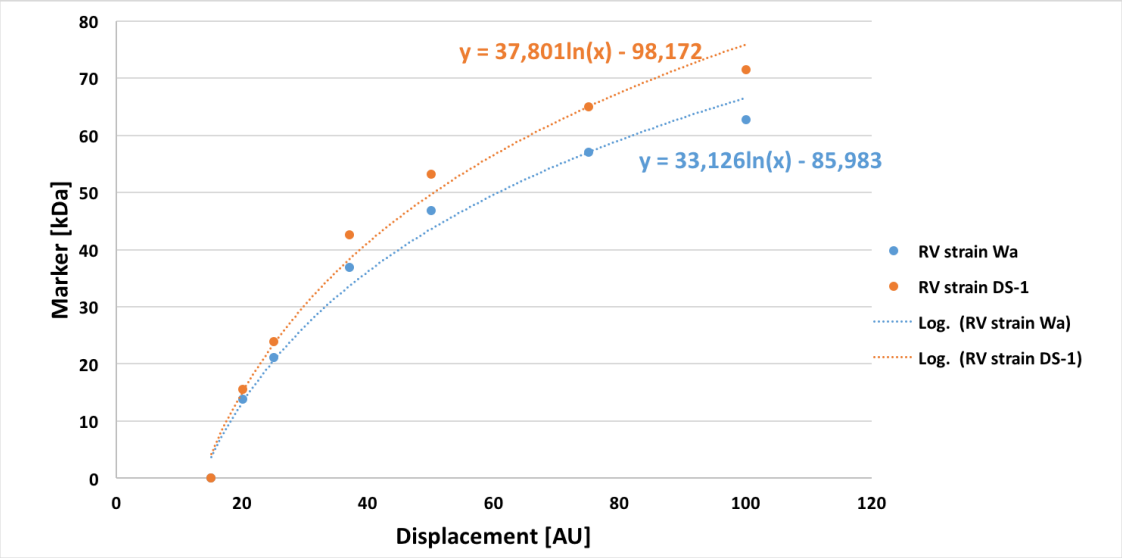

Figure A.3: *Plot of the correlation between marker proteins mass (in kDa) and marker displacement of human RV strains Wa and DS-1. The displacement is measured using the difference between the position of the 15 kDa marker and the remaining markers in Adobe Illustrator. The displacement is given in arbitrary units (AU). The position of the structural proteins is calculated from the logarithmic fit and draw in the SDS-PAGE gel images of figure 3.6a and figure 3.6b*

A.4 Protocol for rotavirus biotinylation with BPH linker and subsequent coupling to magnetic beads

Materials list

- TLP Rotavirus particles purified on a CsCl gradient prepared according to protocol A.3
- BPH linker: EZ-Link Hydrazide-PEG4-Biotin (Thermo Fisher Scientific)
- Dimethylsulfoxid (DMSO)
- 0.1 M MES-buffer supplemented with 1 mM $CaCl_2$ (to stabilise RV) (pH 4.7-5.5) (Thermo Fisher Scientific)
- 1-Ethyl-3-(3-dimethylaminopropyl)carbodiimide (EDC)
- Streptavidin-coated magnetic beads: Dynabeads M-280 Streptavidin (Thermo Fisher Scientific)
- Slide-A-Lyser Dialysis Cassette 10k MWCO, 0.5-3 mL Capacity (Thermo Fisher Scientific)
- 1 mL syringes
- 19-gauge 1.5 inch needles
- Magnetic separation rack
- TNC buffer for rotavirus (20 mM Tris-HCl, 100 mM NaCl, 1 mM $CaCl_2$ at pH 8.0)

Protocol

Prepare a 250 mM linker stock solution by dissolving the BPH linker (mw: 505.26 g/mol) in DMSO. Keep the stock at -20°C. The EDC must not be dissolved before immediate usage, thus weigh off appropriate amount to make a 100 mg/mL EDC in MES buffer solution.

1. Dilute virus samples in 0.1 M MES-buffer supplemented with 1 mM $CaCl_2$ to a final volume of 1 mL. Use at least a dilution of 1:10 virus to MES buffer.

2. Dilute the BPH linker stock solution in a ration of 1:5 in MES buffer and add 25 μL to each virus suspension.

3. Dissolve the EDC to a concentration of 100 mg/mL EDC in MES buffer and add 12.5 μL to each virus suspension.

4. Incubate for 2 h at room temperature with continuous mixing.

5. Stop reaction by dialysing samples against the BPH linker with Slide-A-Lyser Dialysis Cassettes, 10k MWCO, at 4 °C. Load samples into the dialysis chamber with a 1 mL syringe and 19-gauge 1.5 inch needle. Change the dialysis buffer (0.1 M MES-buffer with 1 mM $CaCl_2$) after 2 h, 4 h and dialyse over night.

6. Wash 25 μL Dynabeads M-280 Streptavidin, for each virus suspension, with 1 mL TNC buffer on a magnetic separator rack and discard supernatant. Resuspend beads in 25 μL TNC buffer.

7. Add the dialysed biotinylated virus samples to the magnetic beads in separate tubes.

8. Incubate virus particles with the magnetic beads for 30 min at room temperature with continuous mixing.

9. Separate the magnetic beads from the supernatant on a magnetic rack separator. Keep the supernatant for PCR analysis to analyse the ratio of unbound to bound virus particles.

10. Wash the virus bound magnetic beads with TNC buffer three times to remove any unbound virus particles and resuspend in the original volume. Store at 4 °C.

A.5 Protocol for rotavirus biotinylation with BNHS linker and subsequent coupling to magnetic beads

Materials list

- TLP Rotavirus particles purified on a CsCl gradient prepared according to protocol A.3
- Dimethylsulfoxid (DMSO)
- BNHS: (+)-Biotin N-hydroxysuccinimide ester
- 0.1 M $NaHCO_3$, pH 8.2 with 1 mM $CaCl_2$
- Slide-A-Lyser Dialysis Cassettes, 10k MWCO (Thermo Fisher Scientific)
- 1 mL syringes
- 19-gauge 1.5 inch needles
- Streptavidin-coated magnetic beads: Dynabeads M-280 Streptavidin
- Magnetic separation rack

- TNC buffer for rotavirus (20 mM Tris-HCl, 100 mM NaCl, 1 mM CaCl2 at pH 8.0)

Protocol

1. Dilute virus samples in 0.1 M $NaHCO_3$, pH 8.2 with 1 mM $CaCl_2$ to a final volume of 1 mL.Use at least a dilution of 1:10 virus to buffer.
2. Dilute BNSH in DMSO immediately before use, 10 mg/mL, and add 0.1 mL to each virus suspension.
3. Incubate for 2 h at room temperature with mixing
4. Stop reaction by dialysing samples against the BNSH linker with Slide-A-Lyser Dialysis Cassettes, 10k MWCO, at 4 °C. Load samples into the dialysis chamber with a 1 mL syringe and 19-gauge 1.5 inch needle. Change the dialysis buffer (0.1 M $NaHCO_3$, pH 8.2 with 1 mM $CaCl_2$) after 2 h, 4 h and dialyse over night.
5. Wash 25 μL Dynabeads M-280 Streptavidin, for each virus suspension, with 1 mL TNC buffer on a magnetic separator rack and discard supernatant. Resuspend beads in 25 μL TNC buffer.
6. Add the dialysed biotinylated virus samples to the magnetic beads in separate tubes.
7. Incubate virus particles with the magnetic beads for 30 min at room temperature with continuous mixing.
8. Separate the magnetic beads from the supernatant on a magnetic rack separator. Keep the supernatant for PCR analysis to analyse the ratio of unbound virus particles.
9. Wash the virus bound magnetic beads with TNC buffer three times to remove any unbound virus particles and resuspend in the original volume. Store at 4 °C.

A.6 Protocol for analysis of RV by real-time RT-PCR

Materials list

- RV samples - 140 μL/RNA extraction
- QIAamp Viral RNA Mini Kit (Qiagen, Germany)
- 99 % ethanol
- For real.time RT-PCR:
  - AgPaht-ID One-Step RT-PCR Reagents (Thermo Fisher Scientific)
  - Nuclease-free Water
  - Forward primer (50 μM), nucleotide sequence (5'-3'): ACCATCTACACATGACCCTC [87]
  - Reverse primer(50 μM), nucleotide sequence (5'-3'): ACCATCTACACATGACCCTC [87]
  - TaqMan probe(50 μM), nucleotide sequence (5'-3'): ATGAGCACAATAGTTAAAAGCTAACACTGTCAA [87]
  - Positive rotavirus RNA control
- PCR cycler: Rotor-Gene 6000 (Qiagen, Germany)

Protocol

1. Extract RNA from the virus samples with the QIAamp Viral RNA Mini Kit according to the manufacturers protocol. Store RNA at -20°C.

2. Mix reagents for real time RT-PCR, keep mix at 4 °C at all times. Each sample is performed in duplicates to get an average Ct value for each sample. RT-PCR Mastermix for one reaction of 15 μL (13 μL mastermix + 2 μL RNA template):

4.624 μL	Nuclease-free Water
7.5 μL	2x RT-PCR Buffer
0.12 μL	Forward primer (50 μM)
0.12 μL	Reverse primer (50 μM)
0.036 μL	TaqMan probe (50 μM)
0.6 μL	25x RT-PCR Enzyme mix
13 μL in total	1 x Mastermix

3. Add 13 μL mastermix to each PCR tube and add 2 μL RNA template. Add 2 μL nuclease-freewater (use same water as the mastermix) to the negative controls and 2 μL positive control (rotavirus RNA) to the positive controls. Keep the mix at 4 °C at all times.

4. On a Rotorgene 6000 the real-time RT-PCR is performed accordingly:

Reverse transcription	45 °C	10 min
RT inactivation and poly activation	95 °C	10 min
48 cycles	95 °C 60 °C	15 seconds 45 seconds Plate read

5. Analyse results (Ct threshold = 0.01, Ct < 33 positive, Ct > 33 suspect positive)

A.7 Protocol for hepatitis A virus (HAV) inactivation

Material list

- HAV sample, genotype 1B, kept at -80 ° (cultured at the Environmental Virological Laboratory, Tor Vergata University, Rome, Italy)
- Formaldehyde, for molecular biology, 36.5-38% in H_2O
- Slide-A-Lyser Dialysis Cassette 10k MWCO, 0.5-3 mL Capacity (Thermo Fisher Scientific)
- 1 mL syringes
- 19-gauge 1.5 inch needles
- Phosphate buffered saline (PBS)

Protocol

1. Thaw the HAV sample.

2. Dilute formaldehyde in HAV samples to a final concentration of 1:2000 formaldehyde to HAV sample. Take into account that the formaldehyde solution is already diluted.

3. Incubate the formaldehyde with the HAV sample for 8 days at 4 °C.

4. Remove the formaldehyde from the HAV sample by dialysis using the Slide-A-Lyser Dialysis Cassettes, 10k MWCO, at 4 °C. Load samples with a 1 mL syringe and 19-gauge 1.5 inch needle. Change the dialysis buffer (PBS) after 2 h, 4 h and dialyse over night.

5. Store the inactivated HAV sample at 4 °C for further work.

A.8 Protocol for hepatitis A virus biotinylation with BPH linker and subsequent coupling to magnetic beads

Materials list

- Inactivated HAV particles prepared according to protocol A.7
- BPH linker: EZ-Link Hydrazide-PEG4-Biotin (Thermo Fisher Scientific)
- Dimethylsulfoxid (DMSO)
- 0.2 M MES-buffer (pH 4.7-5.5) (Thermo Fisher Scientific)
- 0.1 M MES-buffer (pH 4.7-5.5) (Thermo Fisher Scientific)
- 1-Ethyl-3-(3-dimethylaminopropyl)carbodiimid (EDC)
- Streptavidin-coated magnetic beads: Dynabeads M-280 Streptavidin (Thermo Fisher Scientific)
- Slide-A-Lyser Dialysis Cassette 10k MWCO, 0.5-3 mL Capacity (Thermo Fisher Scientific)
- 1 mL syringes
- 19-gauge 1.5 inch needles
- Magnetic separation rack
- Phosphate buffered saline (PBS)

Protocol

Prepare a 250 mM linker stock solution by dissolving the BPH linker (mw: 505.26 g/mol) in DMSO. Keep the stock at -20°C. The EDC must not be dissolved before immediate usage, thus weigh off appropriate amount to make a 100 mg/mL EDC in 0.1 MMES buffer solution.

1. Dilute virus samples 1:2 in 0.2 M MES-buffer to a final volume of 1 mL.
2. Dilute the BPH linker stock solution in a ration of 1:5 in MES buffer and add 25 μL to each virus suspension.
3. Dissolve the EDC to a concentration of 100 mg/mL EDC in MES buffer and add 12.5 μL to each virus suspension.
4. Incubate for 2 h at room temperature with continuous mixing.
5. Stop reaction by dialysing samples against the BPH linker with Slide-A-Lyser Dialysis Cassettes, 10k MWCO, at 4 °C. Load samples with a 1 mL syringe and 19-gauge 1.5 inch needle. Change the dialysis buffer (PBS) after 2 h, 4 h and dialyse over night.

6. Wash 25 μL Dynabeads M-280 Streptavidin per mL biotinylated HAV samlpe with 1 mL PBS buffer on a magnetic separator rack and discard supernatant. Resuspend beads in 25 μL PBS buffer.

7. Add the dialysed biotinylated virus samples to the magnetic beads.

8. Incubate virus particles with the magnetic beads for 30 min at room temperature with continuous mixing.

9. Separate the magnetic beads from the supernatant on a magnetic rack separator. Keep the supernatant for PCR analysis to analyse the ratio of unbound virus particles.

10. Wash the virus bound magnetic beads with PBS buffer three times to remove any unbound virus particles and resuspend in the original volume. Store at 4 °C.

A.9 Protocol for real-time PCR analysis of hepatitis A virus samples

Materials list

- QIAamp Viral RNA Mini Kit (Qiagen, Germany)
- 99 % ethanol
- For reverse transcriptase:
  - RNA template samples
  - SuperScript III First-Strand Synthesis System (Invitrogen, Thermo Fisher Scientific)
  - Primer 4/4 (AGTCACACCTCTCCAGGAAAACTT)
  - PCR tubes
  - 1.5 mL Eppendorf tube
  - Thermal cycler for conventional PCR
- For real-time PCR
  - QIAGEN OneStep RT-PCR Kit (Qiagen)
  - Rnase free water
  - Sybr green, diluted 1:16 in sterile nuclease free water
  - Primer 1/4 (TTTGTCTTTTAGTTGTTATTTGTCTGT)
  - Primer 4/4 (AGTCACACCTCTCCAGGAAAACTT)
  - Thermal cycler for real-time PCR

Protocol

1. Extract RNA from the virus samples with the QIAamp Viral RNA Mini Kit according to the manufacturers protocol. Store RNA at -20°C.

2. Mix the reagents for reverse transcriptase. Add the following reagents directly to each PCR tube, keep on ice:

1 μL	Primer 4/4
1 μL	10 mM dNTPs
2 μL	Total

   Mix the remaining reagents for the reverse transcription in an Eppendorf tube, keep it on ice. Mix for one reaction:

2 μL	10x RT Buffer
4 μL	25 mM $MgCl_2$
2 μL	0.1 M DTT
1 μL	RNaseOUT
1 μL	SuperScript III RT
10 μL	Total

3. Reverse transcription: Add 8 μL RNA template sample to each of the PCR tubes. Incubate on a thermal cycler at 42 °C for 2 minutes. Cool on ice for minimum 1 minute. Add 10 μL of the everse transcription PCR mix from the Eppendorf tube to each PCR tubes. Incubate as follows:

95 °C	5 min
42 °C	1 h
95 °C	5 min

4. Add 1 μL RNase H to each tube and incubate at 37 °C for 20 minutes. Store cDNA at -20 °C.

5. Mix reagents for real-time PCR. Perform duplicates of each sample. One reaction consists of 23 μL master mix and 2 μL cDNA template. Master mix:

12.5 μL	Nuclease-free water
5 μL	5 x Qiagen OneStep RT-PCR buffer
1 μL	dNTP mix, 10 mM
1.5 μL	Primer 1/4, 10 μM
1.5 μL	Primer 4/4, 10 μM
0.5 μL	Sybr green, diluted 1:16 in nuclease-free water from stock (1:100)
1 μL	Qiagen OneStep RT-PCR Enzyme mix
23 μL	Total

Add 2 μL cDNA template to each tube. Make 2 negative controls with nuclease-free water

6. Real-time PCR is done as follows:

95 °C	3 min
95 °C	30 s
45 °C	10 s
70 °C	60 s

7. Analyse results (Ct threshold = 0.01, Ct $<$ 33 positive, Ct $>$ 33 suspect positive)

A.10 Protocol and materials for UV immobilisation of aptamers on chips by robotic spotting and subsequent hybridising with rcDNA

Material list

- PEDOT:PSS screen printed PC chips, SD card chip, version 3
- Aptamers with a Poly(T)10-Poly(C)10 tag and spacer
- Autodrop Professional Positioning System, Microdrop Technologies GmbH, Germany
- Autodrop pipette, AD-K-901, type 40, Microdrop Technologies GmbH, Germany
- Spotting buffer (See specific experiment)
- Stratalinker 2400, Stratagene, CA, USA
- Wash buffer (See specific experiment)
- rcDNA

- PerfectHyb Plus Hybridization Buffer
- Glas slides
- Confocal microscope (Zeiss, Germany)

Protocol

1. Spotting and UV cross-linking of aptamers onto chips:

    a) Diluted aptamers to the final concentration in the spotting buffer. Approximately 200 μL of each aptamer solution is needed for spotting.

    b) Mount an Autodrop pipette in the Autodrop Professional Positioning System and fill it with the aptamer solution. Setup the system for spotting micro arrays according to the spotting layout in the specific experiment.

    c) In the Autodrop Professional Positioning software load a spotting file (.mvg) in the image control menu. Spotting distance from pipette to substrate should be 1-1.5 mm. A horizontal spot distance of 0.15-0.2 mm should be used for spotting. Place a chip on the stage and align the fiducials. Spot the micro array.

    d) The spotted array on the chip should be dry before proceeding.

    e) Cross-link aptamers on polymer substrates by UV exposure with a Stratalinker 2400, 254 nm. Time depends on the specific experiment.

    f) First washing step: Wash chips with washing buffer according to the specific experiment. Dry chips with compressed air.

2. Hybridisation with rcDNA

    a) Dilute rcDNA to a final concentration of 500 nM in PerfectHyb Plus Hybridization Buffer and place a drop on each chip in the area where the aptamers were spotted. Cover with a glass slide.

    b) Incubate for 1 hour at 37 °C, protect the fluorophores from bright light.

    c) Second washing step: Wash chips in wash buffer according to the specific experiment. Dry chips with compressed air. Keep chips in the dark.

    d) Inspect the fluorescence by a confocal microscope(see figure A.4 or A.5 for examples).

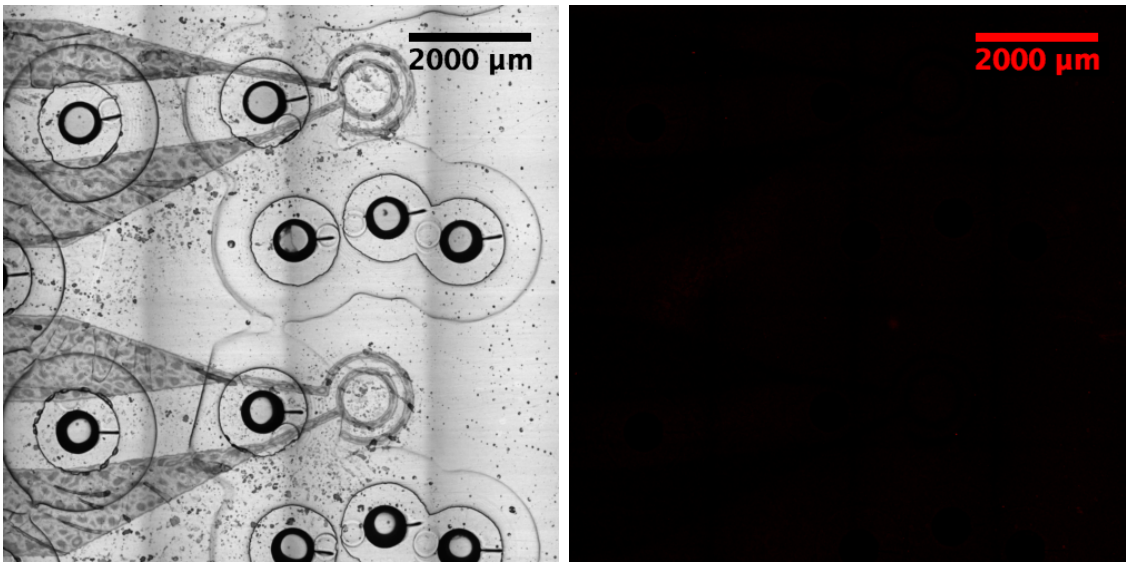

(a) *0.5 µM, 1 min, bright-field* **(b)** *0.5 µM, 1 min, flurescence*

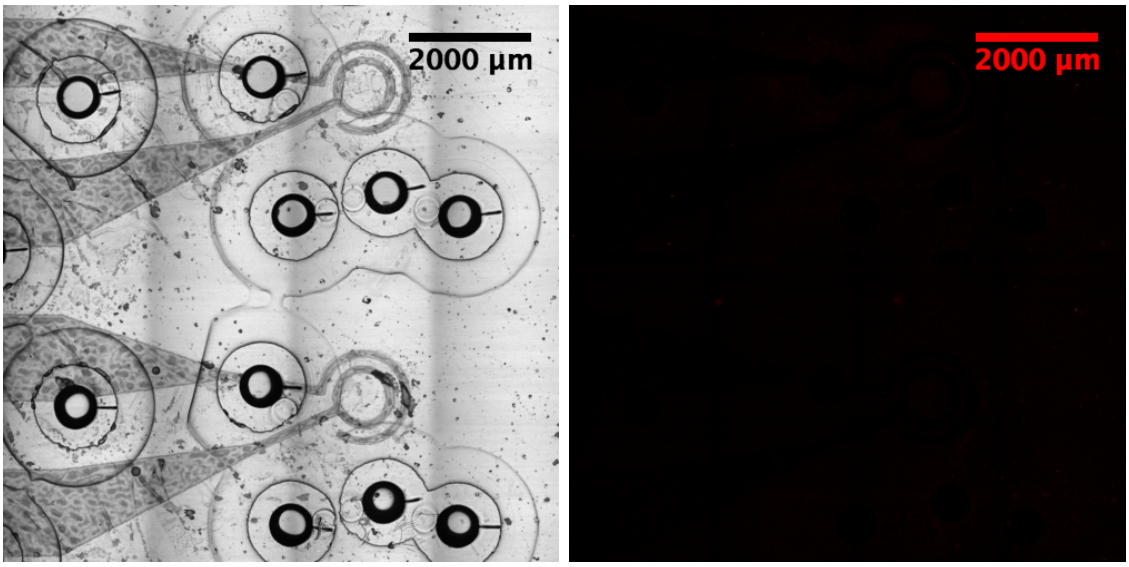

(c) *0.5 µM, 5 min, bright-field* **(d)** *0.5 µM, 5 min, flurescence*

Figure A.4: *Bright-field and fluorescent images of spotted aptamers after rcDNA hybridisation, 0.5 µM, 1 or 5 min UV exposure*

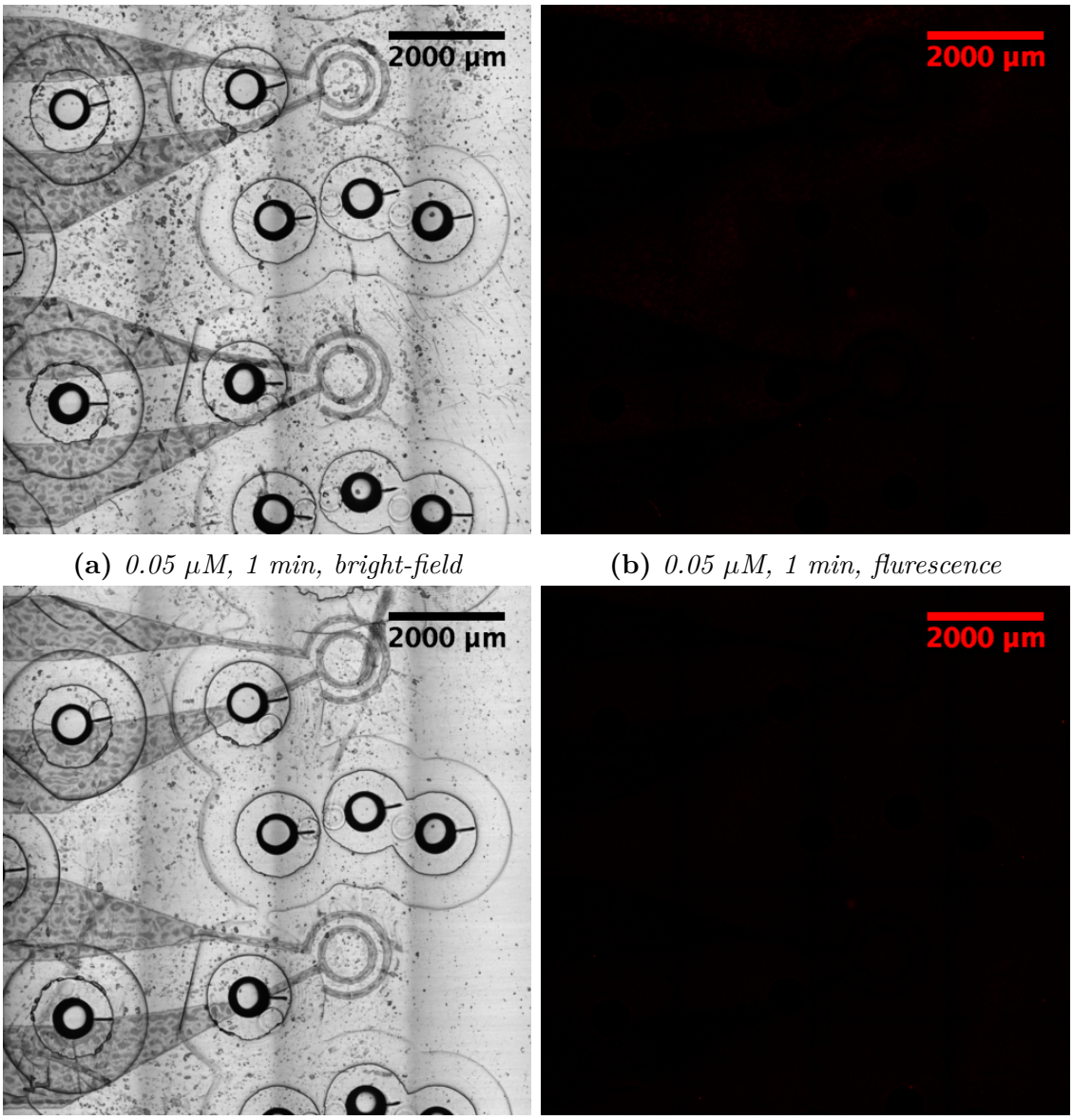

(a) *0.05 µM, 1 min, bright-field*

(b) *0.05 µM, 1 min, flurescence*

(c) *0.05 µM, 5 min, bright-field*

(d) *0.05 µM, 5 min, flurescence*

Figure A.5: *Bright-field and fluorescent images of spotted aptamers after rcDNA hybridisation, 0.05 µM, 1 or 5 min UV exposure*

A.11 Protocol for ELASA based hybridisation assay for examining the UV immobilisation of aptamers on polymer substrates

Material list

- Aptamers, at least two different sequences (e.g. VP1T (see appendix B.2) and SMV25 (see appendix B.3))
- rcDNA to aptamers with a 5' end biotin tag (e.g. rcVP1T or rcSMV25)
- Aptamer dilution buffer: 0.15 M Sodium phosphate buffer with 0.004 % triton X
- 96 well plates
- Stratalinker 2400, Stratagene, CA, USA
- HRP-Conjugate Streptavidin (Thermo Fisher Scientific)
- Hybridisation buffer: PerfectHyb Plus Hybridization Buffer
- Tris buffered saline (TBS): 50 mM Tris Base, 140 mM NaCl, 36 mM HCl, pH between 7.2-7.8
- Wash buffer: TBS with 0.05 % Tween 20, pH 8.0
- Blocking solution: TBS with 1 % bovine serum albumin (BSA)
- Conjugate dilution buffer: TBS with 1 % BSA, 0.05 % Tween 20, pH 8.0
- Stop solution: 2 M H_2SO_4
- TMB: substrate: 1-step Ultra TMB-ELISA (Thermo Fisher Scientific)
- Plate reader: Victor3 from Perkin Elmer

Equilibrate TMB substrate to room temperature before usage.

Protocol

1. Design a plate layout for the experiment, see figure A.6 for an example of plate layout.

2. Dilute aptamers in Aptamer dilution buffer according to the concentrations needed in the plate layout. Dispense 5 μL aptamer solution into each well according to plate layout. Dispense 5 μL Aptamer dilution buffer in the Buffer Control wells. Leave wells to dry in a oven heated to 60 ° C.

3. Illuminate well plates to UV light with the Stratalinker 2400 for the desired amount of time.

4. Wash well plates 3 times with Wash buffer, 250 μL/well.

5. Block wells with Blocking solution, 250 μL/well, for 30 min at room temperature

6. Wash well plates 3 times with Wash buffer, 250 μL/well.

7. Dilute rcDNA in Hybridisation buffer according to the concentrations in the plate layout. Add 30 μL/well, incubate for 60 min at 37 ° C.

8. Wash well plates 3 times with Wash buffer, 250 μL/well.

9. Dilute HRP-Conjugate Streptavidin in Conjugate dilution buffer (1:10000). Add 50 μL/well, incubate for 60 min at room temperature.

10. Wash well plates 5 times with Wash buffer, 250 μL/well.

11. Add TMB substrate to all wells, 100 μL/well, incubate for 15 min at room temperature.

12. Stop reaction by adding 100 μL/well of stop solution.

13. Measure absorbance at 450 nm, 0.1 s, with the plate reader.

14. Process and analyse results by calculating the average background signal (signal of the Buffer Control wells). Subtract the background signal from all wells. Colour the wells according to the background signal value (no colour) and the highest absorbance value (dark colour).

				Immobilized aptamer											
				VP1T			SMV25			Blank		Not used			
				1 µM	100 nM	10 nM	1 µM	100 nM	10 nM	Buffer Control	Buffer Control				
				1	2	3	4	5	6	7	8	9	10	11	12
Compl aptamer	cVP1T	1 µM	A												
		100 nM	B												
		10 nM	C												
		1 nM	D												
	cSMV25	1 µM	E												
		100 nM	F												
		10 nM	G												
		1 nM	H												

Figure A.6: *Example of plate layout for UV ELISA*

A.11.1 OD data values of ELASA based hybridisation assay for examining the UV immobilisation of aptamers on polymer substrates

The data presented in this section is data acquired by the plate reader of the ELASA experiments. The background of the controls have been subtracted the data values of each plate. The background value is listed below each plate. Each plate was coloured individually. The plate were coloured by the "New Formatting Roule", 2-Color scale, minimum: background value (white) and maximum: Highest Value (dark orange) in Microsoft Excel 2016. The numbers in the tables are the optical density (OD) measured at 450 nm, 0.1 s.

Plate 1	Dry	UV							
		VP1T			SMV25				
		1 µM	100 nM	10 nM	1 µM	100 nM	10 nM	blank	blank
cVP1	1µM	1,962	1,725	0,728	-0,141	0,766	-0,161	0,129	-0,177
	100 nM	1,947	1,422	0,369	-0,059	-0,187	-0,201	-0,188	0,422
	10 nM	1,915	1,402	0,225	-0,168	-0,202	-0,201	0,298	-0,147
	1 nM	0,940	0,661	0,091	1,347	-0,187	-0,189	0,375	-0,200
cSMV25	1µM	-0,188	-0,188	-0,198	1,903	1,095	0,025	-0,184	-0,192
	100 nM	-0,110	-0,182	-0,198	1,930	1,090	0,025	0,319	-0,197
	10 nM	-0,151	1,378	-0,192	1,907	1,119	0,149	0,269	-0,138
	1 nM	-0,149	-0,172	-0,197	1,344	0,697	-0,036	-0,191	-0,193
		Subtracted average background - blank				0,244			

Plate 2	Dry	No UV							
		VP1T			SMV25				
		1 µM	100 nM	10 nM	1 µM	100 nM	10 nM	blank	blank
cVP1	1µM	1,783	0,793	1,228	0,034	0,009	0,006	0,028	0,019
	100 nM	1,960	0,634	0,126	0,033	-0,007	-0,007	-0,009	0,000
	10 nM	2,025	0,679	0,148	-0,008	-0,006	-0,005	-0,010	0,000
	1 nM	1,359	0,616	0,110	-0,005	-0,005	0,009	-0,005	-0,006
cSMV25	1µM	0,029	0,000	-0,004	1,188	0,344	0,058	-0,004	-0,001
	100 nM	0,022	0,020	-0,001	1,346	0,393	0,060	-0,006	-0,002
	10 nM	0,002	0,012	0,003	0,867	0,314	0,031	-0,005	-0,005
	1 nM	-0,003	0,019	0,005	1,280	0,295	0,049	0,007	0,002
		Subtracted average background - blank				0,052			

Plate 3	liquid	UV							
		VP1T			SMV25				
		1 µM	100 nM	10 nM	1 µM	100 nM	10 nM	blank	blank
cVP1	1µM	0,127	-0,046	0,590	0,837	0,945	-0,069	-0,052	-0,072
	100 nM	-0,019	0,023	0,062	0,063	0,001	-0,077	-0,078	-0,080
	10 nM	-0,055	-0,072	0,602	-0,062	-0,048	-0,075	-0,064	-0,050
	1 nM	-0,045	-0,068	0,010	-0,047	-0,069	-0,077	-0,032	0,425
cSMV25	1µM	-0,049	-0,081	0,285	0,399	0,713	-0,060	-0,062	-0,042
	100 nM	-0,065	-0,076	0,440	-0,031	0,762	0,254	0,200	0,150
	10 nM	-0,074	-0,067	-0,072	-0,042	-0,062	-0,053	-0,080	-0,002
	1 nM	-0,044	-0,076	-0,077	-0,023	-0,052	-0,083	-0,076	-0,082
		Subtracted average background - blank				0,125			

Plate 4	liquid	No UV							
		VP1T			SMV25				
		1 µM	100 nM	10 nM	1 µM	100 nM	10 nM	blank	blank
cVP1	1µM	-0,018	0,208	-0,012	-0,023	-0,043	0,009	0,003	-0,043
	100 nM	-0,014	-0,048	-0,060	-0,034	-0,052	0,085	0,143	-0,062
	10 nM	-0,026	-0,056	-0,045	-0,050	-0,052	0,008	0,127	-0,066
	1 nM	-0,035	-0,064	-0,063	-0,054	-0,054	-0,037	0,217	-0,064
cSMV25	1µM	-0,058	-0,036	-0,051	-0,052	-0,041	0,643	-0,039	-0,037
	100 nM	0,002	-0,021	-0,036	-0,062	-0,061	0,491	-0,043	-0,067
	10 nM	0,057	-0,045	-0,061	-0,049	-0,053	-0,056	-0,061	-0,067
	1 nM	-0,052	-0,056	-0,056	-0,063	0,337	0,328	0,014	0,050
		Subtracted average background - blank				0,107			

Figure A.7: *Data: Comparison of UV immobilisation in wet or dry stage in Nunclon plates. Two aptamers were tested: VP1T and SMV25. cVP1 and cSMV25 represents the biotinylated rcDNA strands of VP1T and SMV25, respectively*

		Plate #1 - PEDOT:PSS, Nunclon plate, UV exposure, no plasma treatment							
		SMV25			VP1T			Blank	
		10 nM	100 nM	1 µM	10 nM	100 nM	1 µM	control	control
cVP1T	1 µM	0,022	0,011	0,003	0,012	0,072	0,681	-0,005	0,019
Biotin	100 nM	-0,001	-0,008	-0,003	0,001	0,379	1,011	0,002	0,003
	10 nM	-0,010	-0,007	-0,004	0,001	0,048	0,377	0,011	0,017
	1 nM	-0,007	-0,009	-0,021	-0,010	0,129	0,008	0,001	0,006
cSMV25	1 µM	-0,006	0,048	0,220	-0,010	-0,012	-0,006	-0,004	0,007
Biotin	100 nM	-0,009	0,014	0,387	-0,012	-0,007	-0,019	-0,005	0,011
	10 nM	-0,006	0,001	0,307	-0,006	-0,007	-0,010	-0,003	-0,019
	1 nM	-0,013	0,011	0,120	-0,016	-0,018	-0,024	-0,024	-0,016
		Subtracted average background - blank				0,085			
		Plate #2 - PEDOT:PSS, Nunclon plate, NO UV exposure, no plasma treatment							
		SMV25			VP1T			Blank	
		10 nM	100 nM	1 µM	10 nM	100 nM	1 µM	control	control
cVP1T	1 µM	0,014	0,005	0,009	0,006	0,036	0,303	0,018	0,027
Biotin	100 nM	-0,007	0,000	0,000	-0,004	0,077	0,354	-0,007	-0,004
	10 nM	-0,006	0,004	-0,005	-0,007	0,017	0,161	0,011	0,007
	1 nM	-0,011	-0,010	-0,006	0,010	0,021	0,019	-0,005	-0,003
cSMV25	1 µM	-0,006	0,038	0,310	-0,007	-0,004	-0,005	0,004	0,020
Biotin	100 nM	-0,008	0,004	0,161	-0,024	-0,007	-0,014	-0,007	0,004
	10 nM	-0,007	0,002	0,146	-0,014	-0,001	-0,013	-0,019	0,000
	1 nM	-0,017	-0,005	0,115	-0,021	-0,019	-0,022	-0,016	-0,030
		Subtracted average background - blank				0,082			
		Plate #3 - Nunclon plate, UV exposure, no plasma treatment							
		SMV25			VP1T			Blank	
		10 nM	100 nM	1 µM	10 nM	100 nM	1 µM	control	control
cVP1T	1 µM	0,007	0,031	0,026	0,487	1,915	2,138	0,001	0,004
Biotin	100 nM	0,003	0,004	0,005	0,702	1,731	2,135	0,002	-0,001
	10 nM	-0,001	0,006	0,014	0,537	1,950	2,121	0,005	-0,002
	1 nM	-0,002	0,002	0,006	0,469	0,839	0,928	-0,002	-0,001
cSMV25	1 µM	0,303	1,480	2,126	0,001	0,001	0,001	0,000	0,003
Biotin	100 nM	0,276	1,465	2,103	-0,003	-0,003	-0,002	-0,002	0,000
	10 nM	0,287	1,480	2,067	-0,004	-0,002	-0,003	-0,004	-0,003
	1 nM	0,209	0,932	1,482	-0,002	-0,001	0,049	0,004	-0,003
		Subtracted average background - blank				0,042			

Figure A.8: *Data: ELASA experiments on Nunclon plate, PolySorp plate and Nunclon plate with PEDOT:PSS, plates 1-3*

		Plate #4 - Nunclon plate, NO UV exposure, no plasma treatment							
		SMV25			VP1T			Blank	
		10 nM	100 nM	1 µM	10 nM	100 nM	1 µM	control	control
cVP1T	1 µM	0,005	0,011	0,008	0,178	0,785	1,932	0,006	0,005
Biotin	100 nM	-0,003	-0,003	-0,002	0,155	0,823	2,008	-0,003	-0,002
	10 nM	-0,002	-0,002	0,000	0,188	1,035	2,055	-0,004	-0,001
	1 nM	-0,002	-0,002	-0,002	0,198	0,756	1,061	-0,003	-0,002
cSMV25	1 µM	0,082	0,421	1,415	0,000	-0,002	-0,001	-0,001	-0,001
Biotin	100 nM	0,082	0,358	1,339	-0,002	-0,002	0,001	-0,002	0,004
	10 nM	0,072	0,466	1,648	-0,001	-0,003	0,000	-0,001	-0,002
	1 nM	0,040	0,256	1,128	-0,002	-0,002	-0,002	-0,002	0,001
		Subtracted average background - blank				0,041			
		Plate #5 - Polysorb plate,UV exposure, no plasma treatment							
		SMV25			VP1T			Blank	
		10 nM	100 nM	1 µM	10 nM	100 nM	1 µM	control	control
cVP1T	1 µM	0,006	0,006	0,009	0,103	0,482	1,165	0,006	0,009
Biotin	100 nM	-0,001	0,003	0,007	0,127	0,559	1,220	-0,002	-0,001
	10 nM	-0,002	-0,001	0,006	0,093	0,520	1,299	-0,003	-0,002
	1 nM	0,000	0,005	0,006	0,063	0,156	0,267	-0,003	-0,002
cSMV25	1 µM	0,030	0,576	0,782	0,000	0,000	0,000	0,000	0,000
Biotin	100 nM	0,037	0,486	0,746	-0,002	0,010	-0,001	-0,001	-0,002
	10 nM	0,033	0,586	0,822	0,001	0,003	0,002	0,002	-0,002
	1 nM	0,043	0,301	0,427	0,002	0,004	-0,001	-0,001	-0,001
		Subtracted average background - blank				0,039			
		Plate #6 - Polysorb plate,NO UV exposure, no plasma treatment							
		SMV25			VP1T			Blank	
		10 nM	100 nM	1 µM	10 nM	100 nM	1 µM	control	control
cVP1T	1 µM	0,01	0,01	0,01	0,01	0,02	0,20	0,00	0,01
Biotin	100 nM	0,01	0,01	0,00	0,01	0,01	0,21	0,00	0,00
	10 nM	0,00	0,00	0,00	0,00	0,01	0,17	0,00	0,00
	1 nM	0,00	0,00	0,00	0,00	0,02	0,11	0,00	0,00
cSMV25	1 µM	0,01	0,00	0,02	0,00	0,00	0,00	0,01	0,00
Biotin	100 nM	0,00	0,01	0,01	0,00	0,00	0,00	0,00	0,00
	10 nM	0,00	0,00	0,02	0,00	0,00	0,00	0,01	0,00
	1 nM	0,00	0,01	0,03	0,00	0,00	0,00	0,00	0,00
		Subtracted average background - blank				0,04			

Figure A.9: *Data: ELASA experiments on Nunclon plate, PolySorp plate and Nunclon plate with PEDOT:PSS, plates 4-6*

		Plate #1 - PEDOT:PSS, Polysorb plate, CT-tag, UV exposure, plasma treatment							
		VP1T			SMV25			Blank	
		1 µM	100 nM	10 nM	1 µM	100 nM	10 nM	control	control
cVP1T	1 µM	0,267	0,054	-0,006	0,000	-0,012	-0,005	-0,003	0,006
Biotin	100 nM	0,853	0,076	0,004	-0,006	0,001	-0,005	0,002	-0,007
	10 nM	0,217	0,150	0,023	-0,001	-0,006	0,002	-0,008	0,008
	1 nM	0,015	0,009	0,004	-0,001	0,003	0,000	0,005	-0,003
cSMV25	1 µM	0,000	-0,011	-0,001	0,268	0,014	0,008	0,000	-0,001
Biotin	100 nM	-0,009	-0,011	-0,001	0,258	-0,012	0,010	0,001	-0,008
	10 nM	-0,007	-0,005	-0,002	0,208	-0,012	0,001	0,000	-0,001
	1 nM	-0,015	-0,003	-0,008	0,020	-0,021	0,007	0,008	-0,004
		Subtracted average background - blank				0,072			
		Plate #2 - PEDOT:PSS, Polysorb plate, CT-tag, NO UV exposure, plasma treatment							
		VP1T			SMV25			Blank	
		1 µM	100 nM	10 nM	1 µM	100 nM	10 nM	control	control
cVP1T	1 µM	0,200	0,003	-0,013	-0,011	-0,004	-0,006	0,016	0,014
Biotin	100 nM	0,368	0,027	0,004	0,008	0,008	0,000	0,000	-0,002
	10 nM	0,062	0,036	0,004	-0,007	0,001	0,015	-0,008	0,001
	1 nM	-0,014	0,002	0,005	0,001	-0,016	-0,006	0,000	0,000
cSMV25	1 µM	-0,023	-0,013	-0,001	0,156	0,012	-0,012	-0,003	0,002
Biotin	100 nM	-0,021	-0,018	0,004	0,064	0,008	-0,002	0,005	0,008
	10 nM	-0,016	-0,029	-0,008	0,118	0,000	-0,003	-0,016	-0,004
	1 nM	-0,030	-0,034	-0,003	0,002	-0,007	-0,021	-0,016	-0,006
		Subtracted average background - blank				0,087			
		Plate #3 - PEDOT:PSS, Polysorb plate, NO CT-tag, UV exposure, plasma treatment							
		VP1T			SMV25			Blank	
		1 µM	100 nM	10 nM	1 µM	100 nM	10 nM	control	control
cVP1T	1 µM	0,495	0,022	0,022	0,018	0,018	0,008	0,013	0,007
Biotin	100 nM	0,355	0,027	0,000	0,008	-0,001	0,008	0,002	0,006
	10 nM	0,238	0,022	0,005	0,015	0,014	0,012	0,004	0,000
	1 nM	0,012	0,002	0,002	0,004	0,009	0,003	0,001	0,005
cSMV25	1 µM	0,011	0,005	0,003	0,476	0,019	0,002	-0,001	0,015
Biotin	100 nM	-0,015	-0,004	-0,005	0,393	0,026	0,001	-0,005	-0,010
	10 nM	-0,009	-0,009	-0,005	0,487	-0,002	0,003	-0,007	-0,010
	1 nM	-0,010	0,000	0,004	0,116	0,024	-0,005	-0,009	-0,005
		Subtracted average background - blank				0,074			
		Plate #4 - PEDOT:PSS, Polysorb plate, NO CT-tag, NO UV exposure, plasma treatment							
		VP1T			SMV25			Blank	
		1 µM	100 nM	10 nM	1 µM	100 nM	10 nM	control	control
cVP1T	1 µM	0,701	0,062	0,003	-0,002	-0,008	0,036	0,003	0,008
Biotin	100 nM	0,115	0,009	-0,005	-0,002	-0,008	-0,011	-0,012	-0,010
	10 nM	0,026	0,015	-0,003	0,000	-0,007	-0,009	0,014	-0,005
	1 nM	-0,004	-0,008	-0,011	-0,003	-0,004	0,001	0,002	-0,001
cSMV25	1 µM	0,001	-0,007	-0,004	0,204	0,034	0,018	-0,001	-0,003
Biotin	100 nM	-0,006	0,001	0,004	0,220	0,060	-0,004	0,000	-0,004
	10 nM	-0,013	-0,011	-0,006	0,152	0,009	0,004	-0,004	0,001
	1 nM	-0,012	-0,014	0,007	-0,001	-0,012	-0,020	0,017	0,000
		Subtracted average background - blank				0,084			

Figure A.10: *Data: ELASA experiments on PolySorp plate and PolySorp plate with PEDOT:PSS, TC-tag / no TC-tag plates 1-4*

		Plate #5 - Polysorb plate, CT-tag, UV exposure, NO plasma treatment							
		VP1T			SMV25			Blank	
		1 µM	100 nM	10 nM	1 µM	100 nM	10 nM	control	control
cVP1T	1 µM	1,263	0,107	0,014	0,003	0,002	0,004	0,003	0,002
Biotin	100 nM	0,880	0,192	0,016	0,001	-0,001	-0,001	0,003	-0,001
	10 nM	0,785	0,164	0,018	0,003	0,000	-0,001	0,000	0,000
	1 nM	0,214	0,056	0,012	0,002	0,001	-0,001	-0,001	0,000
cSMV25	1 µM	0,013	0,006	0,008	0,566	0,355	0,022	0,000	0,000
Biotin	100 nM	0,005	0,017	0,000	0,654	0,281	0,013	-0,001	0,000
	10 nM	0,015	0,005	0,016	0,642	0,339	0,010	-0,001	0,002
	1 nM	0,037	0,003	0,004	0,300	0,100	0,020	0,000	0,000
		Subtracted average background - blank				0,037			
		Plate #6 - Polysorb plate, CT-tag, NO UV exposure, NO plasma treatment							
		VP1T			SMV25			Blank	
		1 µM	100 nM	10 nM	1 µM	100 nM	10 nM	control	control
cVP1T	1 µM	0,072	0,018	0,022	0,000	-0,001	-0,001	0,003	-0,002
Biotin	100 nM	0,025	0,011	0,007	-0,002	-0,003	-0,003	0,002	-0,002
	10 nM	0,055	0,000	-0,003	-0,003	-0,003	-0,003	-0,004	-0,002
	1 nM	0,013	-0,002	-0,004	-0,003	0,005	-0,003	-0,003	0,005
cSMV25	1 µM	0,006	-0,001	0,010	0,002	-0,002	-0,002	-0,002	-0,001
Biotin	100 nM	0,004	0,010	0,004	0,020	0,014	0,001	-0,002	-0,002
	10 nM	0,002	0,005	0,014	0,015	0,004	0,002	-0,002	0,001
	1 nM	0,005	0,008	0,004	0,010	0,027	0,027	0,005	0,005
		Subtracted average background - blank				0,040			
		Plate #7 - Polysorb plate, NO CT-tag, UV exposure, NO plasma treatment							
		VP1T			SMV25			Blank	
		1 µM	100 nM	10 nM	1 µM	100 nM	10 nM	control	control
cVP1T	1 µM	0,241	0,016	0,007	0,001	0,001	0,002	0,001	0,003
Biotin	100 nM	0,282	0,012	-0,001	-0,001	-0,002	-0,001	-0,001	-0,002
	10 nM	0,172	0,013	0,000	0,000	-0,001	-0,001	-0,002	-0,002
	1 nM	0,137	0,017	0,005	0,002	-0,001	-0,001	-0,002	-0,001
cSMV25	1 µM	0,004	0,002	0,000	0,602	0,034	0,001	0,000	0,001
Biotin	100 nM	0,002	0,004	0,001	0,570	0,028	0,003	-0,001	0,000
	10 nM	0,004	0,002	0,001	0,539	0,034	0,002	-0,001	-0,001
	1 nM	0,004	0,004	0,002	0,182	0,019	0,004	0,001	0,000
		Subtracted average background - blank				0,037			
		Plate #8 - Polysorb plate, NO CT-tag, NO UV exposure, NO plasma treatment							
		VP1T			SMV25			Blank	
		1 µM	100 nM	10 nM	1 µM	100 nM	10 nM	control	control
cVP1T	1 µM	0,054	0,009	0,007	0,007	0,002	0,023	0,019	0,004
Biotin	100 nM	-0,005	-0,005	0,032	0,008	-0,007	0,002	-0,006	0,019
	10 nM	-0,001	-0,006	-0,005	-0,005	-0,001	-0,003	-0,007	0,024
	1 nM	0,002	-0,003	-0,005	-0,007	0,004	-0,007	-0,006	-0,006
cSMV25	1 µM	0,021	0,075	-0,006	-0,003	-0,002	-0,007	-0,007	-0,006
Biotin	100 nM	0,016	-0,004	0,000	0,006	-0,001	-0,004	0,000	0,000
	10 nM	0,004	-0,002	0,000	0,013	-0,005	0,004	-0,005	-0,006
	1 nM	-0,006	-0,004	-0,002	0,003	-0,003	-0,006	-0,005	-0,005
		Subtracted average background - blank				0,044			

Figure A.11: *Data: ELASA experiments on PolySorp plate and PolySorp plate with PEDOT:PSS, TC-tag / no TC-tag plates 5-8*

			Chip plate 9+10, PEDOT:PSS, 2 layers, PC chips, CT-tag, time exp									
			VP1T				Blank	SMV25				Blank
			5 µM	1 µM	100 nM	10 nm	Buffer	5 µM	1 µM	100 nM	10 nm	Buffer
Chip	cVP1T	1 µM	0,099	0,098	0,085	0,078	0,025	-0,001	0,010	0,061	0,049	0,060
plate #9	cSMV25	1 µM	0,007	0,001	0,080	-0,013	-0,094	0,016	-0,020	-0,028	0,002	-0,026
No UV (0 min)	cVP1T	100 nM	-0,018	-0,016	-0,026	-0,011	-0,037	0,032	-0,028	-0,022	-0,024	-0,019
	cSMV25	100 nM	-0,015	-0,019	-0,023	-0,021	-0,042	-0,011	-0,032	-0,029	-0,031	-0,029
Chip	cVP1T	1 µM	0,188	0,152	0,134	0,096	0,063	0,138	0,116	0,146	0,138	0,238
plate #10	cSMV25	1 µM	0,037	-0,014	-0,001	0,006	-0,081	-0,023	-0,026	-0,015	-0,010	-0,013
UV (1 min)	cVP1T	100 nM	0,044	0,046	-0,002	-0,030	-0,016	-0,012	-0,017	0,017	0,006	0,026
	cSMV25	100 nM	0,166	-0,034	-0,028	-0,031	-0,032	0,037	-0,025	-0,018	-0,022	-0,023
			Subtracted average background - blank				0,128					
			Chip plate 11+12, PEDOT:PSS, 2 layers, PC chips, CT-tag, time exp									
			VP1T				Blank	SMV25				Blank
			5 µM	1 µM	100 nM	10 nm	Buffer	5 µM	1 µM	100 nM	10 nm	Buffer
Chip	cVP1T	1 µM	0,265	0,257	0,128	0,077	0,064	0,030	0,090	0,116	0,074	0,185
plate #11	cSMV25	1 µM	-0,032	-0,036	-0,029	-0,031	-0,017	0,074	0,002	-0,022	-0,022	-0,015
UV (5 min)	cVP1T	100 nM	0,320	0,013	-0,035	-0,025	-0,042	-0,042	-0,051	-0,036	-0,045	-0,029
	cSMV25	100 nM	-0,047	-0,054	-0,055	-0,054	-0,065	-0,002	-0,011	-0,051	-0,056	-0,050
Chip	cVP1T	1 µM	0,156	0,317	0,228	0,078	0,022	0,018	0,013	0,017	0,082	0,108
plate #12	cSMV25	1 µM	0,014	-0,009	-0,003	-0,028	-0,036	0,168	0,198	0,001	-0,006	0,017
UV (10 min)	cVP1T	100 nM	0,061	0,036	-0,033	-0,051	-0,038	-0,008	-0,042	-0,040	-0,037	-0,026
	cSMV25	100 nM	-0,071	-0,018	0,008	-0,038	-0,039	0,022	0,044	-0,038	-0,046	-0,046
			Subtracted average background - blank				0,148					
			Chip plate 13+14, PC chips, CT-tag, time exp									
			VP1T				Blank	SMV25				Blank
			5 µM	1 µM	100 nM	10 nm	Buffer	5 µM	1 µM	100 nM	10 nm	Buffer
Chip	cVP1T	1 µM	0,410	0,480	0,050	0,004	-0,006	-0,005	-0,007	-0,004	-0,006	0,001
plate #13	cSMV25	1 µM	0,108	0,017	-0,001	-0,003	-0,006	0,131	0,054	-0,001	-0,004	0,001
No UV (0 min)	cVP1T	100 nM	0,984	0,519	0,042	0,020	-0,005	0,022	-0,006	-0,003	-0,005	0,002
	cSMV25	100 nM	0,135	0,000	-0,006	-0,006	-0,006	0,155	0,034	0,005	-0,003	0,009
Chip	cVP1T	1 µM	1,146	0,756	0,098	0,014	-0,006	0,061	-0,003	-0,003	-0,004	0,001
plate #14	cSMV25	1 µM	0,216	0,660	0,015	-0,007	-0,005	0,521	0,283	0,031	-0,001	-0,005
UV (1 min)	cVP1T	100 nM	1,234	0,878	0,096	0,002	-0,003	0,105	0,018	0,005	0,067	0,008
	cSMV25	100 nM	0,181	-0,003	0,000	0,010	0,021	0,554	0,478	0,062	0,001	0,002
			Subtracted average background - blank				0,049					
			Chip plate 15+16, PC chips, CT-tag, time exp									
			VP1T				Blank	SMV25				Blank
			5 µM	1 µM	100 nM	10 nm	Buffer	5 µM	1 µM	100 nM	10 nm	Buffer
Chip	cVP1T	1 µM	1,254	1,235	0,938	0,142	-0,009	0,096	-0,002	-0,008	-0,009	-0,006
plate #15	cSMV25	1 µM	0,166	0,316	0,001	-0,004	-0,008	0,915	0,993	0,468	0,021	-0,008
UV (5 min)	cVP1T	100 nM	0,939	1,353	1,084	0,140	-0,008	0,421	0,000	-0,008	-0,006	-0,008
	cSMV25	100 nM	0,030	0,003	0,011	-0,002	-0,008	0,771	0,922	0,490	0,088	-0,004
Chip	cVP1T	1 µM	1,483	1,302	0,990	0,163	0,008	0,122	0,057	0,012	0,008	0,019
plate #16	cSMV25	1 µM	0,138	0,162	0,079	0,004	0,001	0,838	0,769	0,238	0,091	0,008
UV (10 min)	cVP1T	100 nM	1,328	1,176	0,848	0,247	0,005	0,067	0,023	0,005	0,002	0,001
	cSMV25	100 nM	0,011	0,017	0,044	0,008	0,000	0,825	0,836	0,436	0,081	0,014
			Subtracted average background - blank				0,052					

Figure A.12: *Data: PC chips with/ without 2 layers PEDOT:PSS, UV exposure time dependence. First repetition*

			Chip plate 1+2, PEDOT:PSS, 1 layer, PC chips, CT-tag									
			VP1T				Blank	Blank	SMV25			Blank
			10 µM	5 µM	1 µM	100 nm	Buffer	Buffer	5 µM	1 µM	100 nm	Buffer
Chip	cVP1T	1 µM	0,095	0,287	0,173	0,117	0,183	0,110	0,080	0,075	0,100	0,412
plate #1	cVP1T	100 nM	-0,044	0,070	0,018	-0,025	-0,015	-0,061	-0,043	-0,050	-0,051	0,020
No UV	cSMV25	1 µM	-0,052	-0,064	-0,066	-0,068	-0,047	-0,061	-0,014	-0,035	-0,061	-0,016
	cSMV25	100 nM	-0,073	-0,077	-0,077	-0,074	-0,055	-0,078	-0,032	-0,073	-0,076	-0,060
Chip	cVP1T	1 µM	0,786	0,663	0,229	0,082	0,029	0,056	0,085	0,024	0,017	0,088
plate #2	cVP1T	100 nM	0,328	0,513	0,125	-0,044	-0,033	-0,067	-0,069	-0,063	-0,062	-0,011
1 min UV	cSMV25	1 µM	-0,065	-0,072	-0,066	-0,077	-0,073	-0,068	0,274	0,025	-0,054	-0,060
	cSMV25	100 nM	-0,078	-0,079	-0,078	-0,081	-0,064	-0,066	0,254	-0,003	-0,071	-0,074
			Subtracted average background - blank				0,122					
			Chip plate 3+4, PEDOT:PSS (1 layer - applied with paint applicator), Polycarbonate chips, CT-tag									
			VP1T				Blank	Blank	SMV25			Blank
			10 µM	5 µM	1 µM	100 nm	Buffer	Buffer	5 µM	1 µM	100 nm	Buffer
Chip	cVP1T	1 µM	0,348	0,185	0,145	0,098	0,091	0,282	0,154	0,045	0,063	0,213
plate #3	cVP1T	100 nM	-0,009	0,068	0,006	-0,062	-0,015	0,019	-0,070	-0,086	-0,061	-0,002
5 min UV	cSMV25	1 µM	-0,029	-0,076	-0,079	-0,082	-0,064	-0,104	0,995	0,677	-0,018	-0,088
	cSMV25	100 nM	-0,093	-0,104	-0,106	-0,108	-0,101	-0,112	0,915	0,303	-0,041	-0,107
Chip	cVP1T	1 µM	0,443	0,187	0,252	0,190	0,108	0,222	0,084	0,005	0,059	0,235
plate #4	cVP1T	100 nM	0,207	0,088	0,037	-0,022	-0,033	-0,057	-0,061	-0,077	-0,060	-0,008
10 min UV	cSMV25	1 µM	-0,091	-0,102	-0,099	-0,107	-0,067	-0,085	0,407	0,035	-0,049	-0,029
	cSMV25	100 nM	-0,102	-0,119	-0,119	-0,118	-0,103	-0,104	0,089	0,005	-0,099	-0,098
			Subtracted average background - blank				0,162					
			Chip plate 5+6, PEDOT:PSS (2 layers - applied with paint applicator), Polycarbonate chips, CT-tag									
			VP1T				Blank	Blank	SMV25			Blank
			10 µM	5 µM	1 µM	100 nm	Buffer	Buffer	5 µM	1 µM	100 nm	Buffer
Chip	cVP1T	1 µM	0,474	0,061	0,093	0,105	0,047	0,215	0,085	0,054	0,052	0,055
plate #5	cVP1T	100 nM	-0,043	-0,065	-0,069	-0,078	0,102	-0,051	-0,067	-0,079	-0,083	0,014
No UV	cSMV25	1 µM	-0,108	-0,077	-0,102	-0,107	-0,103	-0,073	-0,090	-0,094	-0,098	-0,086
	cSMV25	100 nM	-0,109	-0,112	-0,116	-0,114	-0,114	-0,110	-0,111	-0,115	-0,117	-0,085
Chip	cVP1T	1 µM	0,142	0,018	0,037	0,038	0,217	0,086	0,025	0,066	0,098	0,388
plate #6	cVP1T	100 nM	-0,045	-0,059	-0,062	-0,066	-0,003	-0,004	-0,072	-0,068	-0,070	0,043
1 min UV	cSMV25	1 µM	-0,090	-0,089	-0,103	-0,103	-0,090	-0,070	-0,086	-0,093	-0,103	-0,078
	cSMV25	100 nM	-0,114	-0,118	-0,119	-0,123	-0,089	-0,103	-0,108	-0,112	-0,103	-0,109
			Subtracted average background - blank				0,190					

Figure A.13: *Data: PC chips with/ without 1 or 2 layers PEDOT:PSS, UV exposure time dependence. Second repetition*

			Chip plate 7+8, PEDOT:PSS (2 layers - applied with paint applicator), Polycarbonate chips, CT-tag									
			VP1T				Blank	Blank	SMV25			Blank
			10 µM	5 µM	1 µM	100 nm	Buffer	Buffer	5 µM	1 µM	100 nm	Buffer
Chip	cVP1T	1 µM	0,134	0,149	0,091	0,001	0,163	-0,036	-0,009	-0,059	-0,073	0,055
plate #7	cVP1T	100 nM	-0,019	0,056	0,012	-0,120	-0,055	-0,097	-0,105	-0,092	-0,105	-0,030
5 min UV	cSMV25	1 µM	-0,110	-0,116	-0,112	-0,122	-0,109	-0,071	-0,066	-0,062	-0,108	-0,072
	cSMV25	100 nM	-0,127	-0,139	-0,140	-0,140	-0,133	-0,109	0,022	-0,080	-0,111	0,033
Chip	cVP1T	1 µM	0,340	0,179	0,186	0,181	0,431	0,228	0,197	0,211	0,184	0,424
plate #8	cVP1T	100 nM	0,044	-0,025	-0,005	-0,053	0,008	-0,019	-0,058	-0,071	-0,032	-0,006
10 min UV	cSMV25	1 µM	-0,085	-0,125	-0,123	-0,125	-0,092	-0,072	-0,088	-0,099	-0,110	-0,108
	cSMV25	100 nM	-0,134	-0,135	-0,134	-0,134	-0,087	-0,112	-0,098	-0,104	-0,129	-0,128
			Subtracted average background - blank				0,208					
			Chip plate 9+10, Polycarbonate chips, CT-tag									
			VP1T				Blank	Blank	SMV25			Blank
			10 µM	5 µM	1 µM	100 nm	Buffer	Buffer	5 µM	1 µM	100 nm	Buffer
Chip	cVP1T	1 µM	0,474	0,318	-0,001	-0,028	0,107	-0,017	-0,035	-0,037	-0,037	-0,030
plate #9	cVP1T	100 nM	0,484	0,316	0,061	-0,021	-0,042	-0,006	-0,035	-0,035	-0,035	-0,019
No UV	cSMV25	1 µM	-0,035	-0,034	-0,034	-0,033	0,042	-0,032	-0,026	-0,032	-0,034	0,044
	cSMV25	100 nM	-0,033	-0,032	-0,032	-0,031	0,182	-0,032	-0,024	-0,034	-0,033	0,041
Chip	cVP1T	1 µM	0,490	0,390	0,158	-0,022	-0,032	-0,035	-0,041	-0,041	-0,040	-0,026
plate #10	cVP1T	100 nM	0,447	0,441	0,209	0,031	0,007	-0,042	-0,042	-0,042	-0,041	-0,027
1 min UV	cSMV25	1 µM	-0,042	-0,042	-0,041	-0,041	-0,040	-0,028	0,248	0,046	-0,034	0,075
	cSMV25	100 nM	-0,020	-0,041	-0,041	-0,041	-0,019	-0,027	0,315	0,004	-0,035	-0,044
			Subtracted average background - blank				0,079					
			Chip plate 11+12, Polycarbonate chips, CT-tag									
			VP1T				Blank	Blank	SMV25			Blank
			10 µM	5 µM	1 µM	100 nm	Buffer	Buffer	5 µM	1 µM	100 nm	Buffer
Chip	cVP1T	1 µM	0,816	0,871	0,971	0,621	-0,013	-0,005	-0,015	-0,015	-0,022	-0,002
plate #11	cVP1T	100 nM	0,925	0,807	0,865	0,650	0,000	-0,013	-0,010	-0,019	-0,021	-0,008
5 min UV	cSMV25	1 µM	0,033	-0,020	-0,022	-0,021	-0,019	-0,020	0,819	0,770	0,430	0,063
	cSMV25	100 nM	-0,010	-0,022	-0,021	-0,020	-0,015	-0,009	0,775	0,665	0,438	0,025
Chip	cVP1T	1 µM	0,971	0,880	0,948	0,563	0,065	0,022	-0,009	-0,015	-0,016	-0,003
plate #12	cVP1T	100 nM	1,082	0,958	0,911	0,844	0,006	-0,007	-0,013	-0,017	-0,018	-0,004
10 min UV	cSMV25	1 µM	-0,015	-0,016	0,011	-0,018	-0,016	-0,020	0,886	0,750	0,410	-0,017
	cSMV25	100 nM	-0,019	-0,017	-0,017	-0,019	0,013	-0,018	0,648	0,654	0,184	-0,010
			Subtracted average background - blank				0,059					

Figure A.14: *Data: PC chips with/ without 1 or 2 layers PEDOT:PSS, UV exposure time dependence. Second repetition*

			Chip plate 1+2, PEDOT:PSS, 1 layer, PC chips									
			VP1T				Blank	SMV25				Blank
			5 µM	1 µM	100 nM	10 nm	Buffer	5 µM	1 µM	100 nM	10 nm	Buffer
Chip	cVP1T	1 µM	0,343	0,461	0,256	0,124	0,153	0,317	0,097	0,063	0,198	0,155
plate #1	cSMV25	1 µM	0,057	-0,033	-0,044	-0,043	-0,055	0,526	0,290	0,039	0,001	-0,027
UV	cVP1T	100 nM	0,427	0,135	0,021	0,004	0,019	-0,041	-0,047	-0,055	-0,036	-0,046
	cSMV25	100 nM	0,082	-0,022	-0,034	-0,035	-0,037	0,712	0,179	-0,014	-0,070	-0,062
Chip	cVP1T	1 µM	0,407	0,247	0,182	0,130	0,062	0,270	0,186	0,174	0,065	0,072
plate #2	cSMV25	1 µM	0,042	-0,054	-0,031	-0,042	-0,022	0,179	0,035	-0,009	-0,047	-0,036
No UV	cVP1T	100 nM	0,246	0,011	-0,016	-0,047	-0,004	-0,013	-0,058	-0,062	-0,058	-0,058
	cSMV25	100 nM	-0,030	-0,061	-0,063	-0,061	-0,054	0,033	-0,013	-0,068	-0,080	-0,067
			Subtracted average background - blank				0,168					
			Chip plate 3+4, PC chips									
			VP1T				Blank	SMV25				Blank
			5 µM	1 µM	100 nM	10 nm	Buffer	5 µM	1 µM	100 nM	10 nm	Buffer
Chip	cVP1T	1 µM	1,378	1,101	0,738	0,028	-0,006	0,040	-0,005	-0,002	-0,006	-0,006
plate #3	cSMV25	1 µM	0,627	0,022	-0,007	-0,011	0,001	0,854	0,717	0,802	0,072	-0,006
UV	cVP1T	100 nM	1,554	1,152	0,710	0,032	-0,008	0,058	-0,002	-0,003	-0,001	-0,001
	cSMV25	100 nM	0,369	-0,008	-0,007	-0,012	-0,009	1,336	0,615	0,738	0,064	-0,001
Chip	cVP1T	1 µM	0,277	0,028	-0,001	-0,004	0,004	0,012	-0,004	-0,003	-0,003	0,001
plate #4	cSMV25	1 µM	0,137	-0,005	-0,009	-0,007	-0,006	0,306	-0,002	0,001	-0,001	-0,001
No UV	cVP1T	100 nM	0,611	0,027	-0,002	-0,004	-0,001	0,124	0,004	0,007	0,009	0,009
	cSMV25	100 nM	0,673	-0,003	-0,005	-0,003	-0,001	0,119	0,009	0,012	0,019	0,029
			Subtracted average background - blank				0,055					

Figure A.15: *Data: PC chips with/ without 1 layer PEDOT:PSS, UV / no UV exposure, with TC-tag. First repetition*

			Chip plate 1+2, PEDOT:PSS, 2 layers, PC chips, CT-tag									
			VP1T				Blank	SMV25				Blank
			5 µM	1 µM	100 nM	10 nm	Buffer	5 µM	1 µM	100 nM	10 nm	Buffer
Chip	cVP1T	1 µM	0,247	0,243	0,143	0,077	0,061	0,089	0,072	0,097	0,056	0,058
plate #1	cSMV25	1 µM	0,033	-0,012	-0,014	-0,017	-0,027	0,167	0,037	0,001	-0,003	-0,010
UV (5 min)	cVP1T	100 nM	0,186	0,113	0,038	-0,012	-0,034	-0,011	-0,042	-0,037	-0,027	-0,015
	cSMV25	100 nM	-0,027	-0,037	-0,034	-0,031	-0,033	0,078	0,081	-0,022	-0,028	-0,032
Chip	cVP1T	1 µM	0,110	0,091	0,089	0,140	0,082	0,061	0,061	0,074	0,084	0,138
plate #2	cSMV25	1 µM	0,042	-0,005	0,032	-0,035	-0,080	-0,037	0,056	0,005	-0,003	-0,012
No UV	cVP1T	100 nM	-0,002	-0,021	-0,022	0,007	-0,003	0,035	-0,010	-0,008	0,011	-0,012
	cSMV25	100 nM	0,052	-0,043	-0,034	-0,042	-0,053	0,124	-0,021	-0,022	-0,030	-0,027
			Subtracted average background - blank				0,139					
			Chip plate 3+4, PC chips, CT-tag									
			VP1T				Blank	SMV25				Blank
			5 µM	1 µM	100 nM	10 nm	Buffer	5 µM	1 µM	100 nM	10 nm	Buffer
Chip	cVP1T	1 µM	1,599	1,325	1,026	0,289	0,005	0,068	0,012	0,011	0,004	0,007
plate #3	cSMV25	1 µM	0,044	0,020	0,015	0,007	0,005	0,876	0,973	0,592	0,094	0,010
UV (5 min)	cVP1T	100 nM	1,127	1,246	1,045	0,248	-0,001	0,018	0,005	0,003	-0,002	0,002
	cSMV25	100 nM	0,023	0,006	0,002	0,001	-0,004	0,908	0,991	0,673	0,105	0,000
Chip	cVP1T	1 µM	0,442	0,478	0,020	-0,002	-0,007	0,085	-0,004	-0,003	-0,004	-0,003
plate #4	cSMV25	1 µM	0,033	-0,006	-0,004	-0,009	0,001	0,249	0,073	0,008	-0,005	0,003
No UV	cVP1T	100 nM	0,429	0,546	0,019	0,004	-0,005	0,019	-0,008	-0,008	-0,008	-0,006
	cSMV25	100 nM	0,013	-0,003	-0,003	-0,007	-0,006	0,141	0,052	-0,006	-0,008	-0,002
			Subtracted average background - blank				0,053					
			Chip plate 5+6, PEDOT:PSS, 2 layers, PC chips, NO CT-tag									
			VP1T				Blank	SMV25				Blank
			5 µM	1 µM	100 nM	10 nm	Buffer	5 µM	1 µM	100 nM	10 nm	Buffer
Chip	cVP1T	1 µM	0,185	0,098	0,112	0,085	0,223	0,050	0,100	0,115	0,121	0,181
plate #5	cSMV25	1 µM	-0,025	-0,015	-0,010	-0,019	-0,120	-0,014	-0,011	-0,013	-0,016	0,004
UV (5 min)	cVP1T	100 nM	0,206	-0,021	-0,003	0,001	-0,031	0,022	-0,001	0,005	0,003	-0,003
	cSMV25	100 nM	-0,045	-0,050	-0,053	-0,055	-0,063	0,050	-0,022	-0,034	-0,032	-0,033
Chip	cVP1T	1 µM	0,208	0,121	0,138	0,117	0,107	0,010	0,085	0,092	0,053	0,012
plate #6	cSMV25	1 µM	-0,006	-0,018	-0,017	-0,006	-0,035	0,058	-0,033	-0,013	-0,049	-0,053
No UV	cVP1T	100 nM	0,048	-0,037	-0,041	-0,015	-0,043	0,155	-0,031	-0,040	-0,025	-0,034
	cSMV25	100 nM	-0,017	-0,047	-0,051	-0,056	-0,050	0,025	-0,046	-0,048	-0,047	-0,063
			Subtracted average background - blank				0,157					
			Chip plate 7+8, PC chips, NO CT-tag									
			VP1T				Blank	SMV25				Blank
			5 µM	1 µM	100 nM	10 nm	Buffer	5 µM	1 µM	100 nM	10 nm	Buffer
Chip	cVP1T	1 µM	0,618	0,775	0,474	0,148	-0,004	0,025	0,001	-0,005	0,000	0,005
plate #7	cSMV25	1 µM	0,245	0,003	0,015	-0,004	-0,004	0,924	0,655	0,263	0,018	-0,002
UV (5 min)	cVP1T	100 nM	0,572	0,722	0,569	0,161	0,038	0,010	0,000	-0,006	0,009	0,000
	cSMV25	100 nM	0,023	-0,004	-0,005	0,001	0,003	0,965	0,776	0,382	0,013	-0,007
Chip	cVP1T	1 µM	0,127	0,502	0,165	0,081	0,001	0,023	-0,004	-0,003	-0,001	-0,006
plate #8	cSMV25	1 µM	0,017	0,009	-0,005	-0,008	-0,004	0,012	0,048	-0,002	-0,001	-0,004
No UV	cVP1T	100 nM	0,092	0,375	0,257	0,067	-0,005	0,126	-0,006	-0,005	-0,005	-0,005
	cSMV25	100 nM	0,012	-0,007	-0,008	-0,008	-0,002	0,142	0,047	0,040	-0,005	-0,007
			Subtracted average background - blank				0,051					

Figure A.16: *Data: PC chips with/ without 2 layers PEDOT:PSS, UV / no UV exposure, with/without TC-tag. Second repetition*

			Chip plate 1+2, PEDOT:PSS, 1 layer, PC chips, CT-tag									
			VP1T				Blank	SMV25				Blank
			10 µM	5 µM	1 µM	100 nm	Buffer	10 µM	5 µM	1 µM	100 nm	Buffer
Chip	cVP1T	1 µM	0,802	0,713	0,398	0,226	0,199	0,100	0,115	0,015	0,064	0,210
plate #1	cSMV25	1 µM	-0,056	-0,038	-0,043	-0,055	-0,035	0,857	1,027	0,721	0,056	0,023
UV (5 min)	cVP1T	100 nM	1,040	0,796	0,453	0,082	-0,026	-0,048	-0,052	-0,044	-0,041	-0,016
	cSMV25	100 nM	-0,057	-0,056	-0,070	-0,068	-0,062	0,942	1,073	0,630	-0,011	-0,059
Chip	cVP1T	1 µM	0,301	0,266	0,269	0,070	0,025	0,099	0,035	0,045	0,037	0,093
plate #2	cSMV25	1 µM	-0,061	-0,058	-0,057	-0,060	-0,050	0,028	0,221	0,121	-0,041	-0,039
No UV	cVP1T	100 nM	-0,009	0,069	0,022	-0,032	-0,045	-0,091	-0,051	-0,051	-0,056	-0,071
	cSMV25	100 nM	-0,066	-0,074	-0,072	-0,074	-0,075	0,004	0,169	0,013	-0,070	-0,065
			Subtracted average background - blank				0,129					
			Chip plate 3+4, PEDOT:PSS, 2 layers, PC chips, CT-tag									
			VP1T				Blank	SMV25				Blank
			10 µM	5 µM	1 µM	100 nm	Buffer	10 µM	5 µM	1 µM	100 nm	Buffer
Chip	cVP1T	1 µM	0,460	0,396	0,333	0,187	0,096	0,004	0,046	0,033	0,058	0,120
plate #3	cSMV25	1 µM	0,042	-0,004	-0,021	-0,043	-0,080	0,161	0,398	0,066	-0,024	-0,008
UV (5 min)	cVP1T	100 nM	0,195	0,322	0,139	-0,006	-0,049	-0,005	-0,010	-0,024	-0,043	-0,007
	cSMV25	100 nM	-0,024	-0,049	-0,055	-0,062	-0,063	0,018	0,123	0,014	-0,046	-0,044
Chip	cVP1T	1 µM	0,153	0,164	0,137	0,070	0,112	0,063	0,027	0,036	0,016	0,084
plate #4	cSMV25	1 µM	-0,013	-0,033	-0,036	-0,040	-0,033	-0,018	-0,029	-0,031	-0,042	-0,037
No UV	cVP1T	100 nM	-0,001	0,041	0,024	-0,038	-0,055	-0,039	-0,047	-0,047	-0,054	-0,026
	cSMV25	100 nM	-0,062	-0,053	-0,050	-0,057	-0,057	-0,040	-0,042	-0,050	-0,032	0,044
			Subtracted average background - blank				0,141					
			Chip plate 5+6, PC chips, CT-tag									
			VP1T				Blank	SMV25				Blank
			10 µM	5 µM	1 µM	100 nm	Buffer	10 µM	5 µM	1 µM	100 nm	Buffer
Chip	cVP1T	1 µM	1,269	1,054	0,806	0,676	-0,107	-0,067	-0,036	-0,057	-0,105	-0,107
plate #5	cSMV25	1 µM	-0,033	-0,079	-0,063	-0,100	-0,082	0,576	0,547	0,675	0,432	-0,107
UV (5 min)	cVP1T	100 nM	1,039	1,029	0,859	0,685	-0,105	-0,074	-0,102	-0,105	-0,105	-0,105
	cSMV25	100 nM	-0,082	-0,095	-0,097	-0,105	-0,101	0,602	0,532	0,559	0,403	-0,107
Chip	cVP1T	1 µM	0,204	0,291	-0,054	-0,102	-0,109	-0,090	-0,107	-0,108	-0,107	-0,103
plate #6	cSMV25	1 µM	-0,042	-0,108	-0,104	-0,106	-0,108	-0,006	-0,046	-0,099	-0,096	-0,098
No UV	cVP1T	100 nM	0,322	0,170	0,040	-0,098	-0,109	-0,097	-0,109	-0,106	-0,103	-0,090
	cSMV25	100 nM	-0,099	-0,107	-0,108	-0,110	-0,093	-0,089	-0,046	-0,099	-0,093	-0,071
			Subtracted average background - blank				0,148					

Figure A.17: *Data: PC chips with/ without 1 or 2 layers PEDOT:PSS, UV / no UV exposure, with/without TC-tag. Third repetition (part 1)*

			Chip plate 7+8, PEDOT:PSS, 1 layer, PC chips, NO CT-tag									
			VP1T				Blank	SMV25				Blank
			10 µM	5 µM	1 µM	100 nm	Buffer	10 µM	5 µM	1 µM	100 nm	Buffer
Chip	cVP1T	1 µM	0,435	0,642	0,303	0,079	0,031	0,021	0,011	0,007	0,013	0,220
plate #7	cSMV25	1 µM	-0,019	-0,046	-0,055	-0,059	-0,055	0,013	0,107	0,032	-0,034	0,017
UV (5 min)	cVP1T	100 nM	0,091	0,155	0,055	-0,028	-0,035	0,033	-0,056	-0,058	-0,055	-0,037
	cSMV25	100 nM	-0,049	-0,059	-0,050	-0,053	-0,047	0,277	0,746	0,191	-0,010	-0,050
Chip	cVP1T	1 µM	0,882	0,351	0,136	0,069	0,158	-0,029	0,039	0,059	0,055	0,032
plate #8	cSMV25	1 µM	-0,036	-0,041	-0,042	-0,039	-0,005	0,003	0,133	0,035	-0,029	-0,044
No UV	cVP1T	100 nM	-0,025	0,150	0,046	-0,012	-0,050	-0,033	-0,030	-0,040	-0,044	-0,042
	cSMV25	100 nM	-0,052	-0,053	-0,050	-0,050	-0,058	-0,030	-0,013	-0,033	-0,037	-0,039
			Subtracted average background - blank				0,111					
			Chip plate 9+10, PEDOT:PSS, 2 layers, PC chips, NO CT-tag									
			VP1T				Blank	SMV25				Blank
			10 µM	5 µM	1 µM	100 nm	Buffer	10 µM	5 µM	1 µM	100 nm	Buffer
Chip	cVP1T	1 µM	0,341	0,274	0,192	0,107	0,051	0,132	0,108	-0,009	-0,031	0,082
plate #9	cSMV25	1 µM	-0,020	-0,052	-0,054	-0,062	-0,029	0,144	0,024	0,047	-0,063	0,026
UV (5 min)	cVP1T	100 nM	0,068	0,147	0,118	-0,039	-0,023	-0,085	-0,029	-0,030	-0,036	-0,044
	cSMV25	100 nM	-0,077	-0,082	-0,082	-0,076	-0,063	0,019	0,017	-0,032	-0,054	0,087
Chip	cVP1T	1 µM	0,023	0,007	0,005	0,004	0,028	0,018	-0,009	-0,030	-0,041	0,130
plate #10	cSMV25	1 µM	-0,005	-0,061	-0,062	-0,070	-0,045	-0,053	-0,024	-0,054	-0,073	-0,027
No UV	cVP1T	100 nM	0,029	-0,022	-0,031	-0,076	-0,026	0,018	-0,051	-0,058	-0,068	-0,041
	cSMV25	100 nM	-0,079	-0,090	-0,093	-0,091	-0,026	-0,018	-0,075	-0,080	-0,085	-0,077
			Subtracted average background - blank				0,167					
			Chip plate 11+12, PC chips, NO CT-tag									
			VP1T				Blank	SMV25				Blank
			10 µM	5 µM	1 µM	100 nm	Buffer	10 µM	5 µM	1 µM	100 nm	Buffer
Chip	cVP1T	1 µM	0,251	0,355	0,214	0,029	-0,016	0,007	-0,004	-0,009	-0,014	0,014
plate #11	cSMV25	1 µM	0,015	-0,017	-0,018	-0,019	-0,019	0,451	0,518	0,306	0,065	0,005
UV (5 min)	cVP1T	100 nM	0,363	0,296	0,209	0,010	0,001	0,022	-0,018	-0,018	-0,013	-0,012
	cSMV25	100 nM	0,020	-0,018	-0,010	-0,017	-0,018	0,551	0,582	0,446	-0,010	0,060
Chip	cVP1T	1 µM	0,020	0,000	0,004	-0,016	-0,018	-0,010	-0,016	-0,018	-0,017	-0,014
plate #12	cSMV25	1 µM	-0,015	-0,018	-0,017	-0,016	-0,010	-0,005	-0,004	0,000	-0,011	0,022
No UV	cVP1T	100 nM	0,021	0,013	0,015	-0,015	-0,021	-0,008	-0,018	-0,015	-0,017	-0,002
	cSMV25	100 nM	-0,018	-0,019	-0,017	-0,015	-0,011	-0,006	-0,010	-0,005	-0,013	0,032
			Subtracted average background - blank				0,058					

Figure A.18: *Data: PC chips with/ without 1 or 2 layers PEDOT:PSS, UV / no UV exposure, with/without TC-tag. Third repetition (part 2)*

A.12 Data analysis with MATLAB of EIS data from VersaStat

Matlab script for data analysis:

```
%%%%%%%%%%%%%%%%%%%%%%%%%%%%%%%%%%%%%%%%%%
% Julie Kirkegaard, julki, Lyngby 2015 %
%%%%%%%%%%%%%%%%%%%%%%%%%%%%%%%%%%%%%%%%%%

clear all
close all
clc

set(0,'defaultlinelinewidth',1.9)
set(0,'DefaultAxesFontSize',18)

%%
data = load('test_for_chapter_biosensors-no2.txt');

% Removing the first 100 points:
data = data(100:4350,:);

txtE1 = 'E1, Positive';
txtE2 = 'E2, Negative';
txtE3 = 'E3, Positive';
txtE4 = 'E4, Negative';

chipnr = 1;

%%% SAMPLE: 1 mM Penicillin in 1:10 PBS
% Sample change - point of sample change in data point column:
PBS1 = 1400;
Sample1 = 2260;
Sample2 = 3130;
Sample3 = 3900;

% plot:
    % Real_Z = 15
    % Img_Z  = 16
    % |Z|    = 17
RIZ = 17; % R -> real, I -> img, Z -> |Z|

%   Data columns:
%
%   1: Segment #
%   2: Point #
%   3: E(V)
```

```
%   4: I(A)
%   5: elapsed Time(s)  - Changed to start at t = 0 at injection of ...
    first concentration measurement
%   6: ADC Sync Input(V)
%   7: Current Range
%   8: Status
%   9: e Applied(V)
%   10: Frequency(Hz)
%   11: E Real
%   12: E Imag
%   13: I Real
%   14: I Imag
%   15: Z Real
%   16: Z Imag
%%%   17: |Z|      - Calculated
%%%   18: Phase(Z) - Calculated

data(:,17)  = sqrt(data(:,15).^2 + data(:,16).^2);
data(:,18)  = atan(data(:,16)./data(:,15)).*(180/pi);

data = data(2300:3300,:);

time = (data(:,5)-data(1,5))./60;

%% Extracting data from each electrode

% finding index numbers for each electrode
E1 = find (data(:,17) < 204.1e3 & data(:,17) > 203.5e3);
E2 = find (data(:,17) < 193.8e3 & data(:,17) > 193.4e3);
E3 = find (data(:,17) < 202.6e3 & data(:,17) > 202e3);
E4 = find (data(:,17) < 184.5e3 & data(:,17) > 182.7e3);

figure(1)
plot(time(:,1), data(:,RIZ)./1e3,'-or')
hold on
plot(time(E1,1), data(E1,RIZ)./1e3,'-b')
plot(time(E2,1), data(E2,RIZ)./1e3,'-m')
plot(time(E3,1), data(E3,RIZ)./1e3,'-g')
plot(time(E4,1), data(E4,RIZ)./1e3,'- k')
hold off
title('Raw data with overlay of extracted electrode specific data')
xlabel('Time [min]')
ylabel('|Z| [kOhm]')
legend('Raw data',txtE1,txtE2,txtE3,txtE4)

%% Moving average filter

% Simple average of data columns 11-18
window_size = 12;
```

```
filter_E11 = tsmovavg(data(E1,11:18),'s',window_size,1);
filter_E22 = tsmovavg(data(E2,11:18),'s',window_size,1);
filter_E33 = tsmovavg(data(E3,11:18),'s',window_size,1);
filter_E44 = tsmovavg(data(E4,11:18),'s',window_size,1);
% sorting data
filter_E1 = data(E1,:); filter_E1(:,11:18) = filter_E11;
filter_E2 = data(E2,:); filter_E2(:,11:18) = filter_E22;
filter_E3 = data(E3,:);filter_E3(:,11:18) = filter_E33;
filter_E4 = data(E4,:);filter_E4(:,11:18) = filter_E44;

figure(2)
plot(1:length(E1), data(E1,RIZ),'-b')
hold on
plot(1:length(E2), data(E2,RIZ),'-m')
plot(1:length(E3), data(E3,RIZ),'-g')
plot(1:length(E4), data(E4,RIZ),'-k')
plot(1:length(E1), filter_E1(:,RIZ),'-r')
plot(1:length(E2), filter_E2(:,RIZ),'-r')
plot(1:length(E3), filter_E3(:,RIZ),'-r')
plot(1:length(E4), filter_E4(:,RIZ),'-r')
hold off
title(['Chip ',num2str(chipnr), ' - Extracted data with running ...
    average'])
legend(txtE1,txtE2,txtE3,txtE4, 'Running average')
xlabel('data point')
ylabel('|Z|')

%% Removing drift

% t_E1 = 1:length(E1);

sdata_E1 = filter_E1(12:end,RIZ);
t_E1 = 1:length(E1);
detrend_E1 = detrend(sdata_E1);
trend_E1 = sdata_E1 - detrend_E1;


sdata_E2 = filter_E2(12:end,RIZ);
t_E2 = 1:length(E2);
detrend_E2 = detrend(sdata_E2);
trend_E2 = sdata_E2 - detrend_E2;

sdata_E3 = filter_E3(12:end,RIZ);
t_E3 = 1:length(E3);
detrend_E3 = detrend(sdata_E3);
trend_E3 = sdata_E3 - detrend_E3;

sdata_E4 = filter_E4(12:end,RIZ);
t_E4 = 1:length(E4);
```

```
detrend_E4 = detrend(sdata_E4);
trend_E4 = sdata_E4 - detrend_E4;


figure(222)
plot(1:length(E1), data(E1,RIZ),'-r')
hold on
plot(t_E1(12:end),sdata_E1,'-b');
plot(t_E1(12:end),trend_E1,':r')

plot(1:length(E2), data(E2,RIZ),'-r')
plot(t_E2(12:end),sdata_E2,'-m');
plot(t_E2(12:end),trend_E2,':r')

plot(1:length(E3), data(E3,RIZ),'-r')
plot(t_E3(12:end),sdata_E3,'-g');
plot(t_E3(12:end),trend_E3,':r')

plot(1:length(E4), data(E4,RIZ),'-r')
plot(t_E4(12:end),sdata_E4,'-k');
plot(t_E4(12:end),trend_E4,':r')
legend('Original Data','Filtered data','Trend')
xlabel('data point')
ylabel('|Z|')


figure(223)
plot(t_E1(12:end),detrend_E1,'b')
hold on
plot(t_E2(12:end),detrend_E2,'m')
plot(t_E3(12:end),detrend_E3,'g')
plot(t_E4(12:end),detrend_E4,'k')
title(['Chip ',num2str(chipnr), ' - Data with removed drift'])
legend(txtE1,txtE2,txtE3,txtE4)
xlabel('data point')
ylabel('|Z|')
%% Normalizing data in percent

x_E1 = detrend_E1(1:100,:);
x_E1_all = abs(min(detrend_E1(:,:)))+detrend_E1(:,:) ;
x_E1_null = abs(min(x_E1))+x_E1
m_E1 = mean(x_E1_null);
normP_E1 = 100 .* (x_E1_all-m_E1) ./ m_E1;

x_E2 = detrend_E2(1:100,:);
x_E2_all = detrend_E2(:,:);
m_E2 = mean(x_E2);

normP_E2 = 100 .* (x_E2_all-m_E2) ./ m_E2;
```

```
x_E3 = detrend_E3(1:100,:);
x_E3_all = detrend_E3(:,:);
m_E3 = mean(x_E3);
normP_E3 = 100 .* (x_E3_all-m_E3) ./ m_E3;

x_E4 = detrend_E4(1:100,:);
x_E4_all = detrend_E4(:,:);
m_E4 = mean(x_E4);
normP_E4 = 100 .* (x_E4_all-m_E4) ./ m_E4;

figure(3)
plot( 1:length(normP_E1), normP_E1(:,1), '-b')
hold on
plot( 1:length(normP_E2), normP_E2(:,1), '-m')
plot( 1:length(normP_E3), normP_E3(:,1), '-g')
plot( 1:length(normP_E4), normP_E4(:,1), '-k')
hold off
legend(txtE1,txtE2,txtE3,txtE4)
title(['Chip ',num2str(chipnr), ' - EIS detection of 1 mM penicillin'])
xlabel('Number of data points')
ylabel('Relative change in percent [%]')
```

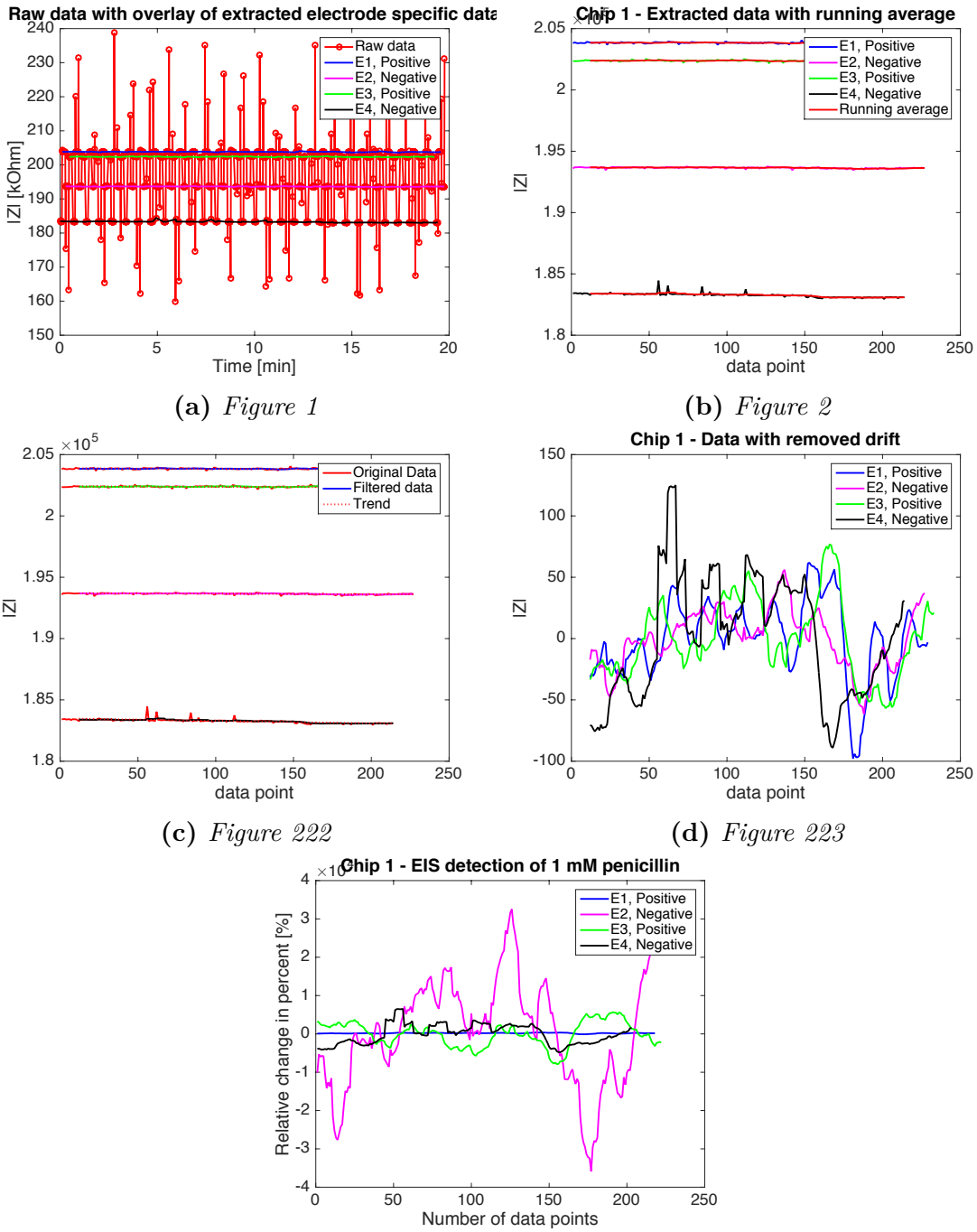

(a) *Figure 1*

(b) *Figure 2*

(c) *Figure 222*

(d) *Figure 223*

(e) *Figure 3*

Figure A.19: *MATLAB figure output for EIS data analysis*

A.13 Plotting of model and data by MATLAB

Matlab script for plotting of model and data:

```
%%%%%%%%%%%%%%%%%%%%%%%%%%%%%%%%%%%%%%%%%
% Julie Kirkegaard, julki, Lyngby 2016 %
%%%%%%%%%%%%%%%%%%%%%%%%%%%%%%%%%%%%%%%%%
clear all
close all
clc

set(0,'defaultlinelinewidth',1.9)
set(0,'DefaultAxesFontSize',25)
%% Loading data and calculate the phase and modulus
data_E3 = load('sweep_e4_1-1000_pbs_2_matlab.txt');

%Modulus and phase of data
    data_E3(:,7) = abs(data_E3(:,3) + 1i*data_E3(:,4));
    data_E3(:,8) = angle(data_E3(:,3) + 1i*data_E3(:,4)).*(180/pi);

% column explanation of data:
% 1 Number
% 2 Frequency/Hz
% 3 impedance R/Ohm
% 4 impedance I/Ohm
% 5 Significance
% 6 Time/s
% 7 Modulus
% 8 Phase

%% Simulation
% elements from simulation
C1 = 1.16e-9;
R1 = 61e3;
R2 = 190e3;
W = 1.1e6;
CPE1 = 3.7e-6;
n1 = 0.93;

freq = data_E3(:,2);

%impedance of the elements
Z_C1 = 1./(1i*freq*C1);
Z_W = W * freq.^(-1/2) *(1-1i);
Z_CPE1 = 1./((1i*freq).^n1 *CPE1);

%impedance of parallel connections
Z_C1_R2 = 1 ./ (1./Z_C1 + 1/R2);
```

```
45 Z_R1_W1 = 1 ./ (1/R1 + 1 ./ (Z_W) );

47 % total impedance
   Z_total = Z_C1_R2  +  Z_R1_W1 + Z_CPE1;
49
   % components of total impedance
51 Z_real = real(Z_total);
   Z_img = imag(Z_total);
53 Z_mod  = sqrt(Z_real(:,1).^2 + Z_real(:,1).^2);
   Z_phase  = atan(Z_img(:,1)./Z_real(:,1)).*(180/pi);
55
   %%
57 freq_range = [1:46]; % frequency index range plotted

59 figure(1)
   h(1) = plot(  data_E3(freq_range,3)/1000 , ...
      -1*data_E3(freq_range,4)/1000,'-*b');
61 hold on
   h(2) = plot(  Z_real(freq_range,1)/1000 , ...
      -1*Z_img(freq_range,1)/1000,'-*r');
63 set(gca,'DataAspectRatio',[1 1 1])
   xlabel('Z_{Re} [kOhm]')
65 ylabel('- Z_{Im} [kOhm]')
   legend('Data','Model')
67 ylim([0 520])
   xlim([0 350])
69 hold off

71 figure(2)
   semilogx( data_E3(freq_range,2) , data_E3(freq_range,7)/1000,'-*b')
73 hold on
   semilogx( freq(freq_range,1) , Z_mod(freq_range,1)/1000,'-*r')
75 ylabel('|Z| [kOhm]')
   xlabel('Frequency [Hz]')
77 legend('Data','Model')
   xlim([0.5 100000])
79 hold off

81 figure(3)
   semilogx( data_E3(freq_range,2) , data_E3(freq_range,8),'-*b')
83 hold on
   semilogx( freq(freq_range,1) , Z_phase(freq_range,1),'-*r')
85 ylabel('Phase(Z) [Degree]')
   xlabel('Frequency [Hz]')
87 legend('Data','Model')
   xlim([0.5 100000])
89 hold off
```

— B —

Aptamer sequences

The aptamers listed here are the aptamers used in the experimental sections of the thesis. The aptamer sequence is listed in bold and the modifications: TC-tag, spacer and dye in normal font.

B.1 HNV-VP1

Sequence: TTTTTTTTTTCCCCCCCCCC /iSp12/**GCCTCTTGTGAGCCTCCTAAC GTCTGTAGTAGGGAGGATGGTCCGGGGCCCCGAGACGACGTTATCAGGCC ATGCTTATTCTTGTCTCCC** [7]

B.2 VP1T

Sequence: TTTTTTTTTTCCCCCCCCCC /iSp12/**GTCTGTAGTAGGGAGGATGG TCCGGGGCCCCGAGACGACGTTATCAGGC** [7]

B.3 SMV-25

Sequence: TTTTTTTTTTCCCCCCCCCC /iSp12/**CATCTGTGTGAAGACTATATGG CGCTCACATATTTCTTTC** [8]

B.4 A22-trunk aptamer

Sequence: TTTTTTTTTTCCCCCCCCCC /iSp12/ **CTGAGTCTCAAAACCGC AATACACTGGTTG** [45]

B.5 Amp3

Sequence: ATTO550/TTTTTTTTTTCCCCCCCCCC/iSp12/**GCGGGCGGTTGTAT AGCGG** [88]

Published by:
DTU Nanotech
Department of Micro- and Nanotechnology
Technical University of Denmark
Ørsteds Plads, building 345C
DK-2800 Kgs. Lyngby